TESIS DE LA UNIVERSIDAD DE ZARAGOZA

2014

43

Lamiaa Mohamed Ahmed Ali

Toxicity Studies of Polymer Based Supermagnetic Iron Oxide Nanoparticles

Departamento

Física de la Materia Condensada

Director/es

Palacio Parada, Fernando
Gutiérrez Martín, Martín

ISSN 2254-7606

Prensas de la Universidad Universidad Zaragoza

Universidad Zaragoza
1542

Tesis Doctoral

TOXICITY STUDIES OF POLYMER BASED SUPERMAGNETIC IRON OXIDE NANOPARTICLES

Autor

Lamiaa Mohamed Ahmed Ali

Director/es

Palacio Parada, Fernando
Gutiérrez Martín, Martín

UNIVERSIDAD DE ZARAGOZA

Física de la Materia Condensada

2014

Toxicity Studies of Polymer-Based Superparamagnetic Iron Oxide Nanoparticles

Colección de Estudios de Física

Vol. XX

Esta colección recoge las tesis presentadas en el Departamento de Física de la Materia Condensada de la Universidad de Zaragoza desde su constitución en 1987.

Colección de Estudios de Física Vol. XX

Toxicity Studies of Polymer Based Superparamagnetic Iron Oxide Nanoparticles

Lamiaa Mohamed Ahmed Ali

Prensas Universitarias
Universidad Zaragoza

Aquí va la hoja de créditos...

Thesis realised under the supervision of

Prof. Fernando Palacio Parada
Instituto of Ciencias de Materiales de Aragón y Departamento de Física de la Materia Condensada, Facultad de Ciencias.

Prof. Martín Gutiérrez Martín
Departamento de Medicina, Facultad de Medicina.

Table of contents

Preface

Over the past decades, *nanotechnology* became one of the most important scientific research areas, which has extended to many aspects of life (industrial, medical, biological, etc.), exploiting the unique physicochemical properties offered by the nanomaterial. Beside the involvement of the nanomaterials in the medical field, *nanomedicine*, the last few years witnessed a tangible progress in the production of consumer products that contain nanomaterials. Nowadays, more than 1000 consumer products containing nanomaterials are available in the market such products are, personal care products (e.g. sunscreen, skin lotions, etc.), food additives, cleaning products, sealants, paints, electronics, fuel cells, tires and many other products. Unfortunately, this vast use contrasts with the limited attempts to evaluate the harmful effects of nanomaterial on public health and environment. This fact highlights the need and importance of *nanotoxicology*.

Along the thesis, we will explore the toxicity of engineered SPIONs based on polymeric route on, cells, blood and organs, as necessary steps for the development of a new nanomaterial. This work occupies the thesis that encompasses of five chapters.

Chapter 1 has the title **"General Introduction and Purpose of the Thesis".** This chapter is a general introduction including the basic definitions of nanotechnology, nanomedicine and nanotoxicology. It displays the importance of nanomedicine in solving several medical and pharmaceutical problems, and the great impact of the use of nanomaterials at the therapeutic and diagnostic levels. Also, explains the magnetic properties of magnetic nanoparticles followed by some examples of the impact of the use of superparamagnetic iron oxide nanoparticles at the diagnostic and therapeutic levels. In addition, in this chapter we discuss the cautions and the steps to be aware of during designing a new nanomaterial. Then, we review the importance of the nanotoxicity studies provided with some examples of the effect of nanomaterials on the cells, blood, environment, etc. Finally, the chapter explains the main purpose of the thesis and describes the general features of the materials to be used.

Chapter 2 has the title of **"In vitro cytotoxicity studies of superparamagnetic**

iron oxide nanoparticles". This chapter starts with an introduction about the nanotoxicology, viewing some examples about nanohazards and their effect on the public health, which in turns underline on the importance of the preventive measures and the nanotoxicology studies. In addition, explaining some of the items of study involving in nanotoxicology such as route of exposure and toxicological mechanisms of nanomaterials. The introduction section ends with explaining the tests used for cytotoxicity studies. The main purpose of this chapter is to study the toxicological behaviour of our bioferrofluids *in vitro* using various toxicological assays. This chapter displays the influence of many factors on the nanoparticles toxicity in cells such as cell type, bead hydrodynamic size, maghemite nanoparticle size, polymer/iron ratio, etc. In addition, discloses that the cell death is due to necrosis, with no evidence of reactive oxygen species production, and the small nanoparticles have an inflammatory effect compared with large ones, which are recommended to be used for further studies due to their lower toxic effect in compared to other sizes.

Chapter 3 has the title of **"Studies at the nano-bio interface level: uptake, subcellular localisation and endocytosis"**. The chapter starts with an illustration of the importance of this type of studies, explaining the main components of the nano-bio interface, the factors affect the nanomaterial internalisation and mechanisms of endocytosis. The main purpose of this chapter is to understand the cytotoxicity caused by our bioferrofluids through studying the nanoparticles uptake and the uptake kinetics, subcellular localisation and mechanism of endocytosis. This chapter displays the influence of many factors on the nanoparticles uptake in cells such as nanoparticles size, cell type, nanoparticles concentrations and time of incubation. The obtained results explain the size and cell type dependent toxicity caused by our bioferrofluids. At the subcellular level, our nanoparticles exist in the endolysosomal compartments and the clathrin-dependent endocytosis is the mechanism that is responsible for nanoparticles internalisation.

Chapter 4 has the title of **"In vitro haemocompatibility studies of superparamagnetic iron oxide nanoparticles".** This chapter shows that the nanomaterial could act either as a pro-coagulant or hypo-coagulant agent, which in

turn, shed the light on the importance of this kind of studies, especially for nanomaterials that are developed for intravenous administration**.** A brief illustration for the blood coagulation mechanism, regulatory mechanisms and coagulation screening tests are also provided. The main purpose of this chapter is to study the toxicity of three different types of polymer coated SPIONs and their separated component in blood. This chapter displays the influence of the surface coating and surface charge on the toxicity behaviour of the bioferrofluids. The three types of bioferrofluids exhibit anticoagulant effect, with no effect on the blood count *in vitro*. No incidence of haemolysis was detected.

Chapter 5 has the title of **"Biodistribution studies of polymer coated superparamagnetic iron oxide nanoparticles"**. This chapter starts with a brief review about the biomedical imaging and MRI, with an illustration of the basic principles of MRI and contrast agents. In addition, this chapter discusses the factors affecting the biodistribution of the nanomaterials. The aim of this chapter is to study the *in vitro* relaxation, in vivo biodistribution, and in vivo toxicity for two polymer coated SPIONs. The obtained results showed that our bioferrofluids are a good T_2 contrast agents with no toxic effect *in vivo*.

Chapter 1

General Introduction and Purpose of the Thesis

1.1 Nanotechnology, nanomedicine and nanotoxicology terms

Nanotechnology has garnered a great interest in last decades. According to the United States (US) Nanotechnology Initiative, Nanotechnology can be defined as "the understanding and control of matter at dimensions of roughly 1–100 nanometers, where unique phenomena enable novel applications" [1]. Nanomaterials have a size comparable to the size of the sub-cellular organelles and proteins Fig. 1.1, hence, they could be exploited to spy or interfere with the cellular machinery giving rise to a new branch of science called "nanomedicine" [2].

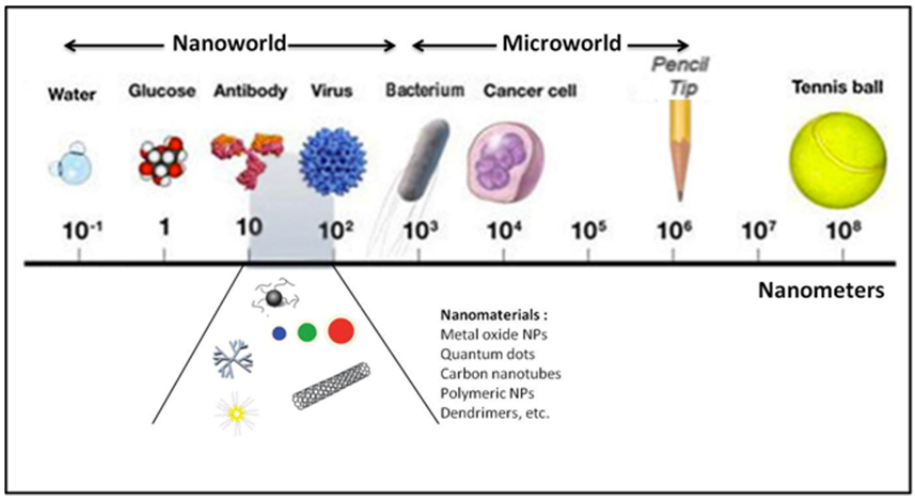

Figure 1.1: Demonstration of the nanomaterials sizes compared with other items [3].

The European Science Foundation (ESF) in its Forward Look Nanomedicine document defined *nanomedicine* as the following "nanomedicine uses nano-sized tools for the diagnosis, prevention and treatment of disease and to gain increased understanding of the complex underlying patho-physiology of disease" [4].

Although, the unique physicochemical properties of nanomaterials have a great positive impact on biomedical applications, the same properties can have a negative impact on the biosystem, since nanomaterials are characterised by a high surface to volume ratio, which may lead to increase their biological reactivity. In addition, their nano-size enables them to breach cells reaching critical sites inside, such as nucleus, mitochondria, etc., which may cause mutations or cell death [5].

Besides the environmental exposure to airborne nano-sized materials coming from natural or anthropogenic sources [6], the rapid evolution in nanotechnology, which extends to many applications (biological, medical and industrial) [5,7,8], increases the risk of exposure. The issue of nanomaterials safety and nanotoxicity should be addressed, as a lesson learned from the medical science´s failure in the past centuries to take safety measures toward quartz and asbestos exposure [9]. Therefore, a new sub-discipline of the nanotechnology called *nanotoxicology* has emerged. Nanotoxicology could be defined as "science of engineered nanodevices and nanostructures that deals with their effects in living organisms" [6].

We can conclude that nanotechnology, nanomedicine and nanotoxicology are three interconnected and closely dependent fields. Therefore, as any new nanomaterial can have an impact on the biological environment with consequences in the medical field, a series of toxicology studies should be carried during its development process. Therefore, for any nanomaterial developed for biomedical applications, toxicological studies should include: synthesis and characterisation with the possibility to minimise batch to batch variation, studying nanomaterial toxicity on cells (*in vitro*), studies of nanomaterial uptake and mechanism of internalisation (endocytosis), studies of nanomaterial toxicity on blood (haemotoxicity) particularly if the nanomaterial is developed for intravenous (iv) injection, studies of the nanomaterial biodistribution (*in vivo)* and their possible toxic effects on tissues and organs, evaluation of their

application (therapeutic or diagnostic) efficiency and finally studying their toxic effect on the environment.

As explained in more detail at the end of this chapter, this thesis will deal with some of these studies as a necessary step in the group for the development of a synthetic nanoplatform for biomedical applications. Along the thesis it will become clear that toxicological issues often depend of properties that are independent of the materials composition, e.g, aggregation and surface charges, in addition to their composition itself. Additionally, nanomaterials can be rather complex systems with a variety of components whose individual toxicity should also be addressed. There is therefore an interrelation between the nanomaterial, its components toxicity and its effects on the biological system it is being developed for.

In the following sections we will revise each of these four fundamental aspects: nanomedicine, magnetic nanoparticles, nanomaterials and their design and nanotoxicity.

1.2 Nanomedicine: a new way to address open medical and pharmaceutical problems

There are many medical problems still waiting to be solved that are associated either with the diagnosis and/or with the treatment of some diseases. For instance, in the case of cancer, early diagnosis is considered a challenge in its treatment, which in many cases is not reached. Moreover, traditional cancer treatment methods (radiotherapy or chemotherapy) are associated with several complications such as the lack of efficient selectivity toward cancerous cells causing systemic toxicity [10]. Another treatment limitation is the inability of chemotherapy to overcome the multidrug resistance (MDR) mechanism -a mechanism of drug efflux from the cancerous cell cytoplasm to the extracellular space- that is associated with several tumour cells leading to treatment failure [11].

Nanomedicine opens new hopes in solving diagnostic and therapeutic problems by developing nanomedicines -an overall term that includes nanopharmaceuticals,

nanoimaging agents, and theranostics[1] [12]-, and exploiting new physicochemical properties, since at the nano-level the material can acquire new properties (electrical, optical or magnetic) not present in the bulk state [13].

Nanomedicines can be organic such as liposomes, micelles, dendrimers, polymeric nanoparticles, fullerenes and carbon nanotubes or inorganic such as magnetic nanoparticles, metal based nanoparticles, ceramic nanoparticles and semiconductors. This versatility in composition and physicochemical properties opens the door for a wide range of medical applications [14]. Therefore, the second half of the 20th century witnessed the birth of the first generation of marketed nanomedicines, their use is varying between diagnosis and therapy, as shown in Table 1.1 where only those related to iron oxide are collected. A rather comprehensive account of nanomedicines already in the market can be found in ref. [12].

1.2.1 Therapeutic nanomedicines

The onset of the use of nanomedicines as therapeutic agents dates back to fifties, when the first polymer-drug-conjugate was synthesised by Jatzkewitz. This was a breakthrough in the manufacturing of nanomedicines as depicted in Fig. 1.2 [15]. The use of nanomaterials as therapeutic agents is a diverse field, ranging from drug/gene delivery systems, antimicrobial agents to antioxidant agents [2,12,16,17].

Traditional delivery strategies for certain drugs (especially anticancer) are associated with many prominent problems such as lack of selectivity which in turns is reflected on the toxicity, failure to avoid MDR mechanism, low bioavailability, the necessity of large dose to achieve high local concentration and fail to improve drug solubility [18]. Nanomedicine reduces these previous problems improving drug delivery strategies. This is achieved by drug encapsulation, surface conjugation or entrapment to the nanomaterials forming "***targeted***" drug delivery systems.

As a result, these approaches transport drugs more efficiently to the target site, increase the local concentration of the drug in the target site, improve drug solubility

[1] Theranostic is a nanomedicine concept which refers to the capacity of a product to act as a diagnostic and therapeutic tool simultaneously.

Table 1.1: First generation of marketed iron oxide-based nanomedicines [12]**.**

Product name	Technology	Indication	Route of admin.	Information source
Superparamagnetic Iron Oxide Imaging Nanoparticles (SPIONS)				
Feridex (ferumoxide)	SPION dextran coating	liver imaging	iv	Bayer Healthcare Pharmaceuticals
Endorem (ferumoxide)	SPION dextran coating	liver imaging	iv	AMAG Pharmaceuticals/Guerbet SA[a]
Gastromark (ferumoxsil)	SPION silicone coating	GI imaging	oral suspension	AMAG Pharmaceuticals [a]
Lumirem (ferumoxsil)	SPION silicone coating	GI imaging	oral suspension	AMAG Pharmaceuticals [a]
Sinerem (ferumoxtran), same as Combidex	ultrasmall particles (USPION)	lymph node imaging	infusion	Guerbet withdrew MAA for Sinerem in 2007 AMAG Pharmaceuticals (phase III)
Resovist	SPIONs	small liver lesions	iv	Bayer Healthcare Pharmaceuticals
Iron Oxide Supplements				
Venofer	iron oxide, sucrose	anemia	iv	Fresenius[a]
Ferrlecit	iron oxide gluconate	anemia	iv	Sanofi-Aventis[a]
Cosmofer	iron oxide, dextran	anemia	iv	GRY-Pharma[a]
various "generic" formulations	iron oxide nanoparticles	anemia	iv	reviewed in refs 508, 509

and protect the drug from degradation. They also open the possibility to deliver a combination of drugs for a combination therapy, or to monitor the drug delivery by delivering a combination of imaging and therapeutic agents, and therefore all these previously mentioned advantages lead to increase patient compliance [18,19].

Drug targeting using nanomedicines is achieved by either passive or active targeting mechanism. Passive targeting is divided into two mechanisms: a) enhanced permeability and retention (EPR) mechanism, which exploits the leaky vasculature of tumour cells [20], b) localised delivery mechanism by intra-tumour injection of drugs conjugated to nanomaterials [21]. However, active targeting is achieved by direct conjugation of the nanomaterials to various *signature molecules*[2] *recognisers* such as ligand [22], antibody [23] or aptamer [24], in order to trigger nanomedicines to specific pathological site.

All the first generation marketed nanomedicines are passively targeted. For instance, Doxil (liposomes-encapsulated doxorubicin), was approved by the US Food and Drug Administration (FDA) in 1995. It triggered drug targeting through EPR mechanism and was used for the treatment of advanced ovarian cancer, metastatic breast cancer and HIV-treated Kaposi´s sarcoma [15]. Although more than 30 years have passed since the first description of ligand conjugated liposomes in 1980, only a handful of active targeted nanomedicines have reached to the clinical trial area, and none have made a significant clinical impact on human health [12,25].

Continual advances in nanofabrication lead to production of nanomedicines not only able to protect the cargo from unfavourable conditions but also controlling its release as a response to physical or chemical stimuli such as light, heat, sonication, magnetic field, pH and redox change [26]. In addition, elongation for blood circulation time could be achieved through polymer coating [27].

An additional merit for nanomedicines as targeted drug delivery system is their ability to deliver drugs across blood brain barrier (BBB) [28]. The delivery property of nanomedicines is not limited to drugs only but also extended to genes [29] and

[2] Signature molecules are biological molecules found in blood, other body fluids or tissues, which are signs of a normal or abnormal process, or of a condition or disease.

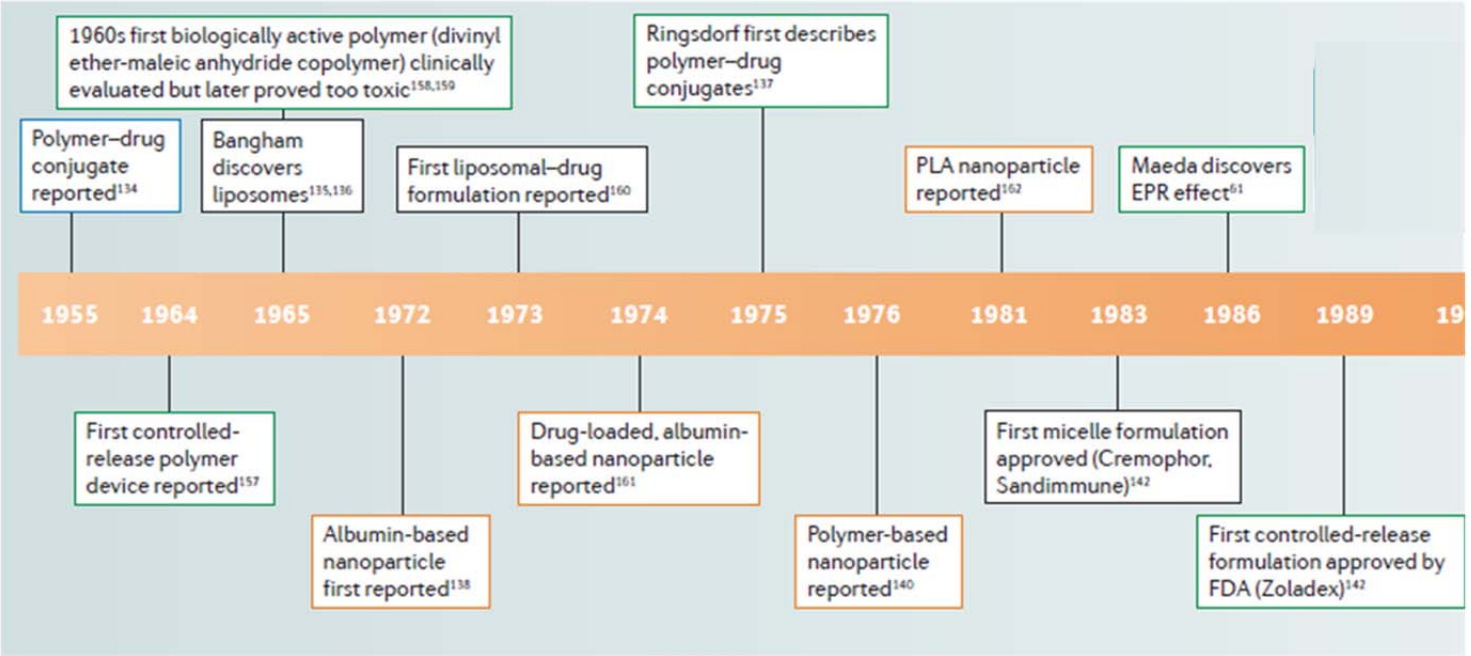

Figure 1.2: Timeline of nanomedicines development [15].

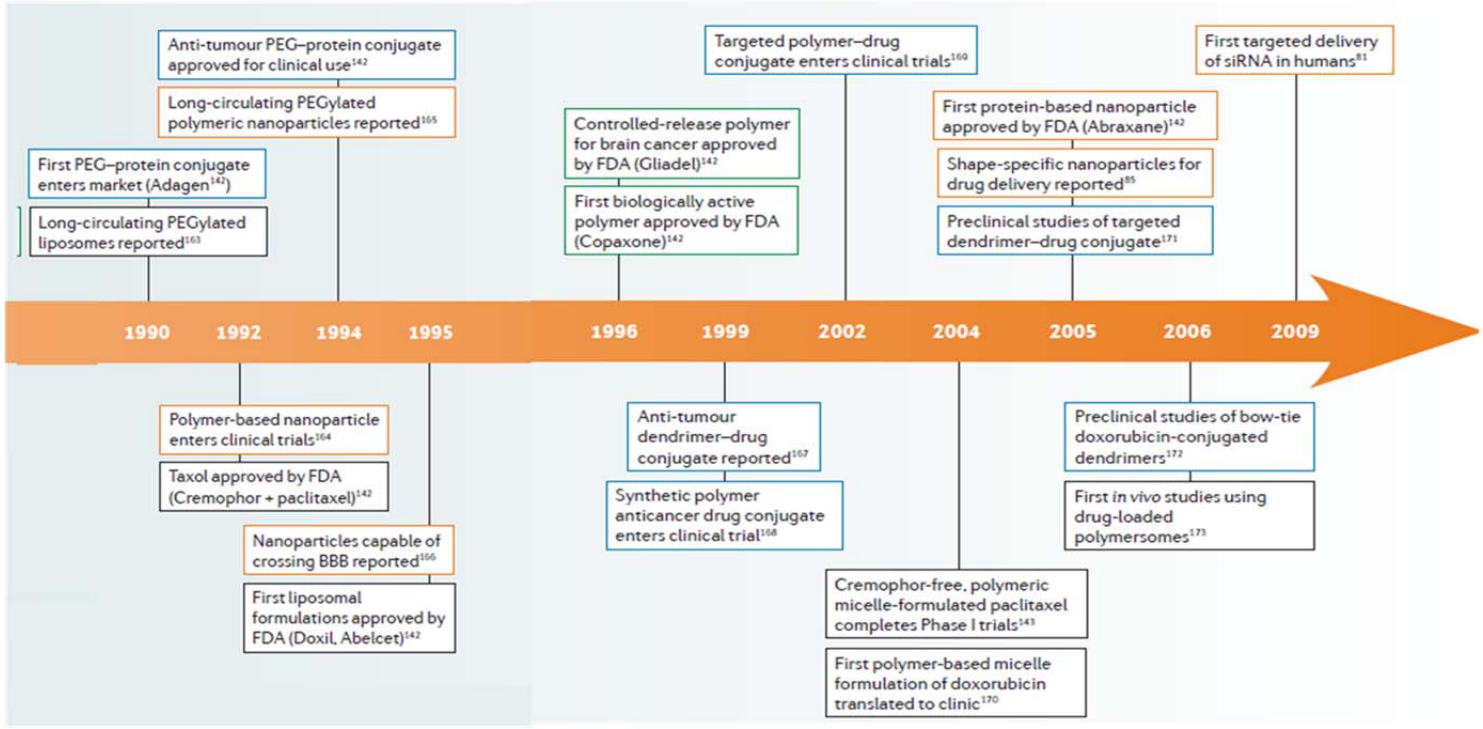

Figure 1.2 (continue): Timeline of nanomedicines development [15].

vaccines [30]. In addition, nanomedicines could also act as agents for hyperthermia [31], tissue engineering helper [32], antimicrobial agents [33], antioxidant agents [34] and they may be consider as an active drug material by themselves [35].

1.2.2 Diagnostic nanomedicines

Next to the therapeutic potential of nanomedicines, they are equally attractive as diagnostic tools either *in vivo*, *ex vivo*, or *in vitro*. Nanomedicines can serve as contrast agents for molecular imaging *in vivo*, thanks to their unique physicochemical properties whether optical [36,37] or magnetic properties [38], or due to their ability to conjugate to fluorescent markers [39]. Detection and/or measurement of a biological molecule were considered another challenge for nanomedicines that has been successfully achieved, as nanomedicines are involved in biosensing [40], lateral-flow immune assay (LFA) [41] and bio-barcode assays [42].

1.3 Magnetic nanoparticles (MNPs)

MNPs are a class of engineered nanomaterials that can be manipulated under the influence of an external magnetic field. They are composed of magnetic elements, such as metals (Fe, Co, Ni), metal oxides (ɣ-Fe_2O_3, Fe_3O_4, $CoFe_2O_4$, CrO_2) and metal alloys (FePt, FeCo, CoPd, CoNi, NiCoPd) [43].

Due to their unique magnetic properties and their ability to function at the molecular and cellular level, certain MNPs are considered an attractive platform for medical applications [44]. In addition, they are important in basic research [45], industrial and environmental applications [46]. Iron oxide maghemite (ɣ-Fe_2O_3) and magnetite (Fe_3O_4) are the most commonly used MNPs for biomedical applications because of their biocompatibility and suitable superparamagnetic properties.

The magnetic properties of MNPs are consequence of the nanomaterial electronic state. In a magnetic material, the open shell electrons possess two important characteristics: their spin state, which gives rise to a magnetic moment, and the magnetic interactions with neighbour ions. Depending on the material composition and temperature either one or both characteristics will affect the magnetism of the

material. If there are no magnetic interactions or they are too weak as compared to the thermal energy, the material will be *paramagnetic*, as depicted in Fig. 1.3(a). However, if interactions are strong enough to propagate through the material, then they will induce magnetic ordering. *Ferromagnets* and *ferrimagnets* are examples of ordered magnetic materials with important industrial applications. They are commonly known as *magnets* and characterise by, in general, possessing strong magnetisation. In the case of ferromagnets, the magnetisation is the result of the parallel alignment of all the magnetic moments in the material Fig. 1.3(b). Ferrimagnets, as ɣ-Fe_2O_3 and Fe_3O_4 however, are composed of ions with at least two different magnetic moments which align anti-parallel to one another Fig. 1.3(c). This results in the formation of two magnetic sub-lattices whose respective magnetisations do not compensate to each other. This unbalance in the sub-lattices magnetisation leads to a net magnetisation in the solid. In the bulk, materials with a net magnetisation minimise their free magnetic energy by splitting their magnetic structure into domains, as shown in Fig. 1.4.

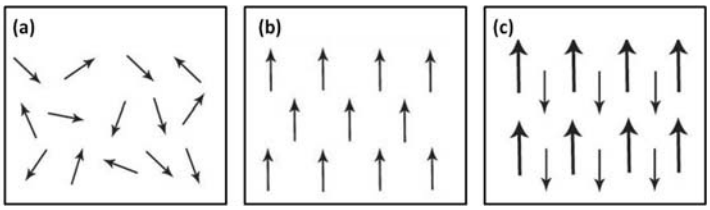

Figure 1.3: Magnetic moment orientations: (a) paramagnetic, the magnetic moments are randomly oriented in the absence of the magnetic field; (b) ferromagnetic, the magnetic moments align parallel to each other under the influence of an external magnetic field; (c) ferrimagnetic, there is more than one type of magnetic ions that align anti-parallel without cancelling each other.

The orientation of each domain magnetisation varies among domains giving a zero total magnetisation at zero magnetic field. If the magnetic material has a size lower than the size of a typical domain, about 20 nm, its behaviour will resemble that of a paramagnet in a large temperature region and it will be called *superparamagnet*. Differences will be a huge magnetic moment and the difficulty to follow an alternating magnetic field below a given temperature known as *blocking temperature*, T_B [2].

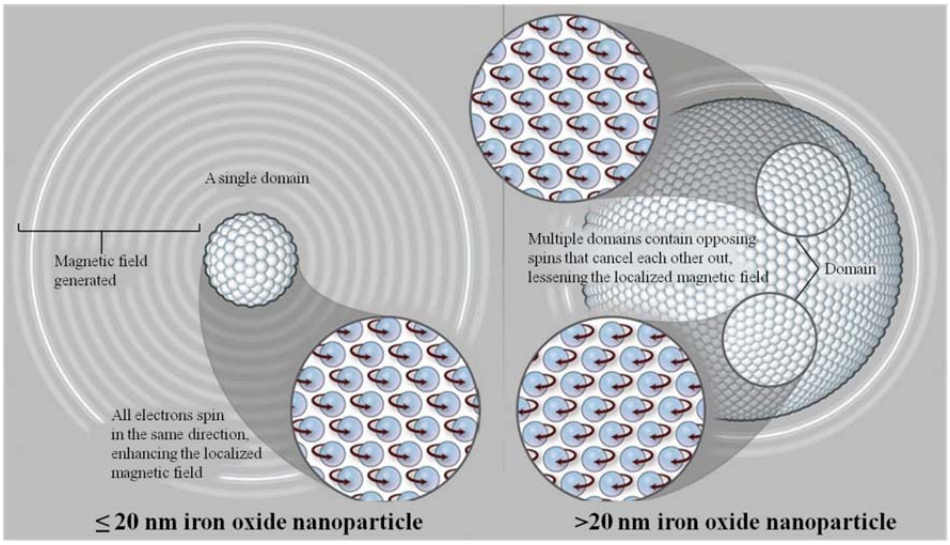

Figure 1.4: Size dependent magnetic properties of magnetic nanoparticles [2].

1.3.1 Superparamagnetic iron oxide nanoparticles

Iron oxide nanoparticles (IONPs) of sizes of about 20 nm and below are generally named superparamagnetic iron oxide nanoparticles due to their superparamagnetic nature. Therefore, SPIONs have a much larger net magnetic moment as compared to that of paramagnetic ions [2]. Due to their acceptable compatibility with biological systems, SPIONs are a subclass of MNPs considered of interest for biomedical applications.

1.3.1.1 Medical and biological applications of superparamagnetic iron oxide nanoparticles

Interest on SPIONs has dramatically increased since the last decades. Due to their reduced toxicity, large magnetic moments and superparamagnetic properties, they can be used in many medical applications which can be summarised as moving, sensing, image contrast and heating. Furthermore they can be functionalised with drugs, bioactive agents, peptides and nucleic acids making them a useful theranostic tool

[47]. These multi-functionalities are summarised in Fig. 1.5 and explained in the next paragraphs.

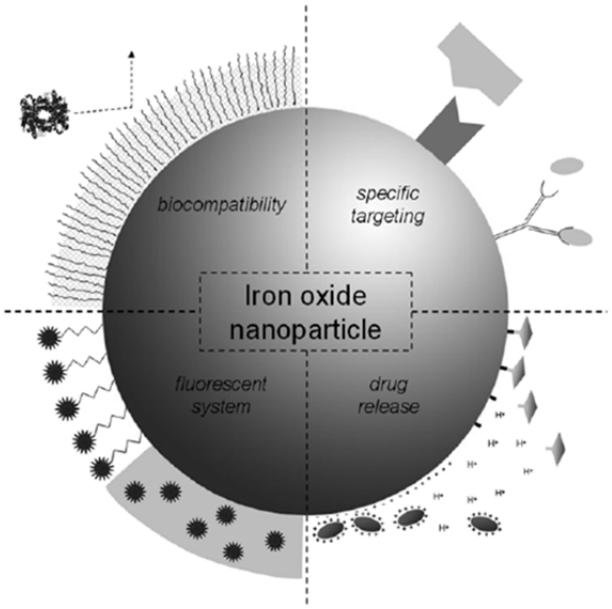

Figure 1.5: Overview of possible modifications on iron oxide nanoparticle surface in order to design a nanoprobe for biomedical applications [48].

1.3.1.1.1 Use of superparamagentic iron oxide nanoparticles in diagnosis

1.3.1.1.1.1 Magnetic resonance imaging (MRI) contrast agent

MR imaging is one of the most useful non-invasive diagnostic tools, which is characterised by high resolution of soft tissues and non-exposure to radiation [49]. Contrast agents used in MRI are divided into two classes: (i) superparamagnetic contrast agents and (ii) paramagnetic complexes contrast agent. Superparamagnetic contrast agents, such as SPIONs, have a strong effect on the local longitudinal (T_1) and transversal (T_2) relaxation times of the protons, with a more pronounced effect on T_2.These agents normally appear hypointense in the final image (negative contrast). The second class of contrast agents are paramagnetic compounds of high spin magnetic ions such as gadolinium, that mainly reduces the T_1 relaxation time and results in a brighter signal (hyperintense) in the final image (positive contrast) [50]. The use of SPIONs as contrast agent has advantages over the use of more conventional paramagnetic gadolinium based solutions, as they have lower toxicity and sub-nanomolar range detection limits, exceeding that of gadolinium by a factor of 100 as a result of their superparamagnetic properties [51].

Thus far, several SPIONs preparations have already been used for clinical practice, especially for liver MRI, such as Ferumoxides (i.e. Endorem® in Europe, Feridex® in the USA and Japan) coated with dextran [52], and Ferucarbutran (i.e. Resovist® in Europe and Japan) coated with carboxydextran [53], currently, these suspensions are discontinued. Furthermore, several SPION preparations have been investigated in human for imaging applications, such as: (a) Feruglose (PEG-feron, NC100150) (Clariscan^{TM}), a preparation of iron oxide particles stabilised with a coating of carbohydrate-polyethylene glycol (PEGylated starch) [54], which development has been discontinued, and (b) VSOP-C184, a very small superparamagnetic iron oxide nanoparticles coated with citrate use for angiography which it is at clinical trial phase I [55–57].

Moreover, the use of IONPs as MRI contrast agents has been exploited in interesting applications in tissue engineering (TE) and regenerative medicine (RM) such as: the *in vivo* tracking of stem cells labelled with IONPs, and the *in vivo* monitoring of transplanted tissues. These applications require a system being able to be examined over a long term (even for weeks or months). IONPs, due to their low cytotoxicity, offer this possibility [48].

MRI and MRI contrast agents are explained in detail in ***chapter 5*** *where the biodistribution of the magnetic nanoparticles studied in this thesis is discussed.*

1.3.1.1.1.2 Magnetic separation for purification and immunoassay

The property of MNPs to be remotely controlled by an external magnetic field makes them a strong candidate for cell labelling/cell separation, a technique called magnetic activated cell sorting (MACS®). In this technique, the used MNPs are attached to a ligand or an antibody for certain signature molecule that is expressed in target cells. A fluid in which the cells of interest exist is incubating with the MNPs, the solution is transferred into a column followed by application of an intense magnetic gradient. The cells of interest remain in the column attached to the MNPs while remaining cells flow through. MACS technique is helpful in cell separation and

in blood purification by removal of specific cytokines such as interleukin-1 or tumour necrosis factor. An example of cell labelling/cell separation using MNPs *in vivo* is explained by Galanzha et al [58]. They explore the role of MNPs in the detection of circulating tumour cells -a crucial problem for the development of metastasis, whose early detection has important prognostic and therapeutic implications-, they functionalised MNP with amino-terminal fragment (ATF) to target the urokinase plasminogen activator receptor (uPAR) that is expressed on many cancerous cells; these functionalised nanoparticles (NPs) facilitate the entrapment of circulating tumour cells in the blood vessels under a magnet overcoming the disadvantages associated with *ex vivo* [59] and *in vivo* [60] methods. The technique allows early diagnosis of cancer and potentially prevention of metastasis.

In addition to cell separation, MNPs can also be used in immunoassays (e.g. detection of viruses or assays for several hormones) [61].

1.3.1.1.2 Use of superparamagnetic iron oxide nanoparticles in therapy

1.3.1.1.2.1 Hyperthermia

Hyperthermia based on MNPs is one of the most promising approaches for cancer therapy. The procedure involves the dispersion of MNPs throughout the target tissue, followed by the application of an alternating magnetic field (AMF) in the radio-frequencies wave range, resulting in the conversion of magnetic energy into thermal one by hysteresis loss or Néel relaxation depending on the particle size. This heat is released to the immediately surrounding tissue, leading to increase the tumour temperature (41-46 ºC) which causes cell death by either apoptosis or necrosis. It is well established that tumour cells are more sensitive to the high temperature than healthy cells. Depending on the temperature and duration of heating hyperthermia either results in direct killing of tumour cells or increase their sensitivity to radio- or chemotherapy [62].

Conventional hyperthermia treatment (e.g. whole-body hyperthermia) inevitably damages healthy cells. MNPs based intracellular hyperthermia overcomes this shortcoming [63]. The concept of intracellular hyperthermia using dextran magnetite nanoparticles was proposed in 1979 by Gordon et al. [64]. The group at Berlin´s

Charité Hospital, led by Andreas Jordan, has been developing hyperthermia using MNPs since 1993 [65]. Nowadays, there are Clinical trials in phase II in Germany to perform hyperthermia on human patients using IONPs by direct injection hyperthermia (DIH) into two kinds of tumours: glioblastoma and prostate [66–69].

It has been reported that the nanoparticle physicochemical properties, such as size [70], surface coating [69] and charge [71] affect the specific absorption rate (SAR), which indicates the heat evolution rate in hyperthermia. In the case of magnetite, the SAR of 35 nm particles is much higher than that of 10 nm particles [70,72].

Till now, hyperthermia is commonly based on the direct injection of highly-concentrated NPs solutions into solid tumours, since the tumour passive-targeting of NPs leads to quite low particles concentration in the tumour cells. Therefore, a new trend geared toward synthesising specific targeted NPs for hyperthermia has emerged [73]. The problem of the systemic administration of these compounds is the low particle concentration within the tumour. To overcome this problem is at the forefront of current research, either by developing more efficient MNPs solution or by improving targeting.

1.3.1.1.2.2 Drug delivery

Conventional drug delivery is associated with several disadvantages such as low local drug concentration, systemic toxicity, etc. Therefore, development of new pharmaceutical techniques for targeted drug delivery has gained immense attention. MNPs are considered as a promising tool for targeted drug delivery. The magnetic functionality enables MNPs to be guided to certain target site using an external magnetic field gradient.

Targeting can also be achieved through direct conjugation of a target moiety (antibody, peptide or aptamer) to the MNP surface. Several studies showed the ability of the MNPs to deliver the drug to its target site with better therapeutic efficiency than free drugs [74]. Two strategies are followed nowadays to exploit the magnetic functionality for stimuli-responsive drug delivery of MNPs: (i) application of

oscillating magnetic field, leading the particles to warm their coating and releasing the drug (ii) the capacity of MNPs to also heat their environment can lead to accelerate drug diffusion [44,75]. The delivery ability of MNPs is not limited to drug, but also extends to genes [76].

Under correct design MNPs could act as a theranostic tool; thanks to their unique physicochemical and magnetic properties, as they would act as targeted drug/gene delivery carrier in a combination with MRI in order to monitor the delivery, and/or in combination with the hyperthermia to facilitate drug release and increase the therapeutic efficiency, or they would act by themselves as agent for hyperthermia and monitored by MRI. All these functions can be used simultaneously [77].

1.4 Hurdles in nanomaterials design for successful biomedical applications

Adequate design does not restrict just to chemical aspects, as important requirements in a nanomaterial for its use in medical applications have also to be considered. Instead, it requires a holistic approach where the exchange of information between medical doctors and biologists, chemists, physicists, and materials scientists will pave the way to achieve this goal.

This section focuses on some important aspects that should be taken into account while designing a nanomaterial for its biomedical applications.

1.4.1 Nanomaterial core

Choosing the nanomaterial core is an important issue that basically depends on the purpose of use and advantages/disadvantages considerations offered by the nanomaterial itself.

As mentioned before, there are two types of nanomaterials; organic and inorganic, both are involved in many biomedical applications, therefore, we will briefly review some examples:

- Quantum dots (QDs): they provide a mean for several biomedical

applications such as *in vivo* imaging, drug delivery, biosensing, cell labelling, immunolabelling, can be used in fluorescence resonance energy transfer (FRET) technology and serve as ideal flourophores for ultrasensitive, multicolour and multiplexing applications in molecular biotechnology and bioengineering [36,78,79]. These applications rely on the several advantages offered by QDs, such as water solubility, broad excitation spectra, tuneable emission spectra, narrow symmetric emission spectra and high photostability [80]. However, the toxicity of some QDs is one of the biggest obstacles for their use in biological systems [81].

- Superparamagnetic iron oxide nanoparticles: they offer attractive biomedical applications such as contrast agent for MRI [82], targeted drug and gene delivery system [83], agents for hyperthermia [69], bioseparation [84], immunisation [85], tissue repair [86] and detoxification of biological fluids [87]. Such a large variety of uses for an inorganic nanomaterial arises from their magnetic functionality, high field irreversibility, high saturation field, low toxicity, biodegradability, deep tissue imaging and their non-invasive tool characteristics. Thus, SPIONs can be moved or fixed by magnetic field gradients, they modify the relaxation time of neighbour protons providing strong contrast enhancement in MRI and they can convert magnetic energy into heat under the effects of an AMF in hyperthermia processes with lower adverse effects than radiotherapy or chemotherapy [88].

- Liposomes: they are organic nanomaterials possessing several advantages such as amphiphilicity, biodegradability, low toxicity, ease modification and targeting potential [20]. They are, therefore, used extensively as a targeted delivery system for drugs, vaccine, anticancer and genes [89], as well as a mean for molecular imaging [90] and hyperthermia [31]. Although liposomes serve as a good model for targeted delivery, these nanomaterials are accompanied with several limitations such as lack of controlled release properties, limited drug

loading volume, oxidation of liposomal phospholipid and poor shelf stability [91].

1.4.2 Stability

The *in vitro* and *in vivo* stability of the nanomaterial suspension is an utmost important issue. In both cases, stability is achieved through grafting or adsorption of a polymeric surfactant or other modifiers to the nanomaterial surface, forming a layer that prevents nanomaterial flocculation [92]. Moreover, the polymer coating can decrease the protein adsorption to the NPs surface. As in the case of MNPs without surface modification, and according to the pH and the ionic strength of the suspending media, nanoparticles can tend to agglomerate, which in turns has a negative impact on their *in vitro* and *in vivo* behaviour and properties. Upon intravenous injection. Agglomeration of MNPs results in increasing the nanoparticle size, which in turn affects on:

- ✓ The NP biodistribution. For instance, NPs with a size more than 200 nm accumulate more in the spleen [93],
- ✓ The NP internalisation into the cell. As each cell has its own optimum size for higher NPs uptake,
- ✓ The subcellular fate of the NPs. Since there are several mechanisms on the cell plasma membrane that are responsible for NPs internalisation, these mechanisms differ according to NPs size [94]. For example, NPs of 60 nm size are internalised through a mechanism known as *caveolin-mediated endocytosis*, which bypasses the endolysosomal system and ends at the cytoplasm. On the other hand, NPs with about 120 nm size are internalised through a mechanism known as *clathrin-mediated endocytosis*, which ends at the endolysosomal system. In some cases this is undesirable due to the harsh acidic condition that may cause acid etching of the MNPs causing a loss of magnetic properties and inducing toxicity. In contrast, presence of the nanomaterial in the endolysosomal compartements maybe favourable, as it is the case of stimuli-responsive nanomaterials, releasing their cargo (e.g. drugs) under acidic condition,

- ✓ The superparamagnetic properties of the NPs. Since the increase in size over a given value reduces superparamagnetic properties.

Besides size effects, the hydrophobic surface of a NP has also a negative impact on its behaviour, since upon intravenous injection, NPs become in contact with blood that contains about 3700 types of plasma proteins. Several types of protein called opsonin, such as immunoglobulin, complement proteins, etc., are adsorbed at the hydrophobic surface of the NPs forming a protein corona, which produces signals to macrophages to come in order to eliminate the NPs from the circulation and send them to the liver, spleen or bone marrow. This process is known as opsonisation, see Fig. 1.6(a).

Protein corona formation affects to the NPs circulation time, biodistribution, clearance, cellular uptake and immunogenicity. A way to resist the protein adsorption, thus increasing NPs blood circulation time, and to reduce NPs aggregation is to carry out surface modification through polymeric coating. The used polymers are either synthetic or naturally and they are either physically or chemically adsorbed to the NPs surface. The most commonly used polymer is polyethylene glycol (PEG) since it is inexpensive, versatile and is currently listed as "generally recognised as safe" (GRAS) by FDA. Addition of PEG to the NPs surface (PEGylation) increases the blood circulation time, reduces the non-specific binding of proteins Fig. 1.6(b), and reduces NPs aggregation, resulting in so called "stealth" behaviour [95].

1.4.3 Targeting

One of the factors governing NPs efficiency is their ability to specifically reach to their action site (targeting). Targeting of a nanomaterial refers to differential spatial localisation of the nanomaterial, which could be achieved through two ways: passive targeting or active targeting. Passive targeting could be accomplished by:

- Direct injection of the nanomaterial into the tumour site, which is helpful in case of local cancers such as prostate, head and neck cancers developing sufficiently large tumours [21].

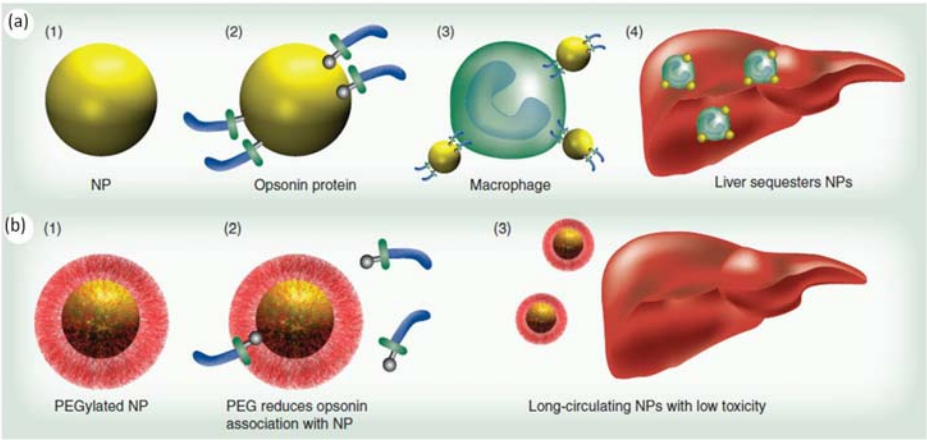

Figure 1.6: Effect of surface modification on the NP circulating time: (a) uncoated NP, the hydrophobic surface of the NP permits the adsorption of opsonin proteins (a2), which in turn facilitate the uptake of the NP by the macrophages (a3), and their accumulation in the liver (a4). (b) PEGylated NP, the PEG coating reduces the non-specific protein adsorption to the NP surface (b2), increasing the NP circulation time (b3) [95].

- Enhanced permeability and retention mechanism that was discovered by Matsumura and Maeda. [96,97] and is only relevant to oncology applications. This mechanism exploits the anatomical difference between normal and tumour tissues. Tumour vasculature has endothelium discontinuities forming pores with average size ranging between 400-600 nm [98]. This allows a larger accumulation of circulating nanomaterials (with a molecular weight above 50 kDa [20]) in tumour tissues than in normal tissues with slower clearance due to lack of effective tumour lymphatic drainage [99,100]. The process is schematically represented in Fig. 1.7(a) [101]. EPR also occurs in inflammatory diseases, but with shorter retention time compared to cancer. EPR effect has been observed for a wide range of nanomaterials such as SPIONs, liposomes and micelles. EPR is associated with several limitations: (1) In large tumours, EPR is absent in the tumour centre, thus causing a decrease of nanomaterial accumulation, (2) The tumour tissue has a pressure called interstitial fluid pressure (IFP), this pressure is higher in the tumour core, diminishing toward the tumour periphery, what it leads to the flow of nanomaterials out of the tumour. These problems can be overcome in two ways: (a) Enhancing EPR effect with decreasing tumour pressure through

co-administration of an adjuvant in addition to nanomaterial injections. Adjuvant can be such as vascular endothelial growth factor (VSGF), bradykinin, nitric oxide, prostaglandins, and transforming growth factor beta (TGFβ) receptor inhibitor. (b) Active targeted nanomaterials.

Active targeting is relevant to oncology applications and other therapeutic areas. This process is achieved by direct conjugation of the nanomaterial to a site-specific targeting moiety, as shown in Fig 1.7(b).

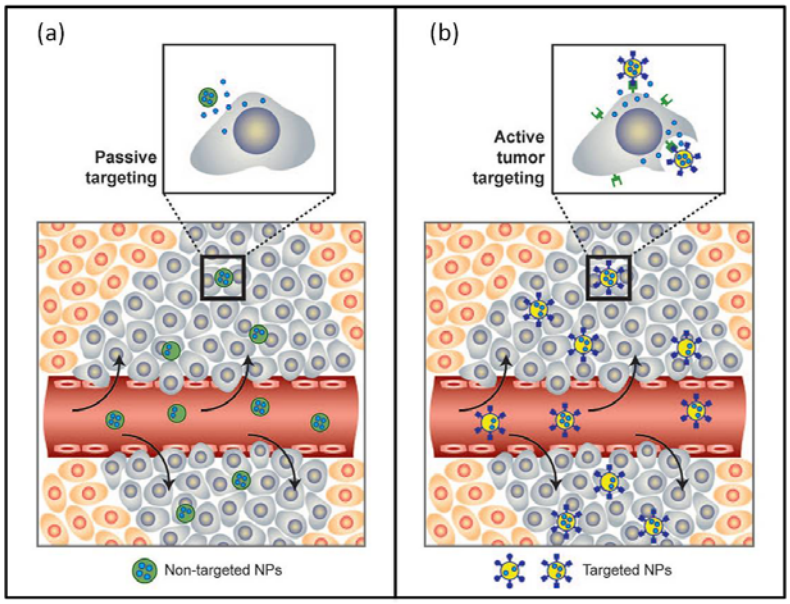

Figure 1.7: Schematic presentation for nanomaterials targeting: (a) passive targeting through enhanced permeability and retention and, (b) active targeting [101].

Targeting success depends on choosing the targeting moiety. It should fulfil several criteria such as low toxicity, abundance, high affinity and specificity toward their receptors at the target site and well suited to chemical modifications by conjugation. In addition, in order to avoid the toxicity of non-target tissues, targeted nanomaterials should bind to signature molecules that are exclusively expressed by the target site (e.g. Prostate-specific membrane antigen (PSMA)). Otherwise undesired effects can arise, as it is the case of targeting transferrin [22] and folate receptors [102]. These receptors are over-expressed by tumour cells and also are expressed to

some degree on many types of non-to-be-targeted cells [15,16] with the result that toxic off-target effects cannot be totally eliminated.

The targeting moiety could be antibodies [23] and their molecular fragments [103], proteins [22] or protein-like molecules, nucleic acid ligand (including aptamer [24]) and small molecules such as vitamins [104], peptides [105] and carbohydrates [106].

Conjugating the targeting moiety to the nanomaterial increases the localisation of the nanomaterial inside target cells. Park et al. showed that antibody- targeted liposomes (Anti-HER2 immunoliposomes containing doxorubicin) have a higher anti-tumour effect in compared with non-targeted counterparts (Liposomes with doxorubicin) [107]. Few years later, Kirpotin et al. disclosed that both targeted and non-targeted liposomes are similarly accumulated in the tumour tissue, and the enhanced anti-tumour effect of the targeted liposomes is due to their localisation in tumour cells, whereas, the non-targeted liposomes are in extracellular stroma or within macrophages [108].

Recently, the attention of scientists has geared toward the subcellular organelles targeting, as the efficiency of nanomaterials could depend on their localisation in a certain organelle. This is the case of gene delivery, in which the nanomaterial containing oligonucleotides as a cargo should be targeted to specific cells, breach the plasma membrane, escape from the endolysosomal compartements in order to avoid the cargo degradation under acidic conditions and then internalise to the nucleus through the nuclear pore with the help of a nanomaterial surface conjugated peptide called nuclear localising signal (NLS).

Many technological trends for effective organelle targeting are emerging, such as those for targeted delivery to the nucleus [109,110], mitochondria [111], cytosol [112] and endosome/lysosome [113].

1.4.4 Reporter nanomaterial

The development of an efficient targeted nanomaterial does not entitle a positive confirmation of the site-specific delivery. Moreover, tracking the nanomaterials inside

the cell is mandatory to explore the nanomaterial localisation in the subcellular organelles and their use for molecular imaging and biosensing.

Nanomaterials by themselves can possess properties that facilitate their detection *in vivo* or *in vitro* such as fluorescent, optical or magnetic properties as in the case of quantum dots, gold nanoparticles or magnetic nanoparticles, respectively. However, several types of nanomaterials do not possess these previously mentioned properties, lacking therefore a way of detection. That is the case of polymeric nanoparticles, ceramic nanoparticles, liposomes, etc. Thus, conjugating the nanomaterial to a fluorescent probe is recommended. Fluorescent probes can be either organic such as dyes, fluorescent proteins and intrinsic fluorophores or inorganic such as lanthanides and QDs. Organic-based fluorescent dyes are widely used in research and diagnostic applications. However, they are associated with many disadvantages, such as fluorescence bleaching, the requirement of coloured matched lasers, etc. Fluorescent nanomaterials (e.g. QDs) can overcome all these disadvantages improving the fluorescent probes utility in the clinical diagnosis [114,115]. However, they can have high toxicity. Several criteria must be taken into account during the selection of the fluorescent probe, such as low toxicity, biodegradability, high photostability, high and spectrally narrow absorption and emission cross sections and ultrasensitive detection.

Fluorescent-SPIONs are considered as dual reporter nanoparticles, where they could be detected through two ways, MRI and fluorescence, as shown in a study carried out by Lee et al. In this study they evaluate the stem cell labelling by fluorescent-SPIONs (*in vitro*) using MRI and fluorescent microscopy. In addition they showed the ability of fluorescent-SPIONs to track labelled human mesenchymal stem cells *in vivo* through fluorescent and MR imaging [116].

1.4.5 Monodispersity

Monodispersity means the state of uniformity. A monodispersed nanomaterial solution means that all nanomaterials in that solution have a narrow distribution of sizes. The main challenge faced by chemists during nanomaterials synthesis is

controlling the polydispersity that has many adverse effects at different levels: (i) At the biological level, it can affect the nanomaterial breaching ability, since the size and the size distribution are important in case of plasma membrane breaching and the passage through pores such as nuclear pores. Therefore, controlling the polydispersity is crucial; otherwise different batches of the same nanomaterial might display different behaviour inside the cell. (ii) At the physical level, it could affect the quantum effects of the nanomaterial that are size-dependent. For instance, (a) a tight control of nanomaterial size and a narrow distribution of sizes are mandatory to obtain a very efficient fluorescent probes capable of emitting narrow light in a very wide range of wavelengths [14]; (b) the magnetic properties of MNP are affected by the size distribution [117].

1.4.6 Nanomaterial physicochemical properties

1.4.6.1 Size

During the nanomaterial synthesis several factors could affect the nanomaterial size such as reactant concentrations, reaction temperature and solvent conditions [2]. Moreover, it is evident that nanomaterial size is completely depending on the surface charge and the suspending medium conditions (e.g. pH, ionic strength, organic molecules). For instance, the nanomaterial size in the blood increases due to protein adsorption and formation of protein corona, as mentioned by Dobrovolskaia et al. [118]. Therefore, characterisation of the nanomaterial in its relevant solution is mandatory.

The size of the nanomaterial has an impact on: (i) The nanomaterial biodistribution and circulation half-life time upon *in vivo* administration. Several studies proved those nanomaterials with sizes less than 5 nm are rapidly cleared from the circulation through extravasation or renal clearance [119] whereas nanomaterials with sizes larger than 200 nm are sequestered by the spleen as results of mechanical filtration and removal by reticuloendothelial system (RES) [97]. Therefore, nanomaterials with sizes ranging from 10-100 nm are optimal for long blood circulation time upon intravenous injection [120]. (ii) The nanomaterial toxicity, as the

size enables the nanomaterials to reach places where larger materials cannot enter, thus modifying nanomaterial toxicity. (iii) The cellular uptake rate of nanomaterials, as each cell has its own optimum size for higher nanomaterial uptake. (iv) The internalisation mechanism and consequently the subcellular fate of the nanomaterials (*detailed discussions on the internalisation mechanisms and their implication for nanomaterial uptake are given in* ***chapter 3***).

1.4.6.2 Shape

Several studies have demonstrated the effect of the shape on the nanomaterial cellular uptake and biodistribution. For instance, it has been showed that the spherical shaped nanomaterials are taken up by cells better than rod shaped ones; which is explained by the greater time needed for membrane wrapping of elongated nanomaterials [121].

Other studies showed that long filamentous nanomaterials have long blood circulation half-life time in compared with short filamentous and spherical shaped counterparts [122]. These results are not absolute since they depend on other factors, such as nanomaterial size, charge, surface coating, etc. Therefore, scientists developed a technique called particle replication in non-wetting template (PRINT) in order to study the effect of the shape independently of the other factors.

1.4.6.3 Charge

The nanomaterial surface charge is the major factor that contributes to the nanomaterial cellular uptake, biodistibution and toxicity. Studies have showed that charged nanomaterials are taken up better by the cells than their neutral counterparts. However, charged nanomaterials have short circulation half-life time due to the non-specific protein adsorption and clearance by RES. Positively-charged nanomaterials have a wide popularity in nanomedical applications due to their efficient cellular internalisation and endosomal escape, but their toxic and immunogenic effect is a subject of controversy [91].

1.5 Nanotoxicity

Since the ancient times, human beings and environment have been exposed to natural nanomaterials (e.g. viruses, forest fires, etc.). Over the years, this exposure has increased due to the unintentional or intentional anthropogenic activities. The great advance in nanotechnology at the industrial, biological and medical levels is one of the major anthropogenic sources of exposure. In addition, the nanomaterial involvement in biomedical application such as MRI, optical imaging, drug delivery, etc., has also to be taken into account. Nowadays, more than 1000 consumer products containing nanomaterials are available on the market such as sunscreens, dental bonding, paints, textile, computer chips, cell phones, etc. Also, nanomaterials are involved in environmental nano-remediation. These vast applications are due to the unique physicochemical properties of nanomaterials. However, the same properties that make the nanomaterials useful in many applications also have a negative impact on human and environment. Nanomaterials gain access into human body through dermal exposure, inhalation, gastrointestinal or injection.

Several studies showed that nanomaterials induce damages to the subcellular organelles such as mitochondria [123] and nucleus [124]. Other studies showed that nanomaterials have the ability to alter the blood coagulation pathway [125], induce platelet aggregation [125] or cause haemolysis [126]. Moreover, several studies showed that nanomaterials in direct contact with cell surface may lead to: (i) formation of reactive oxygen species (ROS) resulting in oxidative stress and inflammation [6]; (ii) lipid peroxidation, resulting in cell damage [127], and (iii) up/down regulation for genes, resulting in cell dysfunction [128]. Therefore, several nanomaterials have been reported as cytotoxic [129,130], neurotoxic [131,132], haemotoxic [133,134], genotoxic [135,136], ecotoxic [137,138] or bactericidal [139].

Based on the foregoing, full attention must be given to the safety and nanotoxicological issues for the new synthesised nanomaterials. Therefore, nanotoxicology is considered an important issue for study and will occupy a major part of this thesis.

1.6 Purpose of the thesis

The main rationale of the thesis is to study the toxicological behaviour of our polymer based superparamagnetic iron oxide nanoparticles *in vitro* and *in vivo*, in order to introduce them in the market as a therapeutic tool (agents for hyperthermia) or as a diagnostic tool (MRI contrast agents).

Being this thesis the first one in the group aimed to investigate the toxicity and biodistribution behaviour of the magnetic nanoparticles and their stable suspension in phosphate buffered saline (in the following called bioferrofluids), i will make rather extensive introductions to each chapter. Experiments, however, will concentrate on specific goals, as natural time limitations of a thesis precludes more comprehensive approaches. In the following i will describe the general characterisation of the bioferrofluids utilised and will list the specific objectives of the thesis. In each chapter specific goals will also be provided.

1.6.1 Bioferrofluids description

Our bioferrofluids consist on maghemite/polymer composite beads dispersed in phosphate buffered saline at pH 7.40. Each bead consists on several maghemite (γ-Fe_2O_3) nanoparticles embedded within a hydrophobic poly(4-vinylpyridine) (P4VP) polymer, and covered with a shell of hydrophilic chains of APEG(200). Samples used in this work have a fraction of PEG chains functionalised with carboxylate groups (APEG(1000)-COO-) that allows the conjugation of antibodies, peptides, fluorescent dye, pharmaceutical agent, etc. In fact, one of the samples used in this work contains a fraction of PEG chains functionalised with fluorescein molecules attached covalently to the end of the chains. These fluorescent nanoparticles are used in chapter 3. The maghemite/polymer composite bead structure is schematically shown in Fig 1.8.

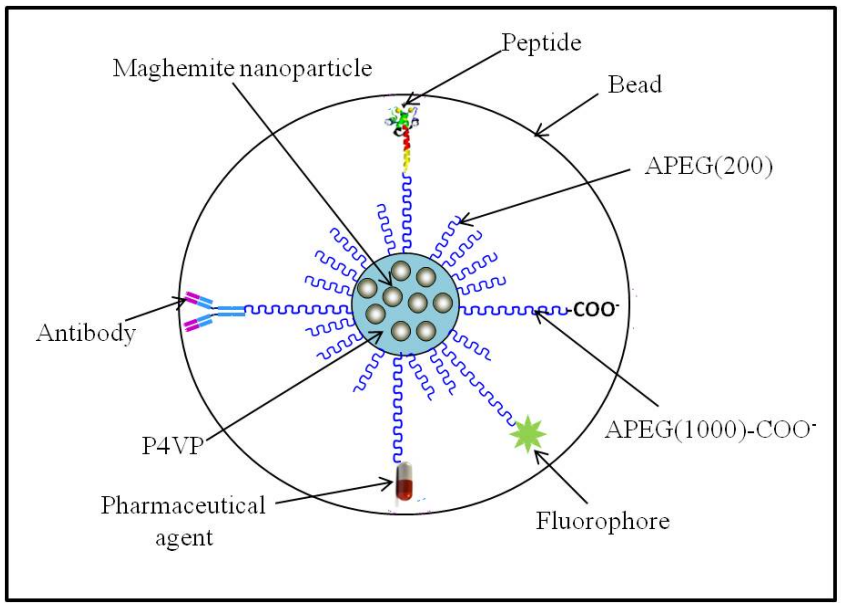

Figure 1.8: Schematic illustration of the maghemite/polymer composite bead structure.

1.6.2 Specific goals of the thesis

This aim will be achieved through several studies. In this thesis we have accomplished some of them such as:

1) Cytotoxicity studies (the content of chapter 2), which aim to study the effect of nanoparticle size and cell type on nanoparticles toxicity.

2) Nano-bio interface studies (the content of chapter 3), which aim to give an explanation for the results of the previous chapter through studying the effect of nanoparticle size and cell type on the cellular uptake rate and endocytosis mechanism.

3) Haematotoxicity studies (the content of chapter 4), which aim to study the effect of nanoparticle and its compositions on the coagulation process, blood cell count and haemolysis in vitro as these nanoparticles are designed for iv injection.

4) Evaluation of SPIONs as a MRI contrast agent and biodistribution and

toxicity studies *in vivo* (the content of chapter 5), which aim to study the relaxivity of the less toxic nanoparticles in vitro in compared to commercialised contrast agent "Endorem®", studying the biodistribution of the less toxic nanoparticles in vivo using MRI and histological studies for their toxic effects in organs.

1.7 References

[1] National Nanotechnology Initiative, the Initiative and Its Implementation Plan, 2000.

[2] B. Y. S. Kim, J. T. Rutka, and W. C. W. Chan, "Nanomedicine.," *N. Engl. J. Med.*, vol. 363, no. 25, pp. 2434–43, 2010.

[3] http://inl.int/what-is-nanotechnology-2

[4] European Science Foundation's Forward Look Nanomedicine: An EMRC Consensus Opinion, 2005; http://www.esf.org.

[5] G. Oberdörster, A. Maynard, K. Donaldson, V. Castranova, J. Fitzpatrick, K. Ausman, J. Carter, B. Karn, W. Kreyling, D. Lai, S. Olin, N. Monteiro-Riviere, D. Warheit, and H. Yang, "Principles for characterizing the potential human health effects from exposure to nanomaterials: elements of a screening strategy.," *Part. Fibre Toxicol.*, vol. 2, p. 8, 2005.

[6] G. Oberdörster, E. Oberdörster, and J. Oberdörster, "Nanotoxicology: An Emerging Discipline Evolving from Studies of Ultrafine Particles," *Environ. Health Perspect.*, vol. 113, no. 7, pp. 823–839, 2005.

[7] C. Medina, M. J. Santos-Martinez, a Radomski, O. I. Corrigan, and M. W. Radomski, "Nanoparticles: pharmacological and toxicological significance.," *Br. J. Pharmacol.*, vol. 150, no. 5, pp. 552–8, 2007.

[8] L. Mazzola, "Commercializing nanotechnology.," *Nat. Biotechnol.*, vol. 21, no. 10, pp. 1137–43, 2003.

[9] A. Seaton, L. Tran, R. Aitken, and K. Donaldson, "Nanoparticles, human health hazard and regulation.," *J. R. Soc. Interface*, vol. 7 Suppl 1, no. September 2009, pp. S119–29, 2010.

[10] M. Chidambaram, R. Manavalan, and K. Kathiresan, "Nanotherapeutics to overcome conventional cancer chemotherapy limitations.," *J. Pharm. Pharm. Sci.*, vol. 14, no. 1, pp. 67–77, 2011.

[11] "Cancer multidrug resistance," *Nat. Biotechnol.*, vol. 18, pp. IT18 – IT20, 2000.

[12] R. Duncan and R. Gaspar, "Nanomedicine(s) under the microscope.," *Mol. Pharm.*, vol. 8, no. 6, pp. 2101–41, 2011.

[13] C. B. Murray, C. R. Kagan, and M. G. Bawendi, "Synthesis and characterisation of monodisperse nanocrystals and close-packed nanocrystal assemblies," *Annu. Rev. Mater. Sci.*, vol. 30, no. 1, pp. 545–610, 2000.

[14] O. Salata, "Applications of nanoparticles in biology and medicine.," *J. Nanobiotechnology*, vol. 2, no. 1, p. 3, 2004.

[15] R. a Petros and J. M. DeSimone, "Strategies in the design of nanoparticles for therapeutic applications.," *Nat. Rev. Drug Discov.*, vol. 9, no. 8, pp. 615–27, 2010.

[16] S. Parveen, R. Misra, and S. K. Sahoo, "Nanoparticles: a boon to drug delivery, therapeutics, diagnostics and imaging.," *Nanomedicine*, vol. 8, no. 2, pp. 147–66, 2012.

[17] T. C. Yih and M. Al-Fandi, "Engineered nanoparticles as precise drug delivery systems.," *J. Cell. Biochem.*, vol. 97, no. 6, pp. 1184–90, 2006.

[18] G. Orive, R. M. Hernández, A. Rodríguez Gascón, A. Domínguez-Gil, and J. L. Pedraz, "Drug delivery in biotechnology: present and future.," *Curr. Opin. Biotechnol.*, vol. 14, no. 6, pp. 659–64, 2003.

[19] L. Zhang, F. X. Gu, J. M. Chan, A. Z. Wang, R. S. Langer, and O. C. Farokhzad, "Nanoparticles in medicine: therapeutic applications and developments.," *Clin. Pharmacol. Ther.*, vol. 83, no. 5, pp. 761–9, 2008.

[20] K. Cho, X. Wang, S. Nie, Z. G. Chen, and D. M. Shin, "Therapeutic nanoparticles for drug delivery in cancer.," *Clin. Cancer Res.*, vol. 14, no. 5, pp. 1310–6, 2008.

[21] S. K. Sahoo, W. Ma, and V. Labhasetwar, "Efficacy of transferrin-conjugated paclitaxel-loaded nanoparticles in a murine model of prostate cancer.," *Int. J. Cancer*, vol. 112, no. 2, pp. 335–40, 2004.

[22] C. H. J. Choi, C. A. Alabi, P. Webster, and M. E. Davis, "Mechanism of active targeting in solid tumors with transferrin-containing gold nanoparticles.," *Proc. Natl. Acad. Sci. U. S. A.*, vol. 107, no. 3, pp. 1235–40, 2010.

[23] P. Kocbek, N. Obermajer, M. Cegnar, J. Kos, and J. Kristl, "Targeting cancer cells using PLGA nanoparticles surface modified with monoclonal antibody.," *J. Control. Release*, vol. 120, no. 1–2, pp. 18–26, 2007.

[24] R. Tong, L. Yala, T. M. Fan, and J. Cheng, "The formulation of aptamer-coated paclitaxel-polylactide nanoconjugates and their targeting to cancer cells.," *Biomaterials*, vol. 31, no. 11, pp. 3043–53, 2010.

[25] J. Shi, Z. Xiao, N. Kamaly, and O. C. Farokhzad, "Self-assembled targeted nanoparticles: evolution of technologies and bench to bedside translation.," *Acc. Chem. Res.*, vol. 44, no. 10, pp. 1123–34, 2011.

[26] C. L. Grigsby and K. W. Leong, "Balancing protection and release of DNA: tools to address a bottleneck of non-viral gene delivery.," *J. R. Soc. Interface*, vol. 7 Suppl 1, pp. S67–82, 2010.

[27] G. Prencipe, S. M. Tabakman, K. Welsher, Z. Liu, A. P. Goodwin, L. Zhang, J. Henry, and H. Dai, "PEG branched polymer for functionalization of nanomaterials with ultralong blood circulation.," *J. Am. Chem. Soc.*, vol. 131, no. 13, pp. 4783–7, 2009.

[28] F. Dilnawaz, A. Singh, S. Mewar, U. Sharma, N. R. Jagannathan, and S. K. Sahoo, "The transport of non-surfactant based paclitaxel loaded magnetic nanoparticles across the blood brain barrier in a rat model.," *Biomaterials*, vol. 33, no. 10, pp. 2936–51, 2012.

[29] Z. Li, S. Zhu, K. Gan, Q. Zhang, Z. Zeng, Y. Zhou, H. Liu, W. Xiong, X. Li, and G. Li, "Poly-L-lysine-modified silica nanoparticles: a potential oral gene delivery system.," *J. Nanosci. Nanotechnol.*, vol. 5, no. 8, pp. 1199–203, 2005.

[30] C. Nembrini, A. Stano, K. Y. Dane, M. Ballester, A. J. van der Vlies, B. J. Marsland, M. A. Swartz, and J. A. Hubbell, "Nanoparticle conjugation of antigen enhances cytotoxic T-cell responses in pulmonary vaccination.," *Proc. Natl. Acad. Sci. U. S. A.*, vol. 108, no. 44, pp. E989–97, 2011.

[31] M. Shinkai, M. Yanase, H. Honda, T. Wakabayashi, J. Yoshida, and T. Kobayashi, "Intracellular hyperthermia for cancer using magnetite cationic liposomes: in vitro study.," *Jpn. J. Cancer Res.*, vol. 87, no. 11, pp. 1179–83, 1996.

[32] J. Ma, H. Wong, L. B. Kong, and K. W. Peng, "Biomimetic processing of nanocrystallite bioactive apatite coating on titanium," *Nanotechnology*, vol. 14, no. 6, pp. 619–623, 2003.

[33] J. Chen, C. Han, X. Lin, Z. Tang, and S. Su, "Effect of silver nanoparticle dressing on second degree burn wound," *Zhonghua Wai Ke Za Zhi*, vol. 44, no. 1, pp. 50–2, 2006.

[34] D. Schubert, R. Dargusch, J. Raitano, and S.-W. Chan, "Cerium and yttrium oxide nanoparticles are neuroprotective," *Biochem. Biophys. Res. Commun.*, vol. 342, no. 1, pp. 86–91, 2006.

[35] T. D. McCarthy, P. Karellas, S. A. Henderson, M. Giannis, D. F. O'Keefe, G. Heery, J. R. A. Paull, B. R. Matthews, and G. Holan, "Dendrimers as drugs: discovery and preclinical and clinical development of dendrimer-based microbicides for HIV and STI prevention.," *Mol. Pharm.*, vol. 2, no. 4, pp. 312–8, 2005.

[36] X. Michalet, F. F. Pinaud, L. A. Bentolila, J. M. Tsay, S. Doose, J. J. Li, G. Sundaresan, A. M. Wu, S. S. Gambhir, and S. Weiss, "Quantum dots for live cells, in vivo imaging, and diagnostics.," *Science*, vol. 307, no. 5709, pp. 538–44, 2005.

[37] G. A. Craig, P. J. Allen, and M. D. Mason, "Synthesis, characterization, and functionalization of gold nanoparticles for cancer imaging.," *Methods Mol. Biol.*, vol. 624, pp. 177–93, 2010.

[38] D. E. Sosnovik, M. Nahrendorf, and R. Weissleder, "Magnetic nanoparticles for MR imaging: agents, techniques and cardiovascular applications.," *Basic Res. Cardiol.*, vol. 103, no. 2, pp. 122–30, 2008.

[39] I. Texier, M. Goutayer, A. Da Silva, L. Guyon, N. Djaker, V. Josserand, E. Neumann, J. Bibette, and F. Vinet, "Cyanine-loaded lipid nanoparticles for improved in vivo fluorescence imaging.," *J. Biomed. Opt.*, vol. 14, no. 5, p. 054005, 2009.

[40] B.Bohunicky and S. A. Mousa, "Biosensors: the new wave in cancer diagnosis," *Nanotechnol. Sci. Appl.*, vol. 4, pp. 1–10, 2011.

[41] G. A. Posthuma-Trumpie, J. Korf, and A. van Amerongen, "Lateral flow (immuno)assay: its strengths, weaknesses, opportunities and threats. A literature survey.," *Anal. Bioanal. Chem.*, vol. 393, no. 2, pp. 569–82, 2009.

[42] C. S. Thaxton, R. Elghanian, A. D. Thomas, S. I. Stoeva, J.-S. Lee, N. D. Smith, A. J. Schaeffer, H. Klocker, W. Horninger, G. Bartsch, and C. A. Mirkin, "Nanoparticle-based bio-barcode assay redefines 'undetectable' PSA and biochemical recurrence after radical prostatectomy.," *Proc. Natl. Acad. Sci. U. S. A.*, vol. 106, no. 44, pp. 18437–42, 2009.

[43] T. K. Indira and P. K. Lakshmi, "Magnetic Nanoparticles – A Review," *iIternational J. Pharm. Sci. Nanotechnol.*, vol. 3, no. 3, pp. 1035– 1042, 2010.

[44] E. Duguet, S. Vasseur, S. Mornet, and J.-M. Devoisselle, "Magnetic nanoparticles and their applications in medicine.," *Nanomedicine (Lond).*, vol. 1, no. 2, pp. 157–68, 2006.

[45] I. Safarik and M. Safarikova, "Magnetic Nanoparticles and Biosciences," *Monatshefte fur Chemie / Chem. Mon.*, vol. 133, no. 6, pp. 737–759, 2002.

[46] A. Akbarzadeh, M. Samiei, and S. Davaran, "Magnetic nanoparticles: preparation, physical properties, and applications in biomedicine.," *Nanoscale Res. Lett.*, vol. 7, no. 1, p. 144, 2012.

[47] V. I. Shubayev, T. R. Pisanic, and S. Jin, "Magnetic nanoparticles for theragnostics.," *Adv. Drug Deliv. Rev.*, vol. 61, no. 6, pp. 467–77, 2009.

[48] A. Figuerola, R. Di Corato, L. Manna, and T. Pellegrino, "From iron oxide nanoparticles towards advanced iron-based inorganic materials designed for biomedical applications.," *Pharmacol. Res.*, vol. 62, no. 2, pp. 126–43, 2010.

[49] H. L. Ma, Y. F. Xu, X. R. Qi, Y. Maitani, and T. Nagai, "Superparamagnetic iron oxide nanoparticles stabilized by alginate: pharmacokinetics, tissue distribution, and applications in detecting liver cancers.," *Int. J. Pharm.*, vol. 354, no. 1–2, pp. 217–26, 2008.

[50] V. Maila and K. Landfester, "Interaction of Nanoparticles with Cells," *Society*, vol. 10, no. 9, pp. 2379–2400, 2009.

[51] C. Yang, A. Rait, K. F. Pirollo, J. A. Dagata, N. Farkas, and E. H. Chang, "Nanoimmunoliposome delivery of superparamagnetic iron oxide markedly enhances targeting and uptake in human cancer cells in vitro and in vivo.," *Nanomedicine*, vol. 4, no. 4, pp. 318–29, 2008.

[52] R. Weissleder, D. D. Stark, B. L. Engelstad, B. R. Bacon, C. C. Compton, D. L. White, P. Jacobs, and J. Lewis, "Superparamagnetic iron oxide: pharmacokinetics and toxicity.," *AJR Am J Roentgenol.*, vol. 152, no. 1, pp. 167–73, 1989.

[53] P. Reimer, E. J. Rummeny, H. E. Daldrup, T. Balzer, B. Tombach, T. Berns, and P. E. Peters, "Clinical results with Resovist: a phase 2 clinical trial.," *Radiology*, vol. 195, no. 2, pp. 489–96, 1995.

[54] K. E. Kellar, D. K. Fujii, W. H. Gunther, K. Briley-Saebø, A. Bjørnerud, M. Spiller, and S. H. Koenig, "NC100150 Injection, a preparation of optimized iron oxide nanoparticles for positive-contrast MR angiography.," *J. Magn. Reson. Imaging*, vol. 11, no. 5, pp. 488–94, 2000.

[55] M. Taupitz, S. Wagner, J. Schnorr, I. Kravec, H. Pilgrimm, H. Bergmann-Fritsch, and B. Hamm, "Phase I clinical evaluation of citrate-coated monocrystalline very small superparamagnetic iron oxide particles as a new contrast medium for magnetic resonance imaging.," *Invest. Radiol.*, vol. 39, no. 7, pp. 394–405, 2004.

[56] M. Wagner, S. Wagner, J. Schnorr, E. Schellenberger, D. Kivelitz, L. Krug, M. Dewey, M. Laule, B. Hamm, and M. Taupitz, "Coronary MR angiography using citrate-coated very small superparamagnetic iron oxide particles as blood-pool contrast agent: initial experience in humans.," *J. Magn. Reson. Imaging*, vol. 34, no. 4, pp. 816–23, 2011.

[57] S. Wagner, J. Schnorr, A. Ludwig, V. Stangl, M. Ebert, B. Hamm, and M. Taupitz, "Contrast-enhanced MR imaging of atherosclerosis using citrate-coated superparamagnetic iron oxide nanoparticles: calcifying microvesicles as imaging target for plaque characterization.," *Int. J. Nanomedicine*, vol. 8, pp. 767–79, 2013.

[58] E. I. Galanzha, E. V Shashkov, T. Kelly, J.-W. Kim, L. Yang, and V. P. Zharov, "In vivo magnetic enrichment and multiplex photoacoustic detection of circulating tumour cells.," *Nat. Nanotechnol.*, vol. 4, no. 12, pp. 855–60, 2009.

[59] S. Nagrath, L. V Sequist, S. Maheswaran, D. W. Bell, D. Irimia, L. Ulkus, M. R. Smith, E. L. Kwak, S. Digumarthy, A. Muzikansky, P. Ryan, U. J. Balis, R. G. Tompkins, D. A. Haber, and M. Toner, "Isolation of rare circulating tumour cells in cancer patients by microchip technology.," *Nature*, vol. 450, no. 7173, pp. 1235–9, 2007.

[60] W. He, H. Wang, L. C. Hartmann, J.-X. Cheng, and P. S. Low, "In vivo quantitation of rare circulating tumor cells by multiphoton intravital flow cytometry.," *Proc. Natl. Acad. Sci. U. S. A.*, vol. 104, no. 28, pp. 11760–5, 2007.

[61] M. Shinkai, "Functional magnetic particles for medical application.," *J. Biosci. Bioeng.*, vol. 94, no. 6, pp. 606–13, 2002.

[62] B. Thiesen and A. Jordan, “Clinical applications of magnetic nanoparticles for hyperthermia.,” *Int. J. Hyperthermia*, vol. 24, no. 6, pp. 467–74, 2008.

[63] T. Kobayashi, “Cancer hyperthermia using magnetic nanoparticles.,” *Biotechnol. J.*, vol. 6, no. 11, pp. 1342–7, 2011.

[64] R. T. Gordon, J. R. Hines, and D. Gordon, “Intracellular hyperthermia. A biophysical approach to cancer treatment via intracellular temperature and biophysical alterations.,” *Med. Hypotheses*, vol. 5, no. 1, pp. 83–102, 1979.

[65] A. Jordan, P. Wust, H. Fähling, W. John, A. Hinz, and R. Felix, “Inductive heating of ferrimagnetic particles and magnetic fluids: physical evaluation of their potential for hyperthermia.,” *Int. J. Hyperthermia*, vol. 9, no. 1, pp. 51–68, 1993.

[66] M. Johannsen, U. Gneveckow, B. Thiesen, K. Taymoorian, C. H. Cho, N. Waldöfner, R. Scholz, A. Jordan, S. A. Loening, and P. Wust, “Thermotherapy of prostate cancer using magnetic nanoparticles: feasibility, imaging, and three-dimensional temperature distribution.,” *Eur. Urol.*, vol. 52, no. 6, pp. 1653–61, 2007.

[67] A. Jordan, R. Scholz, K. Maier-Hauff, M. Johannsen, P. Wust, J. Nadobny, H. Schirra, H. Schmidt, S. Deger, S. Loening, W. Lanksch, and R. Felix, “Presentation of a new magnetic field therapy system for the treatment of human solid tumors with magnetic fluid hyperthermia,” *J. Magn. Magn. Mater.*, vol. 225, no. 1–2, pp. 118–126, 2001.

[68] K. Maier-Hauff, F. Ulrich, D. Nestler, H. Niehoff, P. Wust, B. Thiesen, H. Orawa, V. Budach, and A. Jordan, “Efficacy and safety of intratumoral thermotherapy using magnetic iron-oxide nanoparticles combined with external beam radiotherapy on patients with recurrent glioblastoma multiforme.,” *J. Neurooncol.*, vol. 103, no. 2, pp. 317–24, 2011.

[69] A. Jordan, R. Scholz, K. Maier-Hauff, F. K. H. van Landeghem, N. Waldoefner, U. Teichgraeber, J. Pinkernelle, H. Bruhn, F. Neumann, B. Thiesen, A. von Deimling, and R. Felix, “The effect of thermotherapy using magnetic nanoparticles on rat malignant glioma.,” *J. Neurooncol.*, vol. 78, no. 1, pp. 7–14, 2006.

[70] M. Shinkai and A. Ito, “Functional magnetic particles for medical application.,” *Adv. Biochem. Eng. Biotechnol.*, vol. 91, pp. 191–220, 2004.

[71] M. Yanase, M. Shinkai, H. Honda, T. Wakabayashi, J. Yoshida, and T. Kobayashi, “Intracellular hyperthermia for cancer using magnetite cationic liposomes: an in vivo study.,” *Jpn. J. Cancer Res.*, vol. 89, no. 4, pp. 463–9, 1998.

[72] M. Ma, Y. Wu, J. Zhou, Y. Sun, Y. Zhang, and N. Gu, “Size dependence of specific power absorption of Fe3O4 particles in AC magnetic field,” *J. Magn. Magn. Mater.*, vol. 268, no. 1–2, pp. 33–39, 2004.

[73] M. Shinkai, B. Le, H. Honda, K. Yoshikawa, K. Shimizu, S. Saga, T. Wakabayashi, J. Yoshida, and T. Kobayashi, “Targeting hyperthermia for renal cell carcinoma using human MN antigen-specific magnetoliposomes.,” *Jpn. J. Cancer Res.*, vol. 92, no. 10,

pp. 1138–45, 2001.

[74] B. Chertok, A. E. David, and V. C. Yang, "Polyethyleneimine-modified iron oxide nanoparticles for brain tumor drug delivery using magnetic targeting and intra-carotid administration.," *Biomaterials*, vol. 31, no. 24, pp. 6317–24, 2010.

[75] N. Andhariya, B. Chudasama, R. V. Mehta, and R. V. Upadhyay, "Biodegradable thermoresponsive polymeric magnetic nanoparticles: a new drug delivery platform for doxorubicin," *J. Nanoparticle Res.*, vol. 13, no. 4, pp. 1677–1688, 2010.

[76] L. Prosen, S. Prijic, B. Music, J. Lavrencak, M. Cemazar, and G. Sersa, "Magnetofection: a reproducible method for gene delivery to melanoma cells.," *Biomed Res. Int.*, vol. 2013, p. 209452, 2013.

[77] Q. A. Pankhurst, N. T. K. Thanh, S. K. Jones, and J. Dobson, "Progress in applications of magnetic nanoparticles in biomedicine," *J. Phys. D. Appl. Phys.*, vol. 42, no. 22, p. 224001, 2009.

[78] E. Klarreich, "Biologists join the dots.," *Nature*, vol. 413, no. 6855, pp. 450–2, 2001.

[79] I. L. Medintz, H. Mattoussi, and A. R. Clapp, "Potential clinical applications of quantum dots.," *Int. J. Nanomedicine*, vol. 3, no. 2, pp. 151–67, 2008.

[80] W. C. W. Chan, D. J. Maxwell, X. Gao, R. E. Bailey, M. Han, and S. Nie, "Luminescent quantum dots for multiplexed biological detection and imaging.," *Curr. Opin. Biotechnol.*, vol. 13, no. 1, pp. 40–6, 2002.

[81] F. M. Winnik and D. Maysinger, "Quantum Dot Cytotoxicity and Ways To Reduce It.," *Acc. Chem. Res.*, vol. 46, no. 3, pp. 672–680, 2012.

[82] H. Amiri, R. Bustamante, A. Millán, N. J. O. Silva, R. Piñol, L. Gabilondo, F. Palacio, P. Arosio, M. Corti, and A. Lascialfari, "Magnetic and relaxation properties of multifunctional polymer-based nanostructured bioferrofluids as MRI contrast agents.," *Magn. Reson. Med.*, vol. 66, no. 6, pp. 1715–21, 2011.

[83] L. Brannon-Peppas and J. O. Blanchette, "Nanoparticle and targeted systems for cancer therapy.," *Adv. Drug Deliv. Rev.*, vol. 56, no. 11, pp. 1649–59, 2004.

[84] Y. Jing, L. R. Moore, P. S. Williams, J. J. Chalmers, S. S. Farag, B. Bolwell, and M. Zborowski, "Blood progenitor cell separation from clinical leukapheresis product by magnetic nanoparticle binding and magnetophoresis.," *Biotechnol Bioeng.* , vol. 96, no. 6, pp. 1139–54, 2007.

[85] P. Elamanchili, M. Diwan, M. Cao, and J. Samuel, "Characterization of poly(D,L-lactic-co-glycolic acid) based nanoparticulate system for enhanced delivery of antigens to dendritic cells.," *Vaccine*, vol. 22, no. 19, pp. 2406–12, 2004.

[86] A. K. Gupta and M. Gupta, "Synthesis and surface engineering of iron oxide nanoparticles for biomedical applications.," *Biomaterials*, vol. 26, no. 18, pp. 3995–

4021, 2005.

[87] M. S. Fallon, M. Varshney, D. M. Dennis, and A. Chauhan, "A physiologically-based pharmacokinetic model of drug detoxification by nanoparticles.," *J. Pharmacokinet. Pharmacodyn.*, vol. 31, no. 5, pp. 381–400, 2004.

[88] C. Boyer, M. R. Whittaker, V. Bulmus, J. Liu, and T. P. Davis, "The design and utility of polymer-stabilized iron-oxide nanoparticles for nanomedicine applications," *NPG Asia Mater.*, vol. 2, no. 1, pp. 23–30, 2010.

[89] D. D. Lasic, "Novel applications of liposomes.," *Trends Biotechnol.*, vol. 16, no. 7, pp. 307–21, 1998.

[90] M. Silindir, S. Erdoğan, A. Y. Özer, and S. Maia, "Liposomes and their applications in molecular imaging.," *J. Drug Target.*, vol. 20, no. 5, pp. 401–15, 2012.

[91] N. Kamaly, Z. Xiao, P. M. Valencia, A. F. Radovic-Moreno, and O. C. Farokhzad, "Targeted polymeric therapeutic nanoparticles: design, development and clinical translation.," *Chem. Soc. Rev.*, vol. 41, no. 7, pp. 2971–3010, 2012.

[92] N. Dutta and D. Green, "Nanoparticle stability in semidilute and concentrated polymer solutions.," *Langmuir*, vol. 24, no. 10, pp. 5260–9, 2008.

[93] S. M. Moghimi, C. J. Porter, I. S. Muir, L. Illum, and S. S. Davis, "Non-phagocytic uptake of intravenously injected microspheres in rat spleen: influence of particle size and hydrophilic coating.," *Biochem. Biophys. Res. Commun.*, vol. 177, no. 2, pp. 861–6, 1991.

[94] S. D. Conner and S. L. Schmid, "Regulated portals of entry into the cell.," *Nature*, vol. 422, no. 6927, pp. 37–44, 2003.

[95] J. V Jokerst, T. Lobovkina, R. N. Zare, and S. S. Gambhir, "Nanoparticle PEGylation for imaging and therapy.," *Nanomedicine (Lond).*, vol. 6, no. 4, pp. 715–28, 2011.

[96] Y. Matsumura and H. Maeda, "A new concept for macromolecular therapeutics in cancer chemotherapy: mechanism of tumoritropic accumulation of proteins and the antitumor agent smancs.," *Cancer Res.*, vol. 46, no. 12 Pt 1, pp. 6387–92, 1986.

[97] H. Maeda, "Tumor-selective delivery of macromolecular drugs via the EPR effect: background and future prospects.," *Bioconjug. Chem.*, vol. 21, no. 5, pp. 797–802, 2010.

[98] F. Yuan, M. Dellian, D. Fukumura, M. Leunig, D. A. Berk, V. P. Torchilin, and R. K. Jain, "Vascular permeability in a human tumor xenograft: molecular size dependence and cutoff size.," *Cancer Res.*, vol. 55, no. 17, pp. 3752–6, 1995.

[99] V. P. Torchilin, "Micellar nanocarriers: pharmaceutical perspectives.," *Pharm. Res.*, vol. 24, no. 1, pp. 1–16, 2007.

[100] R. Duncan, "The dawning era of polymer therapeutics.," *Nat. Rev. Drug Discov.*, vol. 2, no. 5, pp. 347–60, 2003.

[101] O. C. Farokhzad and R. Langer, "Impact of nanotechnology on drug delivery.," *ACS Nano*, vol. 3, no. 1, pp. 16–20, 2009.

[102] P. S. Low, W. A. Henne, and D. D. Doorneweerd, "Discovery and development of folic-acid-based receptor targeting for imaging and therapy of cancer and inflammatory diseases.," *Acc. Chem. Res.*, vol. 41, no. 1, pp. 120–9, 2008.

[103] Y. Zhou, D. C. Drummond, H. Zou, M. E. Hayes, G. P. Adams, D. B. Kirpotin, and J. D. Marks, "Impact of single-chain Fv antibody fragment affinity on nanoparticle targeting of epidermal growth factor receptor-expressing tumor cells.," *J. Mol. Biol.*, vol. 371, no. 4, pp. 934–47, 2007.

[104] M.-K. Yoo, I.-K. Park, H.-T. Lim, S.-J. Lee, H.-L. Jiang, Y.-K. Kim, Y.-J. Choi, M.-H. Cho, and C.-S. Cho, "Folate-PEG-superparamagnetic iron oxide nanoparticles for lung cancer imaging.," *Acta Biomater.*, vol. 8, no. 8, pp. 3005–13, 2012.

[105] S. Ji, J. Xu, B. Zhang, W. Yao, W. Xu, W. Wu, Y. Xu, H. Wang, Q. Ni, H. Hou, and X. Yu, "RGD-conjugated albumin nanoparticles as a novel delivery vehicle in pancreatic cancer therapy.," *Cancer Biol. Ther.*, vol. 13, no. 4, pp. 206–15, 2012.

[106] S. Gupta, A. Agarwal, N. K. Gupta, G. Saraogi, H. Agrawal, and G. P. Agrawal, "Galactose decorated PLGA nanoparticles for hepatic delivery of acyclovir.," *Drug Dev. Ind. Pharm.*, 2012.

[107] J. W. Park, K. Hong, D. B. Kirpotin, G. Colbern, R. Shalaby, J. Baselga, Y. Shao, U. B. Nielsen, J. D. Marks, D. Moore, D. Papahadjopoulos, and C. C. Benz, "Anti-HER2 immunoliposomes: enhanced efficacy attributable to targeted delivery.," *Clin. Cancer Res.*, vol. 8, no. 4, pp. 1172–81, 2002.

[108] D. B. Kirpotin, D. C. Drummond, Y. Shao, M. R. Shalaby, K. Hong, U. B. Nielsen, J. D. Marks, C. C. Benz, and J. W. Park, "Antibody targeting of long-circulating lipidic nanoparticles does not increase tumor localization but does increase internalization in animal models.," *Cancer Res.*, vol. 66, no. 13, pp. 6732–40, 2006.

[109] B. Kang, M. A. Mackey, and M. A. El-Sayed, "Nuclear targeting of gold nanoparticles in cancer cells induces DNA damage, causing cytokinesis arrest and apoptosis.," *J. Am. Chem. Soc.*, vol. 132, no. 5, pp. 1517–9, 2010.

[110] C. W. Pouton, K. M. Wagstaff, D. M. Roth, G. W. Moseley, and D. A. Jans, "Targeted delivery to the nucleus.," *Adv. Drug Deliv. Rev.*, vol. 59, no. 8, pp. 698–717, 2007.

[111] S. V Boddapati, G. G. M. D'Souza, S. Erdogan, V. P. Torchilin, and V. Weissig, "Organelle-targeted nanocarriers: specific delivery of liposomal ceramide to mitochondria enhances its cytotoxicity in vitro and in vivo.," *Nano Lett.*, vol. 8, no. 8, pp. 2559–63, 2008.

[112] Z. Zhang, W. Cao, H. Jin, J. F. Lovell, M. Yang, L. Ding, J. Chen, I. Corbin, Q. Luo, and G. Zheng, "Biomimetic nanocarrier for direct cytosolic drug delivery.," *Angew. Chem. Int. Ed. Engl.*, vol. 48, no. 48, pp. 9171–5, 2009.

[113] L. M. Bareford and P. W. Swaan, "Endocytic mechanisms for targeted drug delivery.," *Adv. Drug Deliv. Rev.*, vol. 59, no. 8, pp. 748–58, 2007.

[114] D. Maysinger, J. Lovrić, A. Eisenberg, and R. Savić, "Fate of micelles and quantum dots in cells.," *Eur. J. Pharm. Biopharm.*, vol. 65, no. 3, pp. 270–81, 2007.

[115] U. Resch-genger, M. Grabolle, S. Cavaliere-jaricot, R. Nitschke, and T. Nann, "Quantum dots versus organic dyes as fluorescent labels," *Nat. Methods*, vol. 5, no. 9, pp. 763–75, 2008.

[116] J. Lee, M. A. Smith, W. Liu, E. M. Gold, B. Lewis, and J. A. Frank, "Enhanced stem cell tracking via electrostatically assembled fluorescent SPION-peptide complexes," *Nanotechnology*, vol. 20, no. 35, pp. 355102–355121, 2009.

[117] V. Russier, C. de Montferrand, Y. Lalatonne, and L. Motte, "Size and polydispersity effect on the magnetization of densely packed magnetic nanoparticles," *J. Appl. Phys.*, vol. 112, no. 7, pp. 073926–073937, 2012.

[118] M. a Dobrovolskaia, A. K. Patri, J. Zheng, J. D. Clogston, N. Ayub, P. Aggarwal, B. W. Neun, J. B. Hall, and S. E. McNeil, "Interaction of colloidal gold nanoparticles with human blood: effects on particle size and analysis of plasma protein binding profiles.," *Nanomedicine*, vol. 5, no. 2, pp. 106–17, 2009.

[119] H. S. Choi, W. Liu, P. Misra, E. Tanaka, J. P. Zimmer, B. Itty Ipe, M. G. Bawendi, and J. V Frangioni, "Renal clearance of quantum dots.," *Nat. Biotechnol.*, vol. 25, no. 10, pp. 1165–70, 2007.

[120] C. Chouly, D. Pouliquen, I. Lucet, J. J. Jeune, and P. Jallet, "Development of superparamagnetic nanoparticles for MRI: effect of particle size, charge and surface nature on biodistribution.," *J. Microencapsul.*, vol. 13, no. 3, pp. 245–55, 1996.

[121] A. Verma and F. Stellacci, "Effect of surface properties on nanoparticle-cell interactions.," *Small*, vol. 6, no. 1, pp. 12–21, 2010.

[122] Y. Geng, P. Dalhaimer, S. Cai, R. Tsai, M. Tewari, T. Minko, and D. E. Discher, "Shape effects of filaments versus spherical particles in flow and drug delivery.," *Nat. Nanotechnol.*, vol. 2, no. 4, pp. 249–55, 2007.

[123] N. Li, C. Sioutas, A. Cho, D. Schmitz, C. Misra, J. Sempf, M. Wang, T. Oberley, J. Froines, and A. Nel, "Ultrafine particulate pollutants induce oxidative stress and mitochondrial damage.," *Environ. Health Perspect.*, vol. 111, no. 4, pp. 455–60, 2003.

[124] M. Chen and A. von Mikecz, "Formation of nucleoplasmic protein aggregates impairs nuclear function in response to SiO2 nanoparticles.," *Exp. Cell Res.*, vol. 305, no. 1, pp. 51–62, 2005.

[125] A. Radomski, P. Jurasz, D. Alonso-Escolano, M. Drews, M. Morandi, T. Malinski, and M. W. Radomski, "Nanoparticle-induced platelet aggregation and vascular thrombosis.," *Br. J. Pharmacol.*, vol. 146, no. 6, pp. 882–93, 2005.

[126] A. Mayer, M. Vadon, B. Rinner, A. Novak, R. Wintersteiger, and E. Fröhlich, "The role of nanoparticle size in hemocompatibility.," *Toxicology*, vol. 258, no. 2–3, pp. 139–47, 2009.

[127] A. O. Choi, S. J. Cho, J. Desbarats, J. Lovrić, and D. Maysinger, "Quantum dot-induced cell death involves Fas upregulation and lipid peroxidation in human neuroblastoma cells.," *J. Nanobiotechnology*, vol. 5, p. 1, 2007.

[128] D. Cui, F. Tian, C. S. Ozkan, M. Wang, and H. Gao, "Effect of single wall carbon nanotubes on human HEK293 cells.," *Toxicol. Lett.*, vol. 155, no. 1, pp. 73–85, 2005.

[129] S. J. Cho, D. Maysinger, M. Jain, B. Röder, S. Hackbarth, and F. M. Winnik, "Long-term exposure to CdTe quantum dots causes functional impairments in live cells.," *Langmuir*, vol. 23, no. 4, pp. 1974–80, 2007.

[130] F. Tian, D. Cui, H. Schwarz, G. G. Estrada, and H. Kobayashi, "Cytotoxicity of single-wall carbon nanotubes on human fibroblasts.," *Toxicol. In Vitro*, vol. 20, no. 7, pp. 1202–12, 2006.

[131] T. C. Long, N. Saleh, R. D. Tilton, G. V Lowry, and B. Veronesi, "Titanium dioxide (P25) produces reactive oxygen species in immortalized brain microglia (BV2): implications for nanoparticle neurotoxicity.," *Environ. Sci. Technol.*, vol. 40, no. 14, pp. 4346–52, 2006.

[132] J. Wu, T. Ding, and J. Sun, "Neurotoxic potential of iron oxide nanoparticles in the rat brain striatum and hippocampus.," *Neurotoxicology*, vol. 34, no. null, pp. 243–53, 2013.

[133] S.-Q. Li, R.-R. Zhu, H. Zhu, M. Xue, X.-Y. Sun, S.-D. Yao, and S.-L. Wang, "Nanotoxicity of TiO(2) nanoparticles to erythrocyte in vitro.," *Food Chem Toxicol.*, vol. 46, no. 12, pp. 3626–31, 2008.

[134] G. Barshtein, D. Arbell, and S. Yedgar, "Hemolytic effect of polymeric nanoparticles: role of albumin.," *IEEE Trans. Nanobioscience*, vol. 10, no. 4, pp. 259–61, 2011.

[135] V. Sharma, S. K. Singh, D. Anderson, D. J. Tobin, and A. Dhawan, "Zinc oxide nanoparticle induced genotoxicity in primary human epidermal keratinocytes.," *J. Nanosci. Nanotechnol.*, vol. 11, no. 5, pp. 3782–8, 2011.

[136] H. Xie, M. M. Mason, and J. P. Wise, "Genotoxicity of metal nanoparticles.," *Rev. Environ. Health*, vol. 26, no. 4, pp. 251–68, 2011.

[137] H. Ma, P. L. Williams, and S. A. Diamond, "Ecotoxicity of manufactured ZnO nanoparticles--a review.," *Environ. Pollut.*, vol. 172, no. null, pp. 76–85, 2013.

[138] L. Ellegaard-Jensen, K. A. Jensen, and A. Johansen, "Nano-silver induces dose-response effects on the nematode Caenorhabditis elegans.," *Ecotoxicol. Environ. Saf.*, vol. 80, pp. 216–23, 2012.

[139] N. Tran, A. Mir, D. Mallik, A. Sinha, S. Nayar, and T. J. Webster, "Bactericidal effect of iron oxide nanoparticles on Staphylococcus aureus.," *Int. J. Nanomedicine*, vol. 5, pp. 277–83, 2010.

Chapter 2

In vitro cytotoxicity studies of superparamagnetic iron oxide nanoparticles

2.1 Introduction

With the great advances in nanotechnology at the industrial, biological and medical levels, human beings and their environment frequently become exposed to nanomaterials [1]. The same unique physicochemical properties that make nanomaterials attractive for applications could also cause harm when nanomaterials interact with biological systems and environment [2]. Therefore, exposure risks, toxicity mechanisms and route of entry need to be well understood. Based on that, a new branch of science known as "nanotoxicology" has emerged. Nanotoxicology is different than classical toxicology; while in classical toxicology the factor for considering the dose-effect relationship is the mass/concentration, in nanotoxicology several other factors are involved in addition, such as size, shape, surface area and surface modification [3].

2.1.1 A brief example about nanohazards: Learning from the past is setting out the future

This section shows how negligence in taking preventive measures can lead to lives loss, and it should be a lesson to be learned amid the vast introduction of nanomaterials in the market.

The story began with two toxic substances from peacetime technologies that emerged above all others in terms of death casualties: quartz and asbestos. The

toxicity caused by the inhalation of fine particles of these two substances was recognised in the eighteenth century and at the end of nineteenth century, respectively

Therefore, understanding the toxicity mechanism of these substances was a subject that drew the attention of the concerned industries and scientists. Unfortunately, appropriate epidemiological research to associate exposure and effect was long overdue, while applying preventive measures were not introduced, and workers died and still continue doing it nowadays. ***Therefore, we must be alert; it is not necessary to understand mechanisms before taking strides to prevent an occupational or environmental disease*** [4].

In the twentieth century, the impact of the air pollution on the public health has garnered immense attention; especially after a series of disasters that cost in lives lost, such as the 1930 Meuse Valley fog in Belgium, the 1948 Donora smog in Pennsylvania and the infamous London smog of 5-9th December 1952 that contributed to at least 4,000 deaths in its duration Fig. 2.1. These deaths were due to lung disease and acute cardiac failure, with or without obvious cardio-vascular pathology. Studies showed that no single agent was considered to be at the origin of the severe respiratory symptoms and death; however it was a combination of contaminants, especially irritant contaminants derived from combustion of coal and its products what were considered as the mainly responsibles for death [5].


THIRD DAY OF A LONDON PARTICULAR

Busy Time for Thieves: Traffic Disrupted

FROM OUR LONDON STAFF

FLEET STREET, SUNDAY.

London is still suffering from the worst fog for many years which has brought road traffic almost to a standstill, disrupted and delayed railway services, and caused an unusual amount of footpad crime and burglary.

equipment which are brought out by fog every year. Research workers condemned yellow fog lights penetrative than white driver is unquestion- the yellow light to reflect on windscr-

WORSE THAN 1866 CHOLERA

Deaths After Fog

The rise in deaths in the week after London's great fog early in December was greater than that in the worst week of the cholera epidemic in 1866. This is disclosed in a report of the health committee of London County Council which will be considered by the council on Tuesday.

Our London Correspondence

London Monday Night

All afternoon it was no more than misty with a red sun promising to break through but never quite doing. The river was imitating Whistler and the towers of the Palace of Westminster looked enchanting. Gould is the only style of architecture which the mist flatters. Many motorists had brought their cars to the City and were sad, believing that the worst was over. Housewives were

also be called Chelsea) Fortnight By Private Wire

Clean air policy cuts smog death rate

By our Parliamentary Staff

The lower level of smoke pollution brought about by the clean air policy helped to reduce the number of deaths in the London smog in December, compared with the smog in 1952.

This is the conclusion of the Ministry of Housing and Local Government in its report for 1966, published yesterday (Stationery Office, Cmnd 1976, 4s 6d).

were only a few hundred deaths attributable to the weather; but applications for admission to hospital and the sickness rate showed sharp increases. On both occasions, the new claims for sickness benefit rose by 50 per cent in a week.

The report says that during 1962, 202 smoke-control orders covering 92,100 acres were operative, affecting well over half a million premises. In

Figure 2.1: Headers of press coverage from Guardian Journal on London's smog disaster [10].

After the London's smog, United Kingdom (UK) had set an example of the effective regulation to reduce pollution through "Clean Air Acts" in 1956. In 1968 Lawther et al. demonstrated that over half of the particles in London smog were less than **100 nm** in diameter; however, these crucial results were ignored for 25 years [4]. The toxicological effects of airborne ultrafine particles (UFPs or PM0.1 are a fraction of ambient particulate matter (PM) with a diameter less than 0.1 μm [6]) have been addressed in several studies [6–9].

2.1.2 Nanotoxicology

Epidemiological and toxicological studies with airborne UFPs can be considered as the origin of the nanotoxicology field [2]. Nanotoxicology refers to the study of the interactions of nanomaterials with biological systems, with emphasis on elucidating the relationships between each nanomaterial physicochemical properties and the induction of toxic responses [11], Therefore, this type of studies helps to design new nanomaterials with lower adverse effects on health. Nanotoxicology is considered an interdisciplinary branch of science that needs the collaboration of toxicology, materials science, medicine and molecular biology to reach appropriate risk assessments (benefits/side effects evaluation). Nanotoxicology encompasses many items of study such as routes of exposure, targets of nanomaterials, biodistribution, physicochemical properties, molecular determinant, genotoxicity, and regulatory issues Fig. 2.2. As detailed below, this chapter will focus on the cytotoxicity of the magnetic nanoparticles and their bioferrofluids whose biocompatibility is studied in this Thesis.

2.1.2.1 Routes of exposure to nanomaterials

The term "exposure to nanomaterials" is not a neoteric one, as humans have been exposed to nanomaterials during their evolutionary phases. However, this exposure has increased to a great extent due to several anthropogenic sources such as the industry evolution, combustion-based engine transportation and finally the nanotechnology developments [13]. Paradigms of natural and anthropogenic sources of nanomaterials are summarised in Table 2.1.

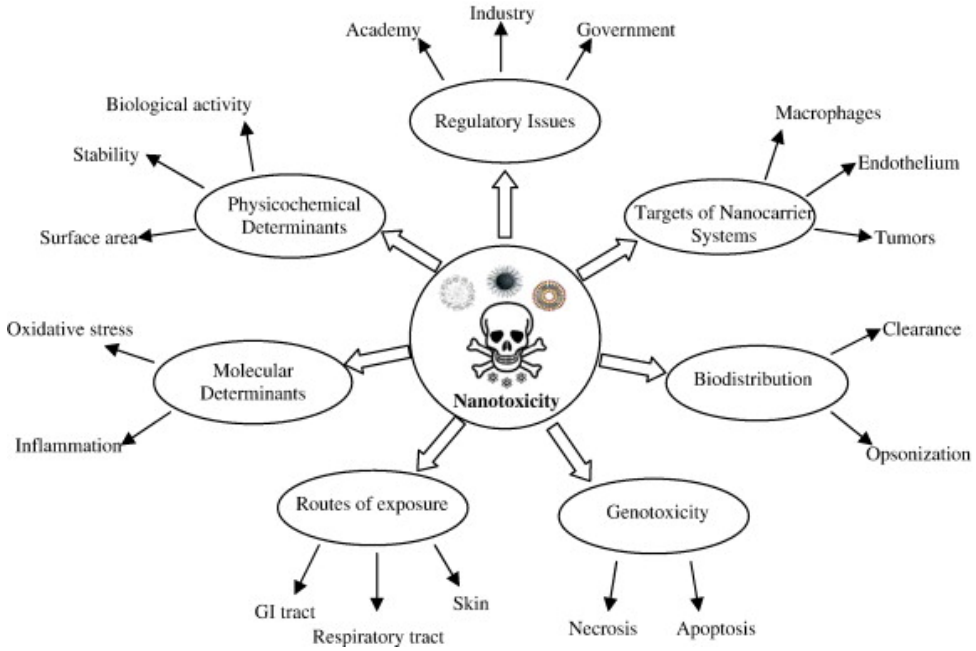

Figure 2.2: Complex array of issues surrounding toxicity of nanomaterials [12].

Table 2.1: Paradigms of natural and anthropogenic sources of nanomaterials [2].

Natural	Anthropogenic	
	Unintentional	Intentional (NPs)
Gas-to-particle conversions	Internal combustion engines	Controlled size and shape, designed for functionality
Forest fires	Power plants	
Volcanoes (hot lava)	Incinerators	Metals, semiconductors, metal oxides, carbon, polymers
Viruses	Jet engines	
Biogenic magnetite: magnetotactic bacteria protoctists, mollusks, arthropods, fish, birds human brain, meteorite (?)	Metal fumes (smelting, welding, etc.)	Nanospheres, -wires, -needles, -tubes, -shells, -rings, -platelets
	Polymer fumes	
Ferritin (12.5 nm)	Other fumes	Untreated, coated (nanotechnology applied to many products: cosmetics, medical, fabrics, electronics, optics, displays, etc.)
Microparticles (< 100 nm; activated cells)	Heated surfaces	
	Frying, broiling, grilling	
	Electric motors	

The exposure of the population to nanomaterials can be either (a) *indirect*, as a result of environmental contaminations with nanomaterials, coming from natural phenomena, nano-remediation or spillage of nanomaterials during industrial process, etc. or (b) *direct*, as occupational exposure in workplaces, exposure from medical or consumer products, etc. [3].Nanomaterials are internalised into the human body via inhalation, ingestion, dermal exposure and injection (e.g. intravenous, subcutaneous, intraperitoneal or intramuscular) as in case of diagnostic/therapeutic nanomaterials, their nano-size enables them to deposit in several organs or translocate from their

original site of entry to other sites in the body [14], causing toxic effects such as in case of inhaled nanomaterials though occupational exposure, air pollution or medical treatment Fig. 2.3. A number of investigators have discovered the toxicity of several nanomaterials in various organs [6,15–20].

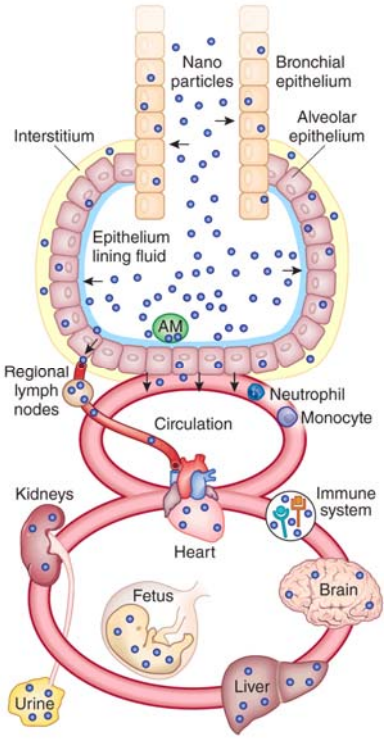

Figure 2.3: Schematic representation of nanomaterials translocation from the lung to regional lymph nodes and blood circulation and then their accumulation in various secondary organs of the body, AM is alveolar macrophages [21].

2.1.2.2 Toxicological mechanisms of nanomaterials

Here we will explain the general mechanisms responsible for the cytotoxicity using examples related to SPIONs, as these are the nanoparticles that we are interested in.

Iron is an important element that plays a significant role in cell physiology, as it is responsible for cell growth and multiplication in view of its role in DNA synthesis [22]. According to that, IONPs were initially considered to be a non-cytotoxic, as they are biodegradable releasing ferric ion, which can enter to the iron pool and participate

in normal iron metabolism. However, several studies showed that small IONPs might cause toxic effect as they can reach high local concentrations within the cells and become more difficult to be cleared from the body [23].

2.1.2.2.1 Physicochemical properties dependent toxicity

In fact, nanomaterials physicochemical properties, uptake and toxicity are three axes related to each other. Nano-sized materials are considered more toxic than larger size ones of the same material [8,20], however, a study carried out by Karlsson et al. showed that not in all cases the nano-sized materials are toxic in compared to micro-sized ones of the same material [24], this study was consistent with a study carried out by Warheit et al. [25]. The "nano" size enables the nanomaterials to reach places where the larger materials cannot enter, such as nucleus [26] or transfer across the placental barrier from pregnant mice to pups [27]. The "nano" size with its corresponding high surface to volume ratio increases the biological reactivity of the nanomaterial due to different interactions with the cell and its components [1]. This increased biological reactivity could be desirable (e.g. antioxidant activity) or undesirable (e.g. toxicity, induction of oxidative stress or of cellular dysfunction) [2]. Mahmoudi et al. illustrated the effect of the surface coating, the hydrodynamic diameter and shape of SPIONs on the cell toxicity. Their results showed that coated SPIONs are less toxic than uncoated ones, the lower toxicity is achieved by increasing the hydrodynamic diameter, and finally the toxicity of SPIONs at the same concentration is increased as cells interact with nanobeads, nanoworms and nanosphere [28]. The relation between toxicity and nanomaterial surface charge has been reported in several studies illustrating that charged nanomaterials are more toxic than neutral charged ones [29,30]. Chemical composition is another factor that could affect the cytotoxicity. A study carried out Karlsson et al. , showed that both Fe_2O_3 and Fe_3O_4 have less toxic effect on cultured cells independently on their size (micro or nano). In contrast, other metal oxides such as nano-sized CuO is more toxic than micro-sized CuO due to the high surface reactivity [24].

2.1.2.2.2 Molecular actions dependent toxicity

Nanomaterials can cause cell toxicity through several mechanisms such as:

Oxidative stress: Oxidative stress is a state that reflects the imbalance between the production of reactive oxygen species and the ability of the cell to detoxify or repair it. ROS species can be subdivided into two groups: *radical ROS* (such as superoxide anion ($O_2^{\bullet-}$), hydroxyl radical ($OH^{\bullet}$)), and *non-radical ROS* (such as hydrogen peroxide (H_2O_2)). Under normal conditions, ROS are produced by the cells as a consequence of aerobic metabolism [31]. Cells can tolerate a small and transient increase in ROS by an antioxidant defence mechanism.

The antioxidant mechanism can be divided into (a) *primary defence mechanism*, which includes several enzymes such as superoxide dismutase, catalase, glutathione peroxidase and reductase, and (b) *secondary defence mechanism*, that is carried out through reduction of glutathione (GSH) [32]. Under normal conditions, more than 95% of glutathione in cells exists in the reduced form (GSH). Reduced levels of GSH will lead to a decrease of the cell capacity to clean ROS and, therefore, to allow oxidative stress.

On the other hand, cells exposed to an environmental stress (such as pathogen or heat) induce a high level of ROS in response. If this high level of ROS persists for long time and cells fail to tolerate it, oxidative stress will be enhanced, resulting in oxidation of proteins, lipids (lipid peroxidation) and DNA (DNA strand breaks), as well as it will give rise to apoptosis or necrosis. Oxidations of protein and DNA have been shown to play a key role in the development of cancer, arteriosclerosis, arthritis and neurodegenerative disorders [33].

Nanomaterials favour the formation of ROS when exposed to light, ultraviolet (UV) light or acidic environment (e.g. lysosomes) or as a result of interaction with cellular components (e.g. mitochondria, redox-active proteins such as NADPH oxidase or cell surface receptors), possible mechanisms for ROS production by nanomaterials are shown in Fig. 2.4 [1,23].

Oxidative stress induced by nanomaterials enhances inflammation through upregulation of redox-sensitive transcription factors, including nuclear factor kappa B (NF-KB), and activated protein 1 (AP-1) [34].

In the case of SPIONs, ROS are induced as a consequence of their degradation in

the lysosomes, Fig 2.4(a), with the consequent release of ferrous ions. These free ions can cross the mitochondrial membrane to induce ROS through Fenton reaction (Equation 2.1) [35].

$$H_2O_2 + Fe^{2+} \dashrightarrow Fe^{3+} + OH^- + OH^{\bullet} \qquad \text{(Equation 2.1)}$$

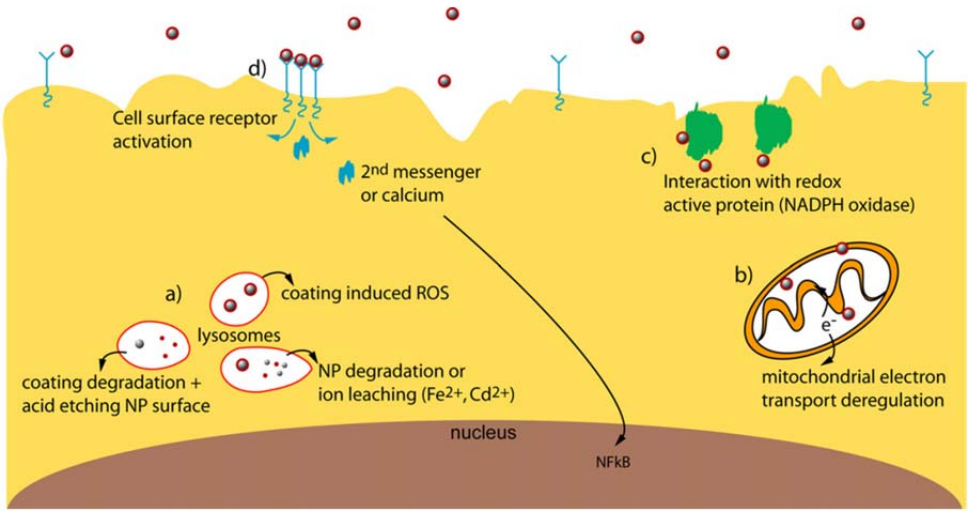

Figure 2.4: Schematic illustration of the different mechanisms of ROS induction by the nanomaterials (a) existence of nanomaterial under harsh acidic conditions (e.g lysosomes) induces ROS, as a result of coating surface reactivity, metal surface exposure to acidic environment or due to leached ions (Fe^{2+}, Cd^{2+}), (b) interaction of nanomaterials with mitochondria, causing mitochondria dysfunction, (c) interaction of nanomaterials with redox active protein such as NADPH oxidase, stimulating production of high amount of ROS in immune system cells, (d) interaction of nanomaterial with surface receptors, activating the intracellular signalling pathways, leading to expression of stress response genes which up-regulate ROS [23].

Up to date, the link between ROS induction by SPIONs and cell toxicity remains unclear. Some studies show that IONP have the ability of ROS induction and subsequently cell damage [36], while others show that they have peroxidise-like activity which can diminish the cellular ROS levels [37–40]. The level of induced ROS depends on the total amount of surface area of internalised IONPs, and the stability of the coating against the intracellular degradation, for instance, citrate-coated IONPs have a much faster maximal ROS induction (4h) compared to dextran- or lipid-coated IONPs [41].

Cytoskeleton defect: The cytoskeleton is composed of three types of filamentous proteins: microfilaments (actin filaments), intermediate filaments and microtubules. Cytoskeleton plays an important role inside the cells, as it affects to cell shape,

motility, division, adhesion and connection with its environment. Furthermore, there is a relationship between cytoskeleton and endocytosis mechanism, as endocytosis develops through the reorganisation of the cytoskeleton. Therefore, the high demands imposed by the nanomaterials on the cellular endocytosis mechanism can affect the cytoskeleton network [42,43]. The association between the cytotoxicity of SPIONs through disruption of the cytoskeleton network and nanomaterial internalisation and their intracellular localisation has been described in several studies. Gupta et al. illustrated the relationship between the cytoskeleton deformation and the surface modification (coating) of SPIONs [42]. Other studies illustrate the relationship between the uncoated SPIONs internalisation by endocytosis and their intracellular localisation and cytoskeleton disorganisation [44]. Soenen et al. showed that the high intracellular concentration of nanoparticles transiently affects actin cytoskeleton and subsequently cell proliferation [45]; in another study Soenen et al. suggest that the mere physical presence of high level of IONPs enclosed in the lysosomes, typically located in the perinuclear region, diminishes the protein expression and strictly hinders the cytoskeleton network [46].

Genotoxicity and intracellular signalling alteration: Nanomaterials can induce genotoxic effects and alteration in the intracellular signalling pathways through two mechanisms: (i) *Primary genotoxicity*, which is related to the direct exposure to the nanomaterial such as: (a) the "nano" size enables the nanomaterial to penetrate the nucleus and directly bind to the DNA [26,47], (b) the localisation of large number of nanomaterials confined in lysosomes in the perinuclear region can prevent the cellular transcription and translation machinery [46], and (c) leaking of metal ions from lysosomes containing nanomaterials can alter protein expression through mRNA degradation. (ii) *Secondary genotoxixity*, which is the result of nanomaterial-cell interactions and releasing of other factors such as ROS. High level of ROS induced by nanomaterials can directly mediate DNA damage through single or double strand breaks. ROS can also alter gene expression and unregulate several transcription factors, such as the activation of redox-sensitive transcription factors, including NF-KB [48]. So far, the relationship between SPIONs and induction of genotoxicity is still ambiguous. Several studies show that SPIONs have no genotoxic effect [49], neither affect stem cell proliferation [50] and gene expression patterns. In contrast, other

studies show that SPIONs can induce genotoxic effects and inhibit stem cell differentiation [51].

2.1.3 Cytotoxicity evaluation tests

Many biomedical applications require the *in vitro* exposure of cultured cells to nanomaterials prior to *in vivo* translocation. Although *in vitro* studies allow simpler, faster and more cost-efficient assessment of defined toxicity endpoints, they do not reflect the real behaviour of nanomaterials *in vivo*. Therefore, validation and complementation with *in vivo* experiments are mandatory [11].

Up to date, a real conclusion about in vitro toxicity of nanomaterials remains ambiguous. This is due to a great variety in: (1) types of nanomaterials, (2) nanomaterial manufacturing methods, (3) nanomaterial physicochemical properties, (4) coating agent, (5) type of cell culture used, (6) variation in experiment conditions (incubation time and concentration), (7) type of assay used and (8) possible interference of the nanomaterial with the assay readout. Therefore, a direct comparison between results obtained from different studies is out of the question [23].

The assessment of nanomaterials cytotoxicity is based on several *in vitro* assays established for hazard characterisation of chemicals; however, nanomaterials are completely different and may interfere with the commonly used assays either through interaction with the assay components due to their high surface to volume ratio and the high adsorption capacity, or through interfering with the detection system due to their optical properties [52,53].

Several assays are used to investigate different aspects of nanomaterials cytotoxicity *in vitro*. (1) *Cell viability assays*, including determination of mitochondrial activity using MTT assay, assessing cell membrane integrity using lactate dehydrogenase (LDH), trypan blue or propidium iodide assay, determination of intracellular esterase activity using Calcein AM assay, detection of intact lysosomes using neutral red assay and detection of apoptosis using fluorescent Annexin V or Caspase substrates detection assay. Obviously, a comparison between the results from one assay with others is impossible as they measure different parameters. (2) *Stress*

response assays, including detection of ROS; detection of any possible secondary effects in case of significant ROS induction, such as lipid or protein peroxidation, cytoplasmic calcium levels, cytoplasmic redox state (GSH detection) or DNA defects. (3) *Detection of inflammatory response* by measuring inflammatory markers such as the chemokine interleukin-8 (IL-8), or tumour necrosis factor α (TNF-α), IL-6, or IL-1β [52].

2.2 Objectives

The aim of this chapter is to study the toxicological behaviour of our bioferrofluids *in vitro* through studying their effects on cell viability using lactate dehydrogenase test and the Acridine orange/Ethidium bromide assay, defining the type of cell death (apoptosis or necrosis) using DNA fragmentation assay and detection of Caspase- 3 activity, investigating their ability to induce oxidative stress by measuring the carbonyl content and glutathione (GSH) detection, and finally, detection of inflammasome activation by measuring interleukin 1β.

In vivo toxicity studies of our bioferrofluids will be discussed in chapter 5.

2.3 Materials and methods

2.3.1 Bioferrofluid preparation and characterisation

Bioferrofluids preparation and characterisation methods are the same as described in Annex I. The preparation compositions of maghemite (γ-Fe_2O_3) nanoparticles in a poly(4-vinylpyridine) matrix are summarised in Table 2.2.

2.3.2 Cytotoxicity studies

All cytotoxicity experiments were performed at the *laboratorio de toxicología molecular, Facultad de veterinaria- Universidad de Zaragoza*, under the supervision of Professor Victor Sorribas.

Table 2.2: Composition of maghemite–P4VP nanocomposites preparation for different samples.

Sample	P4VP (g/L)	1M $FeBr_3$ (mL)	1M $FeBr_2$ (mL)	Fe/pyridine mol ratio	Fe^{2+}/ Fe^{3+} mol ratio	Fe_2O_3 wt %
R1	0.80	1.27	0.64	0.25	0.50	16.00
R2	0.80	2.54	1.27	0.50	0.50	27.60
R3	0.80	3.81	1.90	0.75	0.50	36.30
R4	0.80	5.08	2.54	1.00	0.50	43.20
R7	0.80	4.23	3.39	1.00	0.80	43.20
R8	0.80	4.01	3.61	1.00	0.90	43.20

2.3.2.1 Cell culture

Opossum Kidney (OK) cells were grown in 75 cm^2 Nunclon™ Flask as described in ref. [54], in Dulbecco's Modified Eagle's Medium (DMEM/F12) (Gibco-Life Technologies, Paisley, UK) supplemented with 10% fetal calf serum (FCS), 100 U/ml penicillin, 100 µg/ml streptomycin, and 2 mM L-glutamine.

Primary cultures of rat aortic vascular smooth muscle cells (VSMC) were cultured in 75 cm^2 Nunclon™ Flask as described in ref. [55], in Minimal Eagle's Medium (MEM) (Gibco-Life Technologies, Paisley, UK) supplemented as for OK cells.

Both cell lines were incubated in a 5% CO_2 incubator (lab Line) at 37 ºC with culture medium changes every second day until they became confluent. Cells were then washed twice with phosphate buffered saline (PBS), trypsinised with Trypsin-EDTA 1X (Life Technologies) and re-suspended in their appropriate cell culture medium. Cells were then ready to be used in other assays. The cells were passaged in a split ratio of 1:5 and 1:3 for OK and VSMC respectively. Cell passages were between 55-57 and 6 for OK and VSMC respectively.

2.3.2.2 Cell viability assays

2.3.2.2.1 The lactate dehydrogenase assay

Test principle: LDH assay is a colorimetric assay based on the reduction of

yellow tetrazolium salt INT to a red formazan.

Upon membrane damage, significant amounts of LDH are released from the cytosol of damaged cells. The LDH activity is measured in the cell culture supernatant using a Cytotoxicity Detection kit (Roche, Mannheim, Germany). The reaction is occurred in two steps: in the first step the released LDH reduces NAD^+ to $NADH+H^+$ by oxidation of lactate to pyruvate. In the second step the catalyst (diaphorase) transfers H/H^+ from $NADH+H^+$ to the yellow tetrazolium salt INT, which is reduced to red formazan Fig. 2.5 [56].

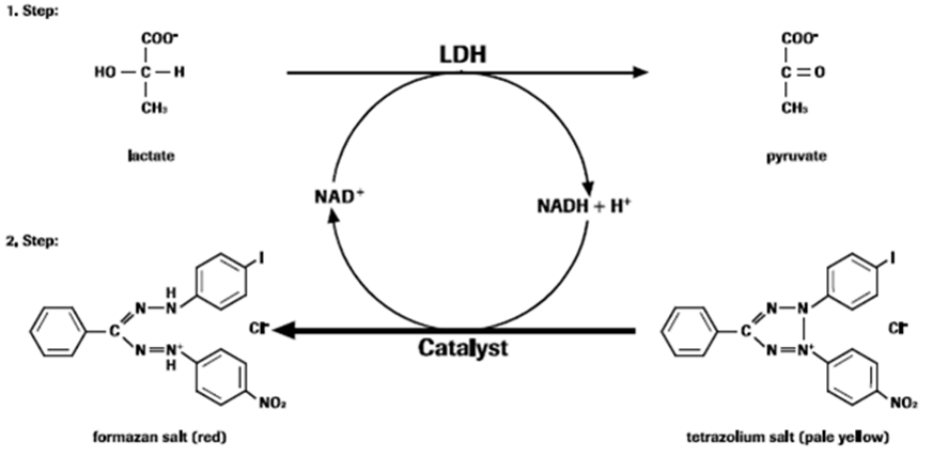

Figure 2.5: LDH activity detection reaction.

Method: For the determination of cytosolic lactate dehydrogenase leakage, both cell lines were grown in 24-well plates, as described in ref. [55], until they became confluent. Cells were made quiescent for 24 hours previous to the treatments with bioferrofluids by incubating them in culture medium containing 0.5 % FCS. After 24 hours, the supernatants were aspirated out, cells were washed twice with PBS. Then, both cell lines were treated with 0.5 % FCS culture medium containing different dilutions (0, 10^{-1}, 10^{-2}, 10^{-3}, 10^{-4}, 10^{-5} and 10^{-6}) of bioferrofluids (R1, R2, R3, R4, R7 and R8). Cells treated with detergent 0.5% triton X-100 were considered as positive control Aliquots were taken from cell supernatant at different time points (0, 1, 2, 3, 4 and 5 days) followed by centrifugation at 4ºC. Then, they were processed to measure

the LDH activity using Cytotoxicity Detection kit with the help of DTX-880 multimode detector system (Beckman Coulter, Indianapolis IN, USA) at 450 nm absorbance. Percentage of cell death was determined with respect to the maximal activity/absorbance obtained by positive control. The dose-response curves were plotted as the log Fe_2O_3 g/L versus the percentage of total LDH activity. The mean lethal concentration (LC_{50}) was determined by non-linear regression equation using GraphPad Prism 5.0 software (San Diego, CA, USA).

2.3.2.2.2 Acridine Orange/Ethidium Bromide (AO/EB) assay

For microscopic evaluation of cell death, fluorescent light microscopy with differential uptake of fluorescent DNA binding dyes (AO/EB staining) was used.

Test principle: Acridine orange (AO) is a nucleic acid selective fluorescent dye that penetrates all cells and binds to DNA and RNA, making them fluorescence green and red, respectively. In contrast, Ethidium Bromide (EB) is only taken up by cells when the cytoplasmic membrane integrity is lost and stains the nucleus red. EB emission dominates over AO, therefore, live cells have a normal green nucleus, early apoptotic cells have bright green nucleus with condensed or fragmented chromatin, late apoptotic cells display condensed and fragmented red chromatin, and cells that have died from direct necrosis have a structurally normal red nucleus.

Method: OK cells were seeded in 8 chamber slides (BD Falcon, Erembodegem, Belgium), and grown in their appropriate culture medium. After overnight growth, the supernatants were aspirated out and the cells were treated with aliquots of 0% FCS culture medium containing different concentrations (0, 0.007, 0.01, 0.02 g/L Fe_2O_3) of bioferrofluids (R1 and R8) for 24 hours. After 24 hours, the supernatants were aspirated out and the cells were washed twice with PBS, stained with acridine orange plus ethidium bromide in PBS as described in ref. [57,58]. The slides were mounted and examined rapidly under Axiovert 200M fluorescence microscopy (Carl Zeiss, Jena, Germany) after excitation at 495 nm. Green and red fluorescence were detected simultaneously using a dual band pass filter for emission at 530 nm and 610 nm. Phase contrast images of cells have been taken as well.

2.3.2.3 Apoptosis Assays

2.3.2.3.1 DNA fragmentation

Apoptosis or program cell death plays an important role in the natural renewal of cells, as well as in several different disease states. During apoptosis, cells undergo many morphological and biochemical changes different to necrosis. One of the biochemical changes is the fragmentation of the nuclear DNA, producing fragments with length varying between 180 to 200bp.

In order to examine the bioferrofluids ability to induce apoptosis, deoxynucleotidyl transferase- dUTP nick end labelling (TUNEL) fluorescent assay was used.

Test principle: TUNEL assay is based on the incorporation of modified dUTP (e.g. fluorescein-dUTP) by the enzyme terminal deoxynucleotidyl transferase (TdT) at the 3'-OH ends of fragmented DNA. The modifications of dUTP are flurophores or small molecules, called haptens.

Method: OK cells were seeded in 8 chamber slides and grown in their appropriate culture medium. After overnight growth, the supernatants were aspirated out and the cells were treated with aliquots of 0% FCS culture medium containing different concentrations (0, 0.007, 0.01, 0.02 g/L Fe_2O_3) of bioferrofluids (R1 and R8) for 24 hours. After 24 hours, the supernatants were aspirated out and the cells were washed twice with PBS. The cells were processed for TUNEL assay under the protocol instructions supplied with Click-iT TUNEL Alexa fluor-488 kit (Molecular Probes-Life Technologies, Paisley, UK), cells treated with DNase I were considered as Positive control. The slides were examined under the Axiovert 200M fluorescence microscopy at excitation filter of 470 ± 20 and emission filter of 525 ± 25. Phase contrast images of cells have been taken as well.

2.3.2.3.2 Caspase- 3 Assay

Members of the caspase family proteases (especially activated caspase-3) are

considered to be crucial mediators for the complex biochemical events associated with apoptosis. Therefore, apoptosis was also evaluated fluorometrically by measuring the activity of caspase-3, which is one of the most commonly used apoptosis assays. The cystein protease Caspase-3 is produced as a zymogen in the cytosol that is activated by cleavage into active caspase-3. Activated caspase-3 has substrate specificity for the amino acid sequence Asp-Glu-Val-Asp (DEVD) and cleaves several proteins leading to apoptosis.

Test principle: In case of apoptosis, the elevated level of activated caspase-3 produced can be detected using EnzChek® Caspase-3 Assay kit #2 (Molecular Probes). Activated caspase-3 detection method is based on measuring the cleavage of caspase-3 substrate (DEVD) that is linked to a flourophore (Rhodamine 110), the flourophore absorbs or emits light when it is separated from the substrate.

Method: OK cells were seeded in 57 cm^2 Petri dishes, grown in their appropriate culture medium until they became confluent. The supernatants were aspirated out and the cells were treated with aliquots of 0% FCS culture medium containing different concentrations (0, 0.007, 0.01, 0.02 g/L Fe_2O_3) of R1 and R8 bioferrofluids for 24 hours. After incubation, the supernatants were aspirated out, followed by cellular wash with PBS thrice. The cells were processed for (a) protein determination using BCA™ protein assay kit (Thermo scientific) and (b) caspase-3 detection under the protocol instructions supplied with EnzChek® Caspase-3 Assay kit #2. The fluorescence was measured with the help of DTX-880 multimode detector system at excitation/emission filters of 496/520 nm. This experiment was repeated 3 times in duplicate. The Mann-Whitney test was used for the statistical analysis of the experimental data. The results are presented as mean ± standard error of mean (SEM). Statistical significance was $p < 0.05$.

2.3.2.4 Oxidative stress

2.3.2.4.1 Carbonyl content measurement

There is a debate over the IONPs and their ability to produce ROS. Many studies stated that IONPs have oxidative capabilities [36], while others stated that IONPs have

peroxidase-like activity [38]. Here we investigated the oxidative capabilities of our bioferrofluids by measuring the carbonyl content of the oxidised proteins.

Proteins are one of the major targets of ROS. Upon oxidation, carbonyl groups (aldehydes and ketones) are introduced into protein side chains by a site-specific mechanism. The OxyELISA™ Oxidized Protein Quantitation Kit (Merck Millipore, Billerica, MA, USA) was used for sensitive immunodetection of these carbonyl groups.

Test principle: The test is based on direct Enzyme-linked immunosorbent assay (ELISA), in which protein samples are immobilised to a 96-well microlitre plate by passive absorption. The carbonyl groups in the protein side chains are then derivatised to 2,4-dinitrophenylhydrazone (DNP-hydrazone) by reaction with 2,4-dinitrophenylhydrazine (DNPH). The DNP-derivatised proteins are then incubated with a mouse monoclonal antibody (conjugated to horseradish peroxidase enzyme (HRP)) specific to the DNP moiety. Subsequent incubation with the enzyme substrate 3,3',5,5'-Tetramethylbenzidine (TMB) results in a coloured product which can be quantified using an spectrophotometer at 450 nm of absorbance.

Method: OK cells were grown in 6-well plate until they became confluent; supernatants were then aspirated out and the cells were treated with aliquots of 0% FCS culture medium containing different concentrations (0, 0.0005, 0.001, 0.002, 0.005, 0.007, 0.01, 0.02 g/L Fe_2O_3) of R1 bioferrofluid for 24 hours. As a positive control, cells were incubated with 1 mM H_2O_2 for 30 minutes. All samples were processed and analysed following the protocol instructions supplied with OxyELISA™ Oxidized Protein Quantitation Kit. The absorbance was measured with the help of DTX-880 multimode detector system at 450 nm. This experiment was repeated 3 times in duplicate. The Mann-Whitney test was used for the statistical analysis of the experimental data. The results are presented as mean ± SEM. Statistical significance was $p < 0.05$.

2.3.2.4.2 Thiol tracker

Glutathione, one of the important antioxidant compounds existing inside the cells.

In the absence of ROS, Glutathione exists in its reduced form (GSH) and can be detected through special dyes that react with its reduced thiol group (-SH).

Test principle: test is based on using a dye that reacts with reduced thiols in intact cells.

Method: OK cells were seeded in 8 chamber slides, and grown in their appropriate culture medium. After overnight growth, the supernatants were aspirated out and the cells were treated with aliquots of 0% FCS culture medium containing different concentrations (0, 0.007, 0.01, 0.02 g/L Fe_2O_3) of bioferrofluids (R1 and R8) for 24 hours. After 24 hours, the supernatants were aspirated out and the cells were washed twice with PBS. The cells were processed following the protocol instructions supplied with ThiolTracker™ Violet Kit (Molecular Probes). The slides were examined under the Axiovert 200M fluorescence microscopy at excitation/emission filters of 405/526 nm. In addition, GSH has been detected fluorometrically for cells grown in black 96-well plate (Fluoronunc, Thermo Nunc, Roskilde, Denmark), and treated with bioferrofluids as previously described. GSH was determined using ThiolTracker™ Violet kit and a DTX-880 fluorometer at excitation filter of 405 nm and emission filter of 526 nm. This experiment was repeated 3 times in triplicate. The statistical analysis of experimental data utilised the Mann-Whitney test. The results are presented as mean ± SEM. Statistical significance was $p < 0.05$.

2.3.2.5 Inflammasome activation

Inflammasome is a multiprotein complex, which participates in the production of the pro-inflammatory cytokines Il-1β and IL-18. The best characterised inflammasome is NLRP3 inflammasome, which consists of the NLR protein NLRP3, the adapter ASC and pro-caspase-1. Activation of the inflammasome can be triggered by several stimuli such as ROS, lysosomal damage, etc., resulting in release of active caspase-1, which in turn activates the conversion of pro-IL-1β and pro-IL-18 to active IL-1β and active IL-18.

2.3.2.5.1 Interleukin 1β measurement

IL-1β is a member of IL-1 cytokine family and an important mediator of the inflammatory response.

Test principle: The test is based on sandwich ELISA, in which an antibody specific for rat IL-1β has been coated onto the wells of the microliter strips provided with Rat IL-1β ELISA kit (Life Technologies), was incubated with the samples. The first incubation allows the binding of the IL-1β to the immobilised antibody, after incubation and wash, a second antibody specific for Rat IL-1β is added. After a second incubation and removal of the excess of second antibody, an enzyme (Streptavidin-Peroxidase) is added, which in turn bind to the second antibody. After a third incubation and washing to remove all the unbound enzyme, a substrate solution is added, which is acted upon by the bound enzyme to produce colour. The colour intensity is directly proportional to IL-1β concentration in the original samples.

Method: OK cells were seeded in 24-well plate, until they became confluent, the supernatants were then aspirated out and the cells were treated with aliquots of 0% FCS culture medium containing different concentrations (0, 0.007, 0.02 g/L Fe_2O_3) of R1 and R8 bioferrofluids for 24 hours. The supernatants were collected and then processed for IL-1β measurement following the manufacturer instructions supplied with Rat IL-1β ELISA kit. The absorbance was measured with the help of DTX-880 multimode detector system at 450 nm. This experiment was repeated 2 times in duplicate. The statistical analysis of experimental data utilised the Mann-Whitney test. The results are presented as mean ± SEM. Statistical significance was $p < 0.05$.

2.3.2.5.2 LysoTracker

Lysosomes are the cellular compartments that can play an important role during the endocytosis. Their role in the bioferrofluids internalisation has been tested using lysoTracker.

.

Test principle: This test is based on the selective accumulation of fluorescent acidotropic probes (consisting of fluorophore linked to weak base) in cellular compartments with low internal pH.

Method: OK cells were seeded in 8 chamber slides, after overnight growth. The supernatants were aspirated out and the cells were treated with aliquots of 0% FCS culture medium containing 0.02 g/L Fe_2O_3 of bioferrofluids (R1 and R8) for 24 hours. The cells were processed following the instructions of LysoTracker DND-99 kit (Molecular Probes). Cells were mounted with ProLong Gold antifade reagent with 4',6-diamidino-2-phenylindole, DAPI, (Molecular Probes). Slides were investigated under the Axiovert 200M fluorescence microscope equipped with ApoTome. Red fluorescence was detected using the long pass filter at 546 ± 6 nm and emission at 590 nm and DAPI excited using the long pass filter at 436 ± 10 nm, and emission at 480 ± 20 nm.

2.4 Results

2.4.1 Bioferrofluids characterisation

Atomic absorption in a plasma spectrometer was used to determine the iron contents of bioferrofluid stock samples used in this work. Concentrations of iron contents are summarised in Table 2.3.

The samples were characterised by DLS. Results showed a single population of particles with a log-normal distribution of hydrodynamic diameters Fig. 2.6. The plots do not show any population of small particles corresponding to isolated maghemite nanoparticles, which according to TEM have sizes below 16 nm, or to empty polymer beads that have a hydrodynamic size of 16 nm, as shown in Table 2.3. Therefore, it can be safely assumed that the suspension is just composed of a single population of maghemite/polymer composite beads. The average hydrodynamic diameter ($\boldsymbol{D_H}$) of the beads increases rapidly with the iron oxide/polymer and Fe(II)/Fe(III) ratios (Table 2.2). The average $\boldsymbol{D_H}$ is ranging between 51 to 112 nm Table 2.3. Measurements of zeta potential of the nanoparticles suspension for all samples yielded average values

close to zero.

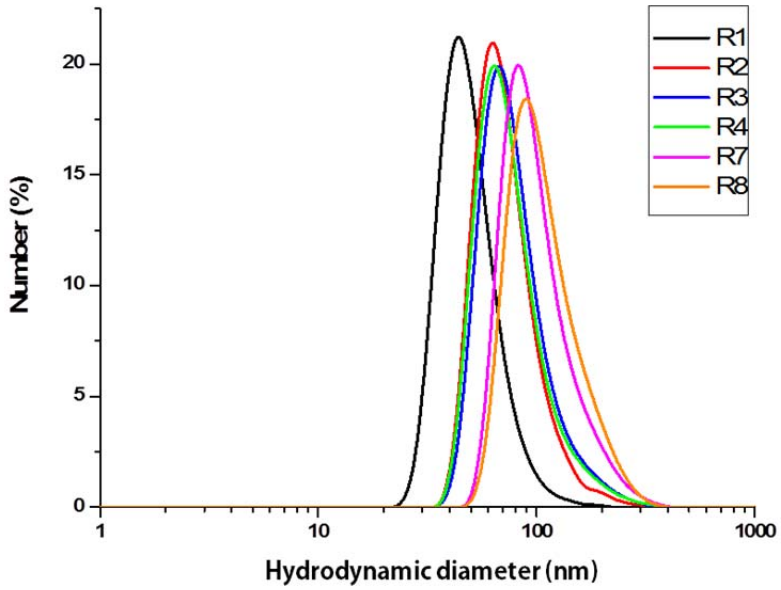

Figure 2.6: Distribution of hydrodynamic diameters in bioferrofluid samples from DLS measurements.

TEM observations do not show separated composite beads as observed in DLS Fig. 2.7. Instead, the polymer appears as a continuous film embedding the maghemite nanoparticles. Chloride and phosphate salts used in the preparation of the PBS particles suspensions are usually grouped in bags, whereas maghemite nanoparticles are uniformly distributed throughout the film. Most of maghemite nanoparticles are rounded, however, a small amount of other minor particle populations, such as thin maghemite rods and larger elongated particles was observed, probably made of goethite according to extra reflections that are occasionally observed in the electron diffraction (ED) patterns. The size of maghemite nanoparticles in the samples increases regularly from 4 nm (sample R1) to 15 nm (sample R8) in relation to the Fe/P4VP and Fe(II)/Fe(III) ratios used in the preparation Table 2.2. The size distribution analysis for the maghemite nanoparticles is shown in Fig. 2.8.

Table 2.3: Bioferrofluids characterisation.

Sample	$[P4VP\text{-}g\text{-}APEG]_3$ (g/L)	$[Fe_2O_3]$ (g/L)	D_H(nm)[a]	PDI[b]	D_P(nm)[c]	SD(nm)	N/L[d] x 10^{18}
blank	26.7	0	16	0.30			
R1	20.3	1.5	51	0.22	4.1	0.7	2.09
R2	22.5	4.2	76	0.21	7.4	1.2	0.90
R3	20.9	4.8	82	0.16	9.4	1.7	0.56
R4	24.6	7.4	79	0.15	12.1	2.8	0.74
R7	19.1	5.5	104	0.13	13.3	2.6	0.24
R8	19.5	5.4	112	0.10	14.4	4.6	0.19

[a]Hydrodynamic diameter; [b]Polydispersity index as obtained from DLS; [c]Maghemite nanoparticle diameter from TEM images; [d]Number of composite beads per litre of suspension.

The whole composition of the maghemite/polymer composite beads does not appear clearly by cryo-TEM Fig. 2.9A. Images showed maghemite nanoparticles are uniformly distributed in the solidified water matrix, surrounded by an area with a slight contrast over the background, which may correspond to the P4VP polymer that has a higher packing density than PEG polymer due to its hydrophobic character.

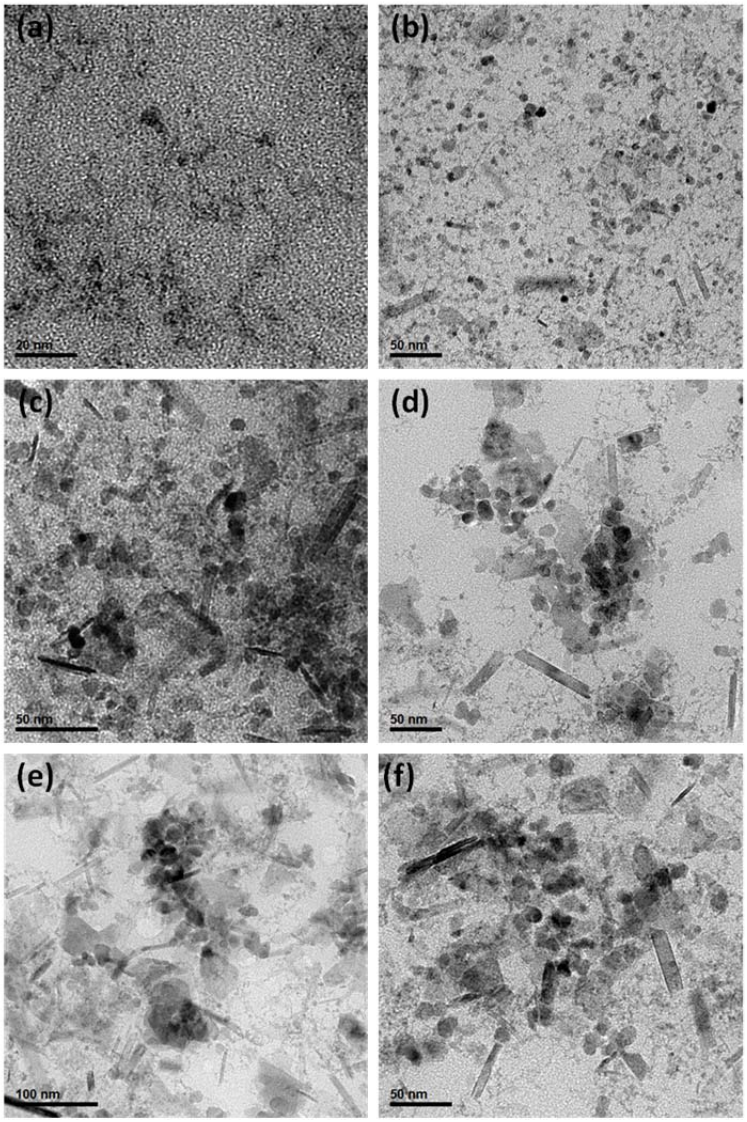

Figure 2.7: TEM images of maghemite magnetic nanoparticles in bioferrofluids (a) R1, (b) R2, (c) R3, (d) R4, (e) R7, and (f) R8.

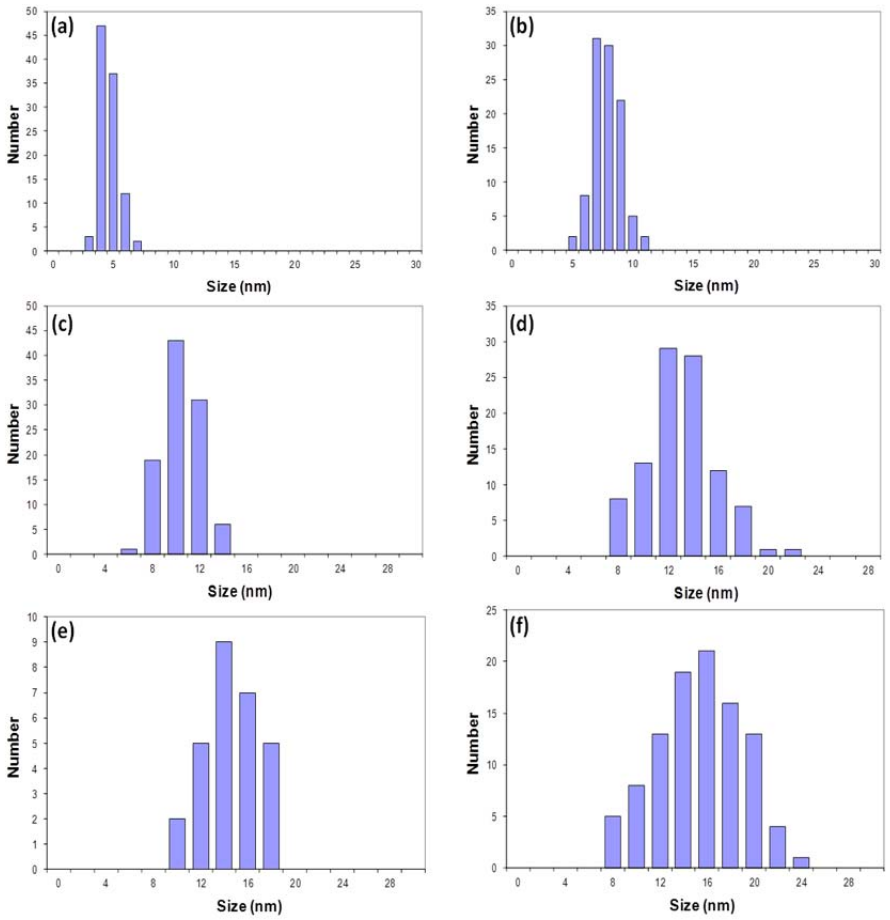

Figure 2.8: Size distribution analysis of spherical maghemite magnetic nanoparticles (a) R1, (b) R2, (c) R3, (d) R4, (e) R7, and (f) R8.

However, the presence of PEG polymer is not revealed due to a low contrast difference between the polymer and the water matrix. Nevertheless, the contour of the whole composite beads becomes apparent after surface functionalisation with antibodies Fig. 9B, or thermometric lanthanide complexes Fig. 9C. It is observed that the beads have an oval shape and contain the maghemite nanoparticles in the interior.

The nanoparticles i study here in this work, however, are the basic ones without antibodies and lanthanides functionalisations. The reason for it stays in part on time constraints and, also, because these kind of functionalised nanoparticles where developed when this thesis was with its last steps.

Figure 2.9: Cryo-TEM images of sample R8 (A), the sample R8 after conjugation with an antibody (B) or lanthanide complexes (C). Inserts show the detailed composition of the composite bead.

2.4.2 Cell Viability assay

2.4.2.1 LDH assay

The cytotoxicity of these bioferrofluids was assayed in two cell lines representing epithelial (OK cells) and mesenchymal (VSMC) origins. Cytotoxicity was first evaluated as total cell death, according to the intracellular LDH released to the incubation medium, as a function of dose and time of treatment.

LDH experiment has been carried out for all samples of bioferrofluids with several dilutions (0, 10^{-1}, 10^{-2}, 10^{-3}, 10^{-4}, 10^{-5} and 10^{-6}) in VSMC and OK cells at different time points (0, 1, 2, 3, 4 and 5 days). Obtained cytotoxicity data in both cell lines showed the classical sigmoidal dose-response curves when plotted as a logarithmic function of iron oxide concentration (Fe_2O_3 g/L) Fig. 2.10. After 1 day of treatment, VSMC showed to be sensitive (higher toxicity response) to all samples of bioferrofluids (R1, R2, R3, R4, R7 and R8) Fig. 2.10(a). In contrast, OK cells showed to be more sensitive to R1 (smaller size) in respect to other samples (R2, R3, R4, R7

and R8) that show lower toxicity compared to R1 Fig. 2.10(b). Fitting the data to a sigmoidal equation by non-linear regression provided values of LC_{50} for each sample that were in the range of 7-16 mg/L Fe_2O_3 and 10-20 mg/L Fe_2O_3 for VSMC and OK cells respectively after 1 day of treatment.

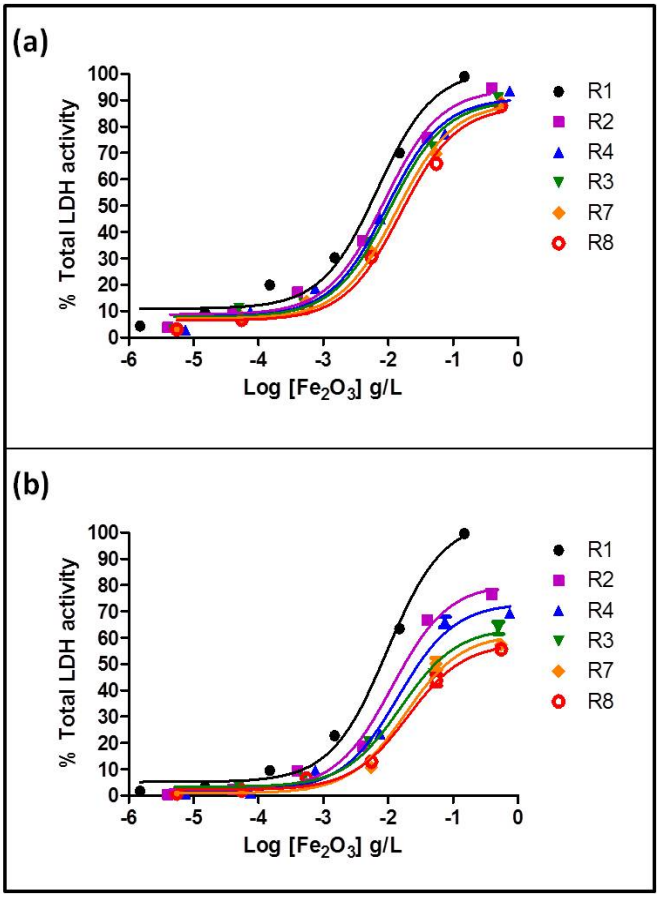

Figure 2.10: LDH activity after 1 day of treatment for all samples of bioferrofluids in both VSMC (a) and OK cells (b).

The experiment was carried out during 5 successive days with the determination of LC_{50} for all bioferrofluids samples in both cell lines, as shown in Fig. 2.11. The data are summarised in Tables 2.4 and 2.5 for VSMC and OK cells respectively. The LC_{50} values for VSMC are smaller than for OK cells, and LC_{50} values decrease with the time in both cell lines.

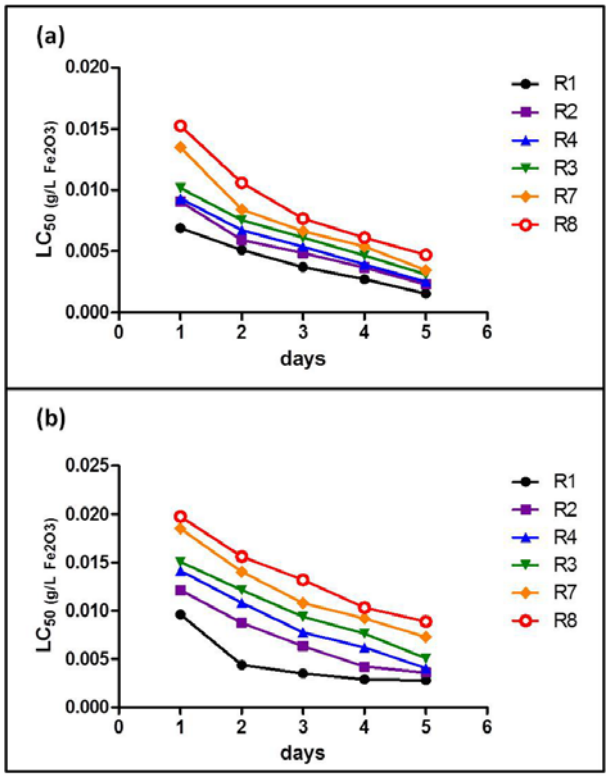

Figure 2.11: Variation of LC_{50} (as g/L Fe_2O_3) with time for all samples of bioferrofluids in VSMC (a) and OK cells (b).

Table 2.4. LC_{50} (as mg/L Fe_2O_3) values for all samples of bioferrofluids in VSMC

	Day 1	Day 2	Day 3	Day 4	Day 5
R1	6.89	5.11	3.70	2.73	1.55
R2	8.63	5.93	4.86	3.68	2.29
R4	9.44	6.72	5.37	3.93	2.50
R3	10.58	7.54	6.13	4.65	3.11
R7	13.50	8.41	6.65	5.39	3.45
R8	15.54	10.59	7.67	6.11	4.71

Table 2.5. LC_{50} (as mg/L Fe_2O_3) values for all samples of bioferrofluids in OK cells.

	Day 1	Day 2	Day 3	Day 4	Day 5
R1	9.60	4.36	3.49	2.86	2.78
R2	11.53	8.72	6.33	4.20	3.57
R4	14.31	10.81	7.73	6.17	4.04
R3	15.67	12.11	9.36	7.61	5.04
R7	18.49	14.01	10.79	9.18	7.26
R8	20.11	15.60	13.17	10.31	8.87

Toxicity was also analysed as a function of compositional and structural parameters of bioferrofluids. When the LC_{50} values after 1 day of treatment were plotted against the maghemite nanoparticle diameters, the bead hydrodynamic diameters and the iron oxide content indicated in Table 2.3, the relationships were linear in both cell lines Fig. 2.12(a), (b) and (c). The slopes of the regressions lines were positive, apparently meaning that toxicity decreases with the increasing of the diameters as well as of the iron oxide content in both cell lines.

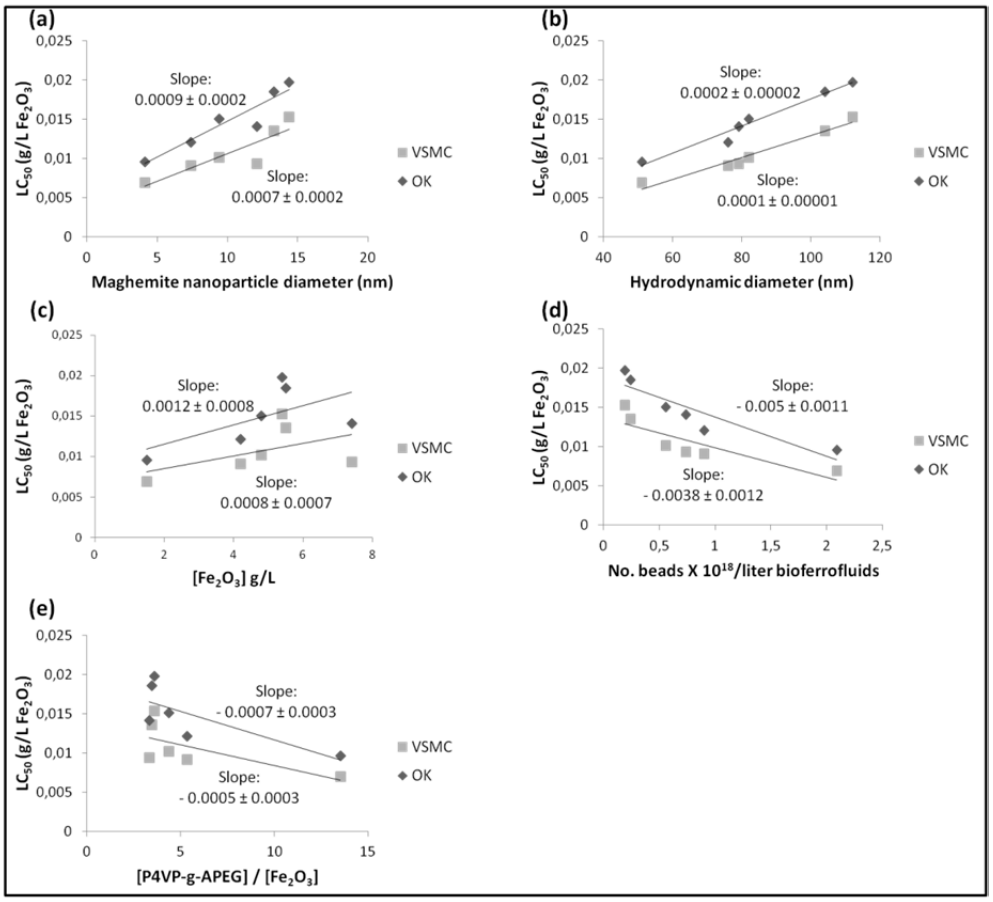

Figure 2.12: Linear correlation between LC_{50} (as g/L Fe_2O_3) after 1 day treatment and maghemite nanoparticles diameters (a), bead hydrodynamic diameters (b), iron oxide content (c), number of beads per litre bioferrofluids (d) and polymer/ iron oxide content ratio (e) for all samples of bioferrofluids in VSMC and OK cells.

In contrast, when the same LC_{50} values were plotted against the number of beads per litre of suspension and the ratio of the organic component (P4VP-g-APEG) and

iron oxide content in both cell lines (Table 2.3), the relationships were linear in both OK and VSMC and the slopes of the regression lines were negative, indicating that the toxicity is directly proportional to these two factors in both cell lines, as shown in Fig. 2.12(d) and (e).

In order to confirm the relationship between the D_H and the cytotoxicity on OK cells, a fixed concentration of iron oxide (0.02 g/L Fe_2O_3) from each sample (R1, R2, R3, R4, R7 and R8) was incubated with OK cells for 1 day. LDH activity was analysed and the results showed an inverse relationship between the hydrodynamic diameter and the cell toxicity, as shown in Fig. 2.13.

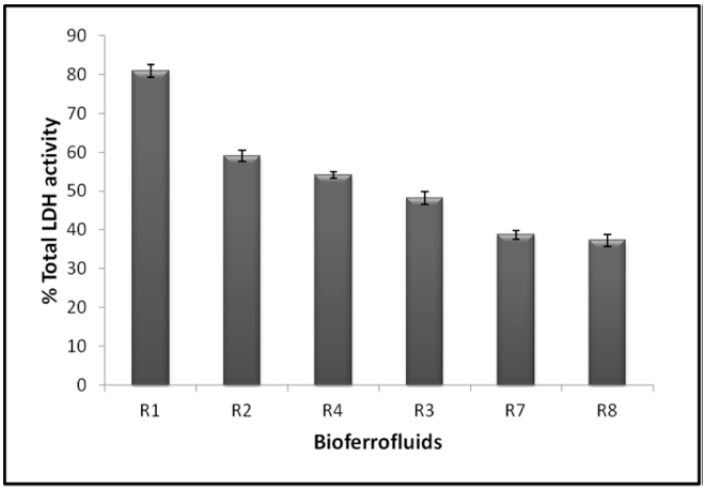

Figure 2.13: Effect of bead hydrodynamic diameter on the cytotoxicity of OK cell after 1 day of treatment.

2.4.2.2. Acridine Orange/Ethidium Bromide assay

Cytotoxicity was confirmed by microscopy using both phase contrast and double staining with AO/EB. Fig. 2.14 shows OK cells treated for 24 hours with R1 bioferrofluids at concentrations lower, similar and higher than the estimated LC_{50}. Dead cells are red stained with EB, while live cells allow only the entrance of AO and therefore fluorescence green with a faint red staining in cytoplasm corresponding to RNA and lysosomes. Phase contrast illumination of the cells suggests a necrotic type

of cell death with no evidence of apoptosis. Identical findings were obtained with R8 bioferrofluids as shown in Fig. 2.15.

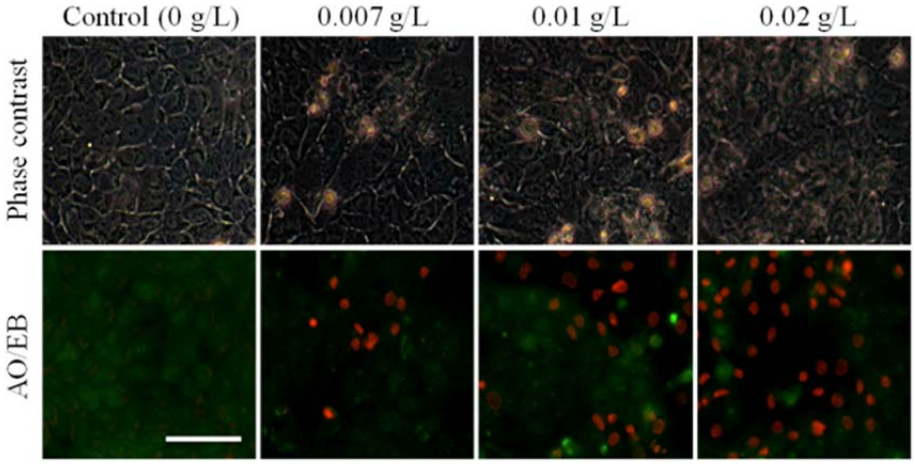

Figure 2.14: Confocal micrographs of AO/EB stained OK cells treated with different concentrations of R1 bioferrofluids for 24 hours. Faint red/orange spotty staining in Control corresponds to the intercalation of AO in RNA and lysosomal staining. Scale bar: 100 µm.

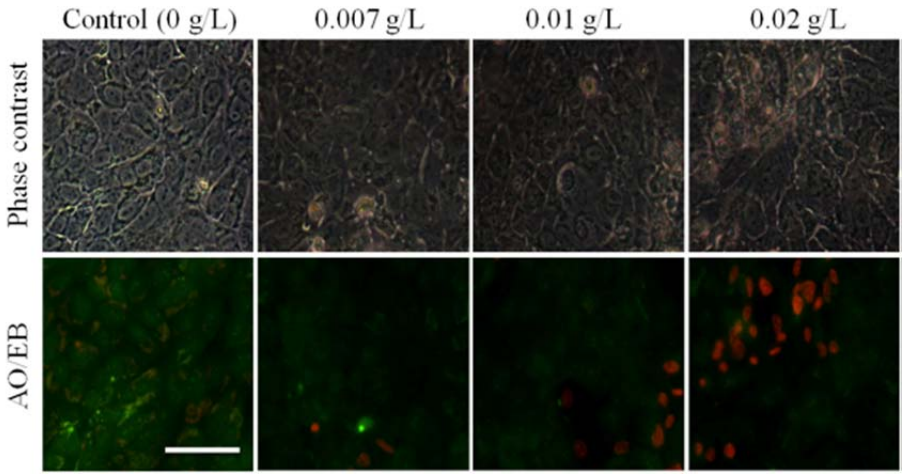

Figure 2.15: Confocal micrographs of AO/EB stained OK cells treated with different concentrations of R8 bioferrofluids for 24 hours. Faint red/orange spotty staining in Control corresponds to the intercalation of AO in RNA and lysosomal staining. Scale bar: 100 µm.

2.4.3 Apoptosis assay

Even if morphology of the cells did not indicate evidence of apoptosis as previously shown in AO/EB assay, two different methods were used to confirm this

point based on the detection of both early and late apoptotic events.

2.4.3.1 DNA fragmentation (late apoptotic event)

OK cells treated with different concentrations of R1 bioferrofluids showed absence of DNA fragmentation, which is indicated as a black field with no fluorescence after using a fluorescent TUNEL assay. However, positive control, as corresponds to DNase I treated cells, was fluorescent green, as shown in Fig. 2.16. Identical findings were obtained with R8 bioferrofluids, as shown in Fig. 2.17. Phase contrast images were taken to confirm the presence of the cells.

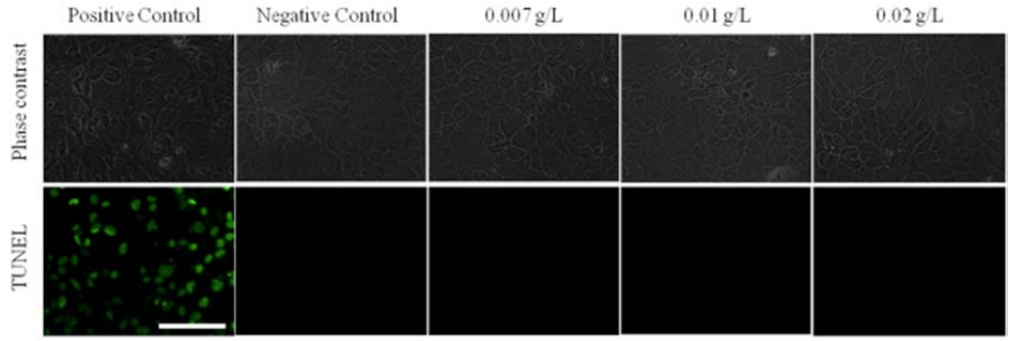

Figure 2.16: Confocal micrographs of fluorescent TUNEL stained OK cells treated with different concentrations of R1 bioferrofluids for 24 hours. Positive control is DNase I treated OK cells. Scale bar: 100 μm.

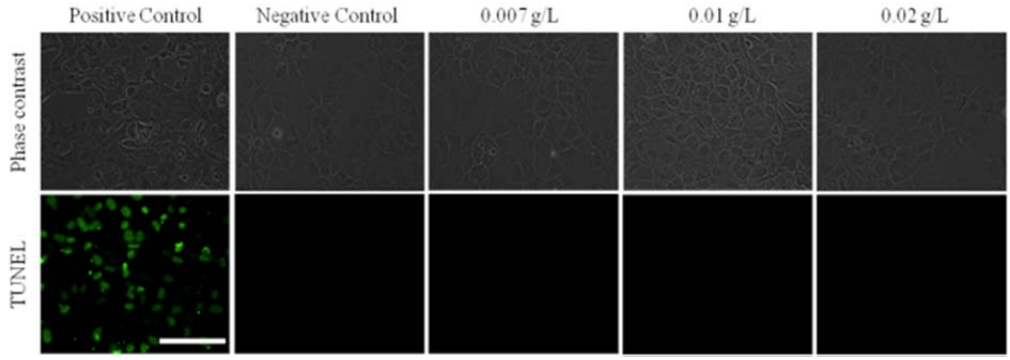

Figure 2.17: Confocal micrographs of fluorescent TUNEL stained OK cells treated with different concentrations of R8 bioferrofluids for 24 hours. Positive control is DNase I treated OK cells. Scale bar: 100 μm.

2.4.3.2 Caspase-3 activity detection (early apoptotic event)

A fluorescent caspase-3 assay was carried out in OK cells treated with different concentrations of R1 and R8 bioferrofluids for 24 hours. Results showed no significant change in caspase-3 level compared to the control (untreated OK cells) Fig. 2.18, resulting in no evidence of apoptosis detected. Data corresponding to caspase-3 activity detection are analysed using Mann-Whitney test and are summarised in Table 2.6.

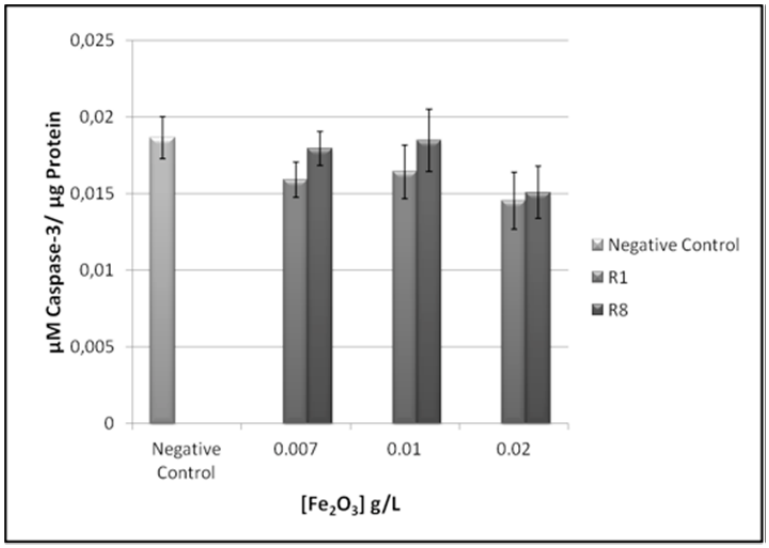

Figure 2.18: Caspase-3 activity detection in OK cells treated with different concentrations of R1 and R8 bioferrofluids for 24 hours. Values represent mean ± SEM (*n*=6).

Table 2.6. Statistical analysis data for caspase-3 activity detection in OK cells treated with different concentrations of R1 and R8 bioferrofluids for 24 hours (*n*=6).

$[Fe_2O_3]$ g/L	R1 bioferrofluids		R8 bioferrofluids	
	Caspase-3 activity Mean ± SD (µM caspase/µg protein)	P (Mann-Whitney)	Caspase-3 activity Mean ± SD (µM caspase/µg protein)	P (Mann-Whitney)
0	0.0186 ± 0.003	-	0.0186 ± 0.003	-
0.007	0.0159 ± 0.003	0.1797	0.0179 ± 0.003	0.8182
0.01	0.0164 ± 0.004	0.4848	0.0185 ± 0.005	0.9372
0.02	0.0146 ± 0.005	0.1320	0.0151 ± 0.004	0.1320

2.4.4 Oxidative stress

2.4.4.1 Carbonyl content measurement

In order to ascertain the toxicity mechanism induced by the NPs, oxidative stress was determined by measuring the carbonyl content in a protein lysate from OK cells treated with different concentrations of R1 for 24 hours. Results showed no significant change in carbonyl content level as compared to the untreated cells (negative control), as shown in Fig.2.19. Data corresponding to measurements of carbonyl content were analysed using Mann-Whitney test and results are summarised in Table 2.7.

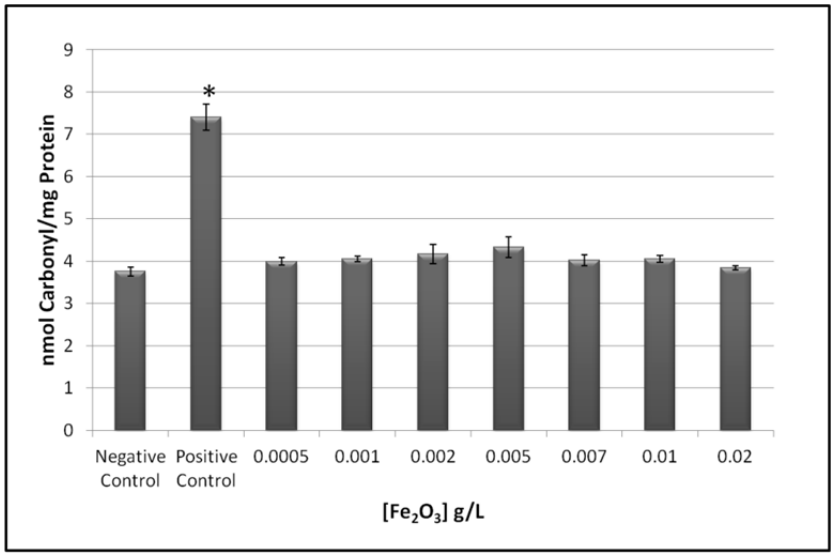

Figure 2.19: Determination of carbonyl content in protein lysate from OK cells treated with different concentrations of R1 bioferrofluids for 24 hours. Positive control is cells treated with 1mM H_2O_2 for 30 minutes. Values represent mean ± SEM (*n*=6), and (*) indicates significant differences between positive control and negative control.

Table 2.7. Statistical analysis data corresponding to measurements of carbonyl content in a protein lysate from OK cells treated with different concentrations of R1 bioferrofluids for 24 hours (n=6).

$[Fe_2O_3]$ g/L	R1 bioferrofluids	
	Carbonyl content (Mean ± SD) (nmol carbonyls/mg protein)	P (Mann-Whitney)
Negative control	3.76 ± 0.25	-
Positive control	7.41 ± 0.76	0.0048
0.0005	3.99 ± 0.22	0.1262
0.001	4.05 ± 0.14	0.1262
0.002	4.16 ± 0.56	0.1262
0.005	4.32 ± 0.60	0.1262
0.007	4.02 ± 0.31	0.0641
0.01	4.06 ± 0.20	0.2273
0.02	3.84 ± 0.12	0.9358

2.4.4.2 Thiol tracker

The existence of oxidative stress was also determined by measuring the abundance of reduced glutathione in OK cells treated with different concentrations of bioferrofluids (R1 and R8) for 24 hours. Thiol tracker was used for both, visualisation under fluorescence microscopy and quantification in fluorometer. Results showed no existence of any change in the concentration of reduced thiol content upon bioferrofluids treatment either visually Fig. 2.20 or fluorometrically Fig. 2.21, suggesting the absence of oxidative stress. Data corresponding to GSH measurement were analysed using Mann-Whitney test and are summarised in Table 2.8.

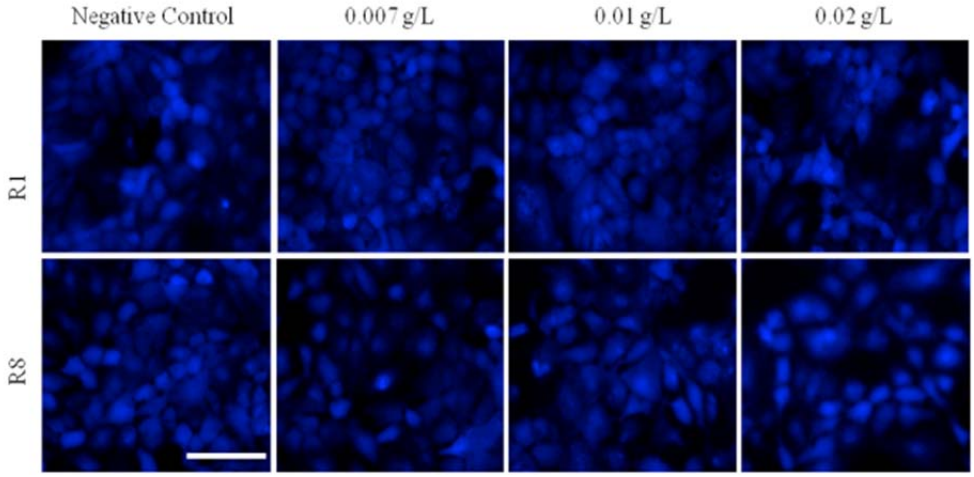

Figure 2.20: Confocal micrographs of Thiol tracker stained OK cells treated with different concentrations of R1 and R8 bioferrofluids for 24 hours. Scale bar: 100 μm.

Table 2.8. Statistical analysis data for GSH measurement in OK cells treated with different concentrations of R1 and R8 bioferrofluids for 24 hours (n=9).

$[Fe_2O_3]$ g/L	R1 bioferrofluids		R8 bioferrofluids	
	GSH measurement Mean ± SD (GSH %)	P (Mann-Whitney)	GSH measurement Mean ± SD (GSH %)	P (Mann-Whitney)
0	100.00 ± 24.71	-	100.00 ± 24.71	-
0.007	128.69 ± 30.01	0.0712	99.07 ± 19.53	0.7577
0.01	118.95 ± 24.91	0.2105	130.05 ± 30.68	0.0549
0.02	122.20 ± 27.83	0.1416	113.45 ± 26.16	0.3510

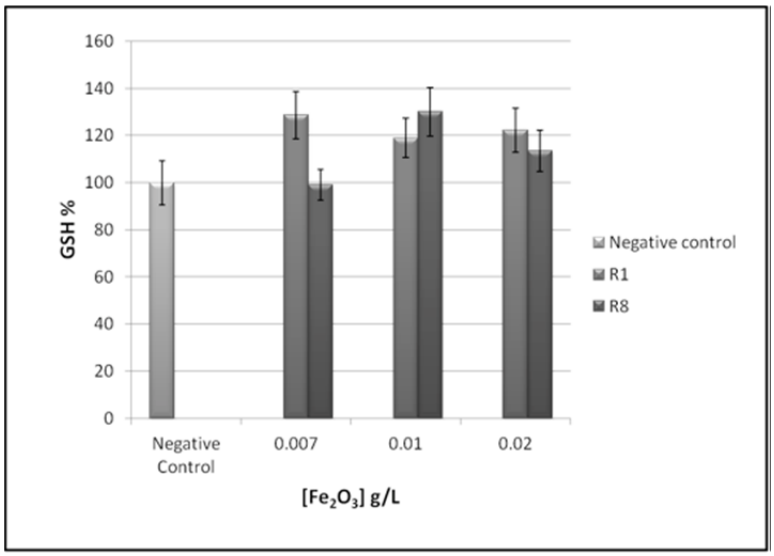

Figure 2.21: Quantitative fluorometric measurement of reduced glutathione in OK cells treated with different concentrations of R1 and R8 bioferrofluids for 24 hours. Values represent mean ± SEM (*n*=9).

2.4.5 Inflammasome activation

2.4.5.1 IL-1β measurement

We checked the possibility of inflammasome activation as a likely toxic response that could be involved in cell death. With this purpose, IL-1β level was measured in cell culture medium of OK cells treated with different concentrations of R1 and R8 bioferrofluids for 24 hours. Results showed a significant increase in IL-1β level at concentration 0.02 g/L Fe_2O_3 of R1 bioferrofluids, while R8 did not, as shown in Fig. 2.22. Data corresponding to IL-1β measurement were analysed using Mann-Whitney test and are summarised in Table 2.9.

Table 2.9. Statistical analysis data for IL-1β level measurement in cell culture medium of OK cells treated with different concentrations of R1 and R8 bioferrofluids for 24 hours (n=4).

$[Fe_2O_3]$ g/L	R1 bioferrofluids		R8 bioferrofluids	
	IL-1β measurement Mean ± SD (% IL-1β expression)	P (Mann-Whitney)	IL-1β measurement Mean ± SD (% IL-1β expression)	P (Mann-Whitney)
0	100.00 ± 8.71	-	100.00 ± 8.71	-
0.007	110.88 ± 5.74	0.1143	109.59 ± 5.41	0.1143
0.02	499.22 ± 48.61	0.0286	110.88 ± 2.18	0.0571

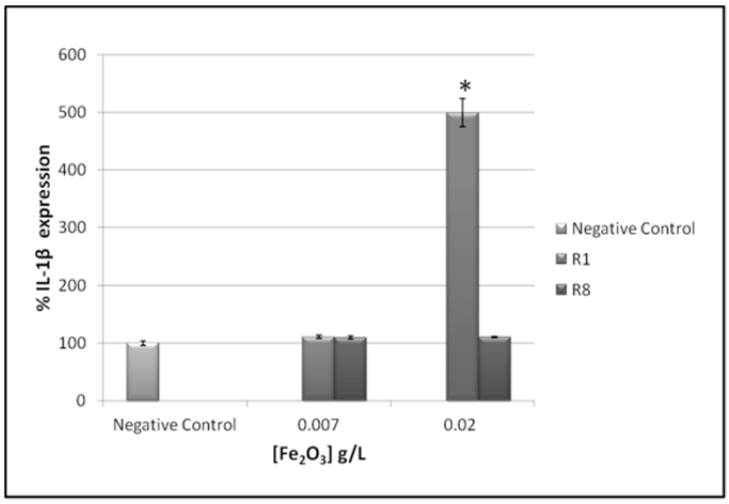

Figure 2.22: Quantitative IL-1β level measurement in cell culture medium of OK cells treated with different concentrations of R1 and R8 bioferrofluids for 24 hours. Values represent mean ± SEM (*n*=4), and (*) indicates significant differences between R1 treated OK cells and negative control.

2.4.5.2 LysoTracker

Finally, we also visually checked the abundance of the lysosomes as a possible target of internalised NPs, because a malfunctioning of these organelles could explain the sudden cell necrosis. Thus, OK cells were treated with R1 and R8 bioferrofluids at concentration 0.02 g/L Fe_2O_3, for 24 hours. Lysosomes visualisation with a LysoTracker revealed that after treatment with 0.02 g/L Fe_2O_3 of either R1 or R8, OK cells showed an increased fluorescence, as shown in Fig.2.23. As a result, we investigated the fate of NPs in the cell as well as the internalisation mechanism, which are the contents of the next chapter.

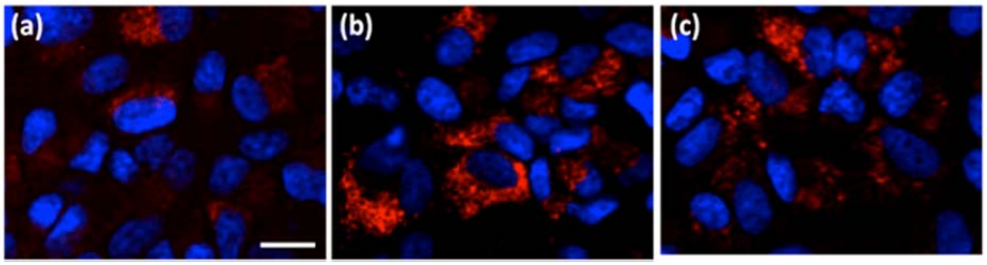

Figure 2.23: Fluorescent labelling of OK cell lysosomes (red) with a LysoTracker before (a) and after treatment with 0.02 g/L Fe_2O_3 of R1 (b) and R8 (c) bioferrofluids. Blue is DAPI staining of nuclei. Scale bar: 20 μm.

2.5 Discussion and conclusions

In general, a biomedical performance, however promising, would be of little significance without a good biocompatibility that must join with efficient cellular uptake. Therefore, the main aim of this chapter is to study the toxicity of our bioferrofluids *in vitro*.

Generally, SPIONs were considered as non-toxic, as iron is involved in many cellular functions, but their unique physicochemical properties would impose toxicity. Our concern about the toxicity starts from the choosing of the core, our synthetic strategy guarantees a precipitation of maghemite nanoparticles only. Several studies showed that maghemite nanoparticles have lower toxicity as compared to magnetite nanoparticles. The reason is that magnetite is a mixture of FeO and Fe_2O_3, which is not stable and undergoes oxidation to form maghemite (equation 2.2), releasing free Fe^{2+} ions that can penetrate the nucleus membrane causing DNA damage or penetrate the mitochondrial membrane producing ROS through Fenton reaction (equation 2.1), which in turn causes DNA damage (genotoxicity) [24,59].

$$Fe_3O_4 + 2H^+ \text{------} \rightarrow \gamma\ Fe_2O_3 + Fe^{2+} + H_2O \quad \text{(Equation 2.2)}$$

Cell viability results showed cell type-dependent toxicity, as bioferrofluids are more toxic in VSMC than OK cells Fig. 2.10. Other authors have emphasised the crucial role of cell type on the toxicity response to nanoparticles [60,61]. Difference in toxicity response between both cell lines to the nanoparticles could be related to the internalised amount of nanoparticles inside both cell lines. VSMC take up more nanoparticles as compared to OK cells, as shown in Fig. 3.10. Several studies illustrate the relationship between toxicity, uptake and intracellular localisation of the nanoparticles inside the cells, as higher uptake rates are usually linked to greater biological effects. In addition, the mere presence of nanoparticles enclosed in the lysosmes causes toxicity, as they reach a high local concentration that exceed LC_{50}, which may lead to sudden death [23,61,62]. A study carried out by Soenen et al. illustrated that the intracellular localisation and intracellular concentration of nanoparticles inside the cell maybe consider the cause of cellular stress that is manifested itself as a reduction in cell proliferation, transit increase in ROS production

and alteration in actin cytoskeleton in murine 3T3 fibroblasts cells treated with positively charged magnetoliposomes [45]. Our mean lethal concentrations are lower than previously reported values. However, taking into account the great variability in methodology, experimental condition, nanoparticle characterisation, concentrations, etc., a comparison of the results is out of question [63,64]. LC_{50} values were decreased with time in both cell lines Fig. 2.11 indicating that the toxicity is due to accumulative effect.

There are several factors influencing the cell toxicity of nanoparticles, such as nanoparticle composition, oxidative state of iron in SPIONs, coating, shape, surface charge, core size, hydrodynamic size, among others [28,35,36]. With respect to the nanoparticles composition, our results show that in both cell lines the toxicity increases by increasing the polymer/iron ratio, Fig. 2.12(e). This is in contradiction with a study carried out by Mahmoudi et al. indicating the inverse relationship between toxicity and polymer/iron ratio [28]. Interestingly, the toxicity and uptake of nanoparticles were depending on the oxidative state of iron (Fe^{2+} or Fe^{3+}), our results showed that by increasing Fe^{2+}/Fe^{3+} ratio (Table 2.2) the toxicity and uptake decreased in both cell lines.

Similar to other preparations, our nanoparticles are surrounded by a PEG coating in order to reduce the interactions with cell membrane and consequently reduce internalisation rate and toxicity [65,66]. These effects are proportional to the percentage of PEG chains on the surface [67] and the molecular weight of PEG [68]. Yu et al. showed that uncoated IONPs induced more than 6 fold increase in cell death as compared to dextran or PEG coated ones [69].

Toxicity is also strongly affected by surface charge, studies show that positively charged NPs are internalised more in cells, and consequently toxicity is also higher [70,71]. However, controlling the number of positive charge could achieve higher uptake with lower toxicity [72]. Samples used in the present work can be considered as neutral or slightly positive, according to Z-potential measurements. Therefore, no toxicity should be expected from surface charge. The mechanism of cell death could

be related to the surface charge. A study carried out by Schaeublin et al., shows that positively charged gold nanoparticles cause apoptosis, while neutral ones cause necrosis in HaCat cells [29].

Beside all the previously mentioned factors that affect the NPs toxicity, a size-dependent toxicity was also observed in both cell lines, see Fig. 2.12(a), (b), which is clearer in case of OK cells, see Fig. 2.13. Toxicity decreases as maghemite core size and bead hydrodynamic size increase, which will be explained in the next chapter by a lower uptake observed in larger nanoparticles sizes, as shown in Fig 3.9(a). A similar finding was observed by Mahmoudi et.al. who observed a decrease in the cellular toxicity of PVA coated SPIONs by increasing the hydrodynamic diameters, due to lower uptake [28]. In addition, cell death seems to be concentration dependent, as indicated by the linear correlations shown in Fig. 2.12(c), and inversely proportional to the total number of nanoparticles (total surface area) Fig. 2.12(d).

The subsequent studies have been focused on OK cells only, as the preliminary *in vivo* studies indicated accumulation of nanoparticles in kidney.

Exposure to SPIONs has been associated with apoptosis [35]. In this work we show that our SPIONs cause necrotic cell death, which is indicated by absence of the common apoptotic markers: DNA fragmentation, see Figs. 2.16 and 2.17, and caspase-3, see Fig. 2.18.

The relationship between SPIONs and ROS induction is not clear. Some studies show the ability of SPIONs to induce ROS [36], others show their peroxidase-like activity [40]. ROS can cause cell death through either apoptosis or necrosis, then, the link between ROS and induction of toxic effect is not clear and seems to be somehow cell type-dependent [73]. ROS induction by nanoparticles depends on several factors such as coating stability, the amount of total surface area of internalised IONPs and also the time of incubation [41,74]. After 24 hours of incubation with R1 bioferrofluids our bioferrofluids did not show any significant changes in carbonyl contents level in OK cells, see Fig. 2.19. There may be two explanations supporting this result. First, the incubation time maybe inadequate, as in this study we measured the carbonyl content level after 24 hours of incubation. Arbab et al. showed that ROS

induction by SPIONs reaches its highest level after 24 hours of incubations and returns to normal after 72 hours [75]. However, Stroh et al. showed that ROS induction by SPIONs reaches its highest level after 90 minutes of incubations and disappears after 24 hours of incubation [41]. All these studies are depending on the coat stability of the nanoparticles as well as other experimental factors (e.g. cell type). Therefore, assessing the carbonyl content in time interval is mandatory. A second explanation can be in the higher stability of our coating (P4VP-g-APEG). Our maghemite nanoparticles are embedded within P4VP that is stable at acidic pH and then coated with PEG. The degradation resistance of P4VP under acidic pH protects the IONPs from degradation in the lysosmes. This explains the persistence of our nanoparticles as intact over a period of 30 days post injection *in vivo* without any toxic effect (chapter 5) and well as the non-oxidative stress induction. Stability of the coat and ROS induction have been the centre of several studies. Soenen et al. showed that the endosomal localisation of different coated SPIONs results in nanoparticles degradation and release of free ions that generate ROS. Thus, citrate coated SPIONs showed faster maximal ROS induction (4h) compared to other SPIONs coated with dextran or lipid [76]. Carbonyl content level results were confirmed by the normal level of GSH in nanoparticles treated cells, as shown in Figs. 2.20 and 2.21.

Many nanomaterials have been reported to induce inflammation as a consequence of an elevated level of ROS or as a consequence of nanomaterial binding and activation of cell surface receptors, see Fig. 2.4(d). This leads to the activation of NF-KB, which in turns activates inflammatory genes, including genes encoding the pro-inflammatory cytokines: TNFα, IL-6 and IL-1β [34,77,78]. The pro-IL-1β is converted to activate IL-1β with the help of Caspase-1, which results from inflammasome activation. Our nanoparticles produced an elevated level of IL-1β at higher concentration (0.02 g/L Fe_2O_3) of R1, see Fig. 2.22, demonstrating the inverse relationship between nanoparticle size and induction of inflammatory effect. Similar results have been observed by Yang et al. using silver nanoparticles [78].

Activation of the inflammasome occurs through several stimuli, one of them being the lysosomal damage. For this reason we have carried out an assay to elucidate the

interrelationship between NPs and lysosome. Our results showed that the fate of nanoparticles seems to be their storage into the lysosomes, see Fig. 2.23. Then, when the experimental *in vitro* conditions lead to a massive internalisation and accumulation into lysosomes, a sudden disorder of this organelle seems to take place and necrosis of the cell arises, as shown in Figs. 2.14 and 2.15. We do not have a direct evidence for the occurrence of this mechanism, however, the accumulation of the nanoparticles in the lysosomes and the increased abundance of these organelles in the cells, see Fig. 2.23, points out to this possibility. Soenen et al. also suggested this possibility as the abundance of lysosomes in the perinuclear region could impede protein transcription, and also cause disruption in the cytoskeleton [46].

From all above we can conclude that our bioferrofluids toxicity is depending on several factors such as cell type, maghemite nanoparticle size, bead hydrodynamic size, polymer/iron ratio, Fe^{2+}/Fe^{3+} ratio, concentration, total nanoparticles number , coating and charge. Nanoparticles cause cell death through necrosis with no evidence of ROS production after 24 hours of incubation in OK cells, small size nanoparticles (sample R1) have an inflammatory effect arising from inflammasome activation and the larger nanoparticles that having higher iron oxide loading (sample R8) are preferred for further work due to their lower toxicity in compared to other sizes.

2.6 References

[1] A. Nel, T. Xia, L. Mädler, and N. Li, "Toxic potential of materials at the nanolevel.," *Science*, vol. 311, no. 5761, pp. 622–7, 2006.

[2] G. Oberdörster, E. Oberdörster, and J. Oberdörster, "Nanotoxicology: An Emerging Discipline Evolving from Studies of Ultrafine Particles," *Environ. Health Perspect.*, vol. 113, no. 7, pp. 823–839, 2005.

[3] Y. zhao, H. Meng, Z. Chen, F. Zhao, and Z. chai, "Biological activities of nanomaterials/nanoparticles" In: Y. zhao and H. S. Nalwa, ed. Nanotoxicology - Interactions of Nanomaterials with Biological Systems. American scientific publishers 2007.

[4] A. Seaton, L. Tran, R. Aitken, and K. Donaldson, "Nanoparticles, human health hazard and regulation.," *J. R. Soc. Interface*, vol. 7 Suppl 1, no. September 2009, pp. S119–29, 2010.

[5] M. KATZ, "Atmospheric pollution: a growing problem in public health.," *Am. J. Public Health Nations. Health*, vol. 45, no. 3, pp. 298–305, 1955.

[6] C. Terzano, F. Di Stefano, V. Conti, E. Graziani, and A Petroianni, "Air pollution ultrafine particles: toxicity beyond the lung.," *Eur. Rev. Med. Pharmacol. Sci.*, vol. 14, no. 10, pp. 809–21, 2010.

[7] A. Nemmar, M. F. Hoylaerts, P. H. Hoet, D. Dinsdale, T. Smith, H. Xu, J. Vermylen, and B. Nemery "Ultrafine Particles Affect Experimental Thrombosis in an In Vivo Hamster Model," *Am. J. Respir. Crit. Care Med.*, vol. 166, no. 7, pp. 998–1004, 2002.

[8] K. Donaldson, V. Stone, P. S. Gilmour, D. M. Brown, and W. MacNee, "Ultrafine particles: mechanisms of lung injury," *Philos. Trans. R. Soc. A Math. Phys. Eng. Sci.*, vol. 358, no. 1775, pp. 2741–2749, 2000.

[9] A Seaton, A Soutar, V. Crawford, R. Elton, S. McNerlan, J. Cherrie, M. Watt, R. Agius, and R. Stout, "Particulate air pollution and the blood.," *Thorax*, vol. 54, no. 11, pp. 1027–32, 1999.

[10] http://www.guardian.co.uk/theguardian/from-the-archive-blog/2012/dec/05/great-smog-london-1952-archive.

[11] H. C. Fischer and W. C. W. Chan, "Nanotoxicity: the growing need for in vivo study.," *Curr. Opin. Biotechnol.*, vol. 18, no. 6, pp. 565–71, 2007.

[12] K. R. Vega-Villa, J. K. Takemoto, J. a Yáñez, C. M. Remsberg, M. L. Forrest, and N. M. Davies, "Clinical toxicities of nanocarrier systems.," *Adv. Drug Deliv. Rev.*, vol. 60, no. 8, pp. 929–38, 2008.

[13] C. Medina, M. J. Santos-Martinez, a Radomski, O. I. Corrigan, and M. W. Radomski, "Nanoparticles: pharmacological and toxicological significance.," *Br. J. Pharmacol.*, vol. 150, no. 5, pp. 552–8, 2007.

[14] A. Nemmar, P. H. Hoet, B. Vanquickenborne, D. Dinsdale, M. Thomeer, M. F. Hoylaerts, H. Vanbilloen, L. Mortelmans, and B. Nemery "Passage of Inhaled Particles Into the Blood Circulation in Humans," *Circulation*, vol. 105, no. 4, pp. 411–414, 2002.

[15] A. A. Shvedova, V. Castranova, E. R. Kisin, D. Schwegler-Berry, A. R. Murray, V. Z. Gandelsman, A. Maynard, and P. Baron, "Exposure to carbon nanotube material: assessment of nanotube cytotoxicity using human keratinocyte cells.," *J. Toxicol. Environ. Health. A*, vol. 66, no. 20, pp. 1909–26, 2003.

[16] J. W. Card, D. C. Zeldin, J. C. Bonner, and E. R. Nestmann, "Pulmonary applications and toxicity of engineered nanoparticles," pp. 400–411, 2008.

[17] Z. Li, T. Hulderman, R. Salmen, R. Chapman, S. S. Leonard, S.-H. Young, A. Shvedova, M. I. Luster, and P. P. Simeonova, "Cardiovascular effects of pulmonary exposure to single-wall carbon nanotubes.," *Environ. Health Perspect.*, vol. 115, no. 3, pp. 377–82, 2007.

[18] A. Radomski, P. Jurasz, D. Alonso-Escolano, M. Drews, M. Morandi, T. Malinski, and M. W. Radomski, "Nanoparticle-induced platelet aggregation and vascular thrombosis.," *Br. J. Pharmacol.*, vol. 146, no. 6, pp. 882–93, 2005.

[19] C.-W. Lam, J. T. James, R. McCluskey, and R. L. Hunter, "Pulmonary toxicity of single-wall carbon nanotubes in mice 7 and 90 days after intratracheal instillation.," *Toxicol. Sci.*, vol. 77, no. 1, pp. 126–34, 2004.

[20] Z. Chen, H. Meng, G. Xing, C. Chen, Y. Zhao, C. Zhu, X. Fang, B. Ma, and L. Wan, "Acute toxicological effects of copper nanoparticles in vivo," vol. 163, pp. 109–120, 2006.

[21] W. G. Kreyling, S. Hirn, and C. Schleh, "Nanoparticles in the lung.," *Nat. Biotechnol.*, vol. 28, no. 12, pp. 1275–6, 2010.

[22] M. Cazzola, G. Bergamaschi, L. Dezza, and P. Arosio, "Manipulations of cellular iron metabolism for modulating normal and malignant cell proliferation: achievements and prospects.," *Blood*, vol. 75, no. 10, pp. 1903–19, 1990.

[23] S. J. Soenen, P. Rivera-Gil, J.-M. Montenegro, W. J. Parak, S. C. De Smedt, and K. Braeckmans, "Cellular toxicity of inorganic nanoparticles: Common aspects and guidelines for improved nanotoxicity evaluation," *Nano Today*, vol. 6, no. 5, pp. 446–465, 2011.

[24] H. L. Karlsson, J. Gustafsson, P. Cronholm, and L. Möller, "Size-dependent toxicity of metal oxide particles--a comparison between nano- and micrometer size.," *Toxicol. Lett.*, vol. 188, no. 2, pp. 112–8, 2009.

[25] D. B. Warheit, T. R. Webb, C. M. Sayes, V. L. Colvin, and K. L. Reed, "Pulmonary instillation studies with nanoscale TiO2 rods and dots in rats: toxicity is not dependent upon particle size and surface area.," *Toxicol. Sci.*, vol. 91, no. 1, pp. 227–36, 2006.

[26] Y.-J. Gu, J. Cheng, C.-C. Lin, Y. W. Lam, S. H. Cheng, and W.-T. Wong, "Nuclear penetration of surface functionalized gold nanoparticles.," *Toxicol. Appl. Pharmacol.*, vol. 237, no. 2, pp. 196–204, 2009.

[27] M. Chu, Q. Wu, H. Yang, R. Yuan, S. Hou, Y. Yang, Y. Zou, S. Xu, K. Xu, A. Ji, and L. Sheng, "Transfer of quantum dots from pregnant mice to pups across the placental barrier.," *Small*, vol. 6, no. 5, pp. 670–8, 2010.

[28] M. Mahmoudi, a Simchi, a S. Milani, and P. Stroeve, "Cell toxicity of superparamagnetic iron oxide nanoparticles.," *J. Colloid Interface Sci.*, vol. 336, no. 2, pp. 510–8, 2009.

[29] N. M. Schaeublin, L. K. Braydich-Stolle, A. M. Schrand, J. M. Miller, J. Hutchison, J. J. Schlager, and S. M. Hussain, "Surface charge of gold nanoparticles mediates mechanism of toxicity.," *Nanoscale*, vol. 3, no. 2, pp. 410–20, 2011.

[30] S. Bhattacharjee, L. H. J. de Haan, N. M. Evers, X. Jiang, A. T. M. Marcelis, H. Zuilhof, I. M. C. M. Rietjens, and G. M. Alink, "Role of surface charge and oxidative stress in cytotoxicity of organic monolayer-coated silicon nanoparticles towards macrophage NR8383 cells.," *Part. Fibre Toxicol.*, vol. 7, p. 25, 2010.

[31] M. F. Cury-Boaventura and R. Curi, "Regulation of reactive oxygen species (ROS)

production by C18 fatty acids in Jurkat and Raji cells.," *Clin. Sci. (Lond).*, vol. 108, no. 3, pp. 245–53, 2005.

[32] S. Arora, J. M. Rajwade, and K. M. Paknikar, "Nanotoxicology and in vitro studies: the need of the hour.," *Toxicol. Appl. Pharmacol.*, vol. 258, no. 2, pp. 151–65, 2012.

[33] M. Valko, M. Izakovic, M. Mazur, C. J. Rhodes, and J. Telser, "Role of oxygen radicals in DNA damage and cancer incidence.," *Mol. Cell. Biochem.*, vol. 266, no. 1–2, pp. 37–56, 2004.

[34] K. Donaldson, L. Tran, L. A. Jimenez, R. Duffin, D. E. Newby, N. Mills, W. MacNee, and V. Stone, "Combustion-derived nanoparticles: a review of their toxicology following inhalation exposure.," *Part. Fibre Toxicol.*, vol. 2, p. 10, 2005.

[35] N. Singh, G. J. S. Jenkins, R. Asadi, and S. H. Doak, "Potential toxicity of superparamagnetic iron oxide nanoparticles (SPION)," *Nano Rev.*, vol. 1, pp. 1–15, 2010.

[36] A. R. Murray, E. Kisin, A. Inman, S.-H. Young, M. Muhammed, T. Burks, A. Uheida, A. Tkach, M. Waltz, V. Castranova, B. Fadeel, V. E. Kagan, J. E. Riviere, N. Monteiro-Riviere, and A. A. Shvedova, "Oxidative Stress and Dermal Toxicity of Iron Oxide Nanoparticles In Vitro.," *Cell Biochem. Biophys.*, vol. 67, no. 2, pp. 461–76, 2013.

[37] L. Gao, J. Zhuang, L. Nie, J. Zhang, Y. Zhang, N. Gu, T. Wang, J. Feng, D. Yang, S. Perrett, and X. Yan, "Intrinsic peroxidase-like activity of ferromagnetic nanoparticles.," *Nat. Nanotechnol.*, vol. 2, no. 9, pp. 577–83, 2007.

[38] H. Wei and E. Wang, "Fe3O4 magnetic nanoparticles as peroxidase mimetics and their applications in H2O2 and glucose detection.," *Anal. Chem.*, vol. 80, no. 6, pp. 2250–4, 2008.

[39] J. Zhuang, K. Fan, L. Gao, D. Lu, J. Feng, D. Yang, N. Gu, Y. Zhang, M. Liang, and X. Yan, "Ex Vivo Detection of Iron Oxide Magnetic Nanoparticles in Mice Using Their Intrinsic Peroxidase-Mimicking Activity.," *Mol. Pharm.*, vol. 9, no. 7, pp. 1983–9, 2012.

[40] D.-M. Huang, J.-K. Hsiao, Y.-C. Chen, L.-Y. Chien, M. Yao, Y.-K. Chen, B.-S. Ko, S.-C. Hsu, L.-A. Tai, H.-Y. Cheng, S.-W. Wang, C.-S. Yang, and Y.-C. Chen, "The promotion of human mesenchymal stem cell proliferation by superparamagnetic iron oxide nanoparticles.," *Biomaterials*, vol. 30, no. 22, pp. 3645–51, 2009.

[41] A. Stroh, C. Zimmer, C. Gutzeit, M. Jakstadt, F. Marschinke, T. Jung, H. Pilgrimm, and T. Grune, "Iron oxide particles for molecular magnetic resonance imaging cause transient oxidative stress in rat macrophages.," *Free Radic. Biol. Med.*, vol. 36, no. 8, pp. 976–84, 2004.

[42] A. K. Gupta and M. Gupta, "Cytotoxicity suppression and cellular uptake enhancement of surface modified magnetic nanoparticles.," *Biomaterials*, vol. 26, no. 13, pp. 1565–73, 2005.

[43] R. Gagescu, J. Gruenberg, and E. Smythe, "Membrane dynamics in endocytosis: structure--function relationship.," *Traffic*, vol. 1, no. 1, pp. 84–8, 2000.

[44] A. K. Gupta and A. S. G. Curtis, "Lactoferrin and ceruloplasmin derivatized superparamagnetic iron oxide nanoparticles for targeting cell surface receptors.," *Biomaterials*, vol. 25, no. 15, pp. 3029–40, 2004.

[45] S. J. H. Soenen, E. Illyes, D. Vercauteren, K. Braeckmans, Z. Majer, S. C. De Smedt, and M. De Cuyper, "The role of nanoparticle concentration-dependent induction of cellular stress in the internalization of non-toxic cationic magnetoliposomes.," *Biomaterials*, vol. 30, no. 36, pp. 6803–13, 2009.

[46] S. J. H. Soenen, N. Nuytten, S. F. De Meyer, S. C. De Smedt, and M. De Cuyper, "High intracellular iron oxide nanoparticle concentrations affect cellular cytoskeleton and focal adhesion kinase-mediated signaling.," *Small*, vol. 6, no. 7, pp. 832–42, 2010.

[47] M. Tsoli, H. Kuhn, W. Brandau, H. Esche, and G. Schmid, "Cellular uptake and toxicity of Au55 clusters.," *Small*, vol. 1, no. 8–9, pp. 841–4, 2005.

[48] Q. Sun, D. Tan, Y. Ze, X. Sang, X. Liu, S. Gui, Z. Cheng, J. Cheng, R. Hu, G. Gao, G. Liu, M. Zhu, X. Zhao, L. Sheng, L. Wang, M. Tang, and F. Hong, "Pulmotoxicological effects caused by long-term titanium dioxide nanoparticles exposure in mice.," *J. Hazard. Mater.*, vol. 235–236, pp. 47–53, 2012.

[49] M. Auffan, L. Decome, J. Rose, T. Orsiere, M. De Meo, V. Briois, C. Chaneac, L. Olivi, J.-L. Berge-Lefranc, A. Botta, M. R. Wiesner, and J.-Y. Bottero, "In vitro interactions between DMSA-coated maghemite nanoparticles and human fibroblasts: A physicochemical and cyto-genotoxical study.," *Environ. Sci. Technol.*, vol. 40, no. 14, pp. 4367–73, 2006.

[50] A. S. Arbab, G. T. Yocum, A. M. Rad, A. Y. Khakoo, V. Fellowes, E. J. Read, and J. A. Frank, "Labeling of cells with ferumoxides-protamine sulfate complexes does not inhibit function or differentiation capacity of hematopoietic or mesenchymal stem cells.," *NMR Biomed.*, vol. 18, no. 8, pp. 553–9, 2005.

[51] Y.-C. Chen, J.-K. Hsiao, H.-M. Liu, I.-Y. Lai, M. Yao, S.-C. Hsu, B.-S. Ko, Y.-C. Chen, C.-S. Yang, and D.-M. Huang, "The inhibitory effect of superparamagnetic iron oxide nanoparticle (Ferucarbotran) on osteogenic differentiation and its signaling mechanism in human mesenchymal stem cells.," *Toxicol. Appl. Pharmacol.*, vol. 245, no. 2, pp. 272–9, 2010.

[52] A. Kroll, M. H. Pillukat, D. Hahn, and J. Schnekenburger, "Current in vitro methods in nanoparticle risk assessment: limitations and challenges.," *Eur. J. Pharm. Biopharm.*, vol. 72, no. 2, pp. 370–7, 2009.

[53] N. a Monteiro-Riviere, a O. Inman, and L. W. Zhang, "Limitations and relative utility of screening assays to assess engineered nanoparticle toxicity in a human cell line.," *Toxicol. Appl. Pharmacol.*, vol. 234, no. 2, pp. 222–35, 2009.

[54] R. Villa-Bellosta and V. Sorribas, "Different effects of arsenate and phosphonoformate

on P(i) transport adaptation in opossum kidney cells.," *Am. J. Physiol. Cell Physiol.*, vol. 297, no. 3, pp. C516–25, Sep. 2009.

[55] A. Martín-Pardillos, C. Sosa, and V. Sorribas, "Arsenic increases Pi-mediated vascular calcification and induces premature senescence in vascular smooth muscle cells.," *Toxicol. Sci.*, vol. 131, no. 2, pp. 641–53, 2013.

[56] https://cssportal.roche.com/LFR_PublicDocs/ras/11644793001_en_07.pdf.

[57] A. J. McGahon, S. J. Martin, R. P. Bissonnette, A. Mahboubi, Y. Shi, R. J. Mogil, W. K. Nishioka, and D. R. Green, "The end of the (cell) line: methods for the study of apoptosis in vitro.," *Methods Cell Biol.*, vol. 46, pp. 153–85, 1995.

[58] H. Giral, R. Villa-Bellosta, J. Catalán, and V. Sorribas, "Cytotoxicity of peroxisome proliferator-activated receptor alpha and gamma agonists in renal proximal tubular cell lines.," *Toxicol. In Vitro*, vol. 21, no. 6, pp. 1066–76, 2007.

[59] H. L. Karlsson, P. Cronholm, J. Gustafsson, and L. Mo, "Copper Oxide Nanoparticles Are Highly Toxic : A Comparison between Metal Oxide Nanoparticles and Carbon Nanotubes," *Chem Res Toxicol.,* vol. 21, no. 9, pp. 1726–32, 2008.

[60] M. Mahmoudi, S. Laurent, M. a Shokrgozar, and M. Hosseinkhani, "Toxicity evaluations of superparamagnetic iron oxide nanoparticles: cell 'vision' versus physicochemical properties of nanoparticles.," *ACS Nano*, vol. 5, no. 9, pp. 7263–76, 2011.

[61] A. D. Lehmann, W. J. Parak, F. Zhang, Z. Ali, C. Röcker, G. U. Nienhaus, P. Gehr, and B. Rothen-Rutishauser, "Fluorescent-magnetic hybrid nanoparticles induce a dose-dependent increase in proinflammatory response in lung cells in vitro correlated with intracellular localization.," *Small*, vol. 6, no. 6, pp. 753–62, 2010.

[62] E. Fröhlich, "The role of surface charge in cellular uptake and cytotoxicity of medical nanoparticles.," *Int. J. Nanomedicine*, vol. 7, pp. 5577–91, 2012.

[63] M. Mahmoudi, H. Hofmann, B. Rothen-Rutishauser, and A. Petri-Fink, "Assessing the in vitro and in vivo toxicity of superparamagnetic iron oxide nanoparticles.," *Chem. Rev.*, vol. 112, no. 4, pp. 2323–38, 2012.

[64] E. Ying and H.-M. Hwang, "In vitro evaluation of the cytotoxicity of iron oxide nanoparticles with different coatings and different sizes in A3 human T lymphocytes.," *Sci. Total Environ.*, vol. 408, no. 20, pp. 4475–81, 2010.

[65] E. Chang, N. Thekkek, W. W. Yu, V. L. Colvin, and R. Drezek, "Evaluation of quantum dot cytotoxicity based on intracellular uptake.," *Small*, vol. 2, no. 12, pp. 1412–7, 2006.

[66] Y. Zhang, N. Kohler, and M. Zhang, "Surface modification of superparamagnetic magnetite nanoparticles and their intracellular uptake," vol. 23, pp. 1553–61, 2002.

[67] S. Essa, J. M. Rabanel, and P. Hildgen, "Characterization of rhodamine loaded PEG-g-PLA nanoparticles (NPs): Effect of poly (ethylene glycol) grafting density," *Int. J. Pharm.*, vol. 411, no. 1–2, pp. 178–187, 2011.

[68] J. Xie, C. Xu, N. Kohler, Y. Hou, and S. Sun, "Controlled PEGylation of Monodisperse Fe3O4 Nanoparticles for Reduced Non-Specific Uptake by Macrophage Cells," *Adv. Mater.*, vol. 19, no. 20, pp. 3163–3166, 2007.

[69] M. Yu, S. Huang, K. J. Yu, and A. M. Clyne, "Dextran and Polymer Polyethylene Glycol (PEG) Coating Reduce Both 5 and 30 nm Iron Oxide Nanoparticle Cytotoxicity in 2D and 3D Cell Culture*," Int J Mol Sci.*, vol. 13, no. 5, pp. 5554–70, 2012.

[70] P. R. Leroueil, S. A. Berry, K. Duthie, G. Han, V. M. Rotello, D. Q. McNerny, J. R. Baker, B. G. Orr, and M. M. B. Holl, "Wide varieties of cationic nanoparticles induce defects in supported lipid bilayers.," *Nano Lett.*, vol. 8, no. 2, pp. 420–4, 2008.

[71] F. Cengelli, D. Maysinger, F. Tschudi-monnet, X. Montet, C. Corot, A. Petri-fink, H. Hofmann, and L. Juillerat-jeanneret, "Interaction of Functionalized Superparamagnetic Iron Oxide Nanoparticles with Brain Structures," *Pharmacology*, vol. 318, no. 1, pp. 108–116, 2006.

[72] S. J. H. Soenen, J. Baert, and M. De Cuyper, "Optimal conditions for labelling of 3T3 fibroblasts with magnetoliposomes without affecting cellular viability.," *Chembiochem*, vol. 8, no. 17, pp. 2067–77, 2007.

[73] B. Díaz, C. Sánchez-Espinel, M. Arruebo, J. Faro, E. de Miguel, S. Magadán, C. Yagüe, R. Fernández-Pacheco, M. R. Ibarra, J. Santamaría, and A. González-Fernández, "Assessing methods for blood cell cytotoxic responses to inorganic nanoparticles and nanoparticle aggregates.," *Small*, vol. 4, no. 11, pp. 2025–34, 2008.

[74] C. C. Berry, S. Wells, S. Charles, and A. S. G. Curtis, "Dextran and albumin derivatised iron oxide nanoparticles: influence on fibroblasts in vitro.," *Biomaterials*, vol. 24, no. 25, pp. 4551–7, 2003.

[75] A. S. Arbab, L. A. Bashaw, B. R. Miller, E. K. Jordan, B. K. Lewis, H. Kalish, and J. A. Frank, "Characterization of biophysical and metabolic properties of cells labeled with superparamagnetic iron oxide nanoparticles and transfection agent for cellular MR imaging.," *Radiology*, vol. 229, no. 3, pp. 838–46, 2003.

[76] S. J. H. Soenen, U. Himmelreich, N. Nuytten, T. R. Pisanic, A. Ferrari, and M. De Cuyper, "Intracellular nanoparticle coating stability determines nanoparticle diagnostics efficacy and cell functionality.," *Small*, vol. 6, no. 19, pp. 2136–45, 2010.

[77] J. Niu, K. Wang, and P. E. Kolattukudy, "Cerium oxide nanoparticles inhibit oxidative stress and nuclear factor-κB activation in H9c2 cardiomyocytes exposed to cigarette smoke extract.," *J. Pharmacol. Exp. Ther.*, vol. 338, no. 1, pp. 53–61, 2011.

[78] E.-J. Yang, S. Kim, J. S. Kim, and I.-H. Choi, "Inflammasome formation and IL-1β release by human blood monocytes in response to silver nanoparticles.," *Biomaterials*, vol. 33, no. 28, pp. 6858–67, 2012.

Chapter 3

Studies at the nano-bio interface level: uptake, subcellular localisation and endocytosis

3.1 Introduction

Since the *in vivo* delivery of the nanomaterials ends with cellular internalisation, studies pertaining to the nano-bio interface are of utmost importance. Good understanding of nanomaterial-cell interactions will, (a) disclose valuable information related to some nanomaterial implications, such as toxicity, (b) determine the intracellular fate of the nanomaterial, (c) help to design an efficient drug delivery system capable of escaping from unfavourable cellular conditions, e.g. lysosomes, (d) improve the subcellular targeting research area in the near future [1,2].

3.1.1 Nano-bio interface

The journey of the nanomaterials internalisation into the cells starts when the nanomaterials come in contact with the plasma cell membrane. At this moment two different worlds (synthetic and biological) are merged, generating what is called nano-bio interface which can be defined as "the interface between the nanomaterials and the biological systems (proteins, membranes, phospholipids, endocytic vesicles, organelles, DNA and biological fluids) that includes the dynamic physicochemical interactions, kinetics and thermodynamic exchanges between nanomaterials surfaces and biological systems surfaces" [3].

Nano-bio interface encompasses three dynamic interacting components as

depicted in Fig. 3.1: (a) the nanomaterial surface, which is affected by the nanomaterial physicochemical properties, (b) the solid-liquid interface, including the changes occurring when the nanomaterial interacts with components in the surrounding medium, (c) the interactions between the solid-liquid interface and the biological system [3].

Let us explain each of these components in more detail.

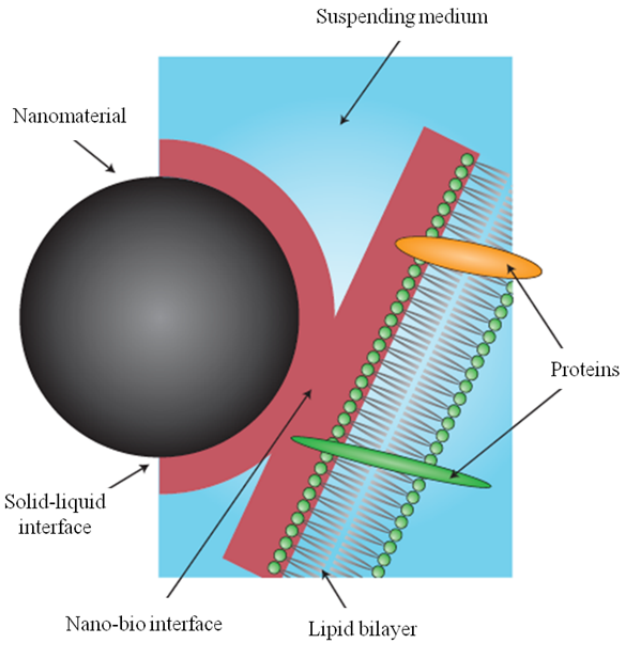

Figure 3.1: Schematic representation of the nano-bio interface [3].

3.1.1.1 The Nanomaterial

The nanomaterial internalisation into the cell following the nanomaterial-cell interaction is affected by many factors. Some of these factors are related to the nanomaterial physicochemical properties such as:

- ✓ The shape: Several studies have demonstrated the shape effect on the cellular uptake of the nanomaterial, for instance, Chithrani et al. studied the shape effect on gold nanoparticles uptake. Results indicated that spherical nanoparticles of sizes 74 and 14 nm were taken up 500% and 375% more than rod shaped nanoparticles of 74x14 nm size, respectively. This could be

explained on the basis that the elongated ones require more time for membrane wrapping [4]. Studying the effect of the shape on cellular uptake is complex and not well understood, since many other factors such as charge and size could influence. Therefore, a new technology known as PRINT is recommended to study the effect of the shape independent of other nanomaterial physicochemical properties [1,5].

- ✓ The size: Several studies have illustrated the effect of size on nanomaterial cellular uptake. For instance, Huang et al. studied the effect of the size on the cellular uptake using Polyvinylpyrrolidone (PVP) coated IONPs with different hydrodynamic diameters (32, 71, 102 and 118 nm) in macrophage cells. Results indicated that the higher uptake occurred at a nanoparticle size of 102 nm, which is considered as an optimum size for cellular uptake [6]. Another example is shown by Chithrani et al. They studied the uptake of gold nanoparticles with different sizes (14, 50 and 74 nm) in Hela cells. Results indicated that the 50 nm particle size is an optimal size for efficient nanoparticles uptake in Hela cells [4]. This study is consistent with a study carried out by Lu et al. In their work they studied the uptake of mesoporous silica nanoparticles with a size range of 30 to 280 nm in Hela cells. Results showed that 50 nm particle size is considered as an optimum size for efficient nanoparticles uptake in Hela cells [7].
- ✓ The charge: Surface charge is considered the most important parameter that is involved in the interactions of the nanomaterials with the biological membranes [8]. Accordingly, the nanomaterial net surface charge strongly determines its ability for internalisation into the cell [9,10]. Several studies showed that positively charged nanomaterials are taken up better by the cells than negatively or neutrally charged nanomaterials. For instance, Cengelli et al. stated that positively charged SPIONs functionalised with amino polyvinyl alcohol (PVA) are taken up by isolated brain-derived endothelial and microglial cells at a much higher level than negatively charged and neutral ones [10]. Villanueva et al. studied the uptake of IONPs functionalised with differently charged carbohydrates in Hela cells. Results showed no intracellular uptake for neutral nanoparticles. However, the negatively charged ones showed uptake and toxicity depending on the coating nature, while the

positively charged nanoparticles showed higher uptake with no toxicity [9]. These results require to be verified in terms of toxicity as they contradict other studies in the literature. As they depend on many other factors explained before, not all the studies are easy to compare. There is a strong correlation between the amount of the charge and the internalisation into the cell. Lorenz et al. showed the direct correlation between the amount of amino groups on the nanoparticle surface and the uptake by Hela cells. However, this relation was not clear for mesenchymal stem cells (MSC) which may be affected by other factors, such as nanoparticle size [11]. Not only the amount of the surface charge affects the nanomaterial-cell interaction but also the ligand arrangement on the nanomaterial surface, as stated by Verma et al. [12]. Although, the positively charged nanomaterials exhibit efficient internalisation into the cells, they have toxic effect due to severe pore formation in the plasma cell membrane [13]. Also they are immunogenic [14], quickly cleared from the circulation by RES and observed to agglomerate with erythrocytes and other blood components *in vivo* [15,16].

3.1.1.2 Interactions between the nanomaterial and the surrounding médium

According to several factors of the medium in which the nanomaterials exist, such as ionic strength, pH and the presence of large organic molecules (e.g. proteins), nanomaterials acquire new physicochemical properties, which in turns affect the nanomaterial-cell interaction and subsequently to the nanomaterial internalisation and its dispersion stability.

3.1.1.2.1 The effect of ionic strength and pH on the nanomaterial dispersion stability

Ionic strength and pH are considered important parameters that control the stability of the nanomaterial dispersion. Ionic strength influences the dispersion stability by changing the electrical double layer thickness, while the pH can affect the stability by altering the zeta potential. Increasing the ionic strength or bring the pH to the nanomaterial isoelectric point will enhance the agglomeration and disrupt the nanomaterial dispersion stability [17]. Jiang et al. studied the effect of ionic strength

and pH on the state of dispersion using 15 nm titanium oxide (TiO_2) nanoparticles. Increasing the ionic strength was associated with 50 fold increase in the hydrodynamic size, while changing the pH was associated with change in the hydrodynamic size and the surface charge [17]. Many of these newly acquired nanomaterial properties determine the forces that operate at the nanomaterial- medium interface Fig. 3.2. These forces include long-range forces arising from attractive van de Waals and repulsive electrostatic double layer interaction, plus short-range forces arising from charge, steric, depletion and solvent interactions [18]. In addition, changing the nanomaterial physicochemical properties will affect on the nanomaterial internalisation rate.

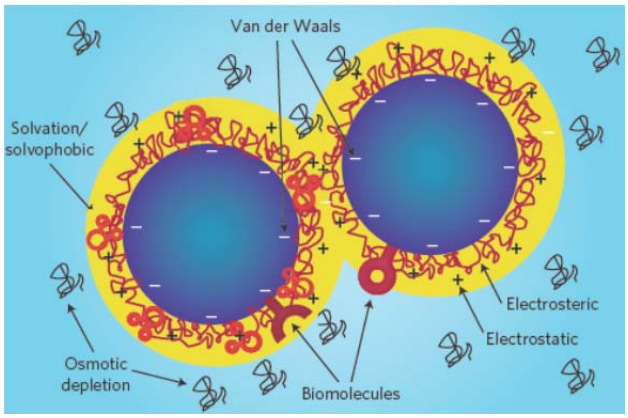

Figure 3.2: Demonstration of the forces involved in the interactions between nanomaterials [3].

3.1.1.2.2 Protein corona

When nanomaterials are introduced into biological fluids (blood, plasma or interstitial fluids), they are exposed to be coated with proteins forming nanomaterial-protein corona complexes. Protein concentration and nanomaterial physicochemical properties (size, charge, coatings, hydrophobicity, etc.) determine which proteins should interact with the nanomaterial and subsequently facilitate nanomaterial internalisation into the cell [19,20]. Albumin, immunoglobulins, complement proteins, fibrinogen and apolipoproteins have been identified as the proteins developing the strongest bonds to carbon nanotubes, iron oxide nanoparticles, liposomes and

polymeric nanoparticles surfaces [21].

The binding between the nanomaterial and protein has a mutual effect on both of them:

(i) Effect of the nanomaterial-protein corona complex on the nanomaterial: The nanomaterial acquires new physicochemical properties upon protein corona formation. Dobrovolskaia et al. studied the effect of the plasma proteins on the nanoparticle size and charge, and on the dispersion stability. The hydrodynamic size of 30 and 50 nm gold nanoparticles increased by 50 upon incubation with the plasma proteins as measured by DLS, and confirmed by other techniques such as TEM and atomic force microscopy (AFM), while the charge decreased. Such increase in size and decrease in surface charge can affect to nanoparticles uptake by the cells. Ultraviolet-visible (UV-Vis) studies proved that the protein corona stabilises the nanoparticles from aggregation [22]. In addition, formation of nanomaterial-protein corona complex affects to the nanomaterial biodistribution and clearance, as described in previous chapters.

(ii) Effect of the nanomaterial-protein corona complex on the proteins: As a result of nanomaterial-protein corona complex formation, proteins could undergo conformational changes resulting in activation [23], loss of function as enzymatic activity [24] and fibrillation [25].

3.1.1.3 Interactions between the nanomaterial and the biological system (Cellular uptake)

After the first interactions of the nanomaterial with biological medium, which can induce many changes and alterations in the nanomaterial physicochemical properties, as described in the previous section, finally the nanomaterial reaches the biological cell membrane. The interactions between the nanomaterials and biological membranes are not straightforward due to the complexity of both systems. The complexity of the plasma cell membrane arises from its selective permeability, flexibility and heterogeneity, while for the nanomaterial is due to its acquired physicochemical properties [3]. Several factors are controlling the nanomaterial uptake by the cells,

such as the nanomaterial physicochemical properties (explained in section 3.1.1.1), cell type [26], cell density [26] and nanomaterial concentration.

Nanomaterial surface ligands (antibodies, proteins, chemical moieties, metallic sites, polymers or surface functionalities) are the responsible to form the first link between the nanomaterial and the plasma cell membrane, resulting in internalisation of the nanomaterial inside the cell by either non-endocytic or endocytic routes of delivery, as depicted in Fig. 3.3 [3].

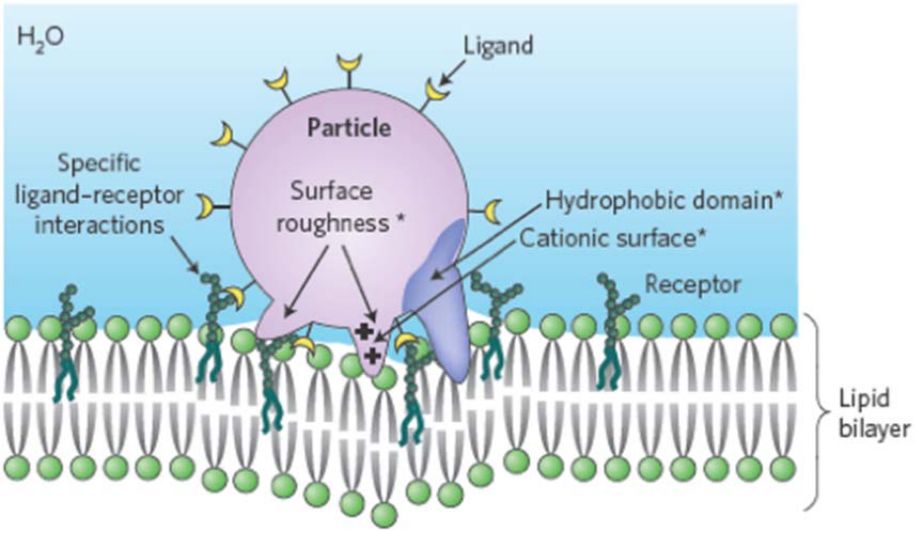

Figure 3.3: Schematic representation of nanomaterial-cell membrane interaction mechanisms that are responsible for nanomaterial internalisation. The parameters controlling the non-endocytic routes are marked by asterisks. In contrast, the endocytic route is controlled by specific ligand-receptor interactions [3].

3.1.1.3.1 Non-endocytic routes of delivery

The non-endocytic pathways are considered efficient tools for gene delivery, since they transport genes directly to the cytoplasm, bypassing the harshness conditions associated with the endocytic pathway such as the lysosomal degradation [27]. This direct penetration of the cell membrane is controlled by the nanomaterial surface properties (e.g. charge, hydrophobicity and roughness) which form non-specific attractive forces to the cell membrane [3].

3.1.1.3.2 Endocytic routes of delivery

Endocytosis is a complex process with multiple mechanisms by which cells transport extracellular and plasma membrane-bound entities into the cell interior. Altogether, these mechanisms have to control the entry into the cell in a coordinated and specific manner and they play a crucial role in many cellular processes [28,29]. According to the mechanism of internalisation, macromolecules such as nanomaterials pass through different environments inside the cells that vary in harshness due to enzymatic or chemical conditions. In addition, these mechanisms define the fate of the nanomaterials inside the cell and their subcellular localisation [1]. The endocytosis mechanisms categorise as a) phagocytosis or b) pinocytosis Fig. 3.4.

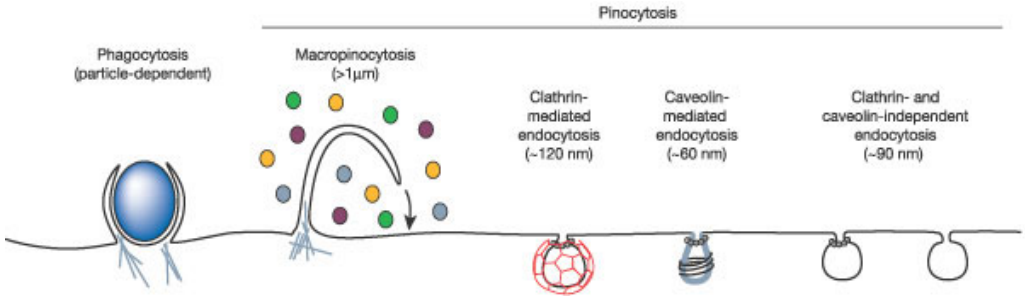

Figure 3.4: Different categories of endocytosis mechanisms [30].

a) **Phagocytosis (cell eating):** This mechanism is restricted to specialised mammalian cells, including macrophages, monocytes and neutrophils. The function of the mechanism is to engulf large pathogens or debris [30].

b) **Pinocytosis (cell drinking):** This mechanism is observed in all types of cells. The function of the mechanism is to internalise fluid surrounding cell [1,31]. Pinocytosis includes a handful of mechanisms distinguished by size and encapsulating vesicles composition as shown in Fig. 3.4:

I. M*acropinocytosis:* In this mechanism, membrane protrusions are formed to collapse onto and fuse with the plasma membrane in order to transport vesicles of microns in size. This mechanism is interesting due to its avoidance of lysosomal degradation [1,30].

II. *Micropinocytosis:* This mechanism is including the remaining mechanisms of pinocytosis that are responsible for the internalisation of nanomaterials with sizes ranging from tens to hundreds of nanometers [1].

- ✓ *Clathrin-mediated endocytosis (CME):* CME is the best studied

mechanism and was believed for long time to be the only mechanism of endocytosis [31]. CME occurs in all types of mammalian cells, transporting essential nutrients such as low-density lipoprotein (LDL) and iron-laden transferrin (Tfn) into cells through their binding to specific receptors, for that CME is considered as a highly selective internalisation mechanism [32,33]. After the formation of ligand-receptor complex, a variety of proteins including cytosolic proteins called clathrins, diffuse into the plasma membrane in order to shape a *coated pit* around the substance to be transferred. Then, it is invaginated and pinched off to form endocytic vesicles of sizes around 120 nm. This process is dynamin-dependent [34]. CME ends with lysosomal degradation which could be: a) harmful for the nanomaterials that could not resist these harsh conditions and lack the way to escape from the endosomal compartements [27], b) beneficial for pH-sensitive delivery system, bypassing cytoplasmic drug resistance mechanisms [35,36].

- ✓ *Caveolae-mediated endocytosis:* Caveolae are flask-shaped invaginations of the plasma membrane coated with caveolin-1, their size ranges from 50 to 80 nm [30,31]. Up to date, no studies have demonstrated the presence of caveolae able to uptake nanomaterials larger than 100 nm [31]. Caveolae mediates the internalisation of Simian virus 40 (SV40) and cholera toxin. However, other studies showed their internalisation by other endocytosis mechanisms [37,38]. This pathway facilitate the internalisation of the nanomaterial without lysosomal degradation to Golgi apparatus and endoplasmic reticulum [1].
- ✓ *Clathrin and caveolin-independent endocytosis:* Caveolae is considered as a type of lipid raft, other types of lipid raft are small in size (40-50 nm) and diffused freely on the plasma membrane. These small rafts can be internalised within any endocytic vesicle. For example, non aggregates cholera toxins bind to rafts associated with glycolipid and internalised by clathrin-coated

vesicles [30].

Currently, many methods are used to study the endocytosis mechanism of a given nanomaterial in a certain cell type, such as:

a) Pharma*cological inhibitors, as methyl-β-cyclodextrin* (mβCD), Genistein, Cytochalasin D, potassium depletion, etc. This method is not efficient, since some inhibitors are non-specific, and may inhibit more than one mechanism. In addition, other inhibitors have a side-effect on cell physiology [31].
b) Cell expressing muted proteins and the use of siRNA. These methods have disadvantages due to their side-effect on cell physiology. Therefore, the best way to study the endocytosis mechanism is try to combine several methodologies [31].
c) Intracellular localisation of nanomaterials, using markers for cellular structures such as Lysotracker, early endosome antigen 1 (EAA1), Caveolin, etc. Measuring the colocalisation is helpful but it should be kept in mind the reasons that cause the false colocalisation depending on the way of detection [31].

3.2 Objectives

The aim of this chapter is to understand the origin of the cytotoxicity caused by our bioferrofluids described in the previous chapter. This will be achieved through several studies at the nano-bio interface level such as: studying the cellular uptake and the uptake kinetics of NPs with exploring the effect of size, cell type, NPs concentrations and time of incubation, determination of the NPs subcellular localisation and finally determination of the endocytotic mechanism by which the NPs are internalised into the cell.

3.3 Materials and methods

3.3.1 Bioferrofluids preparation and characterisation

The preparation and characterisation methods of the bioferrofluids used in this chapter are described in Annex I. Their preparation conditions are summarised in Table 3.1.

Table 3.1: Preparation conditions of maghemite polymer nanocomposites for different samples.

Sample	P4VP (g/L)	1M $FeBr_3$ (mL)	1M $FeBr_2$ (mL)	Fe/pyridine mol ratio	Fe^{2+}/ Fe^{3+} mol ratio
R1`	1.4	2.22	1.11	0.25	0.50
R8`	2.4	12.03	10.83	1.00	0.90

3.3.2 Study of the cellular uptake and the corresponding kinetic behaviour

3.3.2.1 Qualitative determination of uptake using fluorescent nanoparticles

Opossum Kidney cells and vascular smooth muscle cells were seeded in 8 chamber slides (BD Falcon, Erembodegem, Belgium), and grown in their appropriate culture medium. After overnight growth of both cell lines, the supernatants were aspirated out and the cells were treated with 0.007 g/L Fe_2O_3 of fluorescein-labelled R8 nanoparticles (with 112 nm of hydrodynamic diameter) in serum free medium at different time points (4, 8, 12 and 24 hours). After treatment, the supernatants were aspirated out followed by cellular wash for 3 times with pre-warmed PBS. Cells were fixed with 3% (w/v) paraformaldehyde in PBS for 10 minutes at room temperature, followed by 3 times wash with PBS. After that, they were mounted and observed under Axiovert 200M fluorescence microscope equipped with ApoTome (Carl Zeiss, Jena, Germany) with excitation at 470 ± 20 nm and detection with a band pass filter at 525 ± 25 nm.

3.3.2.2 Quantitative iron detection

Both cell lines (OK and VSMC) were seeded in 6-well plastic plates and grown in their appropriate culture medium. When confluent, the culture medium was aspirated out and the cells were treated with different concentrations (0, 0.001, 0.003, 0.007, 0.01 g/L Fe_2O_3) of R1` and R8` bioferrofluids with, respectively, 84 nm and 163 nm of hydrodynamic diameter, in serum free culture medium for 24 hours. Some samples were treated with 0.007 g/L Fe_2O_3 of R8` bioferrofluids at time intervals of 0, 4, 8, 12 and 24 hours. After incubation, the cells were washed several times with PBS, trypsinised, and centrifuged at 4°C for 10 minutes at 1600 rpm. The supernatant was

discarded and the pellet was re-suspended in 400 µL Milli-Q water, using a syringe and a 25G needle. Two aliquots of 25 µL of this suspension were taken to determine the protein content, using a BCA ™ Protein Assay Kit. The remaining 350 µL of this suspension was used to determine the iron content by atomic absorption. With this purpose, the suspensions were placed in Teflon tubes and left for 24 hours at 80°C to dryness. After that, 1 mL of highly purified HNO_3 (>69.0%) was added, and then the samples were digested using a microwave digestor (MVS-2 Berghof). Samples were cooled and then diluted to 5 mL with Milli-Q water. Iron content was determined by graphite furnace atomic absorption spectroscopy (Varian SpectrAA with Zeeman corrector).

3.3.3 Subcellular localisation

3.3.3.1 Immunocytology

Both cell lines (OK and VSMC) were seeded in 8 chamber slides and grown in their appropriate culture medium. After overnight growth, the supernatants were aspirated out and the cells were treated with 0.007 g/L Fe_2O_3 of fluorescein-labelled R8 nanoparticles in serum free medium for 24 hours. After 24 hours, the supernatants were aspirated out and the cells were washed 3 times with cold PBS, fixed with 3% (w/v) paraformaldehyde in PBS for 10 minutes and washed 3 times with cold PBS. They were then incubated with 20 mM glycine in PBS for 10 minutes, washed again 3 times with cold PBS, permeabilised with 0.1% (w/v) saponin in PBS for 30 minutes, washed again and incubated with the primary antibodies for 1 hour at room temperature. For the endoplasmic reticulum and early endosomes detection, an anti-Derlin-1 (Sigma) antibody and an anti-EEA1 antibody (Santa Cruz Biotechnology Inc., Dallas, Texas, USA) were used respectively. After that, the cells were washed 3 times with PBS and then incubated for 30 minutes in the dark with the corresponding Alexa fluorescent secondary antibody, followed by 3 times wash with PBS. Cells were mounted with Prolong®Gold antifade reagent with DAPI (Life Technologies, USA). For co-localisation, an Axiovert 200M fluorescence microscope equipped with ApoTome for structured illumination and Axiovision software were used. Slides were excited at 470 ± 20 nm and green fluorescence was detected with a band pass filter at 525 ± 25 nm. Red fluorescence was excited using the long pass filter at 546 ± 6 nm

and emission at 590 nm, and DAPI was excited using the long pass filter at 436 ± 10 nm and emission at 480 ± 20 nm. Superimposition of green, red and blue fluorescence generated the final merged image.

3.3.3.2 Trackers (Lyso- and Mito- trackers)

Both cell lines (OK and VSMC) were seeded in 8 chamber slides, and grown in their appropriate culture medium. After overnight growth, the supernatants were aspirated out and the cells were treated with 0.007 g/L Fe_2O_3 of fluorescein-labelled R8 nanoparticles in serum free medium for 24 hours. After 24 hours, the supernatants were aspirated out and the cells were washed 3 times with PBS. For visualisation of the endo-lysosomal compartments, cells were incubated with 75 nM of LysoTracker® Red DND-99 (Life Technologies) for 2 hours at 37 ºC, following the manufacturer instructions. After this, the cells were washed with PBS, fixed with 3% (w/v) paraformaldehyde in PBS for 10 minutes, washed again three times, and mounted for microscopy. For mitochondria, cells were incubated with 200 nM of MitoTracker®Red CMXRos (Life Technologies) for 45 minutes at 37 ºC and then they were processed as for Lysotracker. The slides are ready for observation under Axiovert 200M fluorescence microscope equipped with ApoTome. Axiovision software was used. Slides were excited at 470 ± 20 nm, and green fluorescence was detected with a band pass filter at 525 ± 25 nm. Red fluorescence was excited using the long pass filter at 546 ± 6 nm and emission at 590 nm, and DAPI was excited using the long pass filter at 436 ± 10 nm and emission at 480 ± 20 nm. Superimposition of green, red and blue fluorescence generated the final merged image.

3.3.4 Study of endocytosis mechanism

3.3.4.1 Potassium depletion

Opossum Kidney cells, were seeded in 8 chamber slides and grown as previously described. Cells were washed once with potassium-free buffer (in mM, 140 NaCl, 20 Hepes pH 7.4, 1 $CaCl_2$, 1 $MgCl_2$, and 5.55 D-glucose) followed by a wash with hypotonic buffer (potassium-free buffer diluted with water 1:1). After three additional

washes with potassium-free buffer, cells were then incubated for 4 hours with 0.007 g/L Fe_2O_3 of fluorescein-labelled R8 nanoparticles in potassium-free buffer. As a positive control, different wells of OK cells were treated as above with a potassium-containing buffer and incubated with the same fluorescein-labelled R8 nanoparticles concentration and time in potassium-containing buffer. After incubation, the cells were washed, fixed and mounted as explained above and observed with Axiovert 200M fluorescence microscopy. Slides were excited at 470 ± 20 nm and green fluorescence was detected with a band pass filter at 525 ± 25 nm, DAPI excited using the long pass filter at 436 ± 10 nm and emission at 480 ± 20 nm.

3.3.4.2 Chlorpromazine inhibitor

After cell growth in 8 chamber slides as described previously, OK cells were incubated with 10 μg/mL chlorpromazine (Sigma) for 1 hour in serum free culture medium at 37 ºC. Subsequently, cells were incubated with 0.007 g/L Fe_2O_3 of fluorescein-labelled R8 nanoparticles and chlorpromazine for 4 hours. As a positive control, cells were treated with transferrin from human serum conjugated with Alexa fluor®594 (Life Technologies) at a concentration of 50 μg/mL. After incubation, cells were washed, fixed, mounted and observed under Axiovert 200M fluorescence microscopy. Slides were excited at 470 ± 20 nm and green fluorescence was detected with a band pass filter at 525 ± 25 nm. Red fluorescence was excited using the long pass filter at 546 ± 6 nm and emission at 590 nm, and DAPI was excited using the long pass filter at 436 ± 10 nm and emission at 480 ± 20 nm.

3.4 Results

3.4.1 Bioferrofluids characterisation

The iron contents of bioferrofluid stock samples were determined by atomic absorption in a plasma spectrometer. Concentrations of iron contents are 1.8, 8.1 and 8.1 g/L Fe_2O_3 for R1` bioferrofluids, R8` bioferrofluids and fluorescein-labelled R8 nanoparticles (FR8) respectively.

The samples were characterised by TEM and DLS and the results are shown in Figs. 3.5, 3.6 and 3.7. Most of the nanoparticles are spherical and quite homogeneous

in size as shown in Fig. 3.5. The size distribution analysis for the maghemite magnetic nanoparticles is shown in Fig. 3.6. The core size (mean ± SD) is 4.40 ± 0.86 and 13.08 ± 2.33 for R1` and R8` bioferrofluids respectively, the core size of FR8 is similar to that of R8`.

DLS observations for each sample showed a single population of particles as represented in Fig. 3.7. The average hydrodynamic diameter for each sample is 84, 163 and 112 for R1` bioferrofluids, R8` bioferrofluids and FR8 respectively. Measurements of zeta potential of the nanoparticles suspension for all samples yielded average values close to zero.

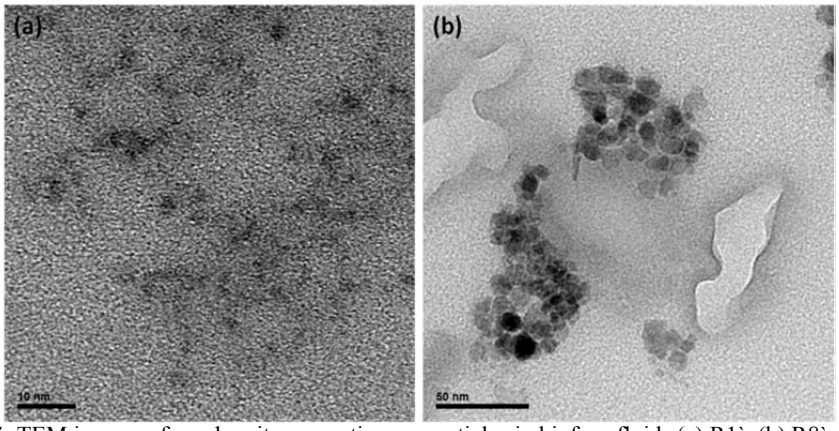

Figure 3.5: TEM images of maghemite magnetic nanoparticles in bioferrofluids (a) R1`, (b) R8`.

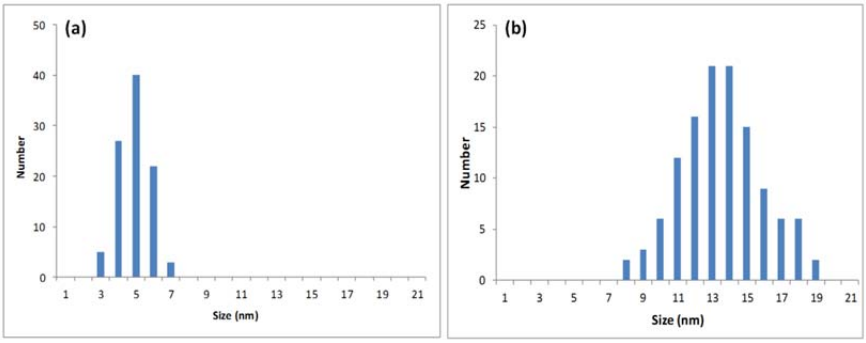

Figure 3.6: Size distribution analysis of spherical maghemite magnetic nanoparticles (a) R1`, (b) R8`.

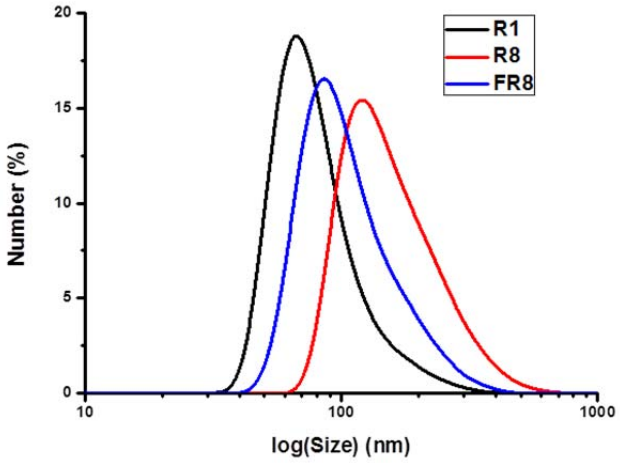

Figure 3.7: Distribution of hydrodynamic diameters in bioferrofluid samples from DLS measurements.

3.4.2 Study of the cellular uptake and the corresponding kinetic behaviour

Nanoparticles internalisation into VSMC and OK cells was studied by two ways: qualitatively using fluorescein-labelled NPs and quantitatively using non-fluorescent NPs and atomic absorption.

3.4.2.1 Qualitative determination of uptake using fluorescent nanoparticles

Both cell lines (OK and VSMC) were treated with a non-toxic dose (0.007 g/L Fe_2O_3) of FR8 for 4, 8, 12 and 24 hours and visualised under fluorescence microscope. A significant amount of fluorescence was observed after 4 hours of incubation, which increased by increasing the incubation time up to 24 hours in both cell lines. FR8 showed a perinuclear dotted pattern of staining in both OK and VSMC Fig. 3.8. In the case of VSMC, nanoparticles were surrounded completely the nuclei (Fig. 3.8, lower panel), while inside OK cells the nanoparticles were located laterally to the nuclei (Fig. 3.8, upper panel), most likely as a consequence of the epithelial origin and differentiation of the cells.

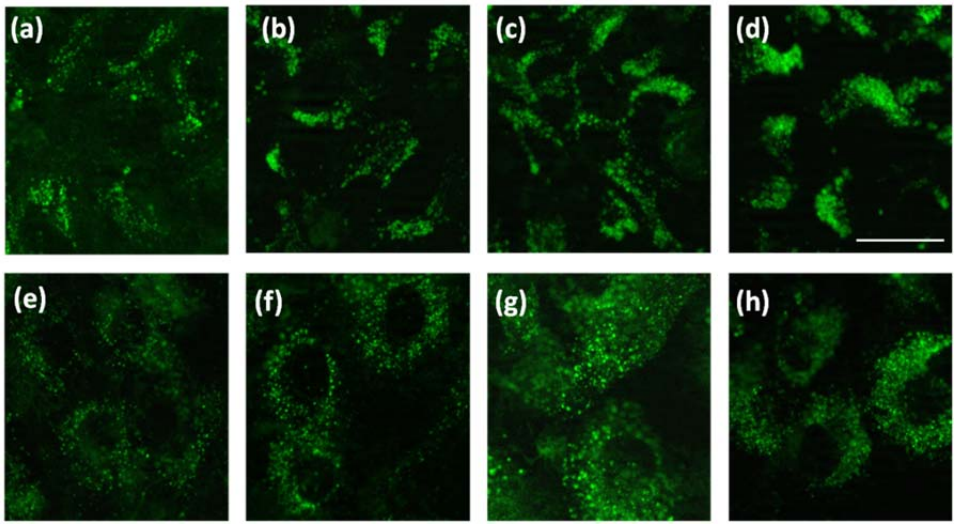

Figure 3.8: Internalisation of fluorescein-labelled R8 nanoparticles in OK and VSMC at different time points of incubation. Upper panel is OK cells after (a) 4, (b) 8, (c) 12 and (d) 24 hours of incubation, lower panel is VSMC after (e) 4, (f) 8, (g) 12 and (h) 24 hours of incubation. Scale bar: 20 µm.

3.4.2.2 Quantitative iron detection

In order to check whether the NPs were internalised into the cells and the detected fluorescence was not an artifact of fluorescent NP decomposition, quantitative determination of iron content inside the cells using atomic absorption was carried out. In this section, we also explore the effects of nanoparticle size, nanoparticle concentration and cell type on the nanoparticle uptake. Both cell lines (OK and VSMC) were treated with different concentrations of R1`and R8` bioferrofluids for 24 hours. Results corresponding to OK cells evidence the effect of the nanoparticle size on cellular uptake, since the cell capacity to internalise R1` (84 nm) is much higher as compared to R8` (163 nm) as shown in Fig. 3.9(a). In the R1` uptake curve a concentration dependent uptake is observed, since the increase in the concentration of the nanoparticles is accompanied by an increase in their cellular uptake. The curve nearly reaches the saturation above the concentration of 0.007 g/L $Fe_2O_3$. On the other hand, in the R8` uptake curve, the concentration increase of the nanoparticles is accompanied with an increase in the cellular uptake until a concentration of 0.007 g/L Fe_2O_3. After this value the uptake slightly decreases at a concentration of 0.01 g/L Fe_2O_3. In case of VSMC, the effect of nanoparticle size on cellular uptake is summarised in Fig. 3.9(b). For R1` and R8` uptake curves, a concentration dependent uptake is also observed, since the increase in the concentration of the nanoparticles is

accompanied by an increase in the cellular uptake. VSMC did not reach the saturation state upon treatment with different nanoparticles concentrations up to 0.01 g/L Fe_2O_3.

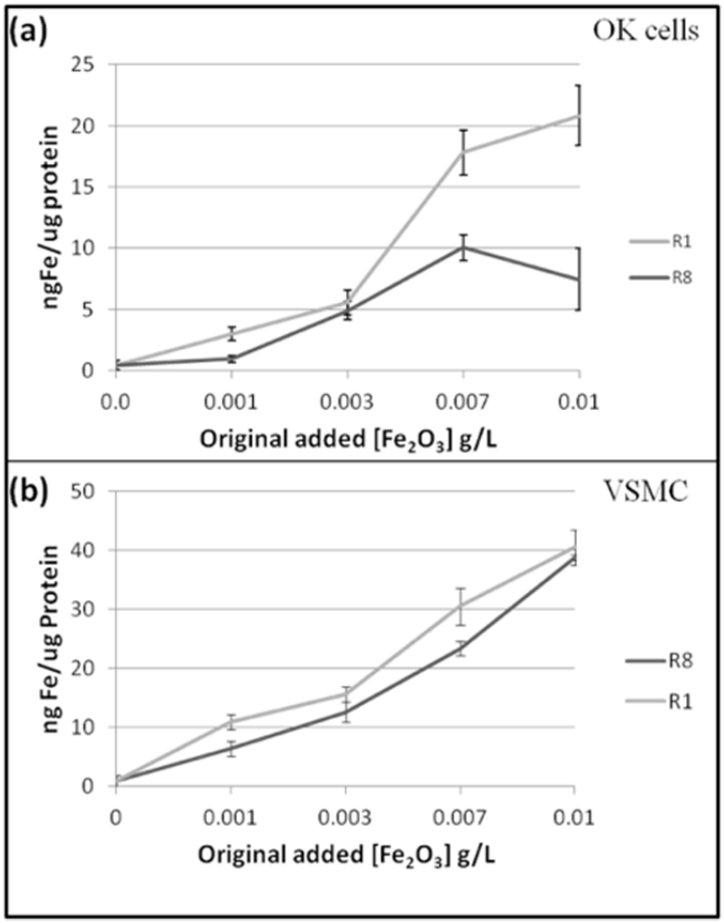

Figure 3.9: Quantitative iron detection for OK cells (a) and VSMC (b), after incubation with different concentrations of R1` and R8` bioferrofluids for 24 hours. Values represent mean ± SEM (*n*=6).

The effect of cell type on the nanoparticles uptake is clearly showed in Fig. 3.10, where VSMC are taken up more R1` Fig. 3.10(a) and R8` Fig. 3.10(b) as compared to OK cells. It is therefore evident that the difference in uptake rates could explain the greater toxicity of these NPs in VSMC than in OK cells as shown in previous chapter

For the quantitative evaluation of the uptake kinetics, we performed a time-course assay of non-fluorescent NPs uptake in VSMC and OK cells. Cells were incubated with R8` at concentration 0.007 g/L Fe_2O_3 for different time periods. The results showed an increase in the uptake with time, where nanoparticles uptake was observed

to be more rapid in the first 4 hours of incubation in OK cells, as shown in Fig. 3.11(a), which reached to the higher uptake at 12 hours of incubation. In the case of VSMC, a steady increase in the uptake with time was observed and the cell did not reach the saturation even after 24 hours of incubation, as shown in Fig. 3.11(b). These results are consistent with those obtained in section 3.4.2.1 using fluorescein-labelled R8 nanoparticles.

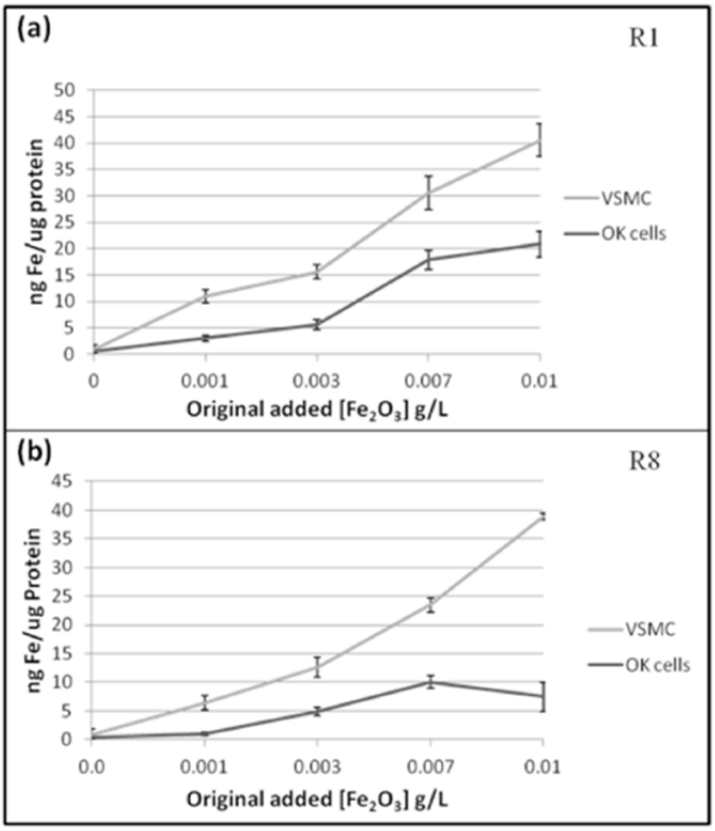

Figure 3.10: Effect of cell type on the nanoparticles uptake. Both cell lines (OK and VSMC) were incubated with different concentrations of R1` (a) and R8` (b) bioferrofluids for 24 hours. Values represent mean ± SEM (*n*=6).

3.4.3 Subcellular localisation

Studying the subcellular fate of the nanomaterial inside the cell helps to give an idea about the endocytosis mechanism, as well as monitoring the localisation of drug delivery nanomaterials. The subcellular localisation was investigated in both cell lines

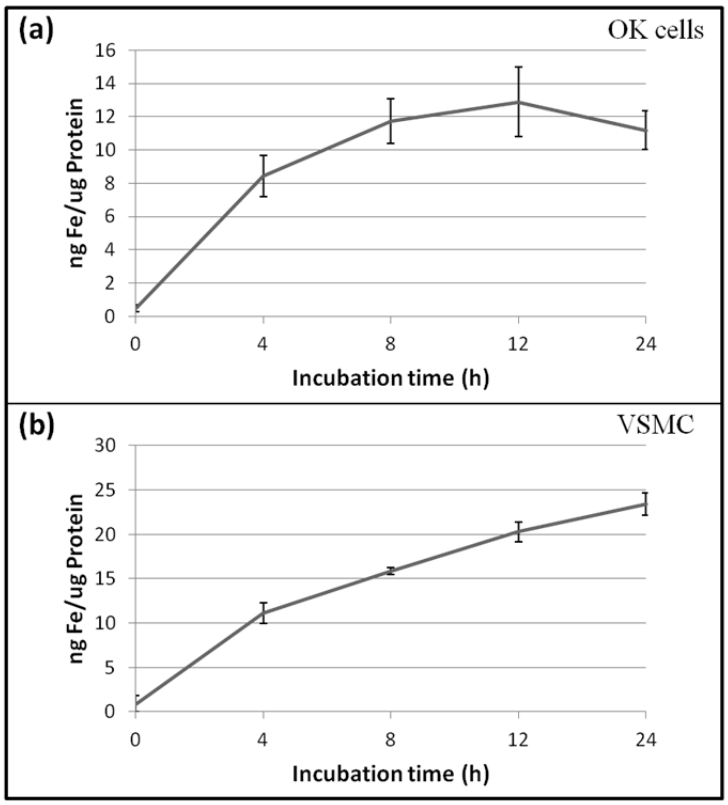

Figure 3.11: Time dependent uptake of R8` bioferrofluids in OK cells (a) and VSMC (b). Values represent mean ± SEM (*n*=6).

(OK and VSMC) treated with a non-toxic dose of FR8 for 24 hours. Different antibodies and trackers were used and images were taken with the help of a fluorescence microscope equipped with ApoTome. Results showed that fluorescein-labelled nanoparticles were not found in the endoplasmic reticulum, Fig. 3.12, the early endosomes, Fig. 3.13, or in the mitochondria, Fig. 3.14, as manifested by the absence of co-localisations with the corresponding antibodies or trackers. However, positive co-localisation indicated by yellow pixel in the merge image was observed in the endo-lysosomal compartments (Lysosomes and late endosomes) after 24 hours of exposure to fluorescein-labelled nanoparticles, as shown in Fig. 3.15.

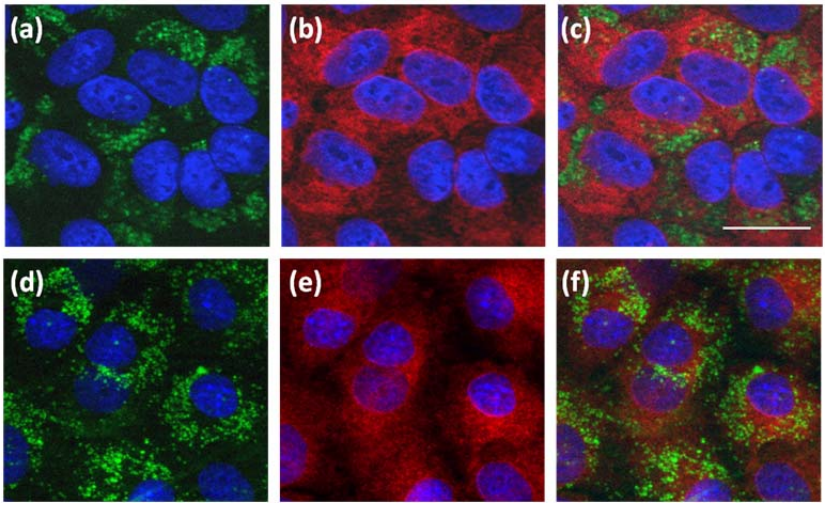

Figure 3.12: Nanoparticles subcellular localisation using an endoplasmic reticulum marker (Anti-Derlin Ab). Cells were treated with fluorescein-labelled R8 nanoparticles at 0.007 g/L Fe_2O_3 for 24 hours. Samples were examined under fluorescence microscope equipped with ApoTome. The higher panel is OK cells with fluorescein-labelled R8 in green and DAPI in blue (a), Anti-Derlin Ab in red and DAPI in blue (b), and the merge image (c). The lower Panel is VSMC with fluorescein-labelled R8 in green and DAPI in blue (d), Anti-Derlin Ab in red and DAPI in blue (e), and the merge image (f). Scale bar: 20 µm.

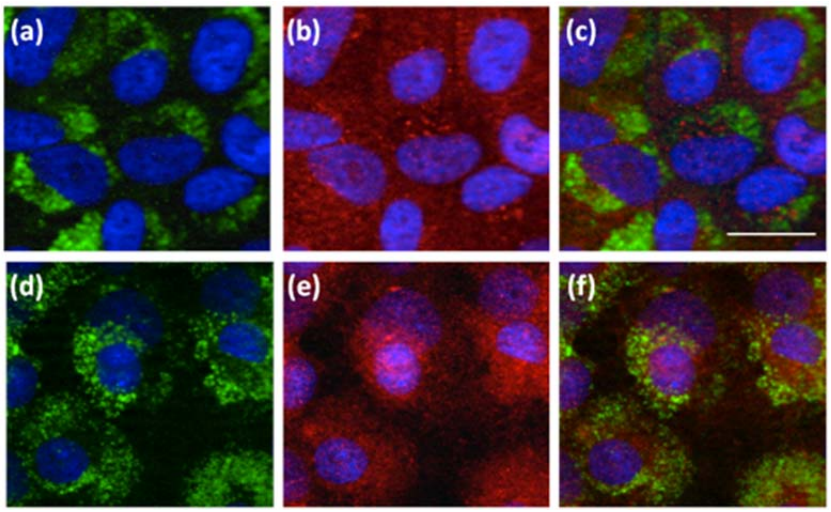

Figure 3.13: Nanoparticles subcellular localisation using an early endosome marker (Anti-EEA1 Ab). Cells were treated with fluorescein-labelled R8 nanoparticles at 0.007 g/L Fe_2O_3 for 24 hours. Samples were examined under fluorescence microscope equipped with ApoTome. The higher panel is OK cells with fluorescein-labelled R8 in green and DAPI in blue (a), Anti- EEA1 Ab in red and DAPI in blue (b), and the merge image (c). The lower Panel is VSMC with fluorescein-labelled R8 in green and DAPI in blue (d), Anti- EEA1 Ab in red and DAPI in blue (e), and the merge image (f). Scale bar: 20 µm.

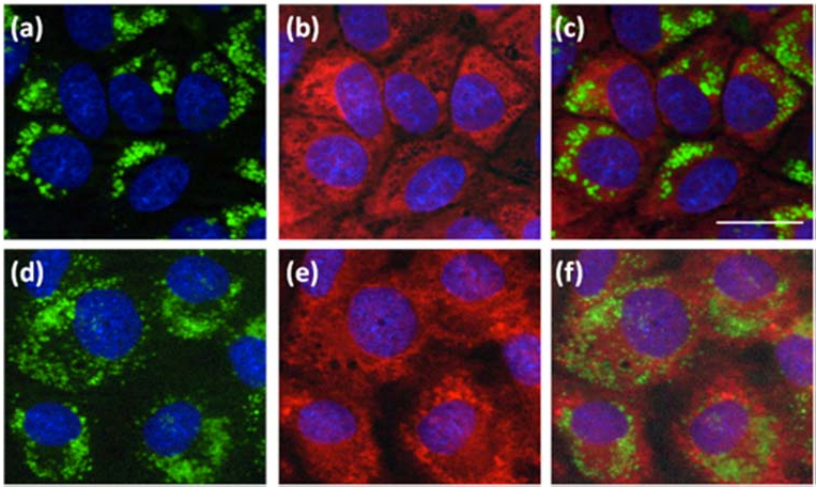

Figure 3.14: Nanoparticles subcellular localisation using MitoTracker®Red CMXRos. Cells were treated with fluorescein-labelled R8 nanoparticles at 0.007 g/L Fe_2O_3 for 24 hours. Samples were examined under fluorescence microscope equipped with ApoTome. The higher panel is OK cells with fluorescein-labelled R8in green and DAPI in blue (a), MitoTracker in red and DAPI in blue (b), and the merge image (c). The lower Panel is VSMC with fluorescein-labelled R8 in green and DAPI in blue (d), MitoTracker in red and DAPI in blue (e), and the merge image (f). Scale bar: 20 µm.

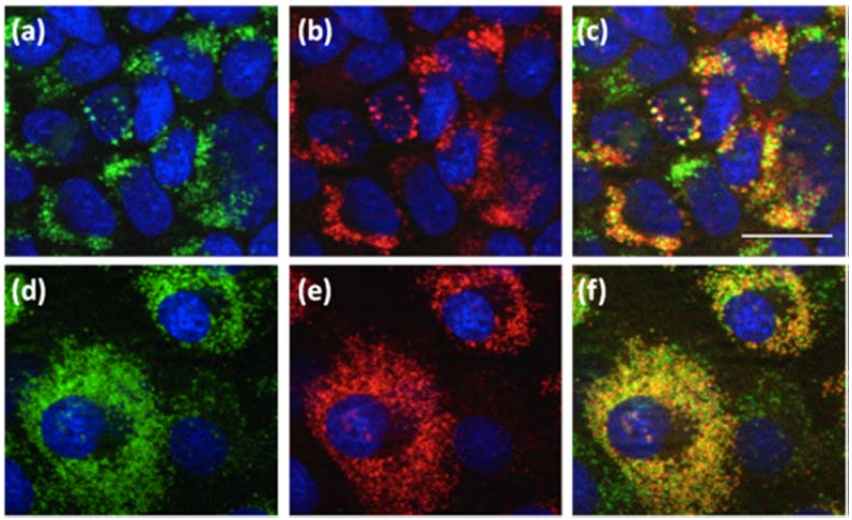

Figure 3.15: Subcellular localisation of nanoparticles using LysoTracker® Red DND-99. Cells were treated with fluorescein-labelled R8 nanoparticles at 0.007 g/L Fe_2O_3 for 24 hours. Samples were examined under fluorescence microscope equipped with ApoTome. The higher panel is OK cells with fluorescein-labelled R8 in green and DAPI in blue (a), LysoTracker in red and DAPI in blue (b), and the merge image (c). The lower Panel is VSMC with fluorescein-labelled R8 in green and DAPI in blue (d), LysoTracker in red and DAPI in blue (e), and the merge image (f). Scale bar: 20 µm.

3.4.4 Study of endocytosis mechanism

There are several methods that can be used to study the endocytosis mechanism of a given nanomaterial in a certain cell type. A method based in pharmacological inhibitors has been used in this work.

3.4.4.1 Potassium depletion

Potassium depletion of cells removes the clathrin-coated pits from the cell membrane and therefore it specifically prevents this pinocytotic mechanism. OK cells were washed with potassium free buffer followed by washing with hypotonic solution and then incubated for 4 hours with potassium free buffer containing 0.007 g/L Fe_2O_3 fluorescein-labelled R8 nanoparticles. Results showed inhibition in the nanoparticles internalisation due to potassium depletion exposure as shown in Fig. 3.16. Therefore, this result suggests that nanoparticles are internalised following a clathrin-dependent endocytosis route.

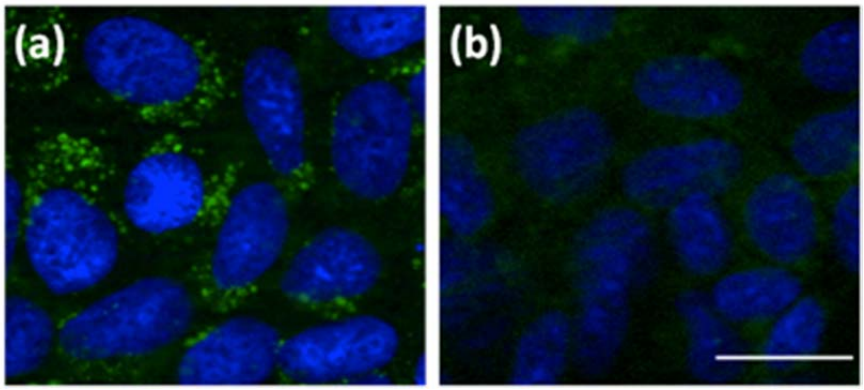

Figure 3.16: Effect of Potassium depletion on the nanoparticles internalisation by OK cells. (a) Positive control cells (b) Potassium depletion treated cells. Scale bar: 20 µm.

3.4.4.2 Chlorpromazine inhibitor

In order to confirm that our nanoparticles internalised through clathrin-mediated endocytois, another inhibitor of clathrin-coated pit formation, like chlorpromazine, was used. OK cells were incubated for 1 hour at 37ºC with 10 µg/ml chlorpromazine, followed by incubation with 0.007g/L Fe_2O_3 fluorescein-labelled R8 nanoparticles and chlorpromazine for 4 hours. The concentration of the inhibitor was adjusted using transferrin, which is considered a ligand exclusively internalised via the clathrin

coated pit pathway. Results showed that nanoparticle internalisation was completely inhibited upon chlorpromazine treatment, as shown in Fig. 3.17. Similar results were obtained using fluorescent transferrin as a positive control. These results confirm that a clathrin-mediated endocytosis route is the responsible for the nanoparticle uptake.

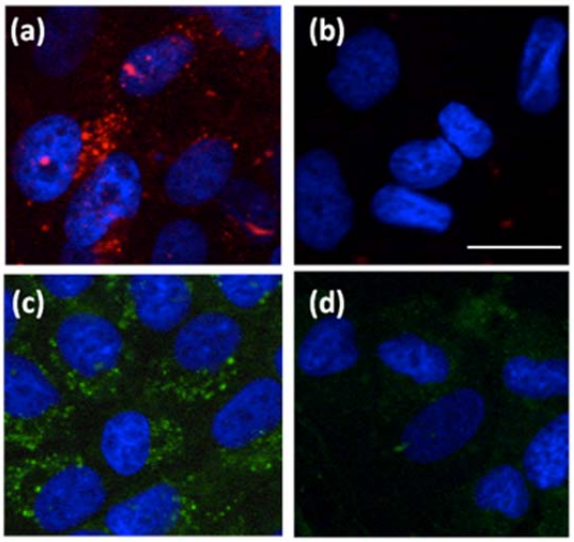

Figure 3.17: Effect of chlorpromazine on nanoparticles uptake by OK cells. (a) cells incubated with transferrin; (b) cells incubated with transferrin and chlorpromazine; (c) cells incubated with fluorescein-labelled R8; (d) cells incubated with fluorescein-labelled R8 and chlorpromazine. Scale bar: 20 μm.

3.5 Discussion and conclusions

The ability of the nanomaterials to breach the plasma cell membrane is considering as a crucial factor for their efficacy in biomedical applications. Hence, studies pertaining to nanomaterial cellular uptake are of utmost importance.

Fluorescent microscope confers the way to visualise the nanomaterials distribution inside the cell. This work has been centred to visualise the internalisation of fluorescein-labelled R8 nanoparticles (112 nm) in two cell lines (OK and VSMC). The nanoparticles were not detected after 2 hours of incubation (data not shown), but were evident after 4 hours of incubation and their internalisation increased in a time dependent manner, as shown in Fig. 3.8. These results were confirmed by quantitative measurements of the cellular iron content using acidic digestion method and atomic absorption spectroscopy, as depicted in Fig. 3.11. It was evident not only a time dependent internalisation, but also a cell type dependent internalisation. Thus, OK cells were reached their higher uptake concentration at 12 hours, as indicated in Fig.

3.11(a), while VSMC did not reach the saturation state up to 24 hours of incubation, as shown in Fig. 3.11(b). This could be explained by different saturation capacity between both cell lines. These kinetic uptake results are consistent with other studies [6,39–41].

Many factors, such as nanomaterial concentration, nanomaterial physicochemical properties, cell type, and others, influence nanomaterial uptake by the cells. In this work, we studied the effect of NPs concentration, NPs size and cell type on the NPs uptake. A concentration dependent uptake was reported for both VSMC and OK cells treated with R1 and R8 bioferrofluids, as shown in Fig. 3.9. However, in OK cells treated with R8 a slight decrease in the curve was noticed at the concentration 0.01 g/L Fe_2O_3, see Fig. 3.9(a), but this decrease could be neglected due to the large error bars. This finding is in agreement with previous studies [6,39,42].

The size dependent uptake was conspicuous in each cell line (OK or VSMC), since R1` (84 nm) internalised into the cells better than R8` (163 nm), as shown in Fig. 3.9. The internalised R1` was 1.78 and 1.30 folds of R8` in OK cells and VSMC incubated with a concentration of 0.007 g/L Fe_2O_3, respectively. This could explain the higher toxic effects associated with R1 as compared with R8 in both cell lines. The pronounced internalisation difference between R1` and R8` could be explained by the influence on their respective uptake due to different endocytosis mechanisms. The size effect on cellular uptake has been of previous concerns [4,7]. For instance, Huang et al. studied the uptake of positively charged PVP-IONPs in mouse macrophage cells using a series of samples with $\boldsymbol{D_p}$ = 8, 23, 37, 65 nm and corresponding hydrodynamic sizes $\boldsymbol{D_H}$ = 32, 71, 102 and 118 nm, results showed a maximum of iron mass uptake per cell for a size of $\boldsymbol{D_p}$ =37 nm and $\boldsymbol{D_H}$=102 as compared with other ones, indicating that $\boldsymbol{D_H}$=102 nm is an optimal size for the macrophages uptake [6].

In another study on immortalised human T cells, internalisation of dextran coated aminated IONPs having similar core sizes ($\boldsymbol{D_p}$ = 6.1, 5.6 and 6.5 nm) but different hydrodynamic sizes ($\boldsymbol{D_H}$ = 33, 53, 107 nm) and different IO loading (numbers of cores: 1.9, 5.2, 11.3), it was found that NPs were substantially uptaken only after a

certain degree of amination and that internalisation rate was considerably higher (one order of magnitude) for $\boldsymbol{D_H}$ = 107 nm nanoparticles [43].. Thus, both studies found a maximum internalisation rate for a hydrodynamic size somewhat above 100 nm. On the other hand, a comparison of cellular uptake of IONPs with $\boldsymbol{D_p}$ = 5 and 30 nm using porcine aortic endothelial cells, before and after coating with dextran or PEG, showed higher iron uptake for 5 nm NPs than 30 nm NPs when coated with dextran and the reverse for uncoated or PEG coated NPs [44]. Unluckily, it is difficult to extract conclusions from these results because data on aggregation and hydrodynamic diameters are missing. In our work, surprisingly, both $\boldsymbol{D_p}$ and $\boldsymbol{D_H}$ have shown a direct impact on cell mortality and cell internalisation

The cell type dependence of nanoparticles uptake was indicated in Fig. 3.10. At a concentration of 0.007 g/L Fe_2O_3, a 1.71 fold increases in the R1` uptake was detected for VSMC as compared to OK cells (see Fig. 3.10(a)), while 2.33 fold increases in the R8` uptake was detected for VSMC as compared to OK cells (see Fig. 3.10(b)). This different behaviour is due to different cell physiology, which might explain the high sensitivity of VSMC toward the nanoparticles (R1 and R8) comparing with OK cells. These results are in agreement with several previous studies [26,45,46].

Several mechanisms are responsible for the nanomaterial internalisation into the cells; each mechanism differs from the other in its components as well as in the internalisation route. During the internalisation, nanomaterials are exposed to different environments and conditions that vary in its harshness; this could be favourable or unfavourable to the nanomaterial depending on its purpose of use as well as on its properties. Hence, good understanding of the nanomaterial internalisation mechanisms and the factors affecting it will help to define the subcellular fate of the nanomaterial inside the cell, as well as improve the designing of an efficient drug delivery carrier.

Fluorescein-labelled R8 nanoparticles were tracked in four different cellular organelles (endoplasmic reticulum, early endosomes, mitochondria and endo-lysosomal compartments) in both cell lines (OK and VSMC) using fluorescent antibodies and trackers with the help of fluorescent microscope equipped with ApoTome. Fluorescein-labelled nanoparticles were not found in the endoplasmic

reticulum, early endosomes, mitochondria or the nucleus, as shown in Fig. 3.12, 3.13 and 3.14. They are, however, observed inside the endo-lysosomal compartments (lysosomes and late endosomes) after 24 hours of incubation in both cell lines (OK and VSMC), as shown in Fig. 3.15. These results are in agreement with previous studies [39,45–47].

The existence of FR8 in the endo-lysosomal compartments suggests that the mechanism responsible of the nanoparticle internalisation is a clathrin-dependent endocytosis one. In order to confirm the endocytosis mechanism, pharmacological inhibitors (potassium depletion and chlorpromazine) were used. Potassium depletion of the cell blocks clathrin-dependent endocytosis by removing clathrin from the membrane, while chlorpromazine blocks this route by inhibiting Rho GTPase. Complete inhibition of FR8 internalisation was detected in OK cells upon potassium depletion treatment as well as chlorpromazine treatment, as shown in Figs. 3.16 and 3.17, indicating that clathrin-dependent endocytosis is the responsible route for the internalisation of FR8. These results are consistent with other previous studies [48,49].Mores studies are required, in order to reveal the R1 endocytosis mechanism, to give an explanation of the size dependent internalisation.

Then, we can conclude that nanoparticles internalisation is dependent on many factors such as, incubation time, nanoparticles concentration, nanoparticles size and cell type. The obtained results give explanations for the caused toxicity by R1 in compared with R8 in both cell lines, as well as, explanations of the high sensitivity of VSMC toward the nanoparticles compared with OK cells. Fluorescein-labelled R8 nanoparticles are accumulated in the endo-lysosomal compartments after 24 hours of incubation with OK and VSMC cells, which should be confirmed by further experiments as electron microscopy techniques. Clathrin-dependent endocytosis is responsible for internalisation of FR8 in OK cells. Further studies should be carried out with R1, in order to investigate its endocytic route of internalisation.

3.6 References

[1] A. Verma and F. Stellacci, “Effect of surface properties on nanoparticle-cell

interactions.," *Small*, vol. 6, no. 1, pp. 12–21, 2010.

[2] J. G. Huang, T. Leshuk, and F. X. Gu, "Emerging nanomaterials for targeting subcellular organelles," *Nano Today*, vol. 6, no. 5, pp. 478–492, 2011.

[3] A. E. Nel, L. Mädler, D. Velegol, T. Xia, E. M. V Hoek, P. Somasundaran, F. Klaessig, V. Castranova, and M. Thompson, "Understanding biophysicochemical interactions at the nano-bio interface.," *Nat. Mater.*, vol. 8, no. 7, pp. 543–57, 2009.

[4] B. D. Chithrani, A. a Ghazani, and W. C. W. Chan, "Determining the size and shape dependence of gold nanoparticle uptake into mammalian cells.," *Nano Lett.*, vol. 6, no. 4, pp. 662–8, 2006.

[5] S. E. A. Gratton, P. A. Ropp, P. D. Pohlhaus, J. C. Luft, V. J. Madden, M. E. Napier, and J. M. DeSimone, "The effect of particle design on cellular internalization pathways.," *Proc. Natl. Acad. Sci. U. S. A.*, vol. 105, no. 33, pp. 11613–8, 2008.

[6] J. Huang, L. Bu, J. Xie, K. Chen, Z. Cheng, X. Li, and X. Chen, "Effects of nanoparticle size on cellular uptake and liver MRI with polyvinylpyrrolidone-coated iron oxide nanoparticles.," *ACS Nano*, vol. 4, no. 12, pp. 7151–60, 2010.

[7] F. Lu, S.-H. Wu, Y. Hung, and C.-Y. Mou, "Size effect on cell uptake in well-suspended, uniform mesoporous silica nanoparticles.," *Small*, vol. 5, no. 12, pp. 1408–13, 2009.

[8] H. Hillaireau and P. Couvreur, "Nanocarriers' entry into the cell: relevance to drug delivery.," *Cell. Mol. Life Sci.*, vol. 66, no. 17, pp. 2873–96, 2009.

[9] A. Villanueva, M. Cañete, A. G. Roca, M. Calero, S. Veintemillas-Verdaguer, C. J. Serna, M. D. P. Morales, and R. Miranda, "The influence of surface functionalization on the enhanced internalization of magnetic nanoparticles in cancer cells.," *Nanotechnology*, vol. 20, no. 11, p. 115103, 2009.

[10] F. Cengelli, D. Maysinger, F. Tschudi-monnet, X. Montet, C. Corot, A. Petri-fink, H. Hofmann, and L. Juillerat-jeanneret, "Interaction of Functionalized Superparamagnetic Iron Oxide Nanoparticles with Brain Structures," *Pharmacology*, vol. 318, no. 1, pp. 108–116, 2006.

[11] M. R. Lorenz, V. Holzapfel, A. Musyanovych, K. Nothelfer, P. Walther, H. Frank, K. Landfester, H. Schrezenmeier, and V. Mailänder, "Uptake of functionalized, fluorescent-labeled polymeric particles in different cell lines and stem cells.," *Biomaterials*, vol. 27, no. 14, pp. 2820–8, 2006.

[12] A. Verma, O. Uzun, Y. Hu, Y. Hu, H.-S. Han, N. Watson, S. Chen, D. J. Irvine, and F. Stellacci, "Surface-structure-regulated cell-membrane penetration by monolayer-protected nanoparticles.," *Nat. Mater.*, vol. 7, no. 7, pp. 588–95, 2008.

[13] P. R. Leroueil, S. A. Berry, K. Duthie, G. Han, V. M. Rotello, D. Q. McNerny, J. R. Baker, B. G. Orr, and M. M. B. Holl, "Wide varieties of cationic nanoparticles induce defects in supported lipid bilayers.," *Nano Lett.*, vol. 8, no. 2, pp. 420–4, 2008.

[14] A. C. Hunter, "Molecular hurdles in polyfectin design and mechanistic background to polycation induced cytotoxicity.," *Adv. Drug Deliv. Rev.*, vol. 58, no. 14, pp. 1523–31, 2006.

[15] M. Morille, C. Passirani, A. Vonarbourg, A. Clavreul, and J.-P. Benoit, "Progress in developing cationic vectors for non-viral systemic gene therapy against cancer.," *Biomaterials*, vol. 29, no. 24–25, pp. 3477–96, 2008.

[16] U. Lungwitz, M. Breunig, T. Blunk, and A. Göpferich, "Polyethylenimine-based non-viral gene delivery systems.," *Eur. J. Pharm. Biopharm.*, vol. 60, no. 2, pp. 247–66, 2005.

[17] J. Jiang, G. Oberdörster, and P. Biswas, "Characterization of size, surface charge, and agglomeration state of nanoparticle dispersions for toxicological studies," *J. Nanoparticle Res.*, vol. 11, no. 1, pp. 77–89, 2008.

[18] Y. Min, M. Akbulut, K. Kristiansen, Y. Golan, and J. Israelachvili, "The role of interparticle and external forces in nanoparticle assembly.," *Nat. Mater.*, vol. 7, no. 7, pp. 527–38, 2008.

[19] T. Cedervall, I. Lynch, S. Lindman, T. Berggård, E. Thulin, H. Nilsson, K. a Dawson, and S. Linse, "Understanding the nanoparticle-protein corona using methods to quantify exchange rates and affinities of proteins for nanoparticles.," *Proc. Natl. Acad. Sci. U. S. A.*, vol. 104, no. 7, pp. 2050–5, 2007.

[20] P. Aggarwal, J. B. Hall, C. B. McLeland, M. a Dobrovolskaia, and S. E. McNeil, "Nanoparticle interaction with plasma proteins as it relates to particle biodistribution, biocompatibility and therapeutic efficacy.," *Adv. Drug Deliv. Rev.*, vol. 61, no. 6, pp. 428–37, 2009.

[21] D. E. Owens and N. A. Peppas, "Opsonization, biodistribution, and pharmacokinetics of polymeric nanoparticles.," *Int. J. Pharm.*, vol. 307, no. 1, pp. 93–102, 2006.

[22] M. a Dobrovolskaia, A. K. Patri, J. Zheng, J. D. Clogston, N. Ayub, P. Aggarwal, B. W. Neun, J. B. Hall, and S. E. McNeil, "Interaction of colloidal gold nanoparticles with human blood: effects on particle size and analysis of plasma protein binding profiles.," *Nanomedicine*, vol. 5, no. 2, pp. 106–17, 2009.

[23] C. Salvador-Morales, E. Flahaut, E. Sim, J. Sloan, M. L. H. Green, and R. B. Sim, "Complement activation and protein adsorption by carbon nanotubes.," *Mol. Immunol.*, vol. 43, no. 3, pp. 193–201, 2006.

[24] D. Shcharbin, M. Jokiel, B. Klajnert, and M. Bryszewska, "Effect of dendrimers on pure acetylcholinesterase activity and structure.," *Bioelectrochemistry*, vol. 68, no. 1, pp. 56–9, 2006.

[25] S. Linse, C. Cabaleiro-Lago, W.-F. Xue, I. Lynch, S. Lindman, E. Thulin, S. E. Radford, and K. A. Dawson, "Nucleation of protein fibrillation by nanoparticles.," *Proc. Natl. Acad. Sci. U. S. A.*, vol. 104, no. 21, pp. 8691–6, 2007.

[26] W. Zauner, N. A. Farrow, and A. M. Haines, "In vitro uptake of polystyrene

microspheres: effect of particle size, cell line and cell density.," *J. Control. Release*, vol. 71, no. 1, pp. 39–51, 2001.

[27] I. A. Khalil, K. Kogure, H. Akita, and H. Harashima, "Uptake Pathways and Subsequent Intracellular Trafficking in Nonviral Gene Delivery," *Sci. Technol.*, vol. 58, no. 1, pp. 32–45, 2006.

[28] B. Nichols, "Caveosomes and endocytosis of lipid rafts.," *J. Cell Sci.*, vol. 116, no. Pt 23, pp. 4707–14, Dec. 2003.

[29] M. R. Birtwistle and B. N. Kholodenko, "Endocytosis and signalling: a meeting with mathematics.," *Mol. Oncol.*, vol. 3, no. 4, pp. 308–20, 2009.

[30] S. D. Conner and S. L. Schmid, "Regulated portals of entry into the cell.," *Nature*, vol. 422, no. 6927, pp. 37–44, 2003.

[31] T.-G. Iversen, T. Skotland, and K. Sandvig, "Endocytosis and intracellular transport of nanoparticles: Present knowledge and need for future studies," *Nano Today*, vol. 6, no. 2, pp. 176–185, 2011.

[32] S. L. Schmid, "Clathrin-coated vesicle formation and protein sorting: an integrated process.," *Annu. Rev. Biochem.*, vol. 66, pp. 511–48, 1997.

[33] F. M. Brodsky, C. Y. Chen, C. Knuehl, M. C. Towler, and D. E. Wakeham, "Biological basket weaving: formation and function of clathrin-coated vesicles.," *Annu. Rev. Cell Dev. Biol.*, vol. 17, pp. 517–68, 2001.

[34] a Hall and C. D. Nobes, "Rho GTPases: molecular switches that control the organization and dynamics of the actin cytoskeleton.," *Philos. Trans. R. Soc. Lond. B. Biol. Sci.*, vol. 355, no. 1399, pp. 965–70, 2000.

[35] M. Murakami, H. Cabral, Y. Matsumoto, S. Wu, M. R. Kano, T. Yamori, N. Nishiyama, and K. Kataoka, "Improving drug potency and efficacy by nanocarrier-mediated subcellular targeting.," *Sci. Transl. Med.*, vol. 3, no. 64, p. 64ra2, 2011.

[36] P. Zou, Y. Yu, Y. A. Wang, Y. Zhong, and A. Welton, "Superparamagnetic Iron Oxide Nanotheranostics for Targeted Cancer Cell Imaging and pH-Dependent Intracellular Drug Release," *Mol. Pharm.*, vol. 7, no. 6, pp. 1974-84, 2010.

[37] H. Shogomori and A. H. Futerman, "Cholera toxin is found in detergent-insoluble rafts/domains at the cell surface of hippocampal neurons but is internalized via a raft-independent mechanism.," *J. Biol. Chem.*, vol. 276, no. 12, pp. 9182–8, 2001.

[38] E.-M. Damm, L. Pelkmans, J. Kartenbeck, A. Mezzacasa, T. Kurzchalia, and A. Helenius, "Clathrin- and caveolin-1-independent endocytosis: entry of simian virus 40 into cells devoid of caveolae.," *J. Cell Biol.*, vol. 168, no. 3, pp. 477–88, 2005.

[39] C. Wilhelm, C. Billotey, J. Roger, J. N. Pons, J.-C. Bacri, and F. Gazeau, "Intracellular uptake of anionic superparamagnetic nanoparticles as a function of their surface coating.," *Biomaterials*, vol. 24, no. 6, pp. 1001–11, 2003.

[40] B. Schopf, T. Neuberger, K. Schulze, A. Petri, M. Chastellain, M. Hofmann, H. Hofmann, and B. Vonrechenberg, "Methodology description for detection of cellular uptake of PVA coated superparamagnetic iron oxide nanoparticles (SPION) in synovial cells of sheep," *J. Magn. Magn. Mater.*, vol. 293, no. 1, pp. 411–418, 2005.

[41] Y.-J. Ma and H.-C. Gu, "Study on the endocytosis and the internalization mechanism of aminosilane-coated Fe3O4 nanoparticles in vitro.," *J. Mater. Sci. Mater. Med.*, vol. 18, no. 11, pp. 2145–9, 2007.

[42] H. Xie, Y. Zhu, W. Jiang, Q. Zhou, H. Yang, N. Gu, Y. Zhang, H. Xu, H. Xu, and X. Yang, "Lactoferrin-conjugated superparamagnetic iron oxide nanoparticles as a specific MRI contrast agent for detection of brain glioma in vivo.," *Biomaterials*, vol. 32, no. 2, pp. 495–502, 2011.

[43] D. L. J. Thorek and A. Tsourkas, "Size, charge and concentration dependent uptake of iron oxide particles by non-phagocytic cells.," *Biomaterials*, vol. 29, no. 26, pp. 3583–90, 2008.

[44] M. Yu, S. Huang, K. J. Yu, and A. M. Clyne, "Dextran and Polymer Polyethylene Glycol (PEG) Coating Reduce Both 5 and 30 nm Iron Oxide Nanoparticle Cytotoxicity in 2D and 3D Cell Culture," pp. 5554–70, 2012.

[45] S. Prijic, J. Scancar, R. Romih, M. Cemazar, V. B. Bregar, A. Znidarsic, and G. Sersa, "Increased cellular uptake of biocompatible superparamagnetic iron oxide nanoparticles into malignant cells by an external magnetic field.," *J. Membr. Biol.*, vol. 236, no. 1, pp. 167–79, 2010.

[46] V. Mailänder, M. R. Lorenz, V. Holzapfel, A. Musyanovych, K. Fuchs, M. Wiesneth, P. Walther, K. Landfester, and H. Schrezenmeier, "Carboxylated superparamagnetic iron oxide particles label cells intracellularly without transfection agents.," *Mol. Imaging Biol.*, vol. 10, no. 3, pp. 138–46, 2008.

[47] Y.-J. Ma and H.-C. Gu, "Study on the endocytosis and the internalization mechanism of aminosilane-coated Fe3O4 nanoparticles in vitro.," *J. Mater. Sci. Mater. Med.*, vol. 18, no. 11, pp. 2145–9, 2007.

[48] B. D. Chithrani and W. C. W. Chan, "Elucidating the mechanism of cellular uptake and removal of protein-coated gold nanoparticles of different sizes and shapes.," *Nano Lett.*, vol. 7, no. 6, pp. 1542–50, 2007.

[49] J. Rejman, V. Oberle, I. S. Zuhorn, and D. Hoekstra, "Size-dependent internalization of particles via the pathways of clathrin- and caveolae-mediated endocytosis.," *Biochem. J.*, vol. 377, no. Pt 1, pp. 159–69, 2004.

Chapter 4

In vitro haemocompatibility studies of superparamagnetic iron oxide nanoparticles

4.1 Introduction

Haemostasis is a very important protective physiological process that maintains blood in a fluid state under normal conditions. It responds to blood vessel injury by rapid formation of blood clot (thrombus), followed by thrombus dissolution (fibrinolysis) and damaged vessel repairs [1]. Human beings are frequently exposed to natural and anthropogenic nanomaterials. As a result, it became evident that airborne nanomaterials have a thrombogenic effect as a result of pulmonary exposure [2–4]. Similarly, medically applied nanomaterials can stimulate blood clotting by the coagulation pathways activation or by inducing platelet aggregation [5]. More interestingly, some reported results show that they can behave as either pro-coagulant or hypo-coagulant agents depending on size [6], coating material [7–10], charge [11,12] and the material composition [13].

Despite the importance and coverage of biomedical applications of metal oxides, not many studies have been focused on the toxicological behaviour of these materials in blood. Thus, Ostomel et al. have investigated the haemostatic response due to surface charges of a variety of metal oxide particles which did not include SPIONs [11], Li et al. have investigated the influence of nano-TiO_2 on erythrocyte [14] and Singh et al. have investigated the disturbance in iron homeostasis caused by SPIONs [15].

As detailed below, this chapter will focus on the haemocompatibility of bioferrofluids. As they are developed for intravenous administration, the assurance they will not

cause any toxicity to blood components when injected is an important issue that should be taken into consideration, especially for a successful development of these nanoparticles. The evaluation of the haemostatic behaviour of nanomaterials is carried out by a set of studies such as the study of the nanomaterials effect on the coagulation process, of their toxicity to blood components and of their haemolytic effect. These studies are explained in details in the next paragraphs.

4.1.1 Studies for nanomaterial toxicity in blood

Blood coagulation studies: Several methods have been used to investigate the effects of the nanomaterials on the coagulation process. They include global tests (prothrombin time (PT), activated partial thromboplastin time (aPTT) and fibrinogen), thrombus – elastography, platelets aggregation and degradation products of fibrinogen and fibrin. Recently, a detailed description of methods has been published [16], which focuses on the global plasma coagulation tests (PT, aPTT and fibrinogen) and platelet aggregation. Some studies have evaluated the compatibility of nanomaterials with the blood coagulation system *in vivo* in mice [8], rats [17] and rabbits [18], while most of the authors have carried them out only *in vitro* [6–8].

Haemolysis studies: The nano-size and the unique physicochemical properties of the nanomaterials can cause haemolysis by acting on the membrane of red blood cells [19]. Therefore, *in vitro* biocompatibility studies should also include evidence of haemolysis. Several studies have revealed the effect of the nanomaterials on the blood by measuring their haemolytic action *in vitro* [20]. However, direct results interpretation of these studies is complicated due to variability in the experimental conditions such as incubation time of blood with the nanomaterials, the wavelength at which the haemoglobin is quantified, the centrifugation forces, blood storage time and conditions and blood source (human or rabbit) [21]. Nanomaterials could interfere with the haemolysis detection assay by several ways. For instance, separation by ultracentrifugation of gold nanoparticles of 5 nm size, which are similar to the size of haemoglobin, could also precipitate the haemoglobin, resulting in a false-negative results. Also, false-negative results could be obtained as in the case of haemoglobin adsorption on the nanomaterial surface. In contrast, false-positive results could be obtained in the case of metal oxide nanoparticles, since they have the ability to oxidise

the haemoglobin. Therefore, modification of the haemolysis detection assay is mandatory depending on the type of nanomaterials [22].

Complete blood count assay: Quantification of leukocytes (white blood cells), erythrocytes (red blood cells) and platelets is important to rule out immediate cytotoxicity of nanomaterials or contact spontaneous platelets aggregation [5,7]. Platelets are very sensitive to contact with biological substances (collagen, adenosine diphosphate (ADP), epinephrine) and others, including ristocetin, solid materials and high shear stress. When this occurs they tend to produce micro aggregates of platelets that are easily detected by modern blood cell counters because they decrease the number of platelets and alter the size distribution curve. Nanomaterials can potentially damage the cell membrane and even the cytoplasm since they can penetrate inside cells. Blood cell counters not only quantify blood cells, but they can also detect abnormalities in shape, size and homogeneity.

In the following we will briefly describe the coagulation process, regulatory factors and related test principles.

4.1.2 Coagulation cascade

Coagulation process occurs after the injury of blood vessels through two processes: a) primary haemostasis, in which, platelets immediately form a plug at the injury site by adhering to subendothelial collagen-von Willebrand factor (vWF) via their glycoprotein (GP) Ib receptors and b) secondary haemostasis that consists of two pathways: i) the extrinsic pathway (initiation pathway) and ii) the intrinsic pathway (propagation pathway), both pathways are merged into a common pathway that ended with the formation of fibrin strands, which strengthen the platelets plug.

The coagulation pathways are a series of reactions in a descending way, in which an inactive enzyme (zymogen) of serine protease (such as coagulation factor IX, X, XI...etc), cofactor (such as FVIII or FV) or transglutaminase (such as FXIII) becomes active and then catalyses the next reaction in the cascade. The coagulation factors are referred as factor (F), Roman numbers and lowercase “a” in case of active form.

In 1964, two different groups proposed the coagulation concept as a waterfall/

cascade model. This model suggests that the intrinsic pathway is the primary pathway that trigger thrombin formation following a vascular damage, while the extrinsic pathway is a complementary one by which the thrombin can be formed [23–25]. The model was improved by important additions and modifications during the following years [26]. Currently, the model underlines the main role of the extrinsic pathway as the initiator of thrombin formation and the intrinsic pathway as the amplification or propagation pathway, as shown in Fig. 4.1.

4.1.2.1 Extrinsic pathway (initiation pathway)

Upon the vascular damage, the tissue factor (TF) -a lipid-dependent transmembrane glycoprotein that is present in subendothelial cells and monocytes necessary for the initiation of blood coagulation cascade and formation of thrombin- becomes exposed to the blood. TF binds to a) the coagulation factor VII that is auto-cleaved within the complex to FVIIa, or to b) the activated form of the coagulation factor VII (FVIIa), since a fraction of coagulation factor VII circulates in blood in its active form. The binding between TF and factor VII/VIIa triggers the coagulation by converting factors IX and X to their active forms FIXa and FXa, respectively, see Fig. 4.1. Factors IXa and Xa may remain associated with TF-bearing cells or diffuse to the blood and bind to the surface of activated platelets that formed the primary platelets plug. Activated platelets have a great potential to bind to the coagulation factors, this ability is due to their negatively charged phospholipids [27].

The formation of thrombin from prothrombin requires the formation of a hydrolytic enzyme called “prothrombinas complex” that consists of FXa, phospholipids, calcium and the activated form of co-factor V (FVa), as described in Fig. 4.1. Factor V is activated by two substances, FXa and thrombin. The generated thrombin -the key enzyme of the coagulation system- initiates several positive feedback amplification reactions in order to increase the clot formation. This happens through activation of several coagulation factors that are involving in the intrinsic pathway as the coagulation factor XI and co-factor VIII, as well as, activation of co-factor V in the common pathway. Also, thrombin activates the conversion of fibrinogen to fibrin and activates the platelets at the injury sites, increasing the

phospholipids at their surface [1]. In addition, the formed thrombin activates the coagulation factor XIII to FXIIIa that rapidly cross-links fibrin monomers [28]. Moreover, thrombin protects the formed clot from solubilisation and proteolysis (fibrinolysis) through the activation of thrombin activatable fibrinolysis inhibitor (TAFI). Now, TAFI inhibits the conversion of plasminogen to plasmin (the primary enzyme of fibrinolysis) by removing the carboxy-terminal lysine residues from fibrin surface, because these lysines are important for the binding of fibrinolytic enzymes to fibrin [29].

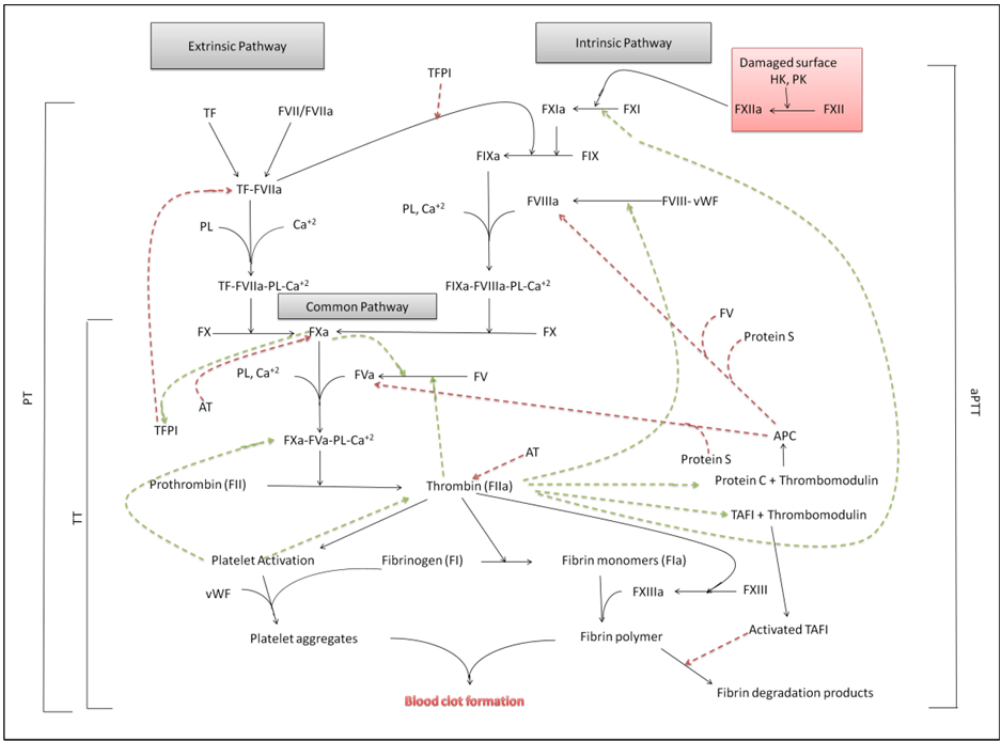

Figure 4.1: Schematic representation of the coagulation cascade. Coagulation proteins are referred as factor (F), Roman numbers and lowercase "a" in case of active form. Green dotted lines represent positive feedback amplification reactions, while red dotted lines represent coagulation inhibition reactions. The red box includes the proteins that are excluded from the revised coagulation cascade model. The efficiency of the extrinsic, intrinsic and common pathways are evaluated by measuring PT, aPTT and Thrombin time (TT) respectively.

4.1.2.2 Intrinsic pathway (propagation pathway)

The thrombin-activated coagulation factor XI (FXIa) initiates the activation of the coagulation factor IX to FIXa. The co-factor VIII circulates bound to the von Willebrand factor - vWF is an important protein that is essential for the adhesion of platelets at the site of injury to form the primary platelets plug. In addition, after

platelets activation vWF works along with fibrinogen to mediate platelets-platelets interaction permiting clot stabilisation. Also vWF protects FVIII from proteolytic degradation in the complex form. Upon thrombin activation, co-factor VIII dissociates from vWF and converts to its active form FVIIIa. FVIIIa binds to FIXa, calcium and phospholipids in order to form the "tenase complex", which catalyses the activation of the coagulation factor X to FXa, which in turn catalyses the formation of thrombin, as described in Fig. 4.1 [30].

When blood comes in contact with a negatively charged surface (contact activation), a group of proteins including coagulation factor XII, high molecular weight kininogen (HK) and prekallikrein (PK), forms a complex leading to the activation of the coagulation factor XII to FXIIa. FXIIa catalyses the conversion of coagulation factor XI to FXIa and, subsequently, the coagulation cascade is initiated in a descending way, as described in Fig. 4.1 [31]. These proteins (HK, PK and FXII) do not appear in the revised coagulation cascade, since inherited deficiency of FXII, HK or PK is asymptomatic. However, deficiency in the coagulation factor XI exhibits haemorrhagic effects [32,33].

4.1.2.3 Common pathway

Both extrinsic and intrinsic pathways are merged in a common pathway, which starts with the conversion of the prothrombin to thrombin in a reaction catalysed by prothrombinase complex.

Thrombin catalyses the conversion of fibrinogen to fibrin monomers, through cleavage of fibrinopeptides A and B from fibrinogen, which alters the surface charge of the molecule. These fibrin monomers are converted to insoluble fibrin polymers (fibrin meshwork) by the action of thrombin-activated factor XIII (FXIIIa), which forms cross-links between and within the fibrin monomers to generate the insoluble fibrin meshwork around platelet aggregates [34]. A portray of the coagulation cascade is shown in Fig. 4.2. The final form of the blood clot is shown in Fig. 4.3.

4.1.2.4 Regulation of blood coagulation by anticoagulant pathways

In order to prevent any massive coagulation action, the coagulation process is

tightly regulated by a number of inhibitors that inhibit the systematic release of thrombin and other pro-coagulant proteases. These coagulation inhibitors (anticoagulants) are:

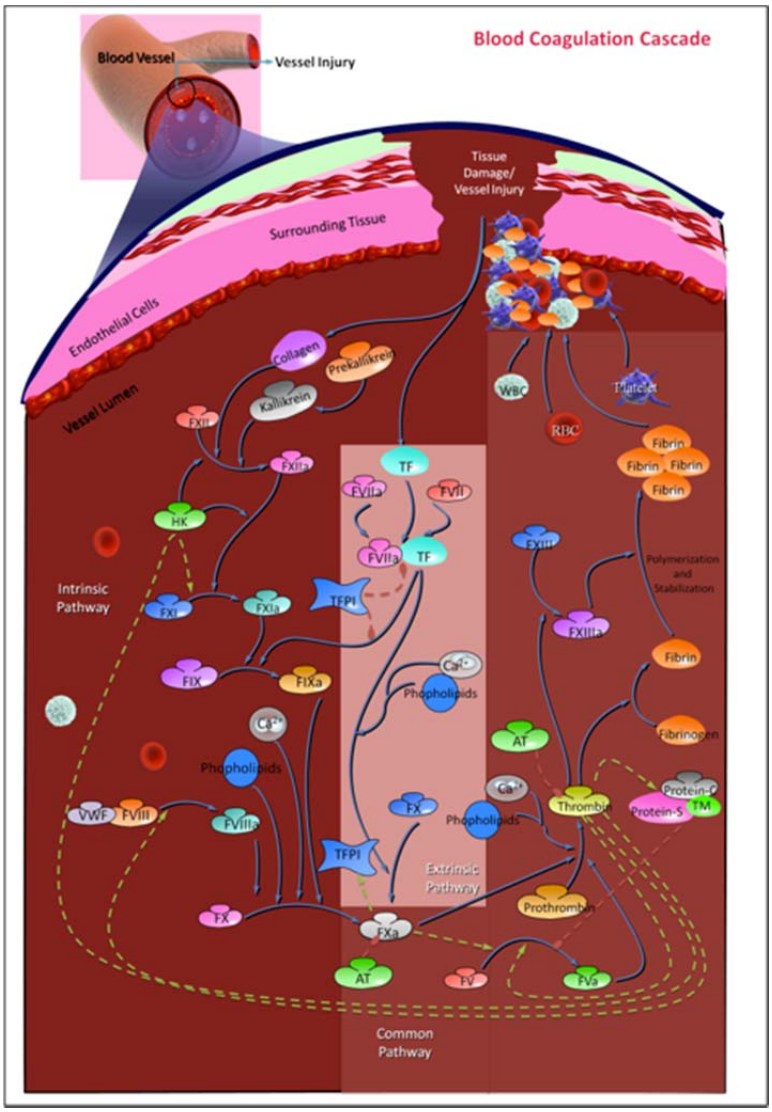

Figure 4.2: A portray of the coagulation cascade.

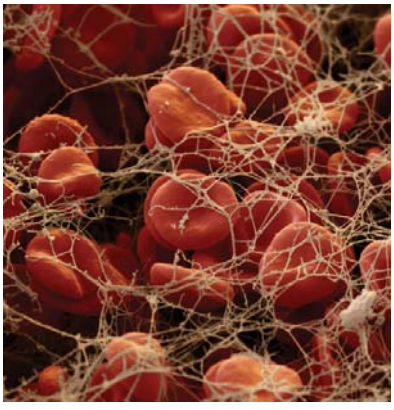

Figure 4.3: Blood clot structure using coloured scanning electron microscope (SEM). It consists of a cross-linked fibrin meshwork (white filaments), in which erythrocytes (red) are trapped [35]

.

- The tissue factor pathway inhibitor (TFPI). An endogenous anticoagulant protein, a serine protease inhibitor, which inhibits further production of FXa and FIXa by the TF-FVIIa complex. The inhibition process occurs in two steps. First, the TFPI binds to and inactivates FXa; second, TFPI-FXa complex binds to and inhibits the TF-FVIIa complex. TFPI circulates in the plasma as a complex with plasma lipoproteins (80%) or free (uncomplexed) (5-20%). Lipoprotein-associated TFPI has less anticoagulant effect than the free TFPI. Free TFPI is released from endothelial cells to the circulation after heparin, non-heparin glycosaminoglycans, pentosan polysulphate, hypersulphated heparin, low-molecular weight heparin and tissue plasminogen activator administration [36].

- Antithrombin (AT). A serine protease inhibitor, which is stimulated by heparin and heparin-like molecules that are present on the surface of the intact endothelial cells as heparan sulfate. It inhibits the coagulation by inhibiting FXa and thrombin [37,38].

- Protein C. A vitamin-K-dependent protein, which is activated on the surface of intact endothelial cells by the binding between thrombin (a procoagulant and anticoagulant factor) and thrombomodulin (an endothelium-bound protein) into activated protein C (APC). APC with free protein S (a Vitamin-K-dependent co-factor protein) form a membrane bound complex, which can cleave factor Va to FV. Factor V acts as an anticoagulant agent that works in synergy with protein S in the degradation of FVIIIa to its inactive form (FVIII). Thus, inhibiting the coagulation process [39].

- Nitric oxide, prostacyclin and ecto-ADPase. These substances are released from the intact endothelium and can cause a decrease in the platelets activity [30].

- Heparan sulfate. It is a glycosaminoglycan that is attached to the surface of intact endothelial cells. It acts as a cofactor for antithrombin.

- Tissue-type plasminogen activator (tPA). It is released from the endothelial cells and binds to lysine residues expressed on the fibrin surface. It catalyses the conversion of plasminogen (plasma protein synthesised in the liver) to plasmin. Plasmin proteolytically cleaves fibrin into fibrin degradation products and D-dimer (fibrinolysis) [40].

4.1.3 Coagulation screening tests

There are several tests used to evaluate the coagulation state *in vitro* as prothrombin time, activated partial thromboplastin time, thrombin time, fibrinogen and platelets count. The most common tests used are PT and aPTT, while thrombin time and fibrinogen test are not considered to be first-line screening tests although they are commonly performed. Platelets count should be checked in any case.

4.1.3.1 Prothrombin Time

The activity of the extrinsic pathway is evaluated by measuring the prothrombin time, an assay that was described in 1935 by Dr. Armand Quick [29]. In this assay tissue factor-phospholipid-calcium mixture or thromboplastin is added to platelets-poor plasma. The most commonly used thromboplastin reagents are those derived from rabbit tissue [41]. Elongated PT time could be obtained in case of factors VII, X, V deficiencies and prothrombin deficiency as occurred with vitamin K-antagonist [42] or severe liver disease [43]. However, normal values of PT are detected in the case of haemophilia (factor VIII or factor IX deficiency). Hence, PT value does not reflect the coagulation process *in vivo* [30].

4.1.3.2 Activated partial thromboplastin time

The activity of the intrinsic pathway is evaluated through measuring the activated partial thromboplastin time; a modified assay from partial thromboplastin time that was discovered by Drs. Langdell, Wagner and Brinkhous in 1953 [29]. In this assay non-physiological, negatively charged compounds (e.g., celite, kaolin, or ellagic acid suspended in a phospholipid mixture) are added to platelets-poor plasma [44]. Presence of such compounds (contact system activator) activates a series of reactions in a descending order ended with the formation of thrombin. Prolonged aPTT could be obtained in case of factors XII, XI, IX, VIII and V deficiencies, prothrombin

deficiency, liver disease, haemophiliaand the presence of anticoagulant agents such as heparin, argatroban, bivalirudin and lepirudin.

4.1.3.3 Thrombin time

This test is used in order to evaluate the efficiency of the common pathway. It is not considered to be a first-line screening test. In this test a bovine or human thrombin is added to platelets-poor plasma, which in turns converts fibrinogen into fibrin. The time for fibrin clot formation is then recorded. Thrombin time is similar to another time called “Reptilase time” (RT) which is more frequently used, but in this test a snake venom activator is added instead of thrombin. The thrombin time is sensitive to heparin while the reptilase time is not. Elongation of TT is associated with amyloidosis, fibrin degradation products, fibrinogen deficiency/abnormality, hypo-albuminaemia and the presence of inhibitors as heparin [45–47].

4.1.3.4 Fibrinogen test

This test is used to detect abnormal bleeding or coagulation disorder. A high level of fibrinogen is associated with several disorders such as inflammation, cardiovascular diseases, strokes and cancer. However, low fibrinogen level increases the risk of bleeding and it is associated with several disorders such as haemodilution, liver diseases and inherited deficiencies (e.g. Hypofibrinogenaemia, afibrinogenaemia and dysfibrinogenaemia). Several methods are used to measure the plasma fibrinogen level such as a) Blombäck and Blombäck method, b) clotting rate assay according to von Clauss, c) immunoassays, including radial immunodiffusion (RID) according to Mancini et al., ELISA or nephelometric, d) total amount of clottable fibrinogen by means of turbidimetric assay according to Ellis and Stransky, e) Chromotime System, and f) prothrombin time-derived fibrinogen assay on ACL coagulometer [48–50].

4.1.3.5 Platelets count

Platelets count is often a part of complete blood count (CBC) assay. Abnormalities in platelets account are associated with bleeding disorders and other bone marrow diseases as leukaemia.

4.1.4 Haemolysis

Haemolysis is the breakdown of red blood cells, which leads to the leaking of haemoglobin and intracellular ingredients such as potassium into the plasma. Haemolysis can lead to life-threatening conditions such as anaemia, jaundice, hypertension, arrhythmia and renal failure [51]. Severe haemolysis could be detected visually with naked eyes. However, this method is unreliable in case of mild haemolysis detection, since the presence of bilirubin in serum may impair the ability to detect haemolysis visually, especially in neonatal samples in which elevated bilirubin concentration commonly happens. Mild haemolysed samples (serum free haemoglobin in the range between 0.3 and 0.6 g/L) could be detected by semi-quantitative spectrophotometer measurement at wavelength 400-800 nm. Oxygenated haemoglobin is detected by two absorption peaks at the wavelengths 540 and 580 nm Fig. 4.4 [52]. In general, absorbed haemoglobin peak at 580 nm is preferable because it is a bit higher. Significant haemolysis is associated with decreasing in erythrocytes, haemoglobin and haematocrit [53].

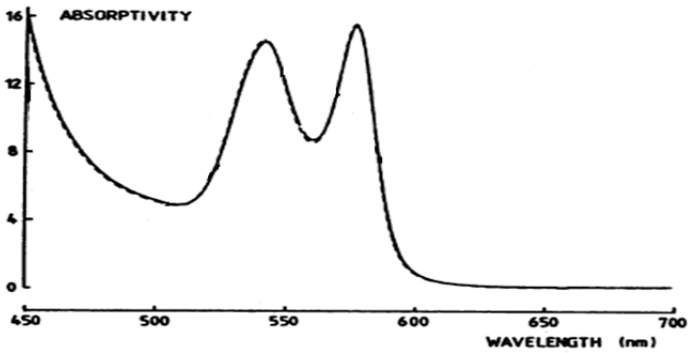

Figure 4.4: Light absorption spectra of human fetal and adult oxygenated haemoglobin. Absorptivity is expressed in L. mmol $^{-1}$.cm^{-1} [52].

4.2 Objectives

The aim of this chapter is to study the *in vitro* toxicity of our bioferrofluids (P4VP-g-APEG bioferrofluids) and its components in blood, through investigating their effect on the coagulation process by measuring the prothrombin time and activated partial thromboplastin time, studying their effect on blood cells through measuring the blood cell count and detection of haemolysis by measuring the free haemoglobin. In

addition, this chapter explores the effect of surface coating of the nanoparticles on the blood haemostasis using two bioferrofluids, one is coated with dimercaptosuccinic acid and the other is coated with dimercaptosuccinic acid with short-chain diamine PEG.

4.3 Materials and methods

4.3.1 P4VP-g-APEG coated bioferrofluids preparation and characterisation

Bioferrofluids preparation and characterisation methods are the same as described in Annex I. The preparation conditions of the maghemite polymer nanocomposites used in this chapter are summarised in Table 4.1.

Table 4.1: Preparation conditions of maghemite polymer nanocomposites for different samples.

Sample	P4VP (g/L)	1M $FeBr_3$ (mL)	1M $FeBr_2$ (mL)	Fe/pyridine mol ratio	Fe^{2+}/ Fe^{3+} mol ratio
H	0.4	1.584	0.794		

The prepared P4VP-g-APEG bioferrofluid was further purified by centrifugation at 196.000 G for 30 minutes and re-dispersed in PBS by ultrasounds. The dispersion was filtered through a sterile 0.22 µm membrane filter to obtain P4VP-g-APEG bioferrofluids.

4.3.2 DMSA-bioferrofluids and DMSA-PEG-$(NH_2)_2$-bioferrofluids preparation and characterization

These bioferrofluids were supplied by Prof. Puerto Morales, from the Instituto de Ciencia de Materiales de Madrid, as part of an ongoing collaboration.

The synthesis was performed in three steps: 1) synthesis of magnetite nanoparticles, 2) surface modification with DMSA and 3) PEG conjugation and dispersion in water. Magnetite nanoparticles were obtained via thermal decomposition of an iron coordination complex as a precursor to ensure nanoparticle homogeneity in

size and shape following the method reported by Sun and co-workers [54,55]. Particle size and shape were studied using a 200 keV JEOL-2000 FXII microscope. A drop of a dilute magnetic nanoparticle suspension in hexane was placed on a carbon coated copper grid and dried at 50 ºC. Size distribution was determined from TEM micrographs through manual measurement of more than 200 particles and data were analysed with Gwyddion 3.25 software to obtain the mean size and standard deviation by gaussian fitting. Particles were coated with meso-2,3-dimercaptosuccinic acid (DMSA) by a ligand exchange process to remove oleic acid, after which a short-chain diamine PEG (PEG-$(NH_2)_2$) was covalently bound to the nanoparticle surface via 1-ethyl-3-(3-dimethylaminopropyl)-carbodiimide hydrochloride (EDC) activation of the carboxylic acids. Colloidal properties of 0.5 mM Fe nanoparticle suspensions in water were characterised by dynamic light scattering using a Nanosizer ZS (Malvern). Z-Average values in intensity at pH 7 were used as the mean hydrodynamic size. The polydispersity degree index was calculated by dividing the standard deviation by the mean size. The Z potential was measured in a 0.01 M KNO_3 solution. Other properties of DMSA-bioferrofluids and DMSA-PEG-$(NH_2)_2$-bioferrofluids have been described in detail in previous publications [56,57].

4.3.3 Coagulation studies

All haemocompatability experiments were performed at the hospital Clinico Universitario Lozano Blesa, Zaragoza, under the supervision of Professor Martín Gutierrez, Doctor Rosa Cornudella and Doctor José Antonio Moreno.

4.3.3.1 Control plasma

Blood samples were obtained from healthy human volunteers. Samples were collected in citrate (0.129 M) vacutainer tubes. The samples were centrifuged at 3500 rpm to obtain platelets-poor plasma (PPP). The plasma was processed for the coagulation studies of PT and aPTT, using PT and aPTT HemoSIL^{TM} reagents and measured by the coagulometer TOP-ACL from IL-Instrumentation. The results were within the reference limits (9-14 s. and 23-37 s. respectively).

4.3.3.2 PPP treated with bioferrofluids

PPP samples were mixed with different concentrations of bioferrofluids (P4VP-g-APEG bioferrofluids, DMSA bioferrofluids and DMSA-PEG-$(NH_2)_2$ bioferrofluids) and processed for the measurement of PT and aPTT.

4.3.3.3 PPP treated with bioferrofluids coating components

To study the effect of the coating on the coagulation, PPP samples were mixed with different concentrations of APEG, P4VP-g-APEG, DMSA, and PEG-$(NH_2)_2$and processed for the measurement of PT and aPTT.

4.3.4 Complete blood counts studies

4.3.4.1 Control blood

Blood samples were obtained from healthy human volunteers. Samples were collected in EDTA K3, 1.8 mg/mL vacutainer. The blood samples were processed for CBC studies using a Coulter LH 780 analyzer from Beckman Coulter.

4.3.4.2 Blood treated with bioferrofluids, and coating materials

Blood samples were mixed with different concentrations of the investigated materials (P4VP-g-APEG bioferrofluids, DMSA bioferrofluids, DMSA-PEG-$(NH_2)_2$ bioferrofluids, APEG, P4VP-g-APEG, DMSA, and PEG-$(NH_2)_2$) and processed for blood cell counting.

4.3.5 Haemolysis studies

4.3.5.1 Control blood

Blood samples were obtained from healthy human volunteers. Samples were collected in Lithium heparin 17 UI/mL vacutainer tubes. The plasma free haemoglobin was analysed after blood centrifugation at 2500 rpm for 5 minutes using a double beam spectrophotometer Analytic Jena –Specord 205 with wavelength range between 500 – 630 nm.

4.3.5.2 Blood treated with bioferrofluids

Whole blood was mixed and incubated with different concentrations of bioferrofluids (P4VP-g-APEG bioferrofluids, DMSA bioferrofluids, and DMSA-PEG-

$(NH_2)_2$ bioferrofluids) for 5 min, then centrifuged at 2500 rpm for 5 min and the plasma processed for the measurement of the free haemoglobin.

4.4 Results

4.4.1 P4VP-g-APEG bioferrofluids characterisation

The iron content of bioferrofluid stock sample was determined by atomic absorption in a plasma spectrometer. Concentration of iron content is 7.78 g/L Fe_2O_3. The sample has 13.36 g/L of P4VP, 12.03 g/L of APEG(200) and 1.34 g/L of APEG(1000)-COO^-, and the necessary amounts of phosphate, sodium, potassium and chloride ions for a standard PBS solution of pH=7.40 and I = 0.15 M.

The sample was analysed by TEM and DLS and the results are shown in Figs. 4.5 and 4.6. TEM images show iron oxide nanoparticles uniformly distributed in a continuous polymer film (insert in Fig. 4.5). Most of the iron oxide nanoparticles are spherical, as shown in Fig. 4.5. A size distribution analysis for the maghemite magnetic nanoparticles is shown in Fig. 4.6(a). The core size (mean ± SD) is 9.1 ± 2.1 nm.

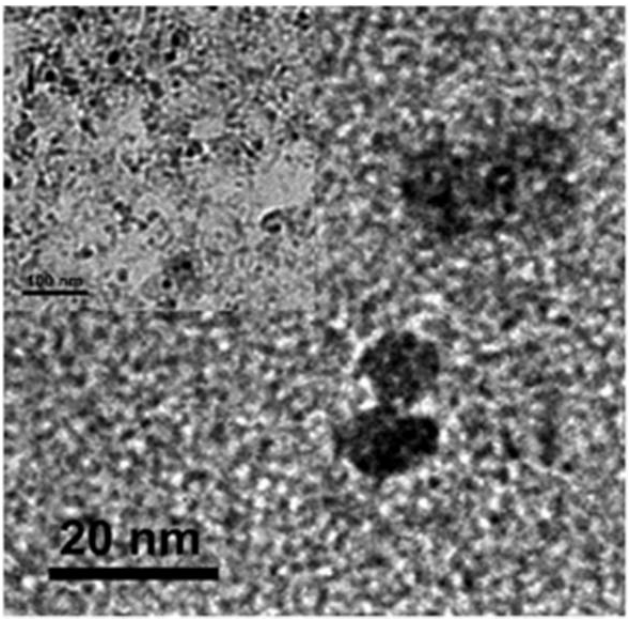

Figure 4.5: TEM images of maghemite magnetic nanoparticles in P4VP-g-APEG bioferrofluids. The inset shows the sample at lower magnification.

DLS observations show a single population of particles with an average hydrodynamic diameter of 80 nm, as shown in Fig. 4.6(b). Measurements of zeta potential of the nanoparticles suspension yielded average values close to zero.

The structures of components of the nanoparticles shell are shown in Diagram 1. The reaction of P4VP and APEG is a Michael addition involving the acrylate double bond and the nitrogen of the pyridine that becomes quaternised and therefore positively charged in this way. The structure of the P4VP-g-APEG graft copolymer is comb-like. The backbone is a polyethylene chain with pyridine side groups. The APEG chains are linked to some of the pyridine groups by N-C bonds between the nitrogen of the pyridine and the β-carbon of the acrylate PEG ester, thus hanging perpendicular to the copolymer backbone as depicted in Diagram 1. Therefore the N of pyridine groups linked to APEG chains are positively charged and the copolymer is cationic.

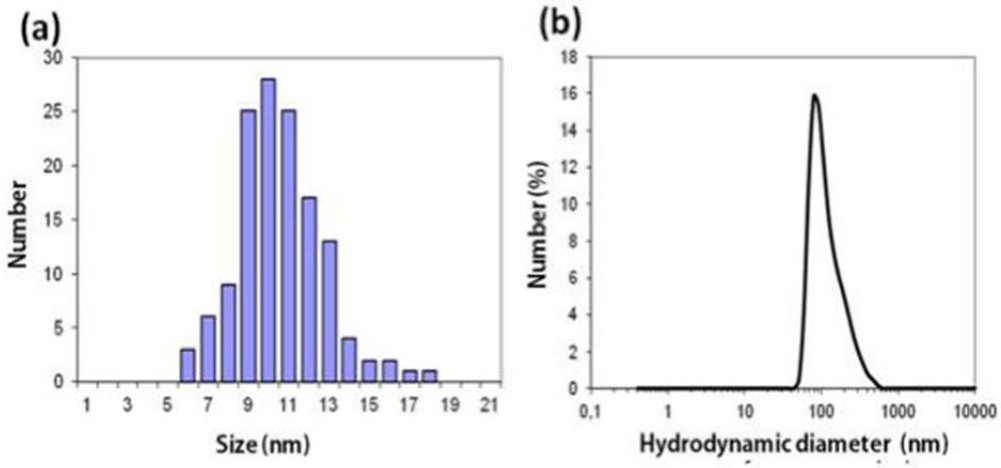

Figure 4.6: P4VP-g-APEG bioferrofluids analysis: (a) Size distribution of spherical maghemite magnetic nanoparticles; (b) Distribution of hydrodynamic diameters in bioferrofluid sample from DLS measurements.

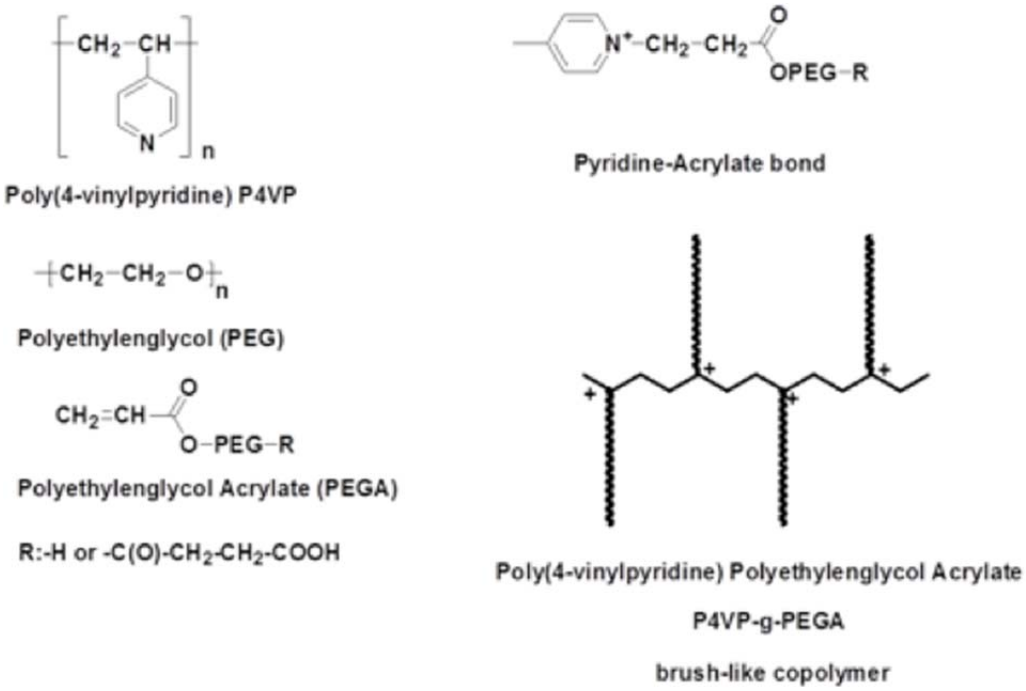

Diagram 1: Structure of polymers and copolymers.

4.4.2 DMSA bioferrofluids and DMSA-PEG-$(NH_2)_2$ bioferrofluids characterisation

The iron contents of bioferrofluids stock samples were determined by atomic absorption in a plasma spectrometer. Concentrations of iron contents are 5.8 and 1 g/L Fe for DMSA bioferrofluids and DMSA-PEG-$(NH_2)_2$ bioferrofluids, respectively.

Magnetite nanoparticles used in this work were obtained via thermal decomposition of iron (III) acetylacetonate in 1-octadecene in the presence of oleic acid. Magnetite magnetic nanoparticles are relatively spherical and well dispersed due to the presence of oleic acid around the particles Fig. 4.7 (a), with an average core size of 7 ± 1 (mean ± SD). A size distribution analysis for the magnetite magnetic nanoparticles is shown in Fig. 4.7(b).

Particles were coated with meso-2,3-dimercaptosuccinic acid after a ligand exchange reaction. In order to increase the biocompatibility of the material, nanoparticles coated with DMSA were chemically modified with PEG. Properties of

DMSA bioferrofluids and DMSA-PEG-$(NH_2)_2$ bioferrofluids have been extensively described in refs. [56,57].

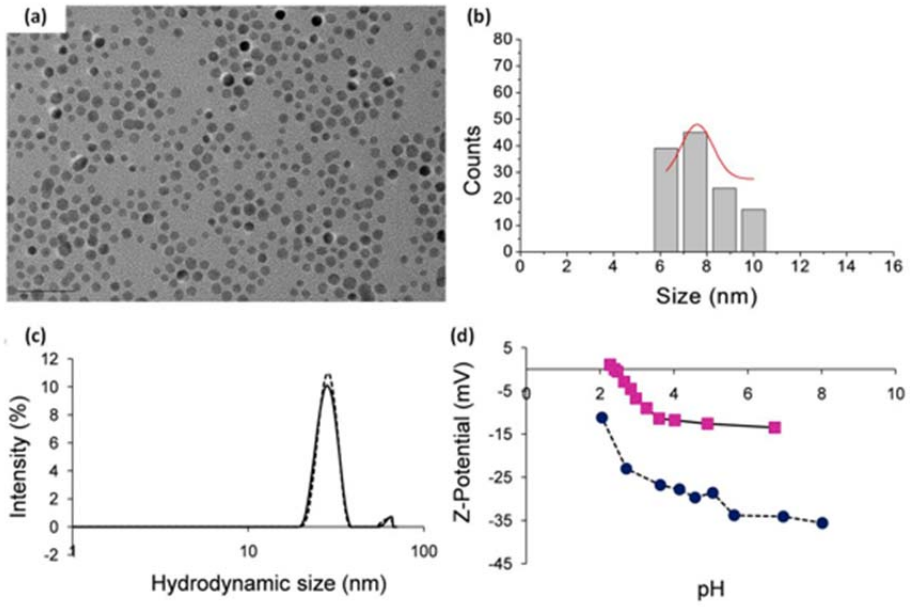

Figure 4.7: DMSA bioferrofluids and DMSA-PEG-$(NH_2)_2$ bioferrofluids characterisation, (a) TEM images of magnetite magnetic nanoparticles of ~7 nm oleic acid coated nanoparticles, (b) Size distribution histograms of spherical magnetite magnetic nanoparticles. Red line indicates the Gaussian fitting function of TEM particle size data, (c) Hydrodynamic sizes for DMSA bioferrofluids (solid line) and DMSA-PEG-$(NH_2)_2$ bioferrofluids (dotted line), (d) Evolution of Z-potential as a function of pH, DMSA bioferrofluids [●], DMSA-PEG-$(NH_2)_2$ bioferrofluids [■].

DLS observations showed a monomodal distribution of DMSA coated nanoparticles with an average hydrodynamic diameter of 22 nm and polydispersity degrees lower than 0.25. After PEG modification, the average hydrodynamic size at pH 7 increases from 22 to 27 nm, as shown in Fig. 4.7(c). The surface charge decreases from approximately -35 mV for DMSA bioferrofluids samples to values between -15 mV for DMSA-PEG-$(NH_2)_2$ bioferrofluids, as shown in Fig. 4.7(d).

4.4.3 Coagulation studies

4.4.3.1 PPP treated with P4VP-g-APEG bioferrofluids

PPP were treated with different concentrations of P4VP-g-APEG bioferrofluids

ranging from 0.07 g/L Fe_2O_3 to 0.38 g/L Fe_2O_3, and processed for the measurement of PT and aPTT. PT shows no significant difference with concentrations of 0.12 g/L of Fe_2O_3 and lower. At this concentration, PT value is 10.79 ± 0.70 s which compares well with its control value 11.30 ± 0.68 s. At the highest concentrations of P4VP-g-APEG bioferrofluids, for instance, at concentration 0.38 g/L Fe_2O_3, PT value is 9.18 ± 0.40 s, which is slightly shorter than the control value 10.66 ± 0.42 s although within our laboratory normal reference range (9-14 s). These results are shown in Fig. 4.8(a).

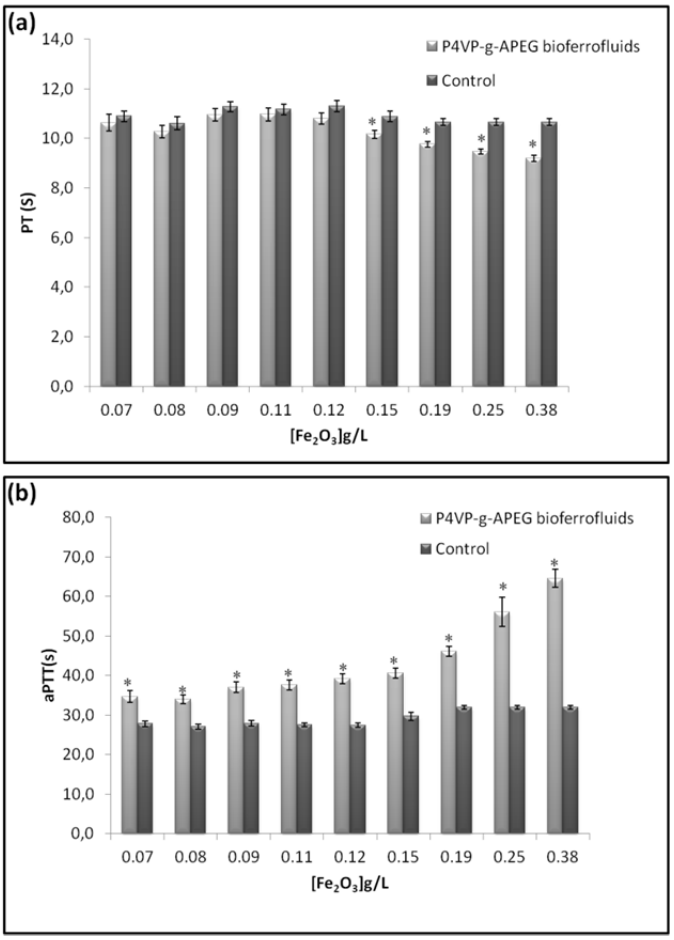

Figure 4.8: The effect of P4VP-g-APEG bioferrofluids on: (a) the prothrombin time in seconds, (b) the activated partial thromboplastin time in seconds. Values represent mean ± SEM (*n*=10), (*) marks significant differences between P4VP-g-APEG bioferrofluids and control.

On the other hand, aPTT shows a rapid increase as the P4VP-g-APEG bioferrofluids concentration increases. For instance, at concentration 0.07 g/L Fe_2O_3, aPTT value is 34.67 ± 4.52 s, significantly different to the control one, 27.76 ± 2.16 s, although within our laboratory normal reference range (23-37 s). In contrast, at concentration 0.38 g/L Fe_2O_3, aPTT value is 64.56 ± 7.21 s, twice the control value of 31.85 ± 1.48 s. The results are shown in Fig. 4.8(b).

Data corresponding to PT and aPTT determinations were analysed using Mann-Whitney test and are summarised in Table 4.2.

In order to explore the cause of the aPTT prolongation, PPP treated with the higher concentration of bioferrofluids (0.38 g/L Fe_2O_3) were used for further studies such as a) mixture test, in which PPP treated with bioferrofluids were mixed with normal plasma (1:1), aPTT measurements showed a prolongation of aPTT value of 55.30 ± 7.22 s as compared to its control value 31.08 ± 3.08 s (*n*=4), b) TT measurements, results showed normal value of TT 28.24 ± 2.90 s as compared to its control value 27.60 ± 3.04 s (*n*=5) (TT reference limits is 15-28 s.), c) coagulation factor measurements, the level of the coagulation factors (VIII, IX, XI, XII) of the intrinsic pathway were evaluated and the results showed a reduction in the level of all of these coagulation factors to 28%, 15%, 11.9% and 12.7%, respectively (normal values are 60-120% for VIII, 70-120% for factors IX, XI and XII).

Table 4.2: Statistical analysis data for the effect of P4VP-g-APEG bioferrofluids on PT and aPTT. The number of samples was 10 for each concentration and the original P4VP-g-APEG bioferrofluids concentration was 7.78 g/L [Fe_2O_3].

Conc. g/L	PT Mean ± SD (s)		P (Mann-Whitney)	aPTT Mean ± SD (s)		P (Mann-Whitney)
	Test	Control		Test	Control	
0.07	10.63 ± 1.07	10.89 ± 0.66	0.3258	34.67 ± 4.52	27.76 ± 2.16	0.0015
0.08	10.27 ± 0.76	10.61 ± 0.80	0.2730	34.03 ± 3.51	27.01 ± 1.87	0.0004
0.09	10.94 ± 0.78	11.28 ± 0.66	0.2899	37.02 ± 4.11	27.88 ± 2.11	0.0002
0.11	10.97 ± 0.82	11.17 ± 0.67	0.4497	37.60 ± 3.88	27.51 ± 1.58	0.0002
0.12	10.79 ± 0.70	11.30 ± 0.68	0.1306	39.19 ± 4.11	27.42 ± 1.88	0.0002
0.15	10.16 ± 0.55	10.88 ± 0.69	0.0156	40.54 ± 4.07	29.65 ± 3.16	0.0002
0.19	9.76 ± 0.35	10.66 ± 0.42	0.0004	46.04 ± 3.96	31.85 ± 1.48	0.0002
0.25	9.47 ± 0.30	10.66 ± 0.42	0.0002	56.06 ± 11.77	31.85 ± 1.48	0.0002
0.38	9.18 ± 0.40	10.66 ± 0.42	0.0002	64.56 ± 7.21	31.85 ± 1.48	0.0002

4.4.3.2 PPP treated with APEG

To study the coating effect on the coagulation process, a APEG blank solution with the same content of APEG(200) + APEG(1000)-COO^- as the one used for the coated nanoparticles (13.36 g/L) has been used. This APEG solution was mixed with PPP at concentrations of 0.13 and 1.33 g/L. No alteration in the coagulation profile has been observed, except the PT at the concentration 1.33 g/L APEG. The PT value for the test sample was 12.40 ± 0.69 s, which is slightly different than the control value 11.47 ± 0.65 s, although it is within our laboratory normal reference range (9-14 s). These results are summarised in Fig. 4.9, while statistical analysis data are shown in Table 4.3.

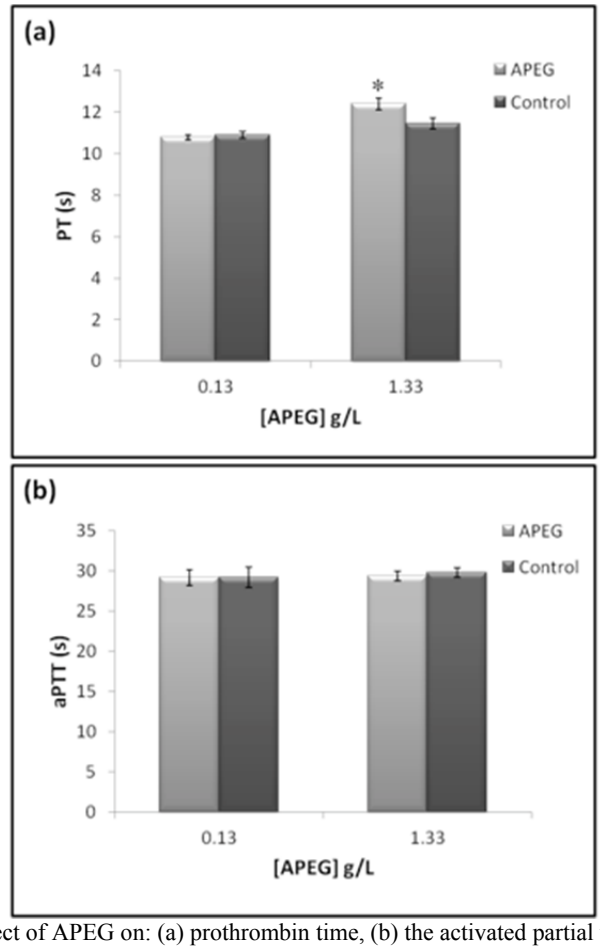

Figure 4.9: The effect of APEG on: (a) prothrombin time, (b) the activated partial thromboplastin time, in seconds. Values represent mean ± SEM (*n*=6), (*) marks significant differences between APEG and control.

Table 4.3: Statistical analysis data for the effect of APEG on PT and aPTT, the number of samples was 6 for each concentration, the original APEG concentration was 13.36 g/L.

Conc. g/L	PT Mean ± SD (s)		P (Mann-Whitney)	aPTT Mean ± SD (s)		P (Mann-Whitney)
	Test	Control		Test	Control	
0.13	10.78 ± 0.31	10.88 ± 0.41	0.63	29.17 ± 2.36	29.18 ± 3.07	0.87
1.33	12.40 ± 0.69	11.47 ± 0.65	0.04	29.35 ± 1.49	29.80 ± 1.47	0.42

4.4.3.3 PPP treated with P4VP-g-APEG

The P4VP-g-APEG blank sample used in this work was prepared under the same conditions and concentrations applied for P4VP-g-APEG bioferrofluids preparations. The PT value does not change at concentration of 1.33 g/L (11.78 ± 1.17 s as compared to control value 11.47 ± 0.65 s) and becomes shorter than the control value at concentration of 0.13 g/L (10.28 ± 0.57 s and 11.30 ± 0.48 s, respectively) and at concentration 0.013 g/L (9.98 ± 0.98s and 11.30 ± 0.48s, respectively). However, PT values for plasma treated with P4VP-g-APEG is significant lower than the control one. However, these values are within our laboratory normal reference range (9-14 s). On the contrary, the aPTT shows a large increase at a concentrations of 1.33 and 0.13 g/L, greater than 120 seconds, the time limit of the equipment. A lower concentration of 0.013 g/L still shows significant differences for aPTT value with respect to the control one (39.63 ± 11.17 s and 31.45 ± 2.01 s, respectively). The results are shown in Fig. 4.10 while statistical analysis data are summarised in Table 4.4.

Table 4.4: Statistical analysis data for the effect of P4VP-g-APEG copolymer on PT and aPTT, the number of samples was 6 for each concentration, the original P4VP-g-APEG concentration was 13.36 g/L.

Conc. g/L	PT Mean ± SD (s)		P (Mann-Whitney)	aPTT Mean ± SD (s)		P (Mann-Whitney)
	Test	Control		Test	Control	
0.013	9.98 ± 0.98	11.30 ± 0.48	0.04	39.63 ± 11.17	31.45 ± 2.01	0.03
0.13	10.28 ± 0.57	11.30 ± 0.48	0.02	> 120	31.45 ± 2.01	-
1.33	11.78 ± 1.17	11.47 ±0.65	0.74	> 120	29.80 ± 1.47	-

4.4.3.4 PPP treated with DMSA bioferrofluids and DMSA-PEG-$(NH_2)_2$ bioferrofluids

PPP were treated with different concentrations of DMSA bioferrofluids ranging from 0.048 g/L Fe to 0.29 g/L Fe, and processed for the measurement of PT and aPTT.

PT shows no significant difference, except at concentrations of 0.058 and 0.29 g/L Fe, in which the PT values for PPP treated with DMSA bioferrofluids were lower than control. However, these values are within our laboratory normal reference range (9-14 s). These results are shown in Fig. 4.11(a) while statistical analysis data are summarised in Table 4.5. On the other hand, aPTT shows a rapid increase as the DMSA bioferrofluids concentration increases. For instance, at lower concentration 0.048 g/L Fe, aPTT value is 40.66 ± 5.23 s, significantly different to the control one which is 30.26 ± 2.48 s, and at the higher concentration 0.29 g/L Fe, aPTT value is 65.58 ± 6.13 s, more than the double value of the control value 27.95 ± 2.35 s. The results are shown in Fig. 4.11(b), while statistical analysis data are summarised in Table 4.5.

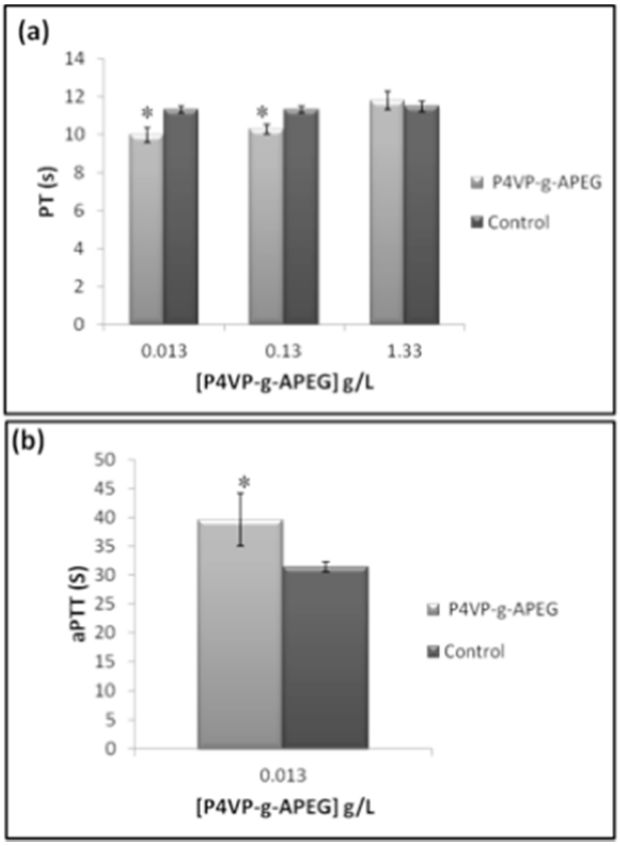

Figure 4.10: The effect of P4VP-g-APEG on: (a) Prothrombin time, (b) the activated partial thromboplastin time, in seconds. Values represent mean ± SEM (*n*=6), (*) marks significant differences between P4VP-g-APEG and control.

Table 4.5: Statistical analysis data for the effect of DMSA bioferrofluids on PT and aPTT, the number of samples was 6 for each concentration, the original DMSA bioferrofluids concentration was 5.8 g/L Fe.

Conc. g/L	PT Mean ± SD (s)		P (Mann-Whitney)	aPTT Mean ± SD (s)		P (Mann-Whitney)
	Test	Control		Test	Control	
0.048	9.35 ± 0.87	9.95 ± 0.96	0.3776	40.66 ± 5.23	30.26 ± 2.48	0.0079
0.058	9.43 ± 0.49	10.22 ± 0.51	0.0438	41.97 ± 2.29	29.80 ± 3.78	0.0022
0.073	8.97 ± 0.72	9.83 ± 0.83	0.1320	51.74 ± 6.99	28.93 ± 1.63	0.0080
0.097	9.64 ± 0.55	10.18 ± 1.11	0.3602	54.15 ± 6.46	29.95 ± 1.90	0.0022
0.145	9.14 ± 0.81	10.43 ± 0.91	0.0666	55.15 ± 9.56	29.57 ± 3.47	0.0022
0.290	8.52 ± 0.40	10.22 ± 0.71	0.0050	65.58 ± 6.13	27.95 ± 2.35	0.0050

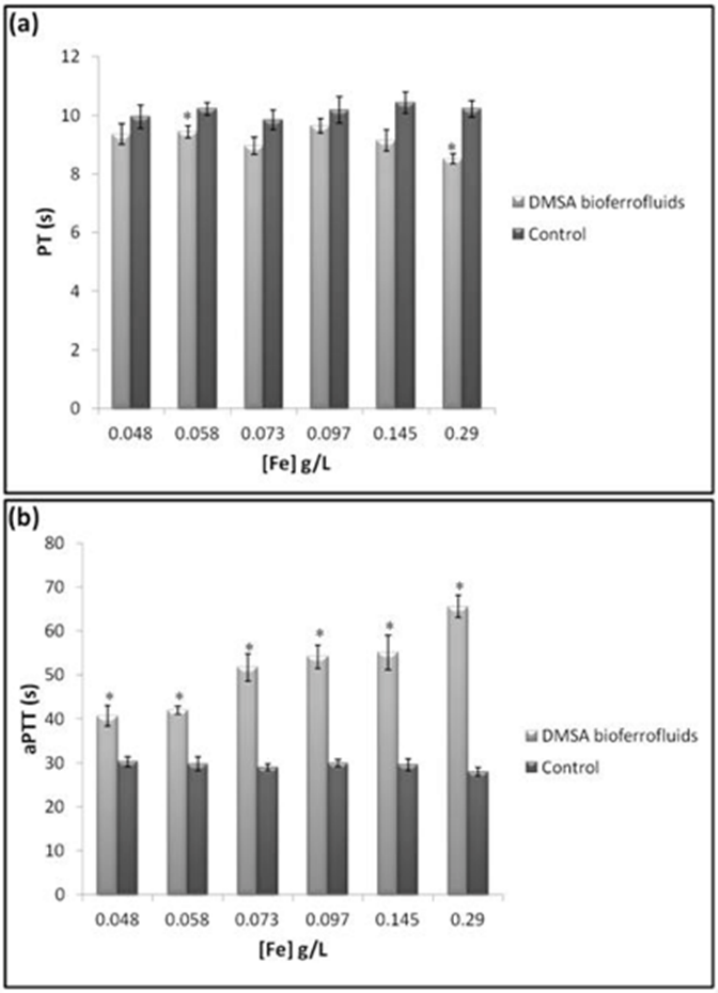

Figure 4.11: The effect of DMSA bioferrofluids on: (a) the prothrombin time, (b) the activated partial thromboplastin time, in seconds. Values represent mean ± SEM (*n*=6), (*) marks significant differences between DMSA bioferrofluids and control.

In order to explore the cause of the aPTT prolongation, PPP treated with the higher concentration of DMSA bioferrofluids (0.29 g/L Fe) were used for further studies such as a) mixture test, in which PPP treated with bioferrofluids were mixed with normal plasma (1:1), aPTT measurements showed normal aPTT value 33.53 ± 0.92 s compared to its control value 30.83 ± 0.74 s (*n*=3), and b) TT measurements, where results showed normal value of TT 27.83 ± 2.57 s compared to its control value 21.83 ± 1.45 s (*n*=3) (TT reference limits is 15-28 s.).

In addition, PPP were treated with different concentrations of DMSA-PEG-$(NH_2)_2$ bioferrofluids ranging from 0.048 g/L Fe to 0.29 g/L Fe, and processed for the measurement of PT and aPTT. PT shows no significant difference with all concentrations Fig 4.12(a), for instance, at high concentration of 0.29 g/L Fe, PT value is 11.78 ± 1.95 s, which compares well with its control value 11.13 ± 1.61 s. In contrast, aPTT shows significant increase as the DMSA-PEG-$(NH_2)_2$ bioferrofluids concentration increases, except for concentration 0.058 g/L Fe Fig. 4.12(b). At this concentration and other concentrations (0.048 and 0.073 g/L Fe) where a significance difference was detected, aPTT values were at the laboratory range (29-37 s). At higher concentration of 0.29 g/L Fe, aPTT value is 49.37 ± 8.71 s, more than the control value 30.16 ± 2.54 s. The statistical analysis data are summarised in Table 4.6.

Table 4.6: Statistical analysis data for the effect of DMSA-PEG-$(NH_2)_2$ bioferrofluids on PT and aPTT, the number of samples was 6 for each concentration, the original DMSA-PEG-$(NH_2)_2$ bioferrofluids concentration was 1 g/L Fe.

Conc. g/L	PT Mean ± SD (s)		P (Mann-Whitney)	aPTT Mean ± SD (s)		P (Mann-Whitney)
	Test	Control		Test	Control	
0.048	11.13 ± 1.27	11.23 ± 1.34	0.8095	32.80 ± 0.99	29.53 ± 1.64	0.0087
0.058	9.67 ± 0.74	9.80 ± 0.83	0.6177	33.98 ± 3.61	29.02 ± 4.08	0.0649
0.073	9.67 ± 1.16	9.75 ± 1.04	0.9360	36.32 ± 2.95	30.52 ± 1.99	0.0079
0.097	10.58 ± 2.35	10.75 ± 2.33	0.8092	40.90 ± 1.92	28.33 ± 2.57	0.0022
0.145	12.2 ± 2.56	11.95 ± 2.49	0.6879	53.23 ± 9.46	29.40 ± 3.31	0.0286
0.290	11.78 ± 1.95	11.13 ± 1.61	0.7483	49.37± 8.71	30.16 ± 2.54	0.0022

In order to explore the cause of the aPTT prolongation, PPP treated with the higher concentration of DMSA-PEG-$(NH_2)_2$ bioferrofluids (0.29 g/L Fe) were used for further studies, such as a) mixture test, in which PPP treated with theses bioferrofluids were mixed with normal plasma (1:1), aPTT measurements showed normal aPTT value 33.40 ± 1.73 s compared to its control value 29.33 ± 2.60 s (*n*=3), b) TT

measurements, results showed normal value of TT 28.37 ± 1.59 s compared to its control value 24.03 ± 0.50 s (*n*=3) (TT reference limits is 15-28 s.).

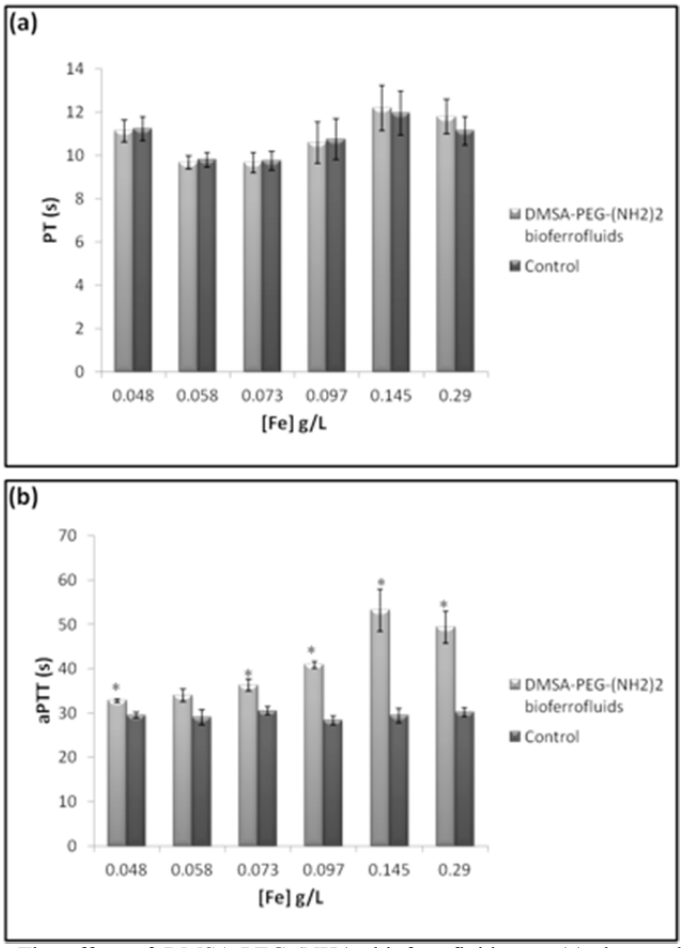

Figure 4.12: The effect of DMSA-PEG-$(NH_2)_2$ bioferrofluids on: (a) the prothrombin time, (b) the activated partial thromboplastin time, in seconds. Values represent mean ± SEM (*n*=6), (*) marks significant differences between DMSA-PEG-$(NH_2)_2$ bioferrofluids and control.

A comparison between DMSA-PEG-$(NH_2)_2$ bioferrofluids, DMSA bioferrofluids and P4VP-g-APEG bioferrofluids on their effect on PT and aPTT is shown in Fig. 4.13 and data summarised in Table 4.7. In the case of PT, a significant difference between test and control values appears in some concentrations. These values are within our laboratory normal reference range (9-14 s). In the case of aPTT, however, the aPTT values for plasma treated with DMSA-PEG-$(NH_2)_2$ bioferrofluids or P4VP-g-APEG bioferrofluids at concentrations 0.05, 0.06 and 0.07 g/L Fe, are significantly

different to the control values, they are within our laboratory normal reference range (23-37 s), In contrast, the aPTT value for plasma treated with DMSA bioferrofluids at these concentrations (0.05, 0.06 and 0.07 g/L Fe) is significantly different than the control and out of laboratory normal reference range.

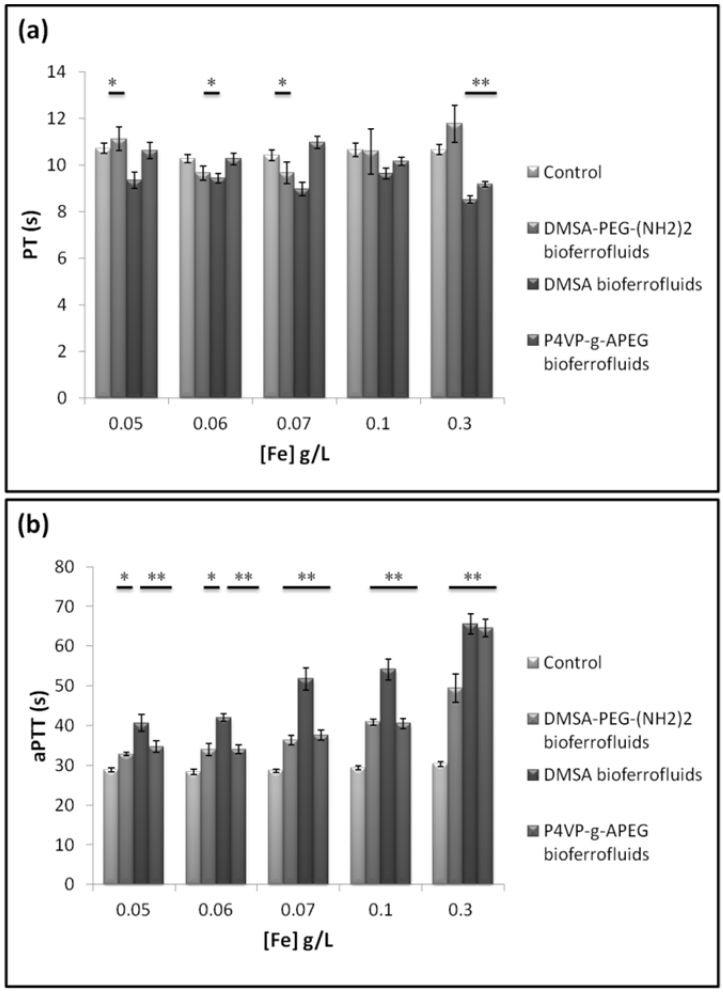

Figure 4.13: The effect of DMSA-PEG-$(NH_2)_2$ bioferrofluids, DMSA bioferrofluids and P4VP-g-APEG bioferrofluids on: (a) the prothrombin time, (b) the activated partial thromboplastin time, in seconds. Values represent mean ± SEM, (* and **) marks significant differences (>0.0001 and <0.0001 respectively) between bioferrofluids and control.

Table 4.7: Statistical analysis data for the effect of DMSA-PEG-$(NH_2)_2$ bioferrofluids, DMSA bioferrofluids and P4VP-g-APEG bioferrofluids on PT and aPTT, the number of samples was 22, 6, 6 and 10 for control, DMSA-PEG-$(NH_2)_2$ bioferrofluids, DMSA bioferrofluids and P4VP-g-APEG bioferrofluids, respectively.

PT Mean ± SD (s)							
Conc. g/L	Control	DMSA-PEG-$(NH_2)_2$ bioferrofluids	Unpaired t-test	DMSA bioferrofluids	Unpaired t-test	P4VP-g-PEG bioferrofluids	Unpaired t-test
0.05	10.70±1.04	11.13 ± 1.27	0.4264	9.35 ± 0.87	0.0066	10.60 ± 1.07	0.8104
0.06	10.30±0.78	9.67 ± 0.74	0.0974	9.43 ± 0.49	0.0192	10.30 ± 0.76	0.9685
0.07	10.40±1.05	9.67 ± 1.16	0.1416	8.97 ± 0.72	0.0041	11.00 ± 0.82	0.1545
0.1	10.70±1.37	10.58 ± 2.35	0.9241	9.64 ± 0.55	0.1218	10.20 ± 0.55	0.2837
0.3	10.70±0.97	11.78 ± 1.95	0.0578	8.52 ± 0.40	<0.0001	9.20 ± 0.40	<0.0001
aPTT Mean ± SD (s)							
Conc. g/L	Control	DMSA-PEG-$(NH_2)_2$ bioferrofluids	Unpaired t-test	DMSA bioferrofluids	Unpaired t-test	P4VP-g-PEG bioferrofluids	Unpaired t-test
0.05	28.90±2.89	32.80 ± 0.99	0.0004	40.66 ±5.23	<0.0001	34.70 ± 4.52	<0.0001
0.06	28.30±3.23	33.98 ± 3.61	0.001	41.97 ± 2.29	<0.0001	34.00 ± 3.51	<0.0001
0.07	28.60±2.03	36.32 ± 2.95	<0.0001	51.74 ± 7.00	<0.0001	37.60 ± 3.88	<0.0001
0.1	29.40±2.68	40.90 ± 1.92	<0.0001	54.15 ± 6.46	<0.0001	40.50 ± 4.07	<0.0001
0.3	30.30±2.55	49.37 ± 8.71	<0.0001	65.58 ± 6.13	<0.0001	64.60 ± 7.21	<0.0001

4.4.3.5 PPP treated with DMSA and PEG-$(NH_2)_2$

The DMSA and PEG-$(NH_2)_2$ blank samples used in this work were prepared under the same conditions and concentrations applied for DMSA bioferrofluids and DMSA-PEG-$(NH_2)_2$ bioferrofluids preparations. PPP was mixed with different concentrations (0.01 and 0.1 g/L) of DMSA. Results show no significance difference with respect to those obtained in PT and aPTT, as shown in Fig. 4.14. Data are summerised in Table 4.8.

PT and aPTT results did not show any significance difference between PPP mixed with different concentrations (0.01 and 0.1 g/L) of PEG-$(NH_2)_2$ and control, results are shown in Fig. 4.15, while the statistical analysis data are summarised in Table 4.9.

Table 4.8: Statistical analysis data for the effect of DMSA on PT and aPTT, the number of samples was 6 for each concentration, the original DMSA concentration was 1 g/L.

Conc. g/L	PT Mean ± SD (s)		P (Mann-Whitney)	aPTT Mean ± SD (s)		P (Mann-Whitney)
	Test	Control		Test	Control	
0.01	10.97 ± 1.19	11.00 ± 1.11	1.0000	28.38 ± 1.68	28.43 ± 1.82	1.0000
0.10	11.25 ± 0.78	10.78 ± 0.74	0.2946	29.95 ± 3.10	30.00 ± 3.45	0.8726

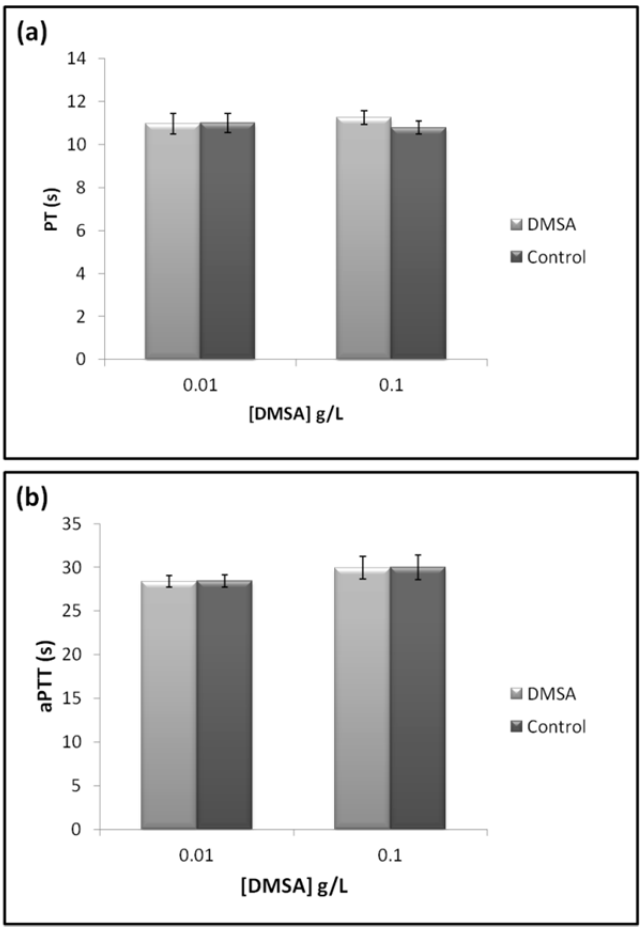

Figure 4.14: The effect of DMSA on: (a) the prothrombin time, (b) the activated partial thromboplastin time, in seconds. Values represent mean ± SEM (*n*=6).

Table 4.9: Statistical analysis data for the effect of PEG-$(NH_2)_2$ on PT and aPTT, the number of samples was 6 for each concentration, the original PEG-$(NH_2)_2$ concentration was 1 g/L.

Conc. g/L	PT Mean ± SD (s)		P (Mann-Whitney)	aPTT Mean ± SD (s)		P (Mann-Whitney)
	Test	Control		Test	Control	
0.01	11.15± 1.12	11.08 ± 1.11	0.8721	29.97 ± 1.70	30.22 ± 2.39	1.0000
0.10	11.22 ± 0.90	10.78 ± 0.74	0.4217	28.10 ± 3.20	30.00 ± 3.45	0.3939

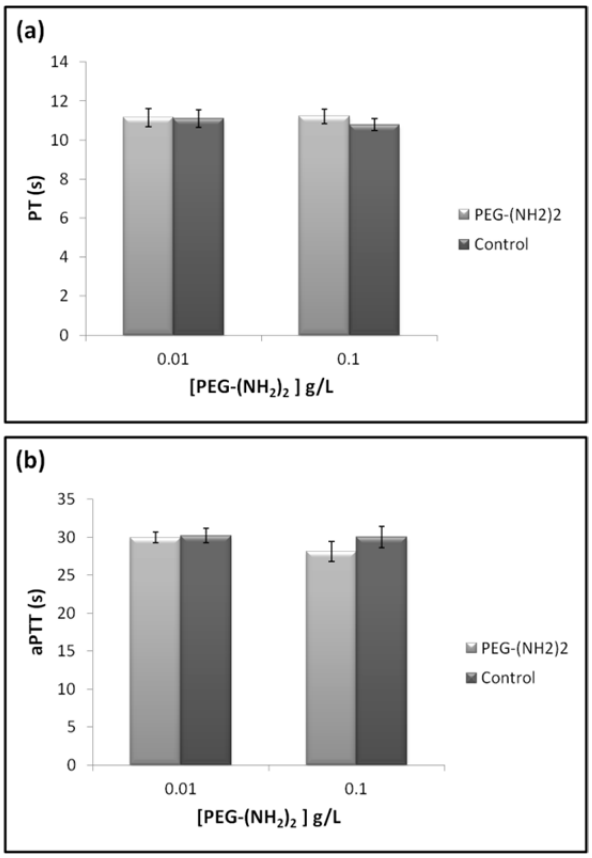

Figure 4.15: The effect of PEG-$(NH_2)_2$ on: (a) the prothrombin time, (b) the activated partial thromboplastin time, in seconds. Values represent mean ± SEM (*n*=6).

4.4.4 Complete blood counts studies

4.4.4.1 Blood treated with P4VP-g-APEG bioferrofluids

Whole blood was treated with different concentrations (0.07 and 0.7 g/L Fe_2O_3) of P4VP-g-APEG bioferrofluids, and processed for CBC measurements. No significant differences were detected in CBC between control and treated blood with P4VP-g-

APEG bioferrofluids in both concentrations, as well as no significant difference in haemoglobin and haematocrit were either observed. The spectrophotometric study of haemoglobin in plasma demonstrates the absence of haemolysis for concentration 0.07 g/L Fe_2O_3. For a concentration of 0.7 g/L Fe_2O_3, the high concentration of particles interfere the spectrophotometric measurements; however, naked eye inspection does not indicate haemolysis. Altogether these data show the safety of nanoparticles in relation to erythrocytes. Platelets and leukocytes do not show significant differences between the control sample and the two concentrations tested, neither the instrument shows flags indicating morphologic alterations and aggregates in any of the studied cell series, demonstrating the safety of nanoparticles on these two cell lines. The only haematological abnormality is in the coagulation tests, with an unexpected increase of aPTT, discussed in detail later. Statistical analysis data are summarised in Table 4.10 and results are shown in Fig. 4.16.

Table 4.10: Statistical analysis data for the effect of P4VP-g-APEG bioferrofluids on CBC, the number of samples was 4 for each concentration, the original P4VP-g-APEG bioferrofluids concentration was 7.78 g/L [Fe_2O_3].

P4VP-g-APEG bioferrofluids			
Conc. g/L	CBC Mean ± SD		P (Mann-Whitney)
	Test	Control	
Erythrocytes (10^6/µL)			
0.07	4.69 ± 0.36	4.61 ± 0.30	0.77
0.7	4.65 ± 0.31	4.66 ± 0.27	>0.99
Leukocytes (10^3/µL)			
0.07	6.79 ± 2.21	6.88 ± 2.21	0.77
0.7	6.13 ± 2.28	6.28 ± 2.20	>0.99
Platelets (10^3/µL)			
0.07	176.25 ± 34.72	180.25 ± 34.22	0.77
0.7	180.95 ± 26.48	193.50 ± 25.72	0.38
Haemoglobin (g/dL)			
0.07	14.39 ± 1.04	14.23 ± 0.91	0.88
0.7	14.22 ± 1.13	14.00 ± 0.95	0.56
Haematocrit (%)			
0.07	42.70 ± 2.09	41.80 ± 1.32	0.38
0.7	40.92 ± 2.97	40.68 ± 1.81	0.77

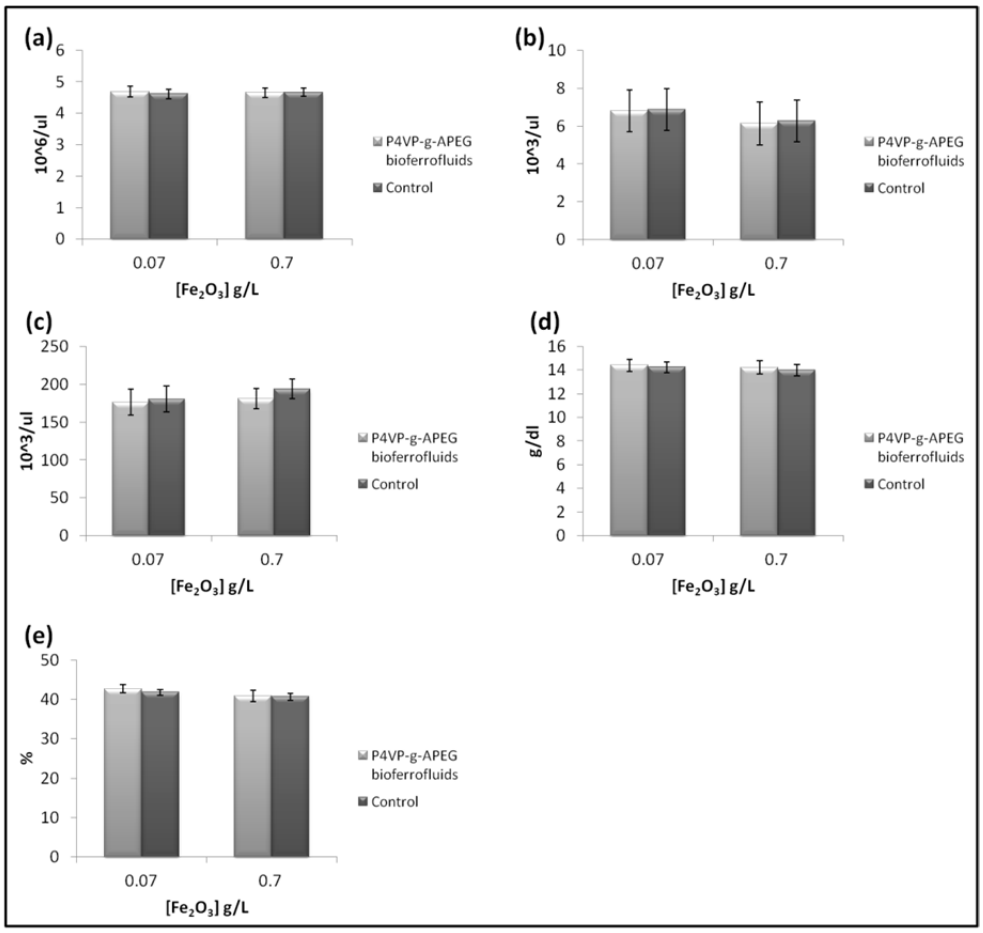

Figure 4.16: The effect of P4VP-g-APEG bioferrofluids on: (a) Erythrocytes, (b) Leukocytes, (c) Platelets, (d) Haemoglobin and (e) Haematocrit. Values represent mean ± SEM (*n*=4).

4.4.4.2 Blood treated with APEG and with P4VP-g-APEG

The CBC (erythrocytes, leukocytes, platelets, Haemoglobin and Haematocrit), corresponding to blood treated with APEG shows a minor difference with control sample only for erythrocytes, haemoglobin and haematocrit at concentration 0.13 g/L (P = 0.04). The CBC corresponding to blood treated with P4VP-g-APEG at concentrations 0.13 and 1.33 g/L did not show in either case significant difference from control blood. The results are shown in Figs. 4.17 and 4.18, while statistical analysis data are shown in Table 4.11.

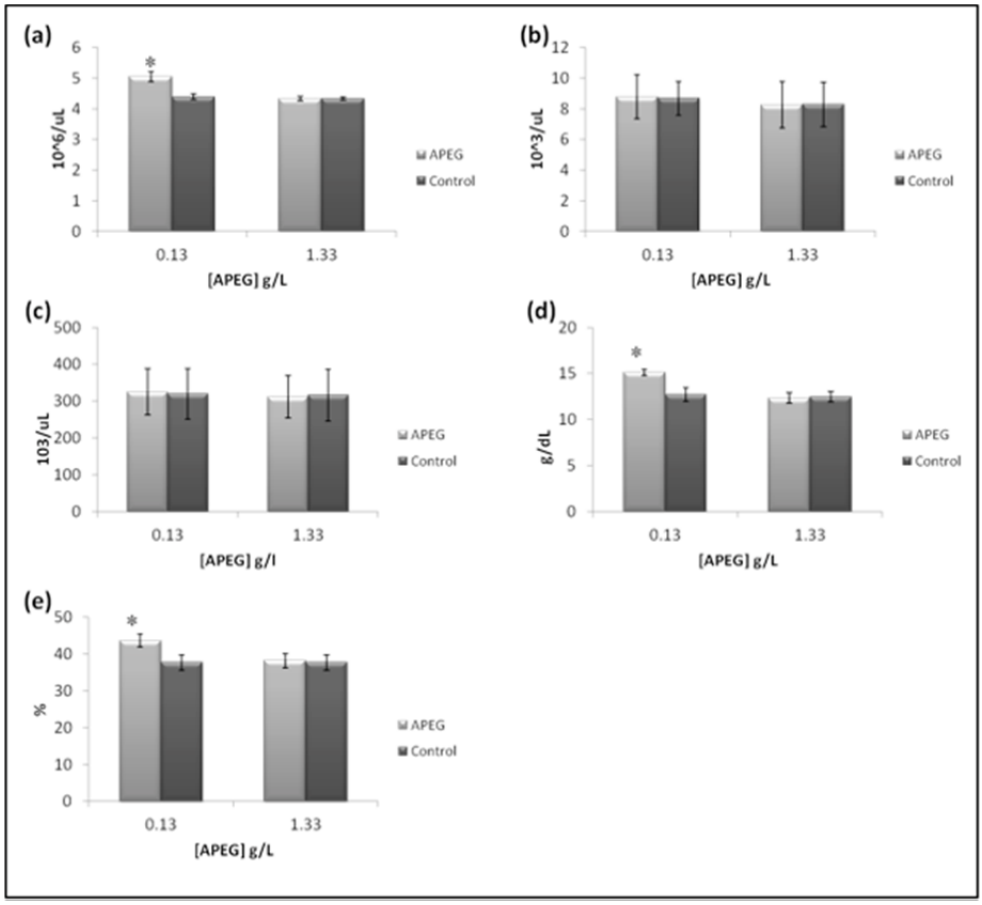

Figure 4.17: The effect of APEG on: (a) Erythrocytes, (b) Leukocytes, (c) Platelets, (d) Haemoglobin and (e) Haematocrit. Values represent mean ± SEM (*n*=3), (*) marks significant differences between APEG and control.

Table 4.11: Statistical analysis data for the effect of APEG and P4VP-g-APEG on CBC, the number of samples was 3 for each concentration, the original APEG and P4VP-g-APEG concentration was 13.36 g/L.

	APEG			P4VP-g-APEG		
Conc. g/L	CBC Mean ± SD		P (Mann-Whitney)	CBC Mean ± SD		P (Mann-Whitney)
	Test	Control		Test	Control	
Erythrocytes (10^6/µL)						
0.13	5.04 ± 0.28	4.38 ± 0.16	0.04	5.19 ± 0.44	4.96 ± 0.65	0.51
1.33	4.33 ± 0.12	4.33 ± 0.10	0.82	5.16 ± 0.41	5.11 ± 0.41	0.51
Leukocytes (10^3/µL)						
0.13	8.76 ± 2.52	8.67 ± 1.90	0.82	7.61 ± 1.99	7.43 ± 2.72	0.82
1.33	8.25 ± 2.63	8.27 ± 2.54	>0.99	5.50 ± 0.90	5.57 ± 0.83	0.51

Continue Table 4.11: Statistical analysis data for the effect of APEG and P4VP-g-APEG on CBC, the number of samples was 3 for each concentration, the original APEG and P4VP-g-APEG concentration was 13.36 g/L.

	APEG			P4VP-g-APEG		
Conc. g/L	CBC Mean ± SD		P (Mann-Whitney)	CBC Mean ± SD		P (Mann-Whitney)
	Test	Control		Test	Control	
Platelets (10^3/μL)						
0.13	324.50 ± 107.72	319.33 ±117.86	0.82	230.48 ± 46.71	228.80 ± 47.34	0.92
1.33	311.30 ± 98.58	316.00±121.52	0.82	229.24 ± 40.71	228.80 ± 47.34	0.83
Haemoglobin (g/dL)						
0.13	15.11 ± 0.61	12.70 ± 1.28	0.04	15.08 ± 0.99	14.93 ± 1.69	0.82
1.33	12.32 ± 0.98	12.43 ± 0.98	0.82	14.92 ± 1.40	15.07 ± 1.46	0.82
Haematocrit (%)						
0.13	43.71 ± 2.93	37.77 ± 3.62	0.04	47.47 ± 2.96	44.43 ± 4.25	0.27
1.33	38.28 ± 3.34	37.77 ± 3.62	0.51	45.72 ± 4.65	44.30 ± 4.48	0.51

4.4.4.3 Blood treated with DMSA bioferrofluids and with DMSA-PEG-$(NH_2)_2$ bioferrofluids

Whole blood was treated with different concentrations (0.05 and 0.1 g/L Fe) of DMSA bioferrofluids and DMSA PEG-$(NH_2)_2$ bioferrofluids, and processed for CBC measurements. The CBC (erythrocytes, leukocytes, platelets, haemoglobin and haematocrit) results did not show significant differences between control samples and blood treated with both bioferrofluids at both concentrations. Results are shown in Figs. 4.19 and 4.20, while statistical analysis data are summarised in Tables 4.12 and 4.13. No significant difference in haemoglobin and haematocrit were either observed. The spectrophotometric study of haemoglobin in plasma demonstrates the absence of haemolysis for both bioferrofluids at these concentrations (0.05 and 0.1 g/L Fe). Altogether these data show the safety of nanoparticles in relation to erythrocytes. Platelets and leukocytes do not show significant differences between the control sample and the two concentrations tested of both bioferrofluids neither the instrument shows flags indicating morphologic alterations and aggregates in any of the studied cell series, demonstrating the safety of nanoparticles on these two cell lines. Normal morphology of cells was also confirmed by optical microscope for stained blood films, as shown in Fig. 4.21.

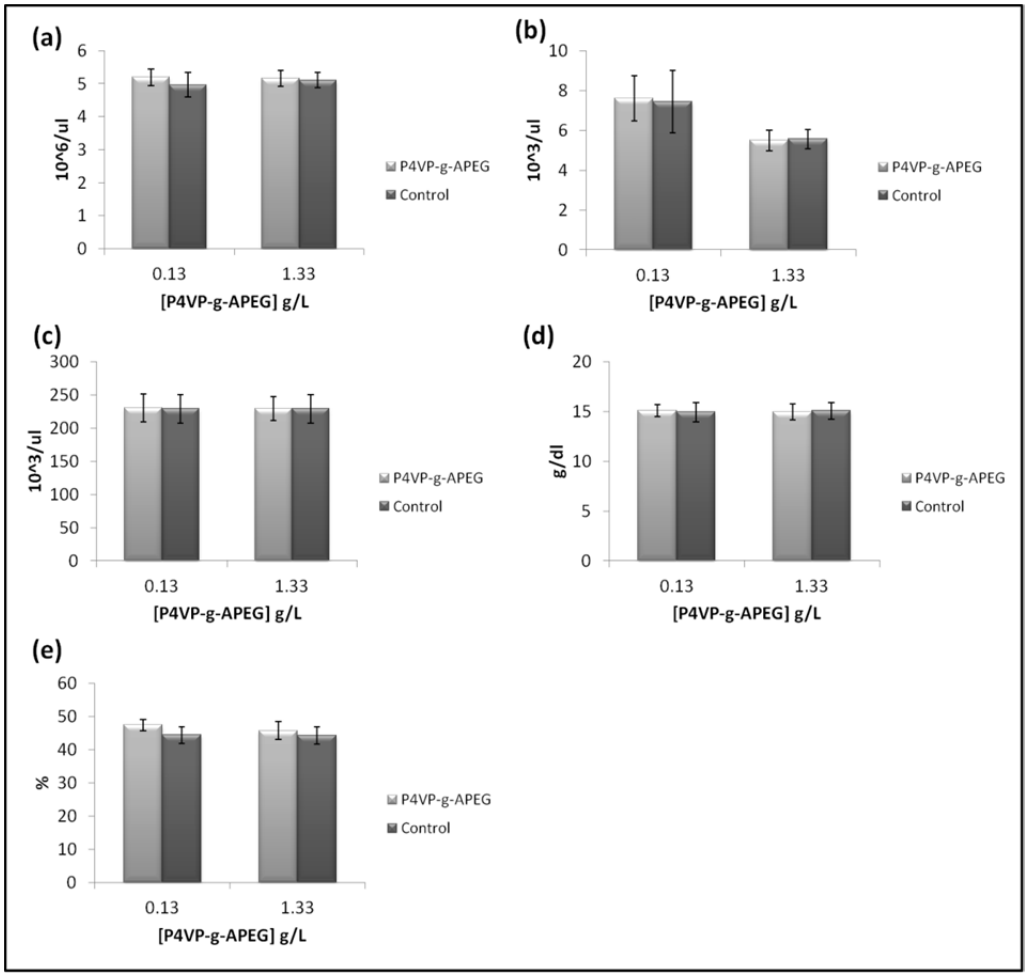

Figure 4.18: The effect of P4VP-g-APEG on: (a) Erythrocytes, (b) Leukocytes, (c) Platelets, (d) Haemoglobin and (e) Haematocrit. Values represent mean ± SEM (*n*=3).

Table 4.12: Statistical analysis data for the effect of DMSA bioferrofluids on CBC, the number of samples was 6 for each concentration, the original DMSA bioferrofluids concentration was 5.8 g/L Fe.

DMSA bioferrofluids			
Conc. g/L	CBC Mean ± SD		P (Mann-Whitney)
	Test	Control	
Erythrocytes (10^6/µL)			
0.05	4.87 ± 0.39	4.49 ± 0.33	0.2403
0.1	4.88 ± 0.36	4.49 ± 0.33	0.0649
Leukocytes (10^3/µL)			
0.05	6.77 ± 1.04	6.78 ± 0.99	0.9361
0.1	7.39 ± 0.94	6.78 ± 0.99	0.3776

Continue Table 4.12: Statistical analysis data for the effect of DMSA bioferrofluids on CBC, the number of samples was 6 for each concentration, the original DMSA bioferrofluids concentration was 5.8 g/L Fe.

DMSA bioferrofluids			
Conc. g/L	CBC Mean ± SD		P (Mann-Whitney)
	Test	Control	
Platelets (10^3/μL)			
0.05	213.50 ± 47.91	220.83 ± 42.08	0.5887
0.1	243.47 ± 42.59	220.83 ± 42.08	0.3939
Haemoglobin (g/dL)			
0.05	14.98 ± 1.03	13.58 ± 0.74	0.0651
0.1	14.70 ± 0.82	13.58 ± 0.74	0.0651
Haematocrit (%)			
0.05	44.29 ± 3.05	40.97 ± 2.57	0.5887
0.1	44.15 ± 2.52	40.97 ± 2.57	0.3939

Table 4.13: Statistical analysis data for the effect of DMSA PEG-$(NH_2)_2$ bioferrofluids on CBC, the number of samples was 6 for each concentration, the original DMSA PEG-$(NH_2)_2$ bioferrofluids concentration was 1 g/L Fe.

DMSA PEG-$(NH_2)_2$ bioferrofluids			
Conc. g/L	CBC Mean ± SD		P (Mann-Whitney)
	Test	Control	
Erythrocytes (10^6/μL)			
0.05	4.66 ± 0.44	4.64 ± 0.43	0.8182
0.1	4.64 ± 0.44	4.64 ± 0.43	0.9372
Leukocytes (10^3/μL)			
0.05	7.46 ± 1.44	7.40 ± 1.52	0.8182
0.1	7.21 ± 1.85	7.40 ± 1.52	1.0000
Platelets (10^3/μL)			
0.05	194.78 ± 39.96	205.00 ± 40.12	0.5887
0.1	195.07 ± 37.18	205.00 ± 40.12	0.5887
Haemoglobin (g/dL)			
0.05	14.30 ± 1.44	14.08 ± 1.44	0.3776
0.1	14.14 ± 1.39	14.08 ± 1.44	0.9361
Haematocrit (%)			
0.05	42.42 ± 3.77	42.07 ± 3.70	0.8182
0.1	42.11 ± 3.86	42.07 ± 3.70	1.000

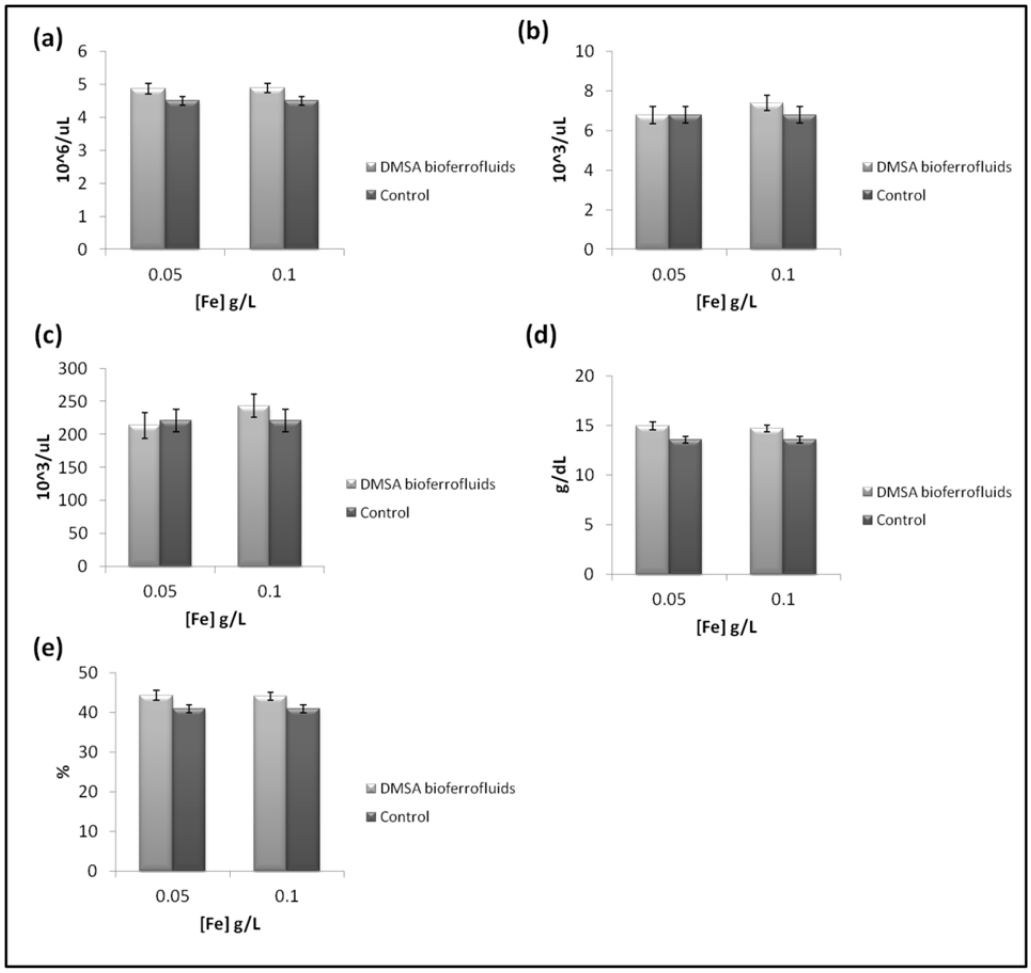

Figure 4.19: The effect of DMSA bioferrofluids on: (a) Erythrocytes, (b) Leukocytes, (c) Platelets, (d) Haemoglobin and (e) Haematocrit. Values represent mean ± SEM (*n*=6).

4.4.4.4 Blood treated with DMSA and with PEG-$(NH_2)_2$

Whole blood was treated with different concentrations (0.01 and 0.1 g/L) of DMSA and PEG-$(NH_2)_2$, and processed for CBC measurements. The CBC (erythrocytes, leukocytes, platelets, Haemoglobin and haematocrit) results did not show significant differences at both concentrations for blood treated with both materials and control. Results are shown in Figs. 4.22 and 4.23, while statistical analysis data are summarised in Tables 4.14 and 4.15

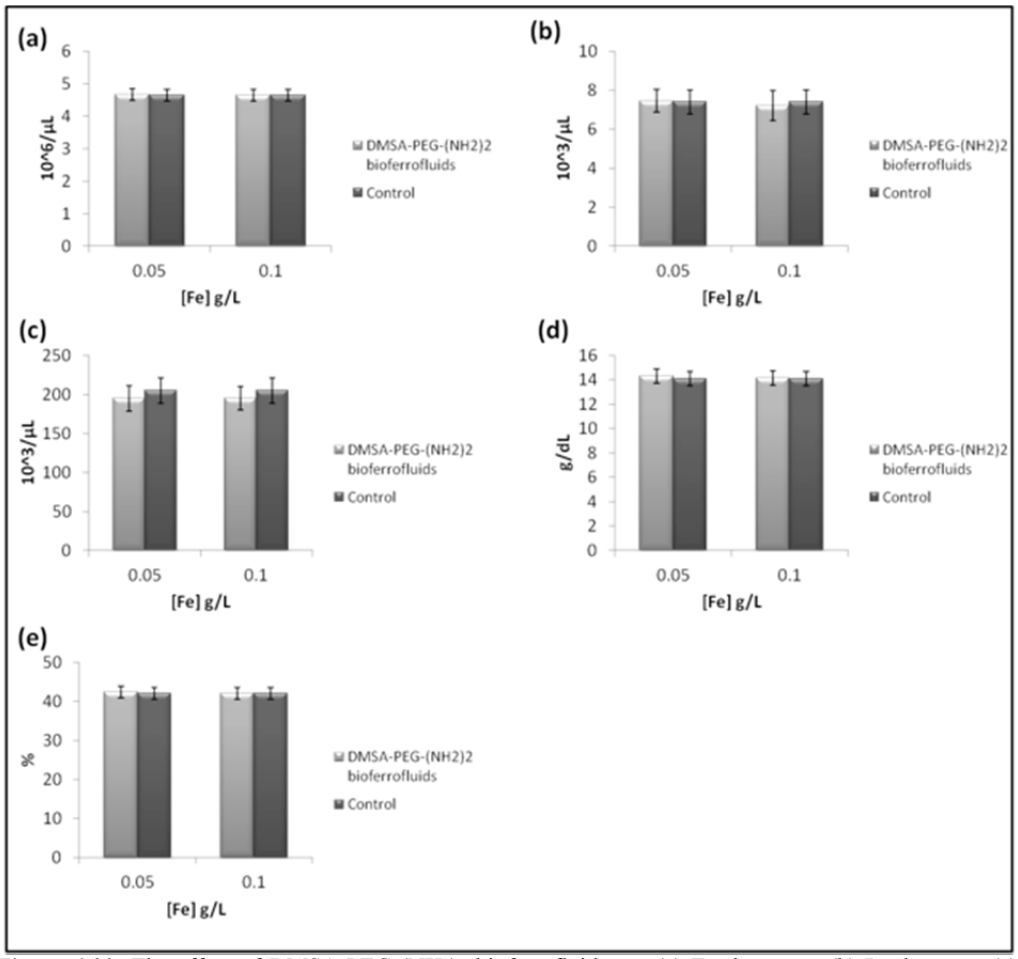

Figure 4.20: The effect of DMSA-PEG-$(NH_2)_2$ bioferrofluids on: (a) Erythrocytes, (b) Leukocytes, (c) Platelets, (d) Haemoglobin and (e) Haematocrit. Values represent mean ± SEM (*n*=6).

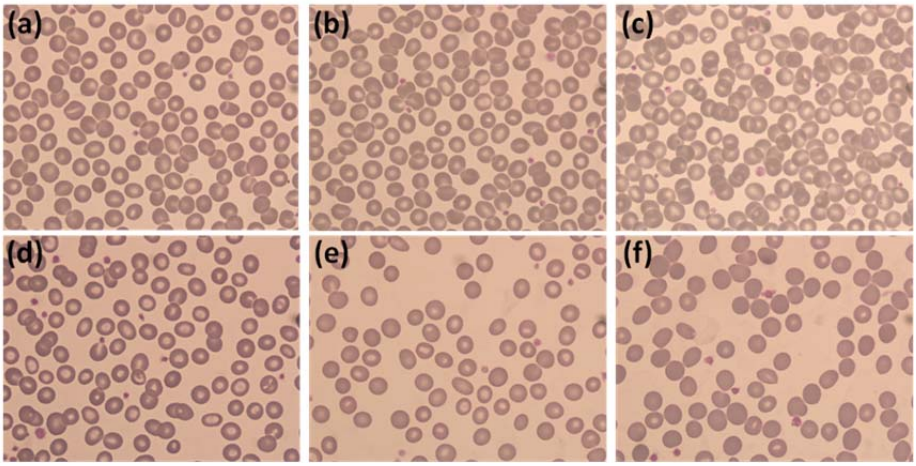

Figure 4.21: Stained films of untreated blood (a, b), and treated blood with DMSA bioferrofluids (upper panel) and DMSA-PEG-$(NH_2)_2$ bioferrofluids (lower panel) at concentrations 0.05 g/L Fe (b, e) and 0.1 g/L Fe (c, f).

Table 4.14: Statistical analysis data for the effect of DMSA on CBC, the number of samples was 4 for each concentration, the original DMSA concentration was 1 g/L.

DMSA			
Conc. g/L	CBC Mean ± SD		P (Mann-Whitney)
	Test	Control	
Erythrocytes (10^6/µL)			
0.01	4.38 ± 0.19	4.28 ± 0.22	0.4857
0.1	4.26 ± 0.15	4.28 ± 0.22	0.8857
Leukocytes (10^3/µL)			
0.01	7.02 ± 0.74	7.28 ± 0.39	0.6857
0.1	7.10 ± 0.43	7.28 ± 0.39	0.6857
Platelets (10^3/µL)			
0.01	248.71 ± 76.03	270.75 ± 76.57	0.4857
0.1	246.13 ± 69.07	270.75 ± 76.57	0.4857
Hemoglobin (g/dL)			
0.01	13.96 ± 0.73	13.33 ± 0.66	0.3429
0.1	13.56 ± 0.37	13.33 ± 0.66	0.5614
Hematocrit (%)			
0.01	41.18 ± 1.70	40.33 ± 1.72	0.3429
0.1	40.26 ± 1.04	40.33 ± 1.72	0.8857

Table 4.15: Statistical analysis data for the effect of PEG-$(NH_2)_2$ on CBC, the number of samples was 4 for each concentration, the original PEG-$(NH_2)_2$ concentration was 1 g/L.

PEG-$(NH_2)_2$			
Conc. g/L	CBC Mean ± SD		P (Mann-Whitney)
	Test	Control	
Erythrocytes (10^6/µL)			
0.01	4.99± 0.25	4.91 ± 0.26	0.4857
0.1	5.05 ± 1.76	4.91 ± 0.26	0.2000
Leukocytes (10^3/µL)			
0.01	6.44 ± 0.83	6.45 ± 0.70	0.8824
0.1	6.22 ± 0.56	6.45 ± 0.70	0.1832
Platelets (10^3/µL)			
0.01	206.04 ± 33.01	215.00 ± 26.41	0.6857
0.1	194.15± 24.96	215.00 ± 26.41	0.4857
Hemoglobin (g/dL)			
0.01	15.81 ± 1.40	15.53± 1.22	0.3094
0.1	15.98± 1.07	15.53± 1.22	0.4678
Hematocrit (%)			
0.01	46.66± 3.43	45.75± 3.56	0.4857
0.1	47.22± 2.71	45.75± 3.56	0.4857

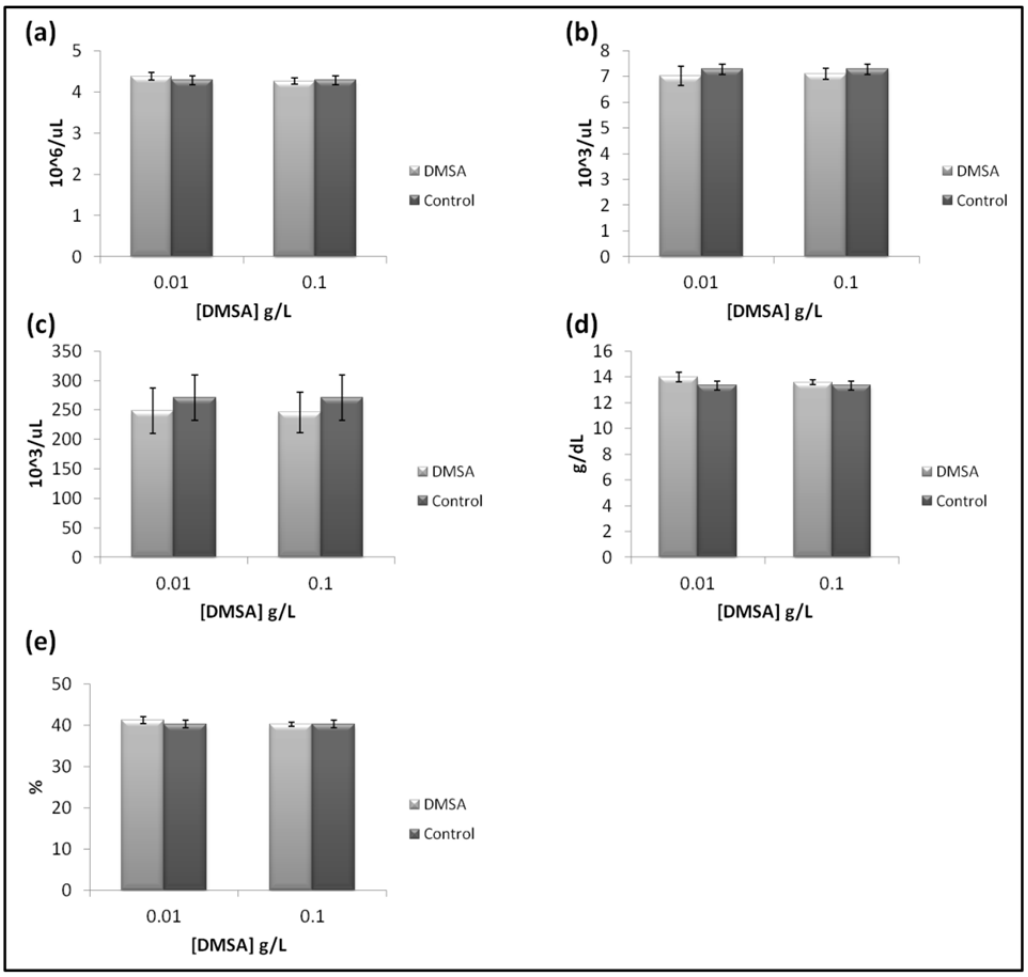

Figure 4.22: The effect of DMSA on: (a) Erythrocytes, (b) Leukocytes, (c) Platelets, (d) Haemoglobin and (e) Haematocrit. Values represent mean ± SEM (*n*=4).

4.4.5 Haemolysis studies

4.4.5.1 Blood treated with P4VP-g-APEG bioferrofluids

Whole blood treated with P4VP-g-APEG bioferrofluids at concentration 0.07 g/L Fe_2O_3 did not show any haemolytic effect observed with naked eyes. Spectrophotometric measurements did not show any peak referred to the free haemoglobin at wavelength 580 nm as shown in Fig. 4.24(b), in addition, the curve was concave (normal) consistent with its control shown in Fig. 4.24(a). This result is confirmed by the results obtained from CBC, where there is no significant decrease in erythrocytes, haemoglobin and haematocrit. However, this assay is not suitable for haemolysis detection at high concentration (0.7 g/L Fe_2O_3) of P4VP-g-APEG

bioferrofluids, since their high concentration could interfere with the spectrophotometric measurements.

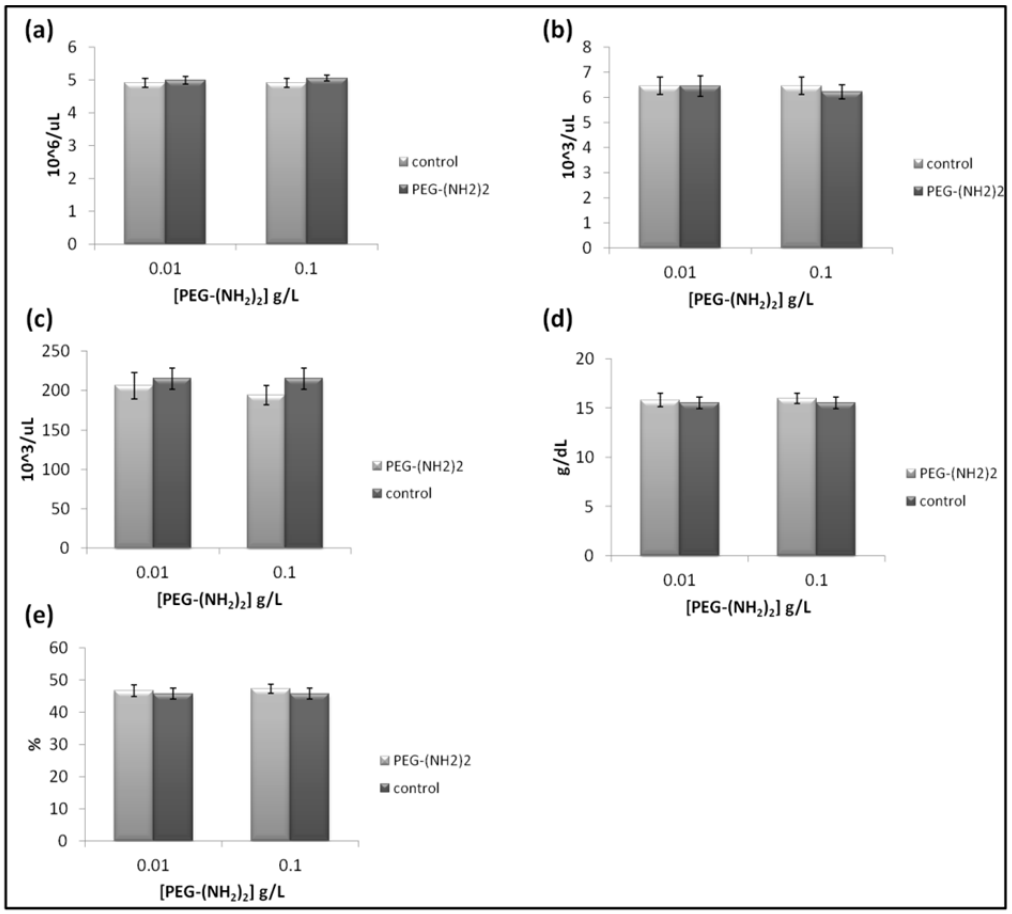

Figure 4.23: The effect of PEG-$(NH_2)_2$ on: (a) Erythrocytes, (b) Leukocytes, (c) Platelets, (d) Haemoglobin and (e) Haematocrit. Values represent mean ± SEM (*n*=4).

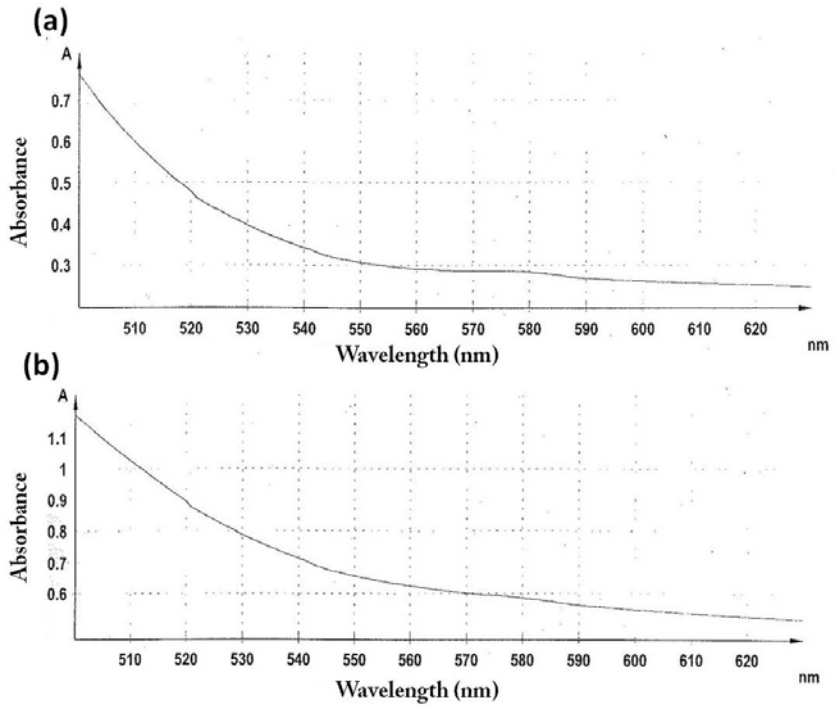

Figure 4.24: Haemolysis detection using spectrophotometer (a) control blood, (b) blood treated with P4VP-g-APEG bioferrofluids at concentration 0.07 g/L Fe_2O_3.

4.4.5.2 Blood treated with DMSA bioferrofluids and with DMSA PEG-$(NH_2)_2$ bioferrofluids

Whole blood was treated with different concentrations (0.05 and 0.1 g/L Fe) of DMSA bioferrofluids and DMSA PEG-$(NH_2)_2$ bioferrofluids, haemolysis results did not show any haemolytic effect observed with naked eyes. Spectrophotometric measurements did not show any peak referred to the free haemoglobin at wavelength 580 nm as shown in Figs. 4.25 and 4.26. These curves were concave, consistent with their control ones. This result is confirmed by the results obtained from CBC, where there is no significant decrease in erythrocytes, haemoglobin and haematocrit.

.

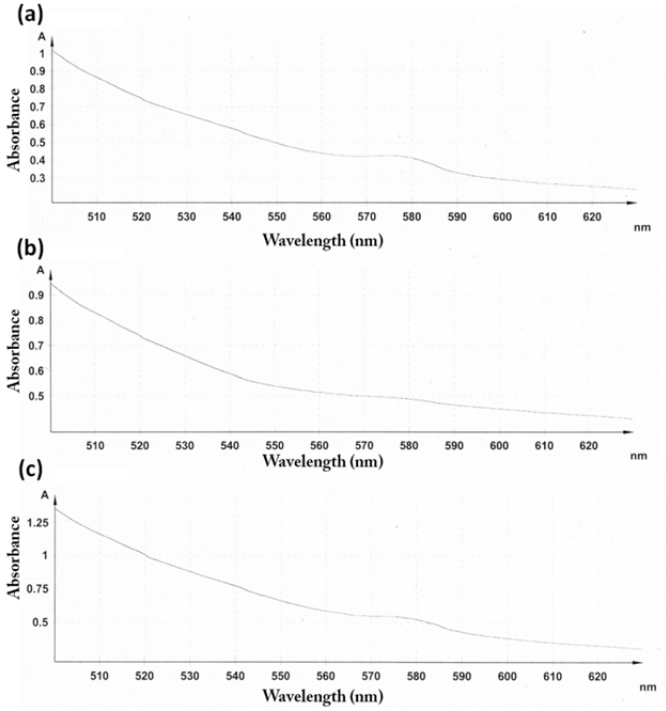

Figure 4.25: Haemolysis detection using spectrophotometer (a) blood control, (b) blood treated with DMSA bioferrofluids at concentration 0.05 g/L Fe and (c) blood treated with DMSA bioferrofluids at concentration 0.1 g/L.

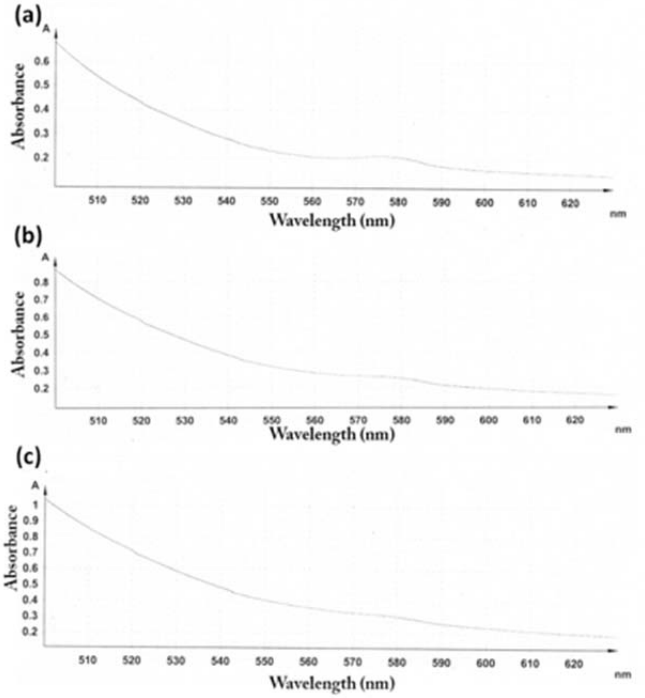

Figure 4.26: Haemolysis detection using spectrophotometer (a) blood control, (b) blood treated with DMSA-PEG-$(NH_2)_2$ bioferrofluids at concentration 0.05 g/L Fe and (c) blood treated with DMSA-PEG-$(NH_2)_2$ bioferrofluids at concentration 0.1 g/L Fe.

4.5 Discussion and conclusions

As explained above, the coagulation cascade is consisting of two pathways; the extrinsic and the intrinsic ones. The efficiency of these pathways is evaluated by measuring PT and aPTT respectively.

In general, a prolonged aPTT suggests either deficiency of one or more coagulation factors or the presence of an anticoagulant in plasma. The usual procedure to elucidate which of these two options is true is to mix the abnormal plasma with normal plasma to see if it corrects the prolongation of aPTT. If that happens, it indicates a deficiency of one or more haemostasis factors (normal plasma corrects the factor deficiency). The next step is to measure the activity of individual coagulation factors involved in the aPTT test. In the event that the normal plasma does not correct the aPTT, the most likely explanation is that an anticoagulant (which inhibits the normal factors) is present in the plasma. Then, it is important to find out if it is a specific or nonspecific anticoagulant with new tests, including the thrombin time and quantifying the activity of factors potentially affected by the anticoagulant at various dilutions.

In this study, it was evident that a prolongation of aPTT was associated with high concentration of P4VP-g-APEG bioferrofluids in plasma. To explore this behaviour, a mixture test was performed. Results showed no correction for the prolongation in aPTT (above 37 s), which indicates the presence of an anticoagulant in the plasma. In order to elucidate whether it is specific or nonspecific a thrombin time test was carried out. The TT value was normal and the activities of all clotting factors (VIII, IX, XI, XII) in the intrinsic pathway were equally decreased, thus indicating that inhibitory activity is non-specific. We therefore conclude that the P4VP-g-APEG bioferrofluid behaves as a non-specific anticoagulant *in vitro*. In one way, this behaviour is similar to that of heparin from the fact that it lengths the aPTT, although heparin has also a specific effect on antithrombin III. In fact, the degrees of aPTT lengthening are comparable in both cases and therefore well within the therapeutic range.

In order to gain insight into the origin of the anticoagulant effect of P4VP-g-APEG bioferrofluids we have studied the P4VP-g-APEG bioferrofluids components separately. The surface of the nanoparticles in the P4VP-g-APEG bioferrofluids is formed by 1/10 in weight of APEG long chains (MW=1000) ending on carboxylic groups and 9/10 of APEG short chains (MW=200) ending on hydroxyl groups (diagram 1). It seems that either component is not likely to be at the origin of aPTT lengthening, because a solution of these compounds in the same concentration as in the P4VP-g-APEG bioferrofluids does not show any effect on aPTT, as shown in Fig 4.9. The APEG hydrophilic chains are linked to the P4VP core by pyridine-acrylate bonds that generate a positive charge on the N atom of the pyridine, thus the resulting P4VP-g-APEG copolymer is polycationic and has a brush-like structure. This copolymer alone produced a strong aPTT lengthening (see Table 4.4), larger than the whole P4VP-g-APEG bioferrofluids, and must be the responsible for the anticoagulant effect. However, the mechanism of action is not clear. In fact, although their effects are comparable to those of heparin, the molecular structure is very different because heparin action is associated to the large presence of negatively charged groups such as sulfate, sulfonamide and carboxylic groups, whereas P4VP-g-APEG copolymer is positively charged. Our results are consistent with some studies [18,20]. For instance, Fernández-Pacheco et al. showed an anticoagulant effect caused by bioferrofluids [18]. The particle structure in this case was very different from ours as they consisted of a mixture of iron and iron oxide nanoparticles encapsulated in a carbon matrix. Although they share as a common feature the presence of carboxylic groups on the surface, this cannot cause of aPTT lengthening as inferred from APEG blank experiments. In another study carried out by Chouly et al. using magnetite dextran nanoparticles, their bioferrofluids (MD1) were similar to our P4VP-g-APEG bioferrofluids in terms of hydrodynamic diameter (75.4 ± 21 nm) and charge (0 mV), in addition they used similar concentrations (0.72 and 7.2 mM Fe). Their results show that these bioferrofluids did not provoke either haemolysis nor platelets aggregations, however, they induce an anticoagulant effect indicated by lengthening of aPTT, while TT values were normal. Authors illustrated the anticoagulant effect due to the particles affinity for blood phospholipids [20].

CBC studies for blood treated with P4VP-g-APEG bioferrofluids and its components (APEG, P4VP-g-APEG) did not show any prejudicial effect on erythrocytes, leukocytes, platelets, haemoglobin and haematocrit. No haemolytic action was detected upon blood treatment with P4VP-g-APEG bioferrofluids at concentration 0.07 g/L Fe_2O_3. These results are in agreement with other studies [20,58]. However, a haemolytic action was detected in some other studies [19].

In addition, in this work we explore the haemostatic behaviour of other two bioferrofluids; DMSA and DMSA PEG-$(NH_2)_2$ ones. These bioferrofluids are different than P4VP-g-APEG bioferrofluids, in terms of hydrodynamic size and charge, as the hydrodynamic diameters of their particles are smaller (22 and 27 nm, respectively, compared to 80 nm of P4VP-g-APEG nanoparticles) and they are negatively charged (-35 mV and -15 mV, respectively, compared to 0 mV of P4VP-g-APEG nanoparticles). The coagulation behaviour of DMSA and DMSA PEG-$(NH_2)_2$ bioferrofluids was similar to P4VP-g-APEG bioferrofluids, as a prolongation in aPTT was observed, as shown in Figs. 4.11 and 4.12. However, the effect was more pronounced in DMSA bioferrofluids than in DMSA PEG-$(NH_2)_2$ and P4VP-g-APEG ones at lower concentrations (see Table 4.7). To explore this behaviour, a mixture test was performed. Results showed correction for the prolongation in aPTT in plasma treated with DMSA bioferrofluids and DMSA PEG-$(NH_2)_2$ bioferrofluids, and in addition, the TT values were normal.

The difference in the anticoagulant behaviour between DMSA bioferrofluids and DMSA PEG-$(NH_2)_2$ bioferrofluids, motivated us to measure the PT and aPTT in PPP treated with DMSA or with PEG-$(NH_2)_2$. Results show that both components are not the cause of the aPTT lengthening associated with the bioferrofluids, as normal levels of PT and aPTT were detected, as shown in Figs. 4.14 and 4.15. Several studies showed the effect of coating on the nanomaterial behaviour in blood and it has been reported that PEGylated poly(N-isopropylacrylamide) nanoparticles are haemocompatible with insignificant toxicity respect to the non-PEGylated ones [7]. Similar results have been reported for poly(lactide-co-glycolide) acid [59]. Negatively charged surfaces are proposed to be a pro-coagulant. In contrast, in this work, negatively charged bioferrofluids have an anticoagulant effect. This could be

explained as a result of their small sizes (22 nm and 27 nm) that make them unable to act as coagulation activating surfaces, as explained by Cecilia et al. using negatively charged polystyrene particles of 24 nm size [60]. We hypothesised that the increase in the negative charge is the responsible factor for the decease of the anticoagulant effect associated with DMSA PEG-$(NH_2)_2$ bioferrofluids in compared with DMSA bioferrofluids.

CBC studies for blood treated with DMSA bioferrofluids and DMSA PEG-$(NH_2)_2$ bioferrofluids and their components (DMSA, PEG-$(NH_2)_2$) did not show any effect on erythrocytes, leukocytes, platelets, haemoglobin and haematocrit. In addition, no haemolytic action was detected upon blood treatment with these both bioferrofluids at concentrations 0.05 and 0.1 g/L [Fe].

Then, we can conclude that P4VP-g-APEG bioferrofluids, DMSA bioferrofluids and DMSA PEG-$(NH_2)_2$ bioferrofluids do not cause any pro-coagulant effect that would prevent them use in intravenous applications. On the contrary, they show an anticoagulant effect that is reflected on a lengthening of the aPTT. The anticoagulant effect of P4VP-g-APEG bioferrofluids is non-specific because it does not affect to the thrombin time and it reduces equally the activity of clotting factors (VIII, IX, XI, XII) in the intrinsic pathway. DMSA bioferrofluids and DMSA PEG-$(NH_2)_2$ bioferrofluids do not affect the TT and the studies of the coagulation factors is mandatory. Therefore, these three bioferrofluids act as circulating anticoagulant agents *in vitro*. APEG component does not seem to have any effect on the coagulation process. The coating copolymer P4VP-g-APEG shows strong anticoagulant behaviour indicating that P4VP is at the origin of the anticoagulant effect associated with P4VP-g-APEG bioferrofluids. DMSA and PEG-$(NH_2)_2$ components do not seem to have any effect on the coagulation process. Therefore, the difference in the anticoagulant response between DMSA bioferrofluids and DMSA PEG-$(NH_2)_2$ bioferrofluids seems to be related to the surface charge. P4VP-g-APEG bioferrofluids, DMSA bioferrofluids and DMSA PEG-$(NH_2)_2$ bioferrofluids, and their components (APEG, P4VP-g-APEG, DMSA and PEG-$(NH_2)_2$) have no effect on the CBC. No haemolytic effect on blood treated with these bioferrofluids was detected *in vitro*. Further experiments using small animals *in vivo* are required to assess the validity of these conclusions.

4.6 Reference

[1] P. A. Gentry, "Comparative aspects of blood coagulation.," *Vet J.*, vol. 168, no. 3, pp. 238–51, 2004.

[2] A. Gojova, B. Guo, R. S. Kota, J. C. Rutledge, I. M. Kennedy, and A. I. Barakat, "Induction of inflammation in vascular endothelial cells by metal oxide nanoparticles: effect of particle composition.," *Environ. Health Perspect.*, vol. 115, no. 3, pp. 403–9, 2007.

[3] G. M. Mutlu, D. Green, A. Bellmeyer, C. M. Baker, Z. Burgess, N. Rajamannan, J. W. Christman, N. Foiles, D. W. Kamp, A. J. Ghio, N. S. Chandel, D. A. Dean, J. I. Sznajder, and G. R. S. Budinger, "Ambient particulate matter accelerates coagulation via an IL-6-dependent pathway.," *J. Clin. Invest.*, vol. 117, no. 10, pp. 2952–61, 2007.

[4] H. Schulz, V. Harder, A. Ibald-Mulli, A. Khandoga, W. Koenig, F. Krombach, R. Radykewicz, A. Stampfl, B. Thorand, and A. Peters, "Cardiovascular effects of fine and ultrafine particles.," *J. Aerosol Med.*, vol. 18, no. 1, pp. 1–22, 2005.

[5] A. Radomski, P. Jurasz, D. Alonso-Escolano, M. Drews, M. Morandi, T. Malinski, and M. W. Radomski, "Nanoparticle-induced platelet aggregation and vascular thrombosis.," *Br. J. Pharmacol.*, vol. 146, no. 6, pp. 882–93, 2005.

[6] A. Mayer, M. Vadon, B. Rinner, A. Novak, R. Wintersteiger, and E. Fröhlich, "The role of nanoparticle size in hemocompatibility.," *Toxicology*, vol. 258, no. 2–3, pp. 139–47, 2009.

[7] N. Gulati, R. Rastogi, A. K. Dinda, R. Saxena, and V. Koul, "Characterization and cell material interactions of PEGylated PNIPAAM nanoparticles.," *Colloids Surf. B. Biointerfaces*, vol. 79, no. 1, pp. 164–73, 2010.

[8] D. Simberg, W.-M. Zhang, S. Merkulov, K. McCrae, J.-H. Park, M. J. Sailor, and E. Ruoslahti, "Contact activation of kallikrein-kinin system by superparamagnetic iron oxide nanoparticles in vitro and in vivo.," *J Control Release.*, vol. 140, no. 3, pp. 301–5, 2009.

[9] M. O. Oyewumi, R. A. Yokel, M. Jay, T. Coakley, and R. J. Mumper, "Comparison of cell uptake, biodistribution and tumor retention of folate-coated and PEG-coated gadolinium nanoparticles in tumor-bearing mice.," *J. Control. Release*, vol. 95, no. 3, pp. 613–26, 2004.

[10] B. Balakrishnan, D. S. Kumar, Y. Yoshida, and A. Jayakrishnan, "Chemical modification of poly(vinyl chloride) resin using poly(ethylene glycol) to improve blood compatibility.," *Biomaterials*, vol. 26, no. 17, pp. 3495–502, 2005.

[11] T. a Ostomel, Q. Shi, P. K. Stoimenov, and G. D. Stucky, "Metal oxide surface charge mediated hemostasis.," *Langmuir*, vol. 23, no. 22, pp. 11233–8, 2007.

[12] A. a. Rugal, V. M. Gun'ko, V. N. Barvinchenko, V. V. Turov, T. V. Semeshkina, and V. I. Zarko, "Interaction of fibrinogen with nanosilica," *Cent. Eur. J. Chem.*, vol. 5, no. 1, pp. 32–54, 2007.

[13] A. M. van den Besselaar, J. Neuteboom, J. Meeuwisse-Braun, and R. M. Bertina, "Preparation of lyophilized partial thromboplastin time reagent composed of synthetic phospholipids: usefulness for monitoring heparin therapy.," *Clin. Chem.*, vol. 43, no. 7, pp. 1215–22, 1997.

[14] S.-Q. Li, R.-R. Zhu, H. Zhu, M. Xue, X.-Y. Sun, S.-D. Yao, and S.-L. Wang, "Nanotoxicity of TiO(2) nanoparticles to erythrocyte in vitro.," *Food Chem Toxicol.*, vol. 46, no. 12, pp. 3626–31, 2008.

[15] N. Singh, G. J. S. Jenkins, R. Asadi, and S. H. Doak, "Potential toxicity of superparamagnetic iron oxide nanoparticles (SPION)," *Nano Rev.*, vol. 1, pp. 1–15, 2010.

[16] B. W. Neun and M. A. Dobrovolskaia, "Method for in vitro analysis of nanoparticle thrombogenic properties.," *Methods Mol Biol.* , vol. 697, pp. 225–35, 2011.

[17] M.-T. Zhu, W.-Y. Feng, B. Wang, T.-C. Wang, Y.-Q. Gu, M. Wang, Y. Wang, H. Ouyang, Y.-L. Zhao, and Z.-F. Chai, "Comparative study of pulmonary responses to nano- and submicron-sized ferric oxide in rats.," *Toxicology*, vol. 247, no. 2–3, pp. 102–11, 2008.

[18] R. FERNANDEZPACHECO, C. MARQUINA, J. GABRIELVALDIVIA, M. GUTIERREZ, M. SOLEDADROMERO, R. CORNUDELLA, A. LABORDA, A. VILORIA, T. HIGUERA, and A. GARCIA, "Magnetic nanoparticles for local drug delivery using magnetic implants," *J Magn Magn Mater*, vol. 311, no. 1, pp. 318–322, 2007.

[19] B. L. Razzaboni and P. Bolsaitis, "Evidence of an oxidative mechanism for the hemolytic activity of silica particles.," *Environ. Health Perspect.*, vol. 87, pp. 337–41, 1990.

[20] C. Chouly, L. Bordenave, R. Bareille, V. Guerin, A. Baquey, D. Pouliquen, C. Baquey, and P. Jallet, "In vitro study of the hemocompatibility of superparamagnetic contrast agent for magnetic resonance imaging.," *Clin. Mater.*, vol. 15, no. 4, pp. 293–301, 1994.

[21] M. a Dobrovolskaia, J. D. Clogston, B. W. Neun, J. B. Hall, A. K. Patri, and S. E. McNeil, "Method for analysis of nanoparticle hemolytic properties in vitro.," *Nano Lett.*, vol. 8, no. 8, pp. 2180–7, 2008.

[22] A.K Patri, M.A Dobrovolskaia, S.T Stern, S.E McNeil. Preclinical Characterization of Engineered Nanoparticles Intended for Cancer Therapeutics. In: Amiji MM, ed. Nanotechnology for Cancer Therapy."

[23] E. W. Davie and O. D. Ratnnoff, "Waterfall sequence for intrinsic blood clotting.," *Science*, vol. 145, no. 3638, pp. 1310–2, Sep. 1964.

[24] R. G. Macfarlane, "An enzyme cascade in the blood clotting mechanism, and its function as a biochemical amplifier.," *Nature*, vol. 202, pp. 498–9, 1964.

[25] E. W. Davie, "A brief historical review of the waterfall/cascade of blood coagulation.," *J. Biol. Chem.*, vol. 278, no. 51, pp. 50819–32, 2003.

[26] E. W. Davie, K. Fujikawa, and W. Kisiel, "The coagulation cascade: initiation, maintenance, and regulation.," *Biochemistry*, vol. 30, no. 43, pp. 10363–70, 1991.

[27] M. Hoffman, D. M. Monroe, and H. R. Roberts, "Cellular interactions in hemostasis.," *Haemostasis*, vol. 26 Suppl 1, pp. 12–6, 1996.

[28] T. J. Hornyak and J. A. Shafer, "Interactions of factor XIII with fibrin as substrate and cofactor.," *Biochemistry*, vol. 31, no. 2, pp. 423–9, 1992.

[29] K. Kottke-Marchant, J. B. Lefkowitz. Chapter 1 -Coagulation Pathway and Physiology. *An Algorithmic Approach to Hemostasis Testing*, 2008

[30] K. a Tanaka, N. S. Key, and J. H. Levy, "Blood coagulation: hemostasis and thrombin regulation.," *Anesth. Analg.*, vol. 108, no. 5, pp. 1433–46, 2009.

[31] Y. T. Wachtfogel, R. A. DeLa Cadena, and R. W. Colman, "Structural biology, cellular interactions and pathophysiology of the contact system.," *Thromb. Res.*, vol. 72, no. 1, pp. 1–21, 1993.

[32] P. H. Bolton-Maggs, B. Young Wan-Yin, A. H. McCraw, J. Slack, and P. B. Kernoff, "Inheritance and bleeding in factor XI deficiency.," *Br. J. Haematol.*, vol. 69, no. 4, pp. 521–8, 1988.

[33] C. S. Kitchens, "The contact system.," *Arch. Pathol. Lab. Med.*, vol. 126, no. 11, pp. 1382–6, 2002.

[34] R. L. Bick and G. Murano, "Physiology of hemostasis.," *Clin. Lab. Med.*, vol. 14, no. 4, pp. 677–707, 1994.

[35] http://medicalstate.tumblr.com/post/4535755510/fibrin-clot-fibrinogen-typically-a-soluble.

[36] B. A. Lwaleed and P. S. Bass, "Tissue factor pathway inhibitor: structure, biology and involvement in disease.," *J. Pathol.*, vol. 208, no. 3, pp. 327–39, 2006.

[37] R. J. Baugh, G. J. Broze, and S. Krishnaswamy, "Regulation of extrinsic pathway factor Xa formation by tissue factor pathway inhibitor.," *J. Biol. Chem.*, vol. 273, no. 8, pp. 4378–86, 1998.

[38] G. Lu, G. J. Broze, and S. Krishnaswamy, "Formation of factors IXa and Xa by the extrinsic pathway: differential regulation by tissue factor pathway inhibitor and antithrombin III.," *J. Biol. Chem.*, vol. 279, no. 17, pp. 17241–9, 2004.

[39] B. Dahlbäck, “Blood coagulation.,” *Lancet*, vol. 355, no. 9215, pp. 1627–32, 2000.

[40] J. J. Emeis, “Regulation of the acute release of tissue-type plasminogen activator from the endothelium by coagulation activation products.,” *Ann. N. Y. Acad. Sci.*, vol. 667, pp. 249–58, 1992.

[41] C. A. Owen, Tests of blood, plasma, and platelets. In: Nichols WL, Bowie EJW, eds. *A history of blood coagulation*. Rochester, MN: Mayo Clinic Foundation, 2001:214–5.

[42] J. H. Levy, K. A. Tanaka, and W. Dietrich, “Perioperative hemostatic management of patients treated with vitamin K antagonists.,” *Anesthesiology*, vol. 109, no. 5, pp. 918–26, Nov. 2008.

[43] A. Tripodi, V. Chantarangkul, M. Primignani, F. Fabris, A. Dell’Era, C. Sei, and P. M. Mannucci, “The international normalized ratio calibrated for cirrhosis (INR(liver)) normalizes prothrombin time results for model for end-stage liver disease calculation.,” *Hepatology*, vol. 46, no. 2, pp. 520–7, 2007.

[44] G. C. White, “The partial thromboplastin time: defining an era in coagulation.,” *J. Thromb. Haemost.*, vol. 1, no. 11, pp. 2267–70, 2003.

[45] H. Bounameaux, G. A. Marbet, B. Lämmle, R. Eichlisberger, and F. Duckert, “Monitoring of heparin treatment. Comparison of thrombin time, activated partial thromboplastin time, and plasma heparin concentration, and analysis of the behavior of antithrombin III.,” *Am. J. Clin. Pathol.*, vol. 74, no. 1, pp. 68–73, 1980.

[46] W. M. Butler and P. E. Baldwin, “Prolongation of thrombin and reptilase times in patients with amyloidosis and acquired factor X deficiency.,” *South. Med. J.*, vol. 77, no. 5, pp. 648–51, 1984.

[47] S. Gandrille, M. H. Jouvin, P. Toulon, P. Remy, J. N. Fiessinger, M. Roncato, N. Moatti, and M. Aiach, “A study of fibrinogen and fibrinolysis in 10 adults with nephrotic syndrome.,” *Thromb. Haemost.*, vol. 59, no. 3, pp. 445–50, 1988.

[48] G. D. O. Lowe, A. Rumley, and I. J. Mackie, “Plasma fibrinogen.,” *Ann. Clin. Biochem.*, vol. 41, no. Pt 6, pp. 430–40, 2004.

[49] G. Palareti and M. Maccaferri, “Specific assays of hemostasis proteins: fibrinogen.,” *Ric. Clin. Lab.*, vol. 20, no. 2, pp. 167–76.

[50] W. Nieuwenhuizen, “Biochemistry and measurement of fibrinogen.,” *Eur. Heart J.*, vol. 16 Suppl A, pp. 6–10; discussion 10, 1995.

[51] L. Fang, S.-H. Fang, Y.-H. Chung, and S.-T. Chien, “Collecting factors related to the haemolysis of blood specimens.,” *J. Clin. Nurs.*, vol. 17, no. 17, pp. 2343–51, 2008.

[52] W. G. Zijlstra, A. Buursma, and W. P. Meeuwsen-van der Roest, “Absorption spectra of human fetal and adult oxyhemoglobin, de-oxyhemoglobin, carboxyhemoglobin, and methemoglobin.,” *Clin. Chem.*, vol. 37, no. 9, pp. 1633–8, 1991.

[53] A.-M. Simundic, E. Topic, N. Nikolac, and G. Lippi, "Hemolysis detection and management of hemolysed specimens," *Biochem. Medica*, vol. 20, no. 2, pp. 154–159, 2010.

[54] S. Sun and H. Zeng, "Size-Controlled Synthesis of Magnetite Nanoparticles," *J. Am. Chem. Soc.*, vol. 124, no. 28, pp. 8204–8205, 2002.

[55] S. Sun, H. Zeng, D. B. Robinson, S. Raoux, P. M. Rice, S. X. Wang, and G. Li, "Monodisperse MFe2O4 (M = Fe, Co, Mn) nanoparticles.," *J. Am. Chem. Soc.*, vol. 126, no. 1, pp. 273–9, 2004.

[56] A. Ruiz, G. Salas, M. Calero, Y. Hernández, A. Villanueva, F. Herranz, S. Veintemillas-Verdaguer, E. Martínez, D. F. Barber, and M. P. Morales, "Short-chain PEG molecules strongly bound to magnetic nanoparticle for MRI long circulating agents.," *Acta Biomater.*, vol. 9, no. 5, pp. 6421–30, 2013.

[57] A. Ruiz, Y. Hernández, C. Cabal, E. González, S. Veintemillas-Verdaguer, E. Martínez, and M. P. Morales, "Biodistribution and pharmacokinetics of uniform magnetite nanoparticles chemically modified with polyethylene glycol.," *Nanoscale*, vol. 5, no. 23, pp. 11400–8, 2013.

[58] H. Wu, G. Liu, Y. Zhuang, D. Wu, H. Zhang, H. Yang, H. Hu, and S. Yang, "The behavior after intravenous injection in mice of multiwalled carbon nanotube / Fe3O4 hybrid MRI contrast agents.," *Biomaterials*, vol. 32, no. 21, pp. 4867–76, 2011.

[59] D. Kim, H. El-Shall, D. Dennis, and T. Morey, "Interaction of PLGA nanoparticles with human blood constituents.," *Colloids Surf. B. Biointerfaces*, vol. 40, no. 2, pp. 83–91, 2005.

[60] C. Oslakovic, T. Cedervall, S. Linse, and B. Dahlbäck, "Polystyrene nanoparticles affecting blood coagulation.," *Nanomedicine*, vol. 8, no. 6, pp. 981–6, 2012.

Chapter 5

Biodistribution studies of polymer coated superparamagnetic iron oxide nanoparticles

5.1 Introduction

Biomedical imaging is a non-invasive technique that is used not only for clinical purposes (e.g. disease diagnosis) but also for fundamental biological studies (e.g. anatomical or physiological studies). This field dates back to November 1895, when the first biomedical imaging technique called "X-ray" was discovered by W. C. Röntgen. Few months later, X-rays were used for clinical diagnosis [1]. X-ray technique was associated with several disadvantages and unwanted side effects, which in turn prompted scientists to develop new techniques able to exceed its limitations. Over the years, invention of new imaging techniques and development of the existing ones came out. Nowadays, many imaging techniques such as X-ray computed tomography (CT), ultrasound, magnetic resonance imaging, Single Photon Emission Computed Tomography (SPECT), Positron Emission Tomography (PET), and optical imaging are commonly used for diagnostic purposes in hospitals [2]. These techniques have received enormous attention, as their possibilities are not limited only to provide images that help in disease diagnosis, but also extended to visualise the molecular abnormalities within cells that are the cause of the disease [3]. As a result, a new discipline known as "*molecular imaging*" has emerged.

In this chapter we will make use of MRI technique, complemented with histological and analytic prospections, to study the biodistribution of the polymer-coated SPIONs whose toxicity is studied in this thesis.

5.1.1 Magnetic resonance imaging

MRI is considered as one of the most promising non-invasive diagnostic tools in medical science, since it provides three-dimensional anatomical images with high spatial resolution in the sub-millimeter range and high soft tissue contrast [4]. MRI is used widely for brain imaging, the central nervous system imaging, tumours detection and the assessment of the cardiovascular system function [5].

MRI technique is based on nuclear magnetic resonance (NMR) together with the proton relaxation in a magnetic field. Its efficiency as an imaging tool is based on the fact that the human body contains fats and water, these two elements possess a large amount of hydrogen atoms that make the human body contains about 63% hydrogen nuclei (^{1}H).

The NMR phenomenon in liquids and in solids was discovered by Edward Purcell and Felix Bloch in 1946, for this discovery they were awarded the Nobel Prize in physics in 1952. Over two decades (up until 1970s), the NMR technique was used for chemical and physical analysis. In 1971, Raymond Damadian used NMR technique in biomedical applications, where he observed that both normal and tumour tissues possess different relaxation times, this discovery has contributed to motivate the scientists to use the magnetic resonance technique as a tool for medical diagnosis. In 1973, Paul C. Lauterbur and Peter Mansfield described the use of magnetic field gradients to localise NMR signals, a technical development that laid the foundation for MRI as it is currently performed nowadays. Afterward, MRI has received the FDA approval in 1985. In 2003, Paul C. Lauterbur and Peter Mansfield received the Nobel Prize in physiology and medicine for their discoveries concerning MRI [6].

MRI by itself can provide diagnostic images that help in distinguishing between normal and diseased tissues. Often these images are not sufficiently accurate due to the small difference in the relaxation time between tissues. It is therefore necessary to use a supplement material that improves the sensitivity of the technique and provides clearer images. This supplement material is known as ***contrast agent***.

Before reviewing the subject of contrast agents, a brief introduction to the MRI technique will be provided first.

5.1.1.1 Principles of MRI

MRI is based on the detection of NMR signals from hydrogen protons in the body when it is placed in a magnetic field [7].

Protons possess a spin and have their own magnetic moment. In the absence of a magnetic field protons are randomly oriented. However, when protons are exposed to an external magnetic field (B_0), their spins align either parallel or anti-parallel to the magnetic field, more spins prefer to align in the lower energy state (parallel). Therefore, the sum of spins moments per volume unit (net magnetisation) is in the direction of the applied magnetic field that we define as the Z axis. Under the effect of the magnetic field the protons perform a motion called precession Fig. 5.1, the precession frequency depends on the strength of the magnetic field, a relation which is described as Larmor equation:

$$GƆ_0 = \gamma B_0$$

$GƆ_0$ is the Larmor frequency (MHz), ɣ is gyromagnetic ratio whose value for the proton is (ɣp) = 42.577 MHz/T and B_0 is the strength of the magnetic field (T).

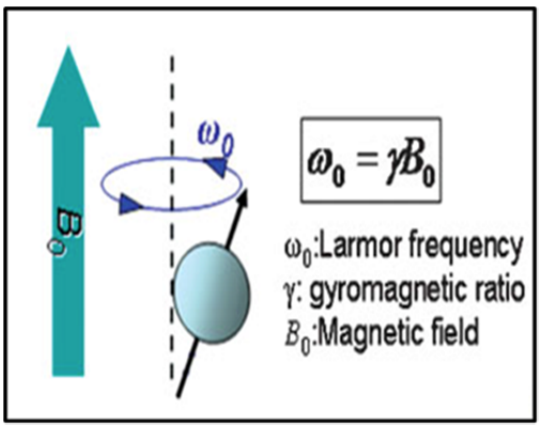

Figure 5.1: Proton precession described by the Larmor equation [8].

When a radio-frequency (RF) pulse of the same frequency of the precessing protons is introduced, Fig. 5.2(a), it has two effects: (a) it causes a resonance process, which transfers energy to protons at the lower energy level (parallel). These protons absorb energy and are excited to the anti-parallel state (higher energy level) resulting in a decrease of the longitudinal magnetisation (M_z), Fig. 5.2(b). Depending on the radio frequency pulse, the longitudinal magnetisation may even totally disappear. At the same time, (b) it makes the protons to precess in phase (pointing at the same direction, at the same time) Fig. 5.2(c), which leads to increase the magnetisation component in the direction transverse to the external magnetic field. This new magnetic vector is called the transverse magnetisation (M_{xy}), Fig. 5.2(c). The transversal magnetic vector does not stand still, but it moves around with the precessing protons, under the precession frequency. The movement of the transverse magnetic vector induces an electric current, which is the MRI signal.

After the disappearance of the RF pulse, the excited protons relax to their initial state, resulting in a decrease of the transverse magnetisation Fig. 5.2(d), which originates a loss of the MRI signal, in a process called transverse relaxation, Fig. 5.3(b). This process is associated with an increase (recovery) of the longitudinal magnetisation, Fig. 5.2(d), in a process called longitudinal relaxation, Fig. 5.3(a).

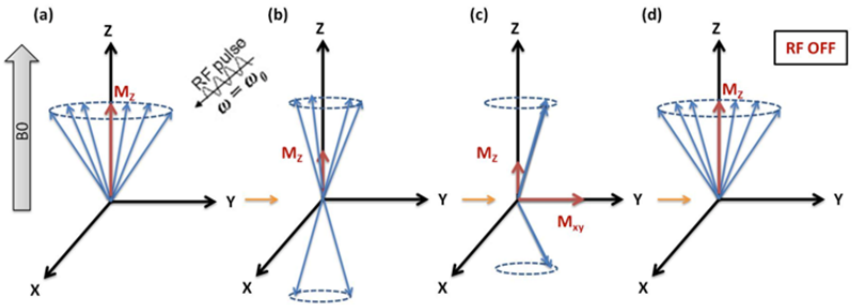

Figure 5.2: Basic principle of magnetic resonance imaging: protons align parallel to the external magnetic field (B_0) with a net magnetisation called longitudinal magnetisation (Mz) (a), when RF pulse of the same frequency of the precessing protons is introduced, some protons absorb energy and go to the anti-parallel state leading to a decrease of the longitudinal magnetisation (b), in addition, RF pulse makes protons to precess in phase, which in turn establishes a new magnetic vector in the transverse direction of the external magnetic field, this magnetic vector is called transverse magnetisation (Mxy) (c), when the RF pulse is switched off, protons possess different precession frequencies and become out of phase, which results in a decrease of the transverse magnetisation; in addition, the excited protons relax to its original state (parallel) leading to an increase (recovery) of the longitudinal magnetisation to its original value (d).

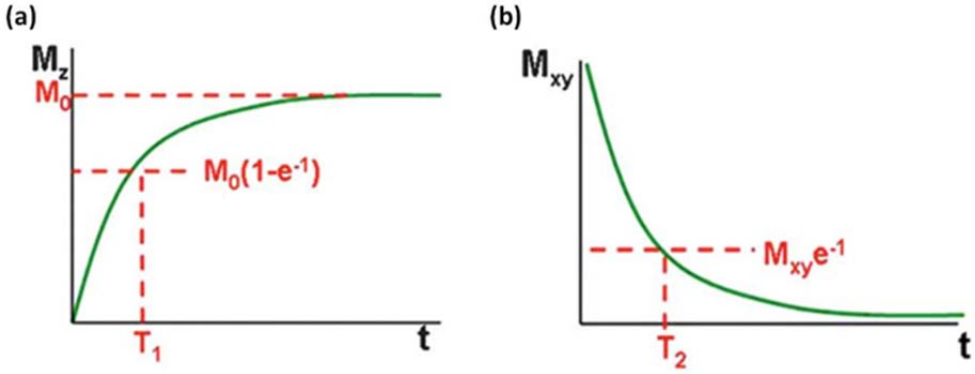

Figure 5.3: The longitudinal relaxation curve (T_1 relaxation curve) (a) and the transverse relaxation curve (T_2 relaxation curve) [8].

The longitudinal relaxation is associated with an exchange of thermal energy with the surrounding (lattice), to where the excited protons transfer energy during their relaxation. Therefore, longitudinal relaxation can also be called spin-lattice relaxation.

During the longitudinal relaxation process, excited protons take time to relax, associated with an increase (recovery) of the longitudinal magnetisation to its original value, Fig. 5.3(a). This time is known as longitudinal/spin-lattice relaxation time (T_1) that can be defined as the time to reduce the difference between the longitudinal magnetisation (M_z) and its equilibrium value (M_0) by a factor of e.

$$Mz=M_o\,(1-e^{-t/T1})$$

Also, the time constant T_1 can be defined as the time when 63% of original longitudinal magnetisation is reached.

T_1 depends on the strength of the external magnetic field. The stronger the magnetic field the larger T_1 value. The value of T_1 in biological tissues is between 300-2000 msec.

The transverse relaxation occurs due to the loss of phase coherence in the precessing spins, which has two origins: (a) inhomogeneity of the external magnetic field, which results in difference in the protons precession frequencies (b) inhomogeneity of the local magnetic field in the tissue- each spin is influenced by the small magnetic field of the neighbour spin (spin-spin interaction)-, which causes difference in the protons precession frequencies. Due to spin-spin interaction, the

transverse relaxation can also be called spin-spin relaxation.

During the transverse relaxation, protons possess different precession frequencies and become out of phase (dephasing), which results in a decrease of the transverse magnetisation with time Fig. 5.3(b). The time required to reduce the transverse magnetisation is called the transverse/spin-spin relaxation time (T_2), which can be defined as the time to reduce the transverse magnetisation (M_{xy}) by a factor of e.

$$M_{xy}=M_{xyo}\ e^{-t/T_2}$$

Also, the time constant T_2 can be defined as the time when the transverse magnetisation is decreased to 37% of its original value.

In comparison with T_1, T_2 is always shorter, and depends less on the strength of the magnetic field. The value of T_2 in biological tissues is between 30-150 msec.

Since the transverse relaxation is affected by the inhomogeneity of the magnetic field produced from tissue and external sources, the total T_2 relaxation time is known as T_2* and is described by the following equation:

$$1/T_2^* = 1/T_2 + \gamma Bs$$

Where γBs represents the relaxation by the field inhomogeneities ($1/T_2$ inhomo) and is called susceptibility effect.

T_2* can be defined as the time constant that describes the exponential decay of signal, due to spin-spin interactions, magnetic field inhomogeneities and susceptibility effects.

According to the relaxation mechanism, contrast agents (CAs) can be divided into two main groups; T_1 contrast agents (Paramagnetic contrast agents) and T_2 contrast agent (superparamagnetic contrast agents).

5.1.2 Contrast agents

The word "*contrast*" indicates the difference in intensities between two adjacent regions within an examined object on a gray or colour scale. According to FDA, a

contrast agent is defined as it is a medical imaging agent that is used to improve the visualisation of tissues, organs and physiologic processes by increasing the relative difference of imaging signal intensities in adjacent regions of the body [9]. Contrast agents are used in many techniques, such as radiography, CT, ultrasonography and MRI.

The MR image contrast is the result of various contributing extrinsic (e.g. strength of the magnetic field, etc.) and intrinsic (e.g. T_1, T_2, T_2*, etc.) parameters. Therefore, the image contrast in MRI is classified into 3 categories: (a) proton density-weighted image, a sequence that is mainly sensitive to proton density ه (b) T_1-weighted image, a sequence that is mainly sensitive to T_1 relaxation time (c) T_2-weighted image, a sequence that is mainly sensitive to T_2 relaxation time [10].

MRI contrast agents are medical imaging agents that facilitate the performance of the imaging tool by improving its sensitivity and detectability, through increasing the relaxation rates of water protons in tissues in which the agents accumulate. Usually, they are chemical agents, but with the continued rapid development in nanotechnology, a new class of contrast agents based on nanoparticles has emerged.

The mechanism of action of MRI contrast agents is more complicated as compared to other techniques, since it depends on the interaction between the MRI contrast agent and the neighbouring water protons, which could be affected by many intrinsic and extrinsic parameters. however, in X-ray or CT contrast agents the mechanism depends on the difference in the electron density [8].

The efficiency of MRI contrast agents depends on their longitudinal (r_1) and transverse (r_2) relaxivities ($mM^{-1}S^{-1}$), which are defined as the increase in the relaxation rates ($1/T_1$ and $1/T_2$ respectively) of protons produced by 1mmol per litre of contrast agent.

$$1/T_{i(post)} = 1/T_{i(pre)} + r_i \cdot C$$

Where i is 1 or 2, $T_{i(post)}$ is the relaxation time of the system after CA administration (S^{-1}), $T_{i(pre)}$ is the relaxation time of the system before CA administration (S^{-1}), r_i is the relaxivity ($mM^{-1}S^{-1}$), and C is the concentration of the CA (mM).

Both r_1 and r_2 are depending on several factors such as the size of CA (increasing the size increases r), chemical structure of the CA molecules, the accessibility of water molecules to the magnetic centre, CA concentration, proton density and the chemical environment [11].

For clinical applications, contrast agents should possess several requirements such as high relaxivity, specificity, tolerance, safety and low toxicity, stability, optimal biodistribution, metabolism and elimination, high contrast enhancement with low dose *in vivo* and minimal cost.

MRI contrast agents can be classified according their (a) magnetic behaviour into soluble paramagnetic metal chelates and superparamagnetic iron oxide particles, (b) effect on proton relaxivity into T_1 contrast agents and T_2 contrast agents, (c) biodistribution into blood pool (intravascular), extracellular or organ-specific agents. The commercially available MRI contrast agents are summarised in Table 5.1.

5.1.2.1 Paramagnetic contrast agents

They are also known as T_1 contrast agents, as they increase the longitudinal relaxation rate ($R_1 = 1/T_1$) of water protons in tissues -where they are accumulated- more than the transverse relaxation rate ($R_2 = 1/T_2$), thus resulting in an increase in signal intensity on T_1-weighted images. Therefore, these agents are positive contrast agents. At low concentration, these CAs can be used as T_1 contrast agent, however at high concentration they can be used as T_2 contrast agents.

Paramagnetic species are metal ions with unpaired electrons, including the transition metal ions, such as manganese (Mn^{+2}, Mn^{+3}), iron (Fe^{+2}, Fe^{+3}), and lanthanide ions, such as gadolinium (Gd^{+3}) and dysprosium (Dy^{+3}). The Gd (III) is the preferred paramagnetic metal ion because it has seven unpaired electrons and high relaxivity, however, it is toxic in its ionic form. Therefore, these paramagnetic metal ions used as CAs are in a complex with a ligand, forming strong chelates, in order to limit the high toxicity and the undesirable biodistribution caused by paramagnetic metal ions alone [10].

These contrast agents can be divided into 3 categories (a) extracellular agents,

Table 5.1 commercially available MRI contrast agents[12–16].

Trade name	Name of compound	Classification	Applications	Producer
Magnevist ®	Gd-DTPA	T_1- agent	Neuro/whole body imaging	Bayer healthcare pharmaceuticals, Inc
Omniscan®	Gd-DTPA-BMA	T_1- agent	Neuro/whole body imaging	GE healthcare
Ablavar®	Diphenylcyclohexyl phosphodiester-Gd-DTPA	T_1- agent	Blood pool imaging	Lantheus Medical Imaging, Inc
ProHance ®	Gd-HP-DO3A	T_1- agent	Neuro/whole body imaging	Bracco Diagnostic Inc
Gadovist ®	Gd-DO3A- butrol	T_1- agent	Neuro/whole body imaging	Bayer healthcare pharmaceuticals, Inc
Dotarem®	Gd-DOTA	T_1- agent	Neuro/whole body imaging	Guerbet S.A.
OptiMARK®	Gd-DTPA-BMEA	T_1- agent	Neuro/whole body imaging	Mallinckrodt, Inc
Multihance ®	Gd-BOPTA	T_1- agent	Centeral nervous system and liver imaging	Bracco Diagnostic Inc
Eovist®	Gd-EOB-DTPA	T_1- agent	Liver imaging	Bayer healthcare pharmaceuticals, Inc
Teslascan	Mn-DPDP	T_1- agent	Liver imaging	GE healthcare
Lumirem®	Ferumoxsil, AMI-121	T_2-agent	Bowel imaging	Guerbet S.A.
Endorem® *	Dextran-coated ferumoxide, AMI-25	T_2-agent	Liver imaging	Guerbet S.A.
Resovist® *	Ferucarbotran, SHU-555A	T_2-agent	Liver imaging	Bayer healthcare pharmaceuticals, Inc
Sinerem® *	Ferumoxtran-10, AMI-227	T_2-agent	Blood pool imaging	Guerbet S.A.
Clariscan® *	Feruglose	T_2-agent	Blood pool imaging	GE healthcare

Gd-DTPA, a complex of gadolinium with diethylenetriaminepentaacetic acid. Gd-DTPA-BMA, a complex of gadolinium with diethylenetriaminepentaacetic acid-Bismethylamide. Gd-HP-DO3A, a complex of gadolinium with 10-(2-Hydroxypropyl)-1,4,7,10-tetraazacyclododecane-1,4,7-triacetato. Gd-DOTA, a complex of gadolinium with 1,4,7,10-tetraazacyclododecane-1,4,7,10-tetraacetic acid. Gd-DTPA-BMEA, bis(methoxyethylamide) derivative of Gd-DTPA, Gd-BOPTA, a complex of gadolinium with the ligand BOPTA, a derivative of DTPA in which one terminal carboxyl group, –C(O)OH is replaced by -C–O–$CH_2C_6H_5$. Gd-EOB-DTPA, a complex of gadolinium with ethoxybenzyl diethylenetriaminepentaacetic acid. MN-DPDP, manganese dipyroxyl diphosphate(*) withdrew from the market.

including the ionic Gd-DTPA and Gd-DOTA, and the neutral Gd-DTPA-BMA, Gd-HP-DO3A, Gd-DO3A-butrol and GD-DTPA-BMEA (b) hepatobiliary (organ specific agents), including Gd-BOPTA and Gd-EOB-DTPA (c) blood pool agents, including MS-325 (Ablavar®), see Table 5.1.

5.1.2.2 Superparamagnetic contrast agents

Superparamagnetic contrast agents are considered as the first nanoparticle-based MRI contrast agents, exploiting the unique physicochemical properties offered by the nanoparticles, such as the high surface area and the size-dependent magnetic properties. They received a great attention after their development as liver contrast agents 20 years ago. This type of CAs has the ability to shorten T_2 and T_2* relaxation times, which is associated with a decrease in the signal intensity, predominant on T_2 and T_2*-weighted images. Thus, these agents are generally known as negative contrast agents.

These CAs consist of an iron oxide core (Fe_3O_4, γFe_2O_3, or other ferrites) coated with macromolecular materials such as dextran, carboxydextran, chitosan, starch, heparin, albumin and polystyrene. SPIONs offer several advantages than other CAs such as strong magnetic efficacy, biodegradability, low toxicity and ease of functionalisation for targeted imaging [17]. The efficiency of CA is based on r_2/r_1 ratio, which increases with increasing the particle size. Better T_2 CA for MRI is the one that increases r_2 and decreases r_1 [18].

According to the overall size of the particles, these CAs can be divided into 3 classes: (1) ultra-small superparamagnetic iron oxide (USPIO) particles, if they possess a hydrodynamic diameter less than 50 nm, (2) superparamagnetic iron oxide (SPIO) particles, if they possess a hydrodynamic diameter more than 50 nm, (3) large particles, if they possess a hydrodynamic diameter more than 200 nm. In the three cases the core diameters are such that the particles are superparamagnetic. Both USPIO and SPIO particles are feasible for intravenous administration, however, the larger particles with their large diameter that could reaches to several micrometers, limits their use only for gastrointestinal tract exploration.

Iron oxide (IO) particles are considered as reticuloendothelial system agents,

therefore, they are used for liver, spleen and lymph node imaging. In addition, they are used for gastrointestinal tract (bowel) imaging and MR angiography (see Table 5.1). Targeted imaging has been achieved using SPIONs conjugated to several targeting moieties, for instance, transferrin conjugated SPIONs for tumour imaging, asialofetuin conjugated SPIONS for liver-specific imaging, secretin conjugated SPIONS for pancrease-specific imaging [17,19,20].

5.1.3 Biodistribution

Nanomaterial biodistribution studies its accumulation in certain organs, which in turn reflects on the toxic behaviour of this nanomaterial. The toxicity of nanomaterials depends on their persistence or clearance from their target organs. Accumulation of nanomaterials in several organs has been detected, for instance accumulation of starch coated SPIONs in lymph nodes [21].

The biodistibution of nanomaterials in biological system depends on several factors:

1) Mode of administration. The fate of nanomaterials inside the body is determined by the way it is administrated [22]. For instance, subcutaneous route is generally considered more appropriate for targeting the regional lymph nodes [23].

2) The body anatomy and physiology. Human body possesses several biological barriers that hinder the passage of nanomaterials to their target tissue, such as:

   - ✓ Epithelium: it acts as a general barrier to prevent the entry of any material to the body, it can be overcome by parenteral injection [24].

   - ✓ Blood: when nanomaterials undergo intravenous administration, several circulating plasma proteins tend to adsorb on their surfaces forming “protein corona”. Protein corona confers a new physicochemical properties to the nanomaterials, and therefore determines the nanomaterial fate in body [25]; for instance, adsorption of certain proteins called opsonin (e.g. immunoglobulin

and complement proteins) to the surface of the nanomaterials leads to clearance of the nanomaterials from the circulation by RES (e.g. macrophages, neutrophils, etc.), through a process called opsonisation. Opsonisation process depends on the size and surface characteristics of the nanomaterial. The majority of opsonised nanomaterials are cleared from circulation to liver and spleen in less than 5 minutes [24]. Opsonisation can be overcome by coating the nanomaterial hydrophobic surface with suitable hydrophilic polymers such as PEG. This reduces the non-specific binding of proteins, leading to prolonged blood circulation time [26]. In addition, formation of protein corona could lead to specific targeting of the nanomaterial to particular organs; for instance, adsorption of apolipoprotein E (apoE) to the surface of several nanomaterials leads to their delivery to brain tissue [27–29].

- ✓ Vascular endothelium: is a continuous and tight junction layer of endothelial cells that lines the inner surface of the blood vessels. Nanomaterials can leave the circulation by breaching the endothelium either by paracellular or transcellular routes. The tight junction makes the gap distance between neighbour cells of less than 2 nm, which in turns prevents the nanomaterials to slip between the cells (Paracellular route). However, in some organs such as liver and spleen, the endothelium is fenestrated, allowing the passage of nanomaterials. In addition, the leaky endothelium is observed in some diseases conditions such as inflammation and tumours, allowing accumulation of nanomaterial in tumours through EPR mechanism [30]. The transcellular route occurs through endocytosis mechanism and requires surface modifications of the nanomaterials [31].

- ✓ Plasma membrane and uptake by cells: the internalisation of nanomaterials into the cells is governed by endocytosis mechanism, which defines the fate of the nanomaterials inside the cells whether in

the cytoplasm or in degradative organelles such as lysosomes. This section is explained in detail in chapter 3 (section 3.1.1.3.1).

3) Nanomaterial physicochemical properties. Nanomaterial composition [32], size [33], shape [34], surface charge [35] and surface modification (e.g. coating [31], targeting [36]) have shown to have influence on the nanomaterial biodistribution. For instance, the accepted size for *in vivo* application is ranging between 10-100 nm [37], larger sizes increase the chance of rapid clearance by opsonisation, while sizes smaller than 5.5 nm are rapidly cleared by glomerular filtration in the kidneys [38].

5.2 Objectives

The aim of this chapter is to study the *in vitro* relaxation, *in vivo* biodistribution - using MRI, histological and analytical studies- and the *in vivo* toxicity for two polymer coated SPIONs; P4VP-g-APEG coated SPIONs (our bioferrofluids) and dextran coated SPIONs (Endorem®).

5.3 Materials and methods

5.3.1 Bioferrofluids preparation and characterisation

Bioferrofluids preparation and characterisation methods are the same as described in Annex I. The preparation conditions of the maghemite polymer nanocomposites used in this chapter is the same as described in the corresponding section of chapter 3 (see section 3.3.1).

5.3.2 In vitro relaxation measurement

In vitro MR imaging was performed with a Biospec Tomograph system (Bruker Medical systems, Karlsruhe, Germany) operating at 200 MHz (4.7 T) and equipped with a 33 cm bore magnet (Oxford Ltd., UK). The system was operating using Paravision 5.1 software (Bruker, Germany). Samples were prepared in physiological saline solutions at different concentrations of bioferrofluids and Endorem® (in mM iron), then inserted in a 7.2 cm internal diameter (i.d) birdcage coil. The transverse relaxation times (T_2) were measured using a standard spin echo multi echo sequence with the following parameters: Repetition time (TR)/echo times (TE) = 2000/5.9 ms,

field of view (FOV) = 8x4cm^2, matrix size (MTX) = 128x128, slice thickness of 2 mm, number of echoes = 16. For the measurement of the longitudinal relaxation time, a fast T_1 mapping technique based on a IR-SNAPSHOT sequence was used [39]. The acquisition parameters were FOV = 8x8cm^2, MTX = 128x128, slice thickness of 2 mm, TR/TE = 10/3.7 ms, excitation pulse angle = 5º, and a 5ms Sech-shaped inversion pulse.

Longitudinal and transversal relaxation rates ($1/T_1$ and $1/T_2$) were plotted as a function of iron concentration and r_1 and r_2 relaxivities were obtained by the slope of the fitting straight line.

5.3.3 In vivo MR imaging

To obtain MR images, 6-7 weeks old BALB/c mice weighting 19-22 grams were anesthetised by inhalation in an induction box with O_2 containing 1:1.5% isofluorane. An animal bed and a magnetic field compatible small animal physiological monitor (SA instrument, Inc, USA) were used to fix the animal and monitor the respiration rate. Mice were fixed to the animal bed in the supine position and a receiver surface coil was placed over their head. The mice were inserted in a 7.2 cm i.d transmitter coil and then into the magnet 4.7T Fig. 5.4. A Standard tube containing 1mM gadolinium-DTPA was inserted in the FOV to standardise images. Aqueous suspensions of either bioferrofluid or Endorem® were intravenously injected via the tail vein at a dose of 23.5 mg Fe/Kg body weight.

In order to evaluate the performance of the bioferrofluid as a contrast agent compared to Endorem®, mapping of the cerebral blood flow (CBF) and cerebral blood volume (CBV) was carried out through bolus tracking method (first passage) [40]. Regional CBV (rCBV) can be also measured using blood pool contrast agents at the steady-state concentration of contrast agent in blood, by acquiring T_2* images before and after contrast agent injection and using the relationship [41]:

$$rCBV = K \times \ln \frac{SI\ (pre)}{SI\ (post)}$$

Where *K* is a constant depending on instrumental parameters, SI pre and SI post are brain signal intensity values before and after contrast agent injection respectively.

First-passage images were acquired using an EPI sequence with the following parameters: MTX = 128x128, FOV = 2.5x2.5cm^2, slice thickness = 2mm, 4 EPI shots, TR/TE = 25/6.6ms, number of excitation (NEX) = 2 (time resolution of 5 images/s). Images were continuously recorded for 60 s.

Steady-state images were acquired before and during 2 h after injection of the contrast agent using a gradient echo sequence with the following parameters: TR/TE = 186.4/ 12 ms, flip angle = 30º, MTX = 256x256, FOV = 2.5x2.5 cm^2, slice thickness = 1 mm, NEX = 4. Since the drop of signal in brain is purely due to the contrast agent present in the blood, the time dependence of SI in the brain will provide an insight in the time of permanence of contrast agents in the blood.

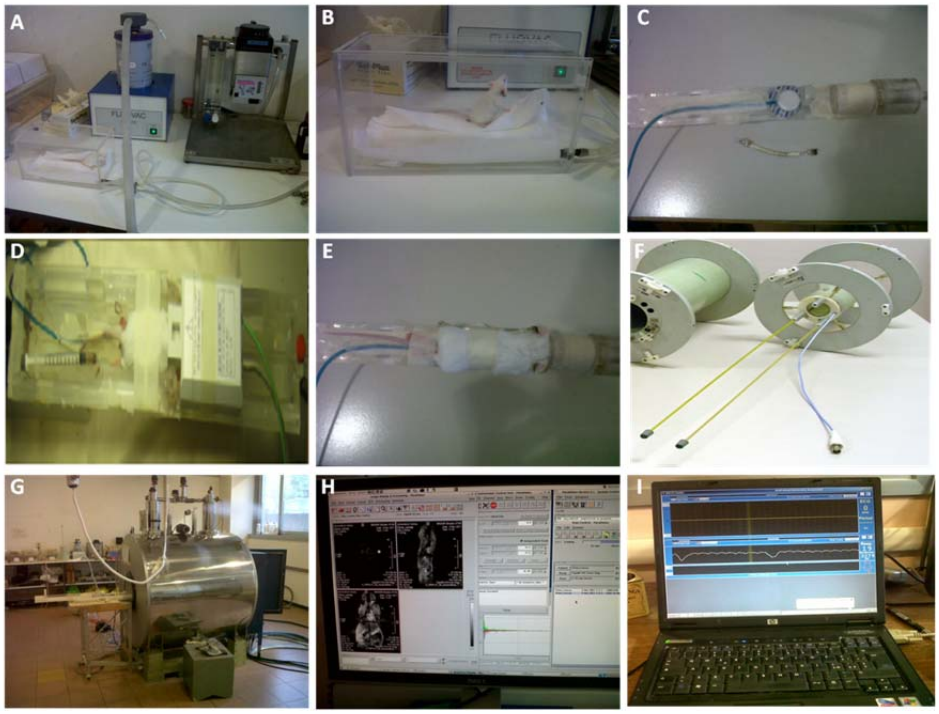

Figure 5.4: Procedure illustration of MRI experiments *in vivo*. Mouse was anesthetised by inhalation inside an induction box with O_2 containing 1:1.5% isofluorane (A, B). To fix the animal and monitor its respiration rate, an animal bed and a magnetic field compatible sensor for respiration were used, a standard tube containing 1mM gadolinium-DTPA is also used to standardise images (C). For brain imaging, mouse was fixed to the animal bed in the supine position and a receiver surface coil was placed over his head. (D). For whole body MR imaging, mouse was fixed to the animal bed in the supine position with the help of adhesive, then inserted into transmitter/receiver coil (3.5 cm i.d birdcage coil) (E, F). Mouse was inserted into 4.7T Biospec Tomograph system (G). MR imaging was operating using Paravision 5.1 software (H) and the animal respiration rate was monitored during the whole experiment time (I).

5.3.3.1 Imaging analysis

In the first passage images, signal enhancement was calculated according to the following equation:

$$Enhancement\ (\%) = \frac{SI\ (t) - SI\ (0)}{SI\ (0)} \times 100$$

Where SI(t) is the signal intensity at time t, SI(0) is the signal intensity before injection.

Steady state images were acquired using T_2*-weighted sequence. Signal Intensity ratio values were obtained by defining the regions-of-interest (ROIs) in the brain. These values were normalised to the standard, divided by the pre-contrast value and plotted as a function of time.

Regional CBV maps were calculated according to the following equation:

$$rCBV = K \times \ln \frac{SI\ (pre)}{SI\ (post)}$$

Where *K* is a constant depending on instrumental parameters, SI pre and SI post are brain signal intensity values before and after contrast agent injection respectively.

5.3.4 Biodistribution studies using MRI

A total number of 16, 8 for each contrast agent, 6-7 weeks old BALB/c mice weighting 19-22 grams were used. MR imaging studies were performed with 4.7T Biospec Tomograph system using a transmitter/receiver coil (3.5 cm i.d birdcage coil). Mouse was anesthetised and fixed in the supine position to an animal bed. A magnetic field compatible sensor for respiration was placed under the mouse abdomen and connected to a small animal physiological monitor to record the respiration rate. A Standard tube containing 1mM gadolinium-DTPA was inserted in the FOV to standardise images. Aqueous suspensions of either bioferrofluids or Endorem® were intravenous injected via the tail vein at the clinical dose (20μmole Fe/kg body weight). Images for the whole body were taken before injection (Pre) and at different time points after injection (5 min-2 h, 24 h, 7 days, 15 days, 30 days and 60 days). Quantitative T_2 maps were acquired using a spin echo multi-echo sequence with the following parameters: TR/TE = 2000/5.9 ms, FOV = 3x6cm^2, MTX = 128x128, slice

thickness of 2 mm, number of echoes = 16. T_2*-weighted images were acquired using gradient echo sequence with the following parameters: TR/TE = 1000/4.4 ms, FOV = 3x6 cm^2, MTX = 256x128, slice thickness of 2 mm, flip angle (FA) = 10º. All animal studies were approved by the Institutional Animal care and Use Committee.

5.3.4.1 Imaging analysis

For the quantitative analysis of obtained images, regions-of-interest were defined in the identical site of liver and kidney. The T_2 values in these ROIs were obtained by using the image sequence analysis (ISA) tool of Paravision 5.1 software, which performs a best fitting of the equation:

$$SI(T_E) = SI(0)e^{\frac{-TE}{T_2}} + C$$

where, $SI(T_E)$ is the signal intensity at certain echo time, SI(0) is the signal intensity at zero time, T_E is the echo time, T_2 is the transverse relaxation time, C is a constant, to the experimental data, thus providing T_2 value in each selected ROI.

T_2*-weighted images were analysed by calculating the ratio between signal intensity after contrast agent injection (SI(post)) and signal intensity before (SI(pre)) at each time point for each organ:

$$R = SI\ (post)/SI\ (Pre)$$

Within a given image, signal intensity values were normalised to the signal intensity of brain instead of the standard due to its absence in some images. This normalisation is needed to account for possible instrumental drifts during the acquisition times. Preliminary experiments showed that the signal intensity of brain is not affected by the used contrast agent dosages.

5.3.5 Statistical analysis

Not all the 16 mice were used for the statistical analysis. This is because some animals were excluded from the experiment due to image artifacts arising from animal respiration movement, also at each time point one animal was sacrificed. Obtained data were presented in the curves as (mean ± SEM), the number of readingsat each time point is indicated by symbol (*n*), data were analysed using Mann-Whitney test.

5.3.6 In vivo toxicity studies

At each time point (2 h, 24 h, 7 days, 15 days, 30 days and 60 days), animals were sacrificed, dissected tissues (liver, spleen, kidney, lungs and heart) were fixed in 10% neutral buffered formalin for 4h followed by a dehydration in ascending grades of ethanol (70%, 80%, 90% and 100%), emersion in xylol, and then inclusion within paraffin wax. Coronal sections (4-6 µm thick) were cut using microtome (Leitz Wetzlar, Germany). Slides mounted sections were deparaffinised, rehydrated, and stained with using hematoxylin and eosin (H&E) according to standard clinical pathology protocols. Slides were dehydrated and then mounted. Prepared slides were visualised under Olympus BX51 microscope equipped with a digital camera. A pathologist was consulted to evaluate any signs of toxicity present.

5.3.7 Qualitative iron detection using Prussian blue assay

The principle of this assay is that ferric ion in the presence of ferrocyanide ion forms ferrous ferrocyanide salt (white color), oxidation of this salt using hydrochloric acid produces ferric ferrocyanide (Prussian blue), which is highly coloured and highly water-insoluble complex.

The slides mounted liver and kidney sections were deparaffinised, rehydrated and processed for iron detection using Prussian blue assay. Samples were incubated with a mixture of 5% potassium hexacyanoferrate II [$K_4[Fe(CN)_6].3H_2O$] and 5% HCL for 45 mins. Stained sections were washed and counter-stained with nuclear fast red for 1 min to provide histological cellular distributions. The slides were dehydrated and then mounted. Prepared slides were observed under Olympus BX51 microscope equipped with a digital camera.

5.3.8 Quantitative iron detection by atomic absorption

6-7 weeks old BALB/c mice weighting 19-22 grams were used. Aqueous suspensions of either bioferrofluids or Endorem® were intravenous injected via the tail vein at the dose of 23.5 mgFe/kg body weight. Mice were sacrificed 2 h and 24 h after injection. Dissected tissues (liver and kidney) were processed for quantitative iron detection, tissue samples were placed in a Teflon tubes and left for 24 h at 80°C to dryness. 2 mL of highly purified HNO_3 (>69.0%) was added, and then the samples

digested using a microwave digestor (MVS-2 Berghof). Samples were cooled and then diluted to 5 mL with Milli-Q water. Iron content was determined by Inductively Coupled Plasma Optical Emission Spectrometry (ICP-OES) Perkin–Elmer plasma 40.

5.4 Results

5.4.1 Bioferrofluids characterisation

The bioferrofluids used in this chapter is (R8`), the same bioferrofluids that has used in chapter 3 (see section 3.4.1). Briefly, the bioferrofluids concentration is 8.1 g/L Fe_2O_3. The core diameter is 13.08 ± 2.33 nm and the hydrodynamic diameter is 163 nm.

A well-known commercialised MRI contrast agent, Endorem®, (Guerbet, France), was used in this work. Endorem® is composed of magnetite core with a size range between 6-9 nm, which is coated with a polymeric coating of dextran. The hydrodynamic diameter of Endorem® is ranging between 80-150 nm. Measurement of the hydrodynamic diameter in our laboratory yields an average of hydrodynamic diameter of 110 nm. The Endorem® concentration is 11.2 g/L Fe.

5.4.2 In vitro relaxation measurement

Transverse (T_2) and longitudinal relaxation times (T_1) were measured for both, Endorem® and bioferrofluids, prepared in physiological saline solutions at different iron concentrations (in mM). It was evident that these bioferrofluids exhibit the typical property of superparamagnetic iron oxide nanoparticles of shortening T_2 relaxation time, as increasing the nanoparticles concentration is associated with a decrease in the signal intensity Fig. 5.5. Obtained values of transverse and longitudinal relaxation rates ($1/T_2$, s^{-1} and $1/T_1$, s^{-1}, respectively) of bioferrofluids and Endorem® were plotted versus the iron concentration in mM Fig. 5.6. Both $1/T_2$ and $1/T_1$ relaxation rates are linearly proportional to the iron concentration, see Figs. 5.6(a) and 5.6(b). The relaxivity coefficient values (r_2 and r_1) were obtained by the slope of the fitting straight lines. r_2 values are 113.99 ± 11.08 (r ± C.I) and 82.8 ± 8.28 $mM^{-1}s^{-1}$, while r_1 values are 2.11 ± 0.21and 0.45 ± 0.05 $mM^{-1}s^{-1}$ for Endorem® and bioferrofluids respectively. These results indicate that these bioferrofluids have a lower r_2 and r_1 compared to commercial Endorem®. The efficiency of a T_2 contrast agent depends on

its r_1, r_2, and r_2/r_1 ratio. A better efficiency is associated with higher r_2/r_1 ratio [42]. The r_2/r_1 ratio values were 54.02 and 184 for Endorem® and bioferrofluids respectively, these results indicate that these bioferrofluids are useful as T_2 contrast agent.

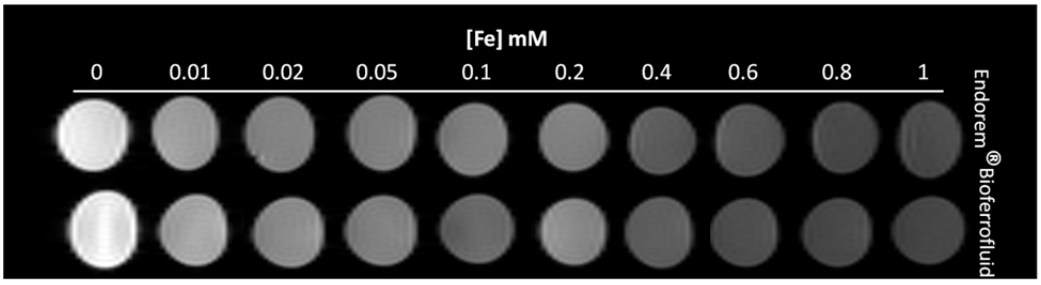

Figure 5.5: T_2-weighted MR imaging of bioferrofluids and Endorem® in physiological saline at different iron concentrations (in mM).

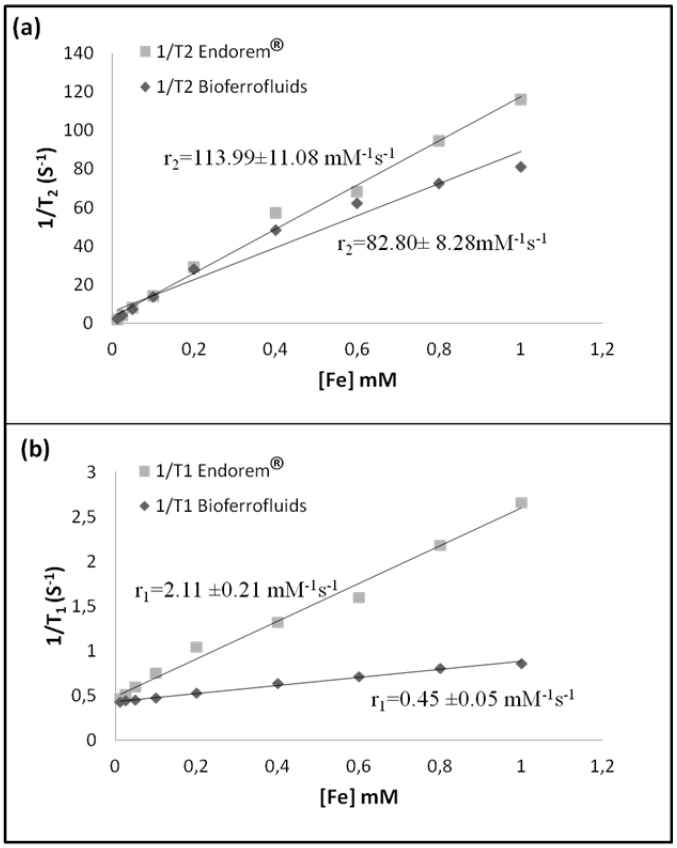

Figure 5.6: Comparative analysis of the transverse relaxation rates ($1/T_2$, s^{-1}) (a) and longitudinal relaxation rates ($1/T_1$, s^{-1}) (b) of bioferrofluids and Endorem® as a function of iron concentration (mM). Relaxation coefficients (r_2, r_1) were calculated from the slopes of each plot.

5.4.3. In vivo MR imaging

First passage experiments were performed in order to assess the usefulness of investigated contrast agent in cerebral perfusion experiments. A dynamic first-passage bolus tracking method was used. Mice were injected with Endorem® and bioferrofluids at a dose of 23.5 mg Fe/Kg body weight, and images were acquired during 60s following the injection. The obtained signal intensity values were normalised according to the following equation:

$$Enhancement\ (\%) = \frac{SI\ (t) - SI\ (0)}{SI\ (0)} \times 100$$

Where SI(t) is the signal intensity at time t, SI(0) is the signal intensity before injection.

A first-passage contrast agent curve plotting the enhancement (%) versus the acquisition times is shown in Fig. 5.7. These results clarify the effect of both Endorem® and bioferrofluids on the signal intensity *in vivo*. Both cause a decrease in the signal intensity values with a different extent. The signal intensity decreases more with Endorem® than with the bioferrofluids. These results are in agreement with the *in vitro* studies.

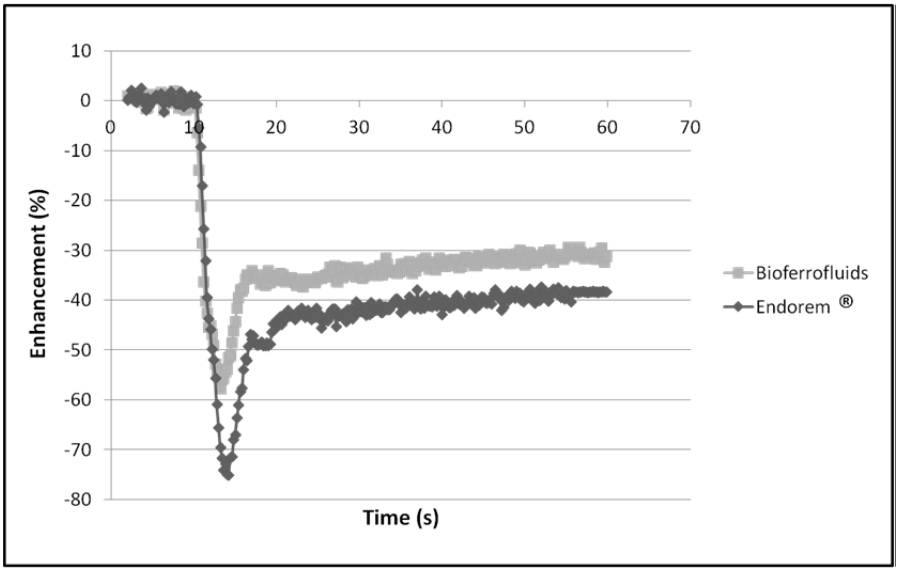

Figure 5.7: A dynamic first-passage bolus tracking curve for both Endorem® and bioferrofluids during an acquisition time of 60s.

To evaluate the performance of the bioferrofluid as a contrast agent compared to Endorem® in steady-state condition, T_2*-weighted images in brain were acquired before (pre) and during 2 h after (post) injection of Endorem® and bioferrofluids at a dose of 23.5 mg Fe/Kg body weight. Before injection, the brain appeared clear Figs. 5.8(a) and 5.8(e). Few minutes after injection of Endorem® and bioferrofluids, a decrease in the signal intensity was observed for both contrast agents Figs. 5.8(b) and 5.8(f), which is indicated by darkening in the brain vasculature (hypointense) that emphasises the existence of the contrast agents in the circulation. Two hours after injection, a hypointense brain was observed for the mouse injected with Endorem® Fig. 5.8(c), however, a cleared brain was observed for the mouse injected with bioferrofluids that emphasises the clearance of bioferrofluids from the circulation Fig. 5.8(g). Figs. 5.8(d) and 5.8(h) show rCBV maps calculated according to the previously mentioned equation (section 5.3.3.1) for Endorem® and bioferrofluid respectively.

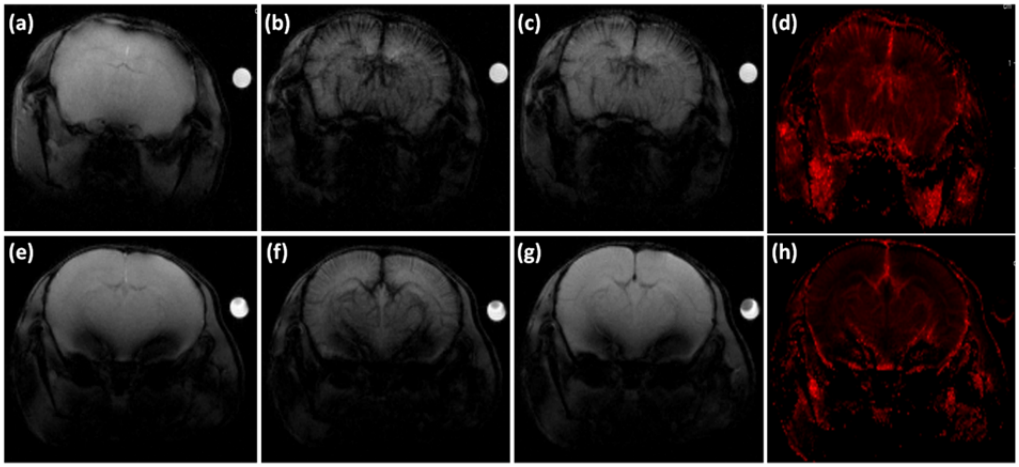

Figure 5.8: T_2*-weighted images for a mouse brain before (a, e), 5 min (b, f), and 2 h (c, g) after injection of Endorem® (upper panel) and bioferrofluids (lower panel). rCBV maps for Endorem® and bioferrofluids are shown in (d) and (h) respectively.

For a quantitative data analysis, signal intensity values in T_2*-weighted images were obtained by identifying the ROIs in the brain. These values were normalised to the signal intensity of the standard, and then the signal intensity ratio was calculated according to the following equation:

$$R = SI\ (post)/SI\ (Pre)$$

Where, SI(post) is the signal intensity after injection, SI(pre) is the signal intensity before injection.

These data were plotted in a curve as a function of the acquisition time Fig. 5.9. It was evident that both contrast agents attenuate the signal intensity inside the brain in few minutes after injection, since signal intensity ratio values were 0.51± 0.11 and 0.67 ± 0.16 (mean ± SD) for Endorem® and bioferrofluids respectively. With time increasing, a very little increase in the signal intensity ratio was observed for Endorem®, however, a dramatic increase in the signal intensity ratio was observed for bioferrofluids, which is after 2 h returns to the pre-injection value Fig. 5.9, indicating a complete clearance from the circulation. From Fig. 5.9 curve, it is apparently clear that bioferrofluids have a half life time in blood shorter than Endorem®. Statistical significant difference between Endorem® and bioferrofluids in signal intensity ratio results was detected using Mann-Whitney test. Data are summarised in Table 5.2.

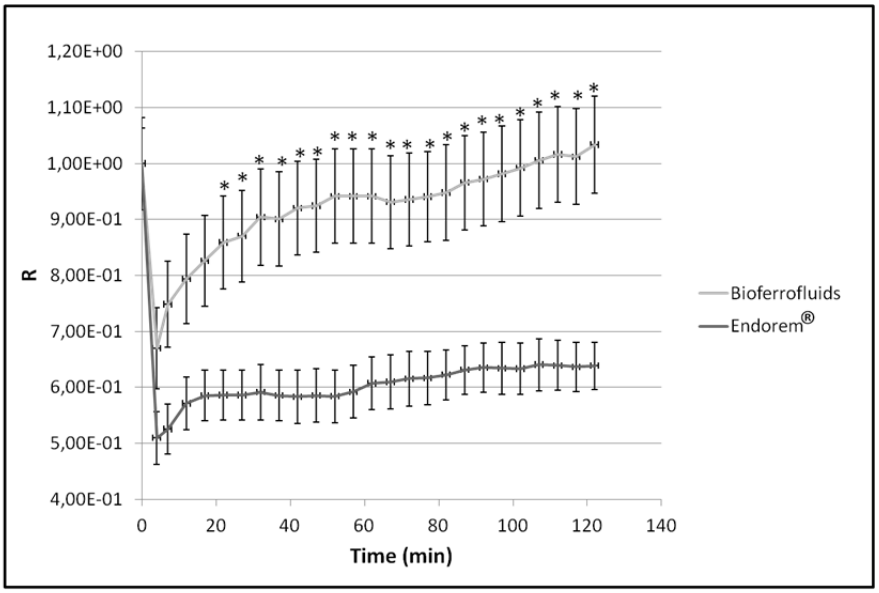

Figure 5.9: Signal intensity ratio values of bioferrofluids and Endorem® in brain during 2 h after injection. Data are presented as (mean ± SEM). (*) marks significant differences between Endorem ® and bioferrofluids, according to Mann-Whitney test (P = 0.0079), (*n* = 5).

Table 5.2: Signal intensity ratio (R) values of bioferrofluids and Endorem® in brain during 2 h after contrast agent injection, *n* = 5.

Time (min.)	R (mean ± SD)		P (Mann -Whitney)
	Bioferrofluids	Endorem®	
0	1.00 ± 0.18	1.00 ± 0.14	1.0000
4	0.67 ± 0.16	0.51 ± 0.11	0.2222
7	0.75 ± 0.17	0.53 ± 0.10	0.0556
12	0.79 ± 0.18	0.57 ± 0.11	0.0749
17	0.83 ± 0.18	0.59 ± 0.10	0.0556
22	0.86 ± 0.19	0.59 ± 0.10	0.0079
27	0.87 ± 0.18	0.59 ± 0.10	0.0079
32	0.90 ± 0.19	0.59 ± 0.11	0.0079
37	0.90 ± 0.19	0.59 ± 0.10	0.0079
42	0.92 ± 0.19	0.58 ± 0.11	0.0079
47	0.93 ± 0.19	0.59 ± 0.11	0.0079
52	0.94 ± 0.19	0.58 ± 0.11	0.0079
57	0.94 ± 0.19	0.59 ± 0.11	0.0079
62	0.94 ± 0.19	0.61 ± 0.11	0.0079
67	0.93 ± 0.19	0.61 ± 0.11	0.0079
72	0.94 ± 0.19	0.62 ± 0.11	0.0079
77	0.94 ± 0.18	0.62 ± 0.11	0.0079
82	0.95 ± 0.19	0.62 ± 0.10	0.0079
87	0.97 ± 0.19	0.63 ± 0.10	0.0079
92	0.97 ± 0.19	0.64 ± 0.10	0.0079
97	0.98 ± 0.19	0.63 ± 0.10	0.0079
102	0.99 ± 0.19	0.63 ± 0.10	0.0079
107	1.01 ± 0.19	0.64 ± 0.10	0.0079
112	1.02 ± 0.19	0.64 ± 0.10	0.0079
117	1.01 ± 0.19	0.64 ± 0.10	0.0079
122	1.03 ± 0.19	0.64 ± 0.10	0.0079

5.4.4 Biodistribution studies

Superparamagnetic iron oxide nanoparticles are known for their ability to shorten the transverse relaxation times (T_2 and T_2*). Therefore, accumulation of SPIONs in any organ will produce a decrease in MR signal intensity. In other words, the organs will appear darker (hypointense).

To evaluate the biodistribution of bioferrofluids and Endorem® in mouse body, T_2 and T_2*-weighted images were performed. Mice were injected with bioferrofluids and Endorem® at the clinical dose (20 μmole Fe/Kg), T_2 and T_2*-weighted images were acquired before (pre), 5 min-2 h, 24 h, 7 days, 15 days, 30 days and 60 days after (Post) injection.

Signal intensity values in T_2*-weighted images, as well as quantitative T_2 values were obtained by identifying ROIs in liver and kidney. T_2 values were obtained by

using the ISA tool of Paravision 5.1 software, according to the following equation:

$$SI(T_E) = SI(0)e^{\frac{-TE}{T_2}} + C$$

$SI(T_E)$ is the signal intensity at certain echo time, SI(0) is the signal at zero time, T_E is the echo time, T_2 is the transverse relaxation time, C is a constant.

Signal intensity values in T2*-weighted images were normalised to the signal intensity of brain, and then the signal intensity ratio was calculated according to the following equation:

$$R = SI\ (post)/SI\ (Pre)$$

Where, SI(post) is the signal intensity after injection, SI(pre) is the signal intensity before injection.

Before injection, T_2 values in the liver were 39.27 ± 2.98 (mean ± SD) and 40.30 ± 1.46 ms in the bioferrofluid and Endorem® groups, respectively. Few minutes after contrast agent injection, a decrease in T_2 values was detected; 33.11 ± 2.93 and 29.11 ± 1.47 ms for bioferrofluids and Endorem® injected mice groups respectively Fig. 5.10(a). These results are compatible with signal intensity ratio results Fig. 5.10(b), as a decrease in the signal intensity ratio values was also observed. Statistical significant difference was detected using Mann-Whitney test between Endorem® and bioferrofluids in T_2 and signal intensity ratio results. Data are summarised in Tables 5.3 and 5.4. The darkening in the liver tissue due to contrast agent accumulation after 2 h of injection is shown in Fig. 5.11.

Estimation for the iron concentration in liver could be obtained from the following equation:

$$\frac{1}{T_2(t)} = \frac{1}{T_2(0)} + r_2C$$

Where, $1/T_2(t)$ (in s^{-1}) is the transverse relaxation rate of a system after contrast agent administration, $1/T_2(0)$ (in s^{-1}) is the transverse relaxation rate of a system before

contrast agent administration, r_2 (in $s^{-1}mM^{-1}$) is the relaxivity of the contrast agent in the desired system, C is the concentration (in mM).

By using the experimentally determined T_2 values for the liver in both bioferrofluids and Endorem® after 2 h of injection and the r_2 relaxivity (measured in physiological saline) we could estimate an iron concentration of about of 0.05 μM in both cases. This concentration confirms the similarity between the bioferrofluids and Endorem® in decreasing the T_2 and T_2*.

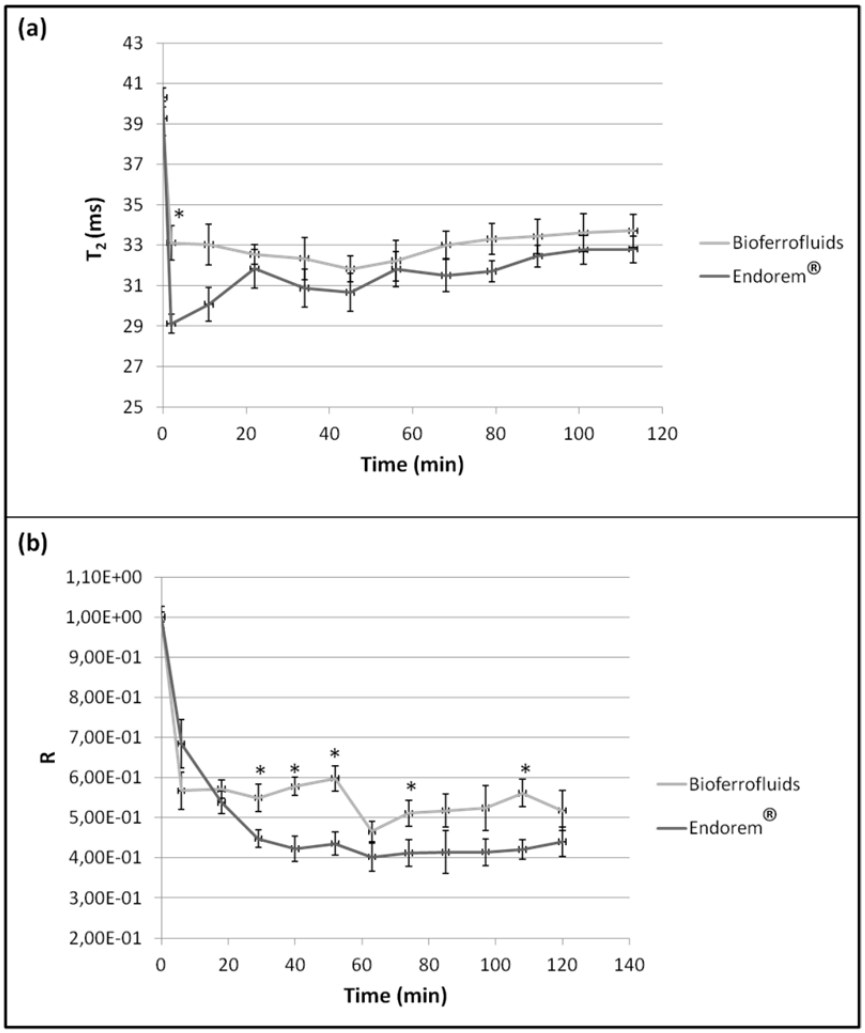

Figure 5.10: Transverse relaxation time values (a) and signal intensity ratio values (b) of bioferrofluids and Endorem® in liver during 2 h after contrast agent injection. Data are presented as (mean ± SEM), (*) marks significant differences between Endorem ® and bioferrofluids, according to Mann-Whitney test, *n* = 10

Table 5.3: Transverse relaxation time values of bioferrofluids and Endorem® in liver during 2 h after contrast agent injection, *n* = 10.

Time (min.)	T_2 (ms) (mean ± SD)		P (Mann -Whitney)
	Bioferrofluids	Endorem®	
0	39.27 ± 2.98	40.30 ± 1.46	0.7169
2	33.11 ± 2.93	29.11 ± 1.47	0.0014
11	33.03 ± 3.48	30.07 ± 3.61	0.0602
22	32.54 ± 1.70	31.83 ± 3.05	0.6209
34	32.34 ± 3.61	30.87 ± 2.93	0.3734
45	31.83 ± 2.18	30.67 ± 3.01	0.3734
56	32.23 ± 3.45	31.81 ± 2.77	0.5752
68	33.01 ± 2.36	31.50 ± 2.49	0.1563
79	33.31 ± 2.63	31.71 ± 1.65	0.0927
90	33.44 ± 2.93	32.46 ± 1.71	0.4887
101	33.61 ± 3.24	32.77 ± 2.28	0.5310
113	33.71 ± 2.78	32.80 ± 2.10	0.4483

Table 5.4: Signal intensity ratio values of bioferrofluids and Endorem® in liver during 2 h after contrast agent injection, *n* = 10.

Time (min.)	R (mean ± SD)		P (Mann -Whitney)
	Bioferrofluids	Endorem®	
0	1.00 ± 0.04	1.00 ± 0.09	1.0000
6	0.57 ± 0.15	0.68 ± 0.19	0.1655
18	0.57 ± 0.07	0.54 ± 0.09	0.2263
29	0.55 ± 0.11	0.45 ± 0.07	0.0342
40	0.58 ± 0.07	0.42 ± 0.10	0.0022
52	0.60 ± 0.10	0.44 ± 0.09	0.0015
63	0.47 ± 0.08	0.40 ± 0.11	0.0961
74	0.51 ± 0.10	0.41 ± 0.10	0.0115
85	0.52 ± 0.13	0.41 ± 0.17	0.1655
97	0.52 ± 0.18	0.41 ± 0.10	0.1617
108	0.56 ± 0.18	0.42 ± 0.08	0.0058
120	0.52 ± 0.16	0.44 ± 0.12	0.3527

T_2 and signal intensity ratio values were also calculated for the Kidney. T_2 values before injection were 85.76 ± 11.85 and 94.94 ± 22.63 ms (mean ± SD), while few minutes after injection T_2 values became 83.66 ± 8.51 and 79.49 ± 15.16 ms for bioferrofluids and Endorem® respectively Fig. 5.12(a), results of signal intensity ratio are shown in Fig. 5.12(b). Statistical significant difference was detected using Mann-Whitney test between Endorem® and bioferrofluids in T_2 and signal intensity ratio results. Data are summarised in Tables 5.5 and 5.6.

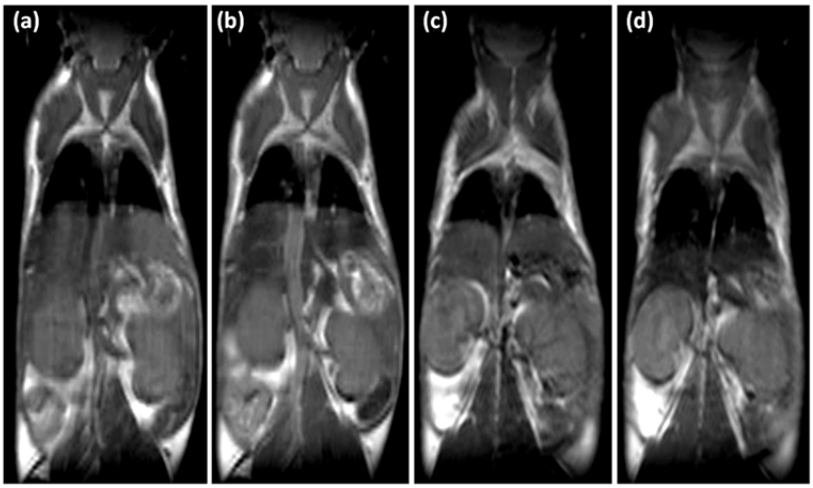

Figure 5.11: Coronal sections of T_2- weighted images of mice bodies before (pre) and 2 h after (post) injections of bioferrofluids and Endorem® at a dose of 20 µmole Fe/Kg body weight. (a) is before injection of bioferrofluids, (b) is 2 h after bioferrofluids injection, (c) is before injection of Endorem®, (d) is 2 h after Endorem® injection.

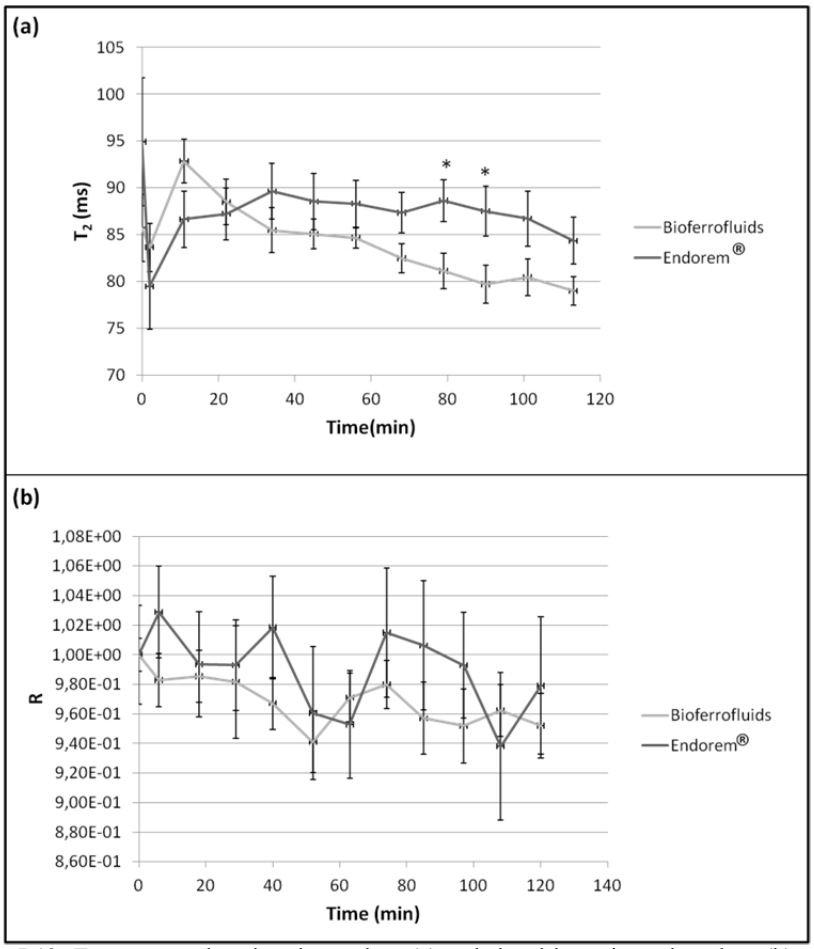

Figure 5.12: Transverse relaxation time values (a) and signal intensity ratio values (b) of bioferrofluids and Endorem® in kidney during 2 h after contrast agent injection. Data are presented as (mean ± SEM), (*) marks significant differences between Endorem ® and bioferrofluids, according to Mann-Whitney test, $n = 10$.

Table 5.5: Transverse relaxation time values of bioferrofluids and Endorem® in kidney during 2 h after contrast agent injection *n* = 10.

Time (min.)	T_2 (ms) (mean ± SD)		P (Mann -Whitney)
	Bioferrofluids	Endorem®	
0	85.76 ± 11.85	94.94 ± 22.63	0.6936
2	83.66 ± 8.51	79.49 ± 15.16	0.7427
11	92.85 ± 7.71	86.65 ± 9.88	0.1310
22	88.48 ± 8.06	87.25 ± 9.19	0.5994
34	85.49 ± 7.88	89.64 ± 9.91	0.4307
45	85.08 ± 5.27	88.55 ± 9.91	0.3933
56	84.66 ± 3.52	88.32 ± 8.28	0.1679
68	82.50 ± 5.17	87.36 ± 7.22	0.0569
79	81.15 ± 6.24	88.64 ± 7.38	0.0256
90	79.72± 6.71	87.52 ± 8.87	0.0256
101	80.47 ± 6.41	86.74 ± 9.71	0.1007
113	79.02 ± 5.05	84.37 ± 8.25	0.0878

Table 5.6: Signal intensity ratio values of bioferrofluids and Endorem® in kidney during 2 h after contrast agent injection *n* = 10.

Time (min.)	R (mean ± SD)		P (Mann -Whitney)
	Bioferrofluids	Endorem®	
0	1.00 ± 0.04	1.00 ± 0.11	1.0000
6	0.98± 0.06	1.03 ± 0.10	0.3405
18	0.99 ± 0.06	0.99 ± 0.11	0.8325
29	0.98 ± 0.13	0.99 ± 0.10	0.8053
40	0.97 ± 0.06	1.02 ± 0.11	0.5034
52	0.94 ± 0.07	0.96 ± 0.14	0.9719
63	0.97 ± 0.06	0.95 ± 0.12	0.5726
74	0.98 ± 0.05	1.01 ± 0.14	0.9718
85	0.96 ± 0.08	1.01 ± 0.14	0.3786
97	0.95 ± 0.08	0.99 ± 0.11	0.5973
108	0.96 ± 0.06	0.93 ± 0.16	1.0000
120	0.95 ± 0.07	0.98 ± 0.15	0.8326

T_2 and T_2*-weighted images were also acquired at several time points after injection (24 h, 7 days, 15 days, 30 days and 60 days) for liver and kidney. As it can be noticed, by increasing the time a decrease in darkness of the liver was observed for both contrast agents Fig. 5.13. T_2 and signal intensity ratio values in liver and kidney were calculated and plotted as a function of the acquisition time Figs. 5.14 and 5.15. Statistical significant difference was detected using Mann-Whitney test between Endorem® and bioferrofluids, control (pre) and bioferrofluids and control (pre) and Endorem® in T_2 and signal intensity ratio results. Data are summarised in Tables 5.7 - 5.10.

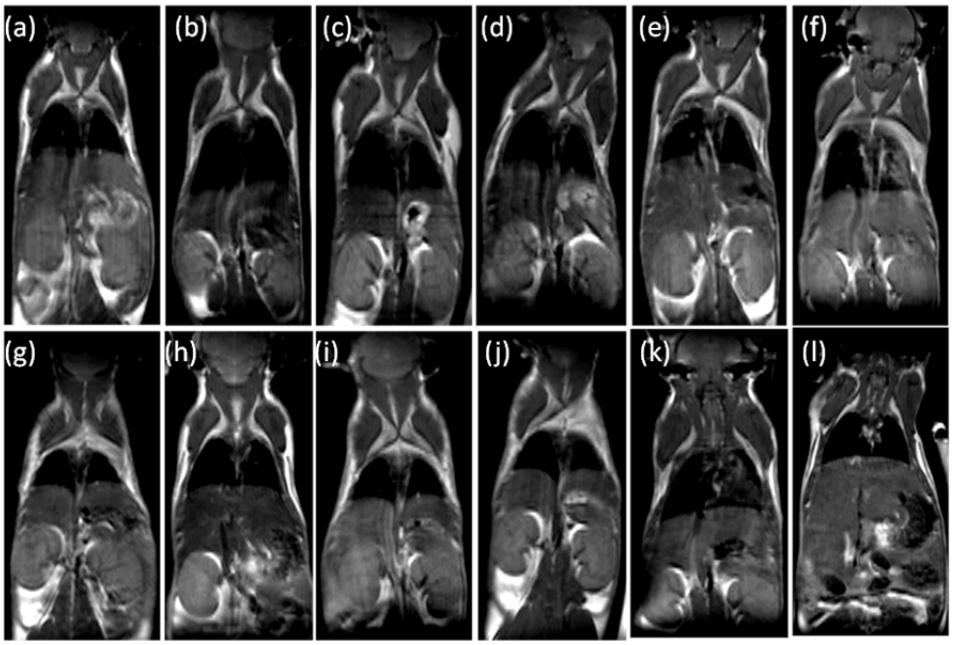

Figure 5.13: Coronal sections of T_2- weighted images of mice bodies before (pre) (a, g), 24 h (b, h), 7 days (c, i), 15days (d, j), 30 days (e, k) and 60 days (f, l) after (post) injections with bioferrofluids (upper panel) and Endorem® (lower panel), at a dose of 20 μmole Fe/Kg body weight.

Fig. 5.14 shows the time dependence in liver T_2 (Fig. 5.14(a)) and signal intensity ratio (Fig. 5.14(b)). After the sharp decrease in both T_2 and signal intensity ratio values observed at 2 h after injection, increasing time was associated with an increase in T_2 and R values as expected as contrast agent clearance from liver. In T_2 results, statistical significance difference between bioferrofluids and Endorem® was observed at 7, 15 and 30 days after injection Fig. 5.14(a), which is not observed in signal intensity ratio results that showed no significance difference between both contrast agents Fig. 5.14(b).

Comparing the pre-contrast values to post-contrast values in both contrast agents, showed a significance difference in T_2 values between bioferrofluids and control (pre) till 30 days after injection Table 5.7, while in signal intensity ratio showed significance difference till 15 days after injection Table 5.8. However, in the case of Endorem®, both T_2 and signal intensity ratio values showed statistical significance difference to the control (pre) till 15 days after injection Table 5.7 and 5.8.

Table 5.7: Transverse relaxation time values of bioferrofluids and Endorem® in liver during 60 days after contrast agent injection, (till 15 days *n* = 10, at 30 days *n* = 8 and at 60 days *n* = 4).

Time (days)	T_2 (ms) (mean ± SD)		P (Mann - Whitney) Bioferrofluids vs. Endorem	P (Mann - Whitney) Bioferrofluids vs. control	P (Mann - Whitney) Endorem vs. control
	Bioferrofluids	Endorem®			
0	39.27 ± 2.98	40.30 ± 1.46	0.7169	-	-
0.083	33.71 ± 2.78	32.80 ± 2.10	0.4483	0.0005	< 0.0001
1	32.08 ± 2.83	32.81 ± 1.88	0.4483	0.0001	< 0.0001
7	29.60 ± 2.88	34.26 ± 1.44	0.0003	< 0.0001	< 0.0001
15	31.32 ± 2.93	35.36 ± 2.44	0.0051	0.0001	0.0002
30	35.41 ± 1.56	38.38 ± 3.46	0.0155	0.0062	0.3599
60	36.47 ± 0.89	37.67 ± 2.11	0.7302	0.1264	0.0759

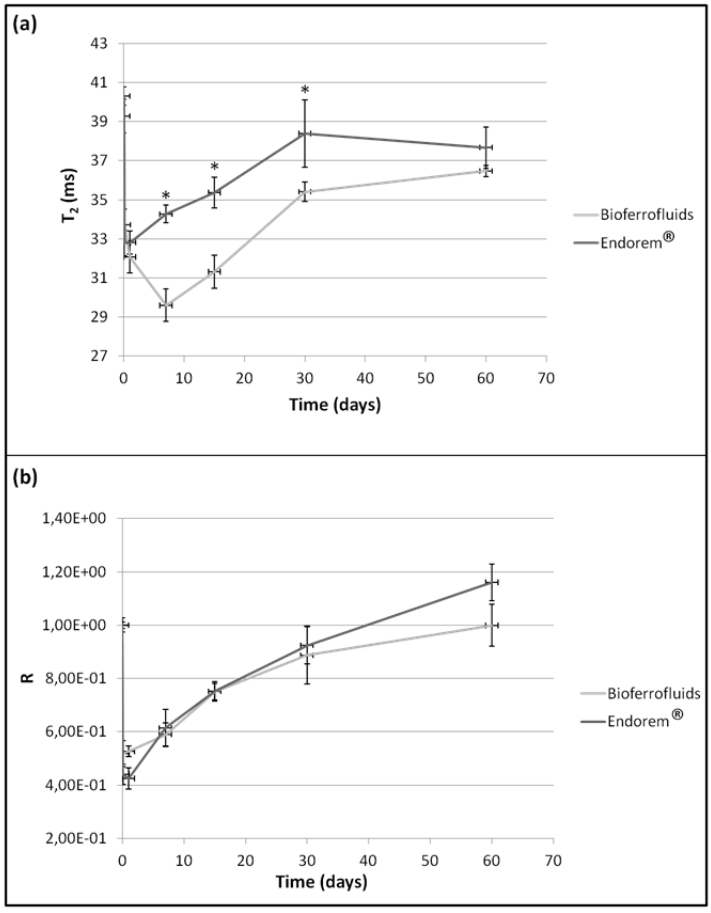

Figure 5.14: Transverse relaxation time values (a) and signal intensity ratio values (b) of bioferrofluids and Endorem® in liver during 60 days after contrast agent injection. Data are presented as (mean ± SEM), (*) marks significant differences between Endorem ® and bioferrofluids, according to Mann-Whitney test, (till 15 days *n* = 10, at 30 days *n* = 8 and at 60 days *n* = 4).

Table 5.8: Signal intensity ratio values of bioferrofluids and Endorem® in liver during 60 days after contrast agent injection, (till 15 days *n* = 10, at 30 days *n* = 8 and at 60 days *n* = 4).

Time (days)	R (mean ± SD)		P (Mann - Whitney) Bioferrofluids vs. Endorem	P (Mann - Whitney) Bioferrofluids vs. control	P (Mann - Whitney) Endorem vs. control
	Bioferrofluids	Endorem®			
0	1.00 ± 0.04	1.00 ± 0.09	1.0000	-	-
0.083	0.52 ± 0.16	0.44 ± 0.12	0.3527	0.0002	< 0.0001
1	0.53 ± 0.06	0.42 ± 0.12	0.0630	0.0002	< 0.0001
7	0.59 ± 0.14	0.61 ± 0.17	0.7925	0.0002	0.0002
15	0.75 ± 0.10	0.75 ± 0.11	0.8939	0.0002	< 0.0001
30	0.89 ± 0.31	0.92 ± 0.17	0.4772	0.083	0.2198
60	1.00 ± 0.16	1.16 ± 0.14	0.2454	1.000	0.0475

In Fig. 5.15, both T_2 and signal intensity ratio values of the kidney are reported. No significance difference was observed between bioferrofluids and Endorem® in T_2 results during 60 days after contrast agent injection Fig. 5.15(a). However, a significance difference between bioferrofluids and Endorem® in signal intensity ratio was detected at 15 days after contrast agent injection Fig. 5.15(b).In case of Endorem® injection, T_2 values were decreased until 15 days and then increased from 30 days and above after injection Fig. 5.15(a). However, T_2 values of the kidney in case of bioferrofluids injection decreased monotonically with time until 60 days after injection Fig. 5.15(a). Statistical significance difference between pre-contrast and after Endorem® injection in T_2 values was observed at 15 days after injection, while in case of bioferrofluids, statistical significance was observed at 2 h, 15 and 60 days after injection Table 5.9.

Table 5.9: Transverse relaxation time values of bioferrofluids and Endorem® in kidney during 60 days after contrast agent injection, (till 15 days *n* = 10, at 30 days *n* = 8 and at 60 days *n* = 4).

Time (days)	T_2 (ms) (mean ± SD)		P (Mann - Whitney) Bioferrofluids vs. Endorem	P (Mann - Whitney) Bioferrofluids vs. control	P (Mann - Whitney) Endorem vs. control
	Bioferrofluids	Endorem®			
0	85.76 ± 11.85	94.94 ± 22.63	0.6936	-	-
0.083	79.02 ± 5.05	84.37 ± 8.25	0.0878	0.0356	0.2372
1	86.36 ± 8.54	85.16 ± 12.65	0.6936	0.7427	0.3579
7	81.64 ± 12.45	87.71 ± 13.82	0.3579	0.3246	0.5545
15	77.19 ± 8.43	61.05 ± 22.01	0.0726	0.0256	0.0054
30	77.45 ± 7.38	72.47 ± 22.32	0.6070	0.0806	0.0630
60	64.65 ± 5.59	72.53 ± 15.64	0.7302	0.0127	0.1027

Signal intensity ratio values of Kidney after Endorem® Injection was concurrent with T_2 values, as R values decreased until 15 days and then increased from 30 days and above after injection Fig. 5.15(b), a statistical significance between "pre" and "post" contrast values was detected at 1 and 15 days after injection Table 5.10. In case of Bioferrofluids, the R values decreased until 7 days then increased at 15 days and decreased again at 60 days Fig. 5.15(b), a statistical significance between "pre" and "post" contrast values was detected at 1 and 60 days after injection Table 5.10. Difference between T_2 and R values in Kidney in case of bioferrofluids is due to the experimental error; however, after 60 days of injection both R and T_2 values were lower than the pre-contrast values.

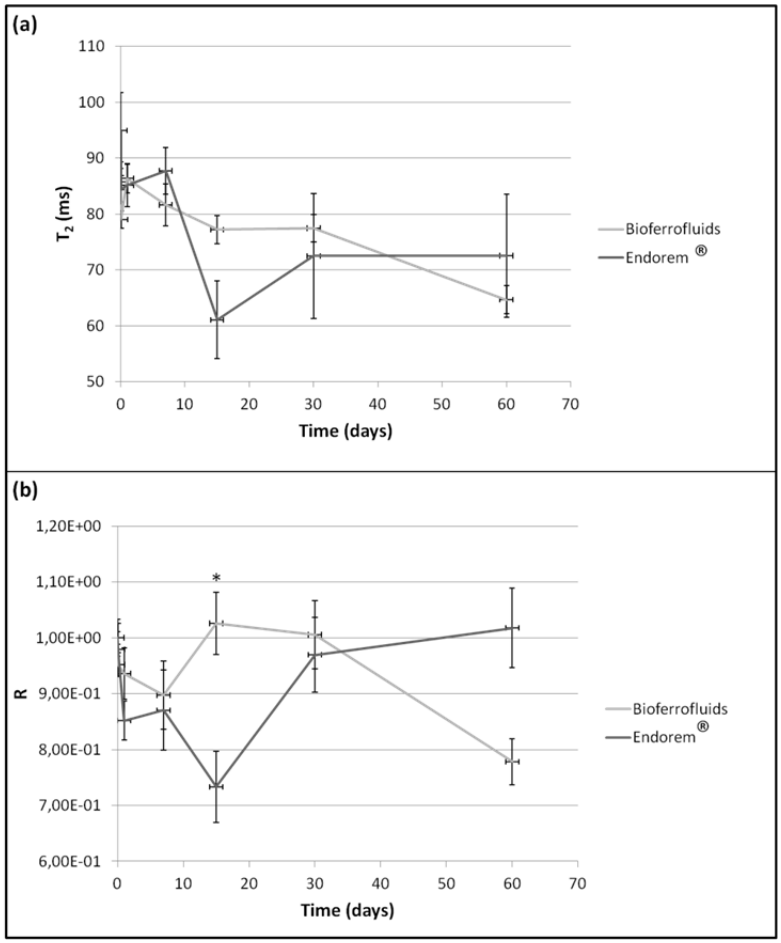

Figure 5.15: Transverse relaxation time values (a) and signal intensity ratio values (b) of bioferrofluids and Endorem® in kidney during 60 days after contrast agent injection. Data are presented as (mean ± SEM), (*) marks significant differences between Endorem ® and bioferrofluids, according to Mann-Whitney test, (till 15 days n = 10, at 30 days n = 8 and at 60 days n = 4).

Table 5.10: Signal intensity ratio values of bioferrofluids and Endorem® in kidney during 60 days after contrast agent injection, (till 15 days *n* = 10, at 30 days *n* = 8 and at 60 days *n* = 4).

Time (days)	R (mean ± SD)		P (Mann - Whitney) Bioferrofluids vs. Endorem	P (Mann - Whitney) Bioferrofluids vs. control	P (Mann - Whitney) Endorem vs. control
	Bioferrofluids	Endorem®			
0	1.00 ± 0.04	1.00 ± 0.11	1.0000	-	-
0.083	0.95± 0.07	0.98 ± 0.15	0.8326	0.1138	0.7333
1	0.94 ± 0.15	0.85 ± 0.11	0.3150	0.0375	0.0091
7	0.90 ± 0.19	0.87 ± 0.18	1.0000	0.0837	0.1748
15	1.03 ± 0.18	0.73 ± 0.18	0.0067	0.8600	0.0039
30	1.01 ± 0.15	1.00 ± 0.19	0.4381	0.2898	0.5049
60	0.78 ± 0.08	1.02 ± 0.14	0.0571	0.0048	0.8318

5.4.5 Qualitative iron detection using Prussian blue assay

In order to confirm that the shortening in the transverse relaxation times and signal intensity ratio results from contrast agent accumulation in organs, Prussian blue assays were carried out to detect free ferric ions in liver and Kidney. Results showed that there is an accumulation of both bioferrofluids and Endorem® in liver after 2 h of injection, which is indicated by presence of blue dots Fig. 5.16.

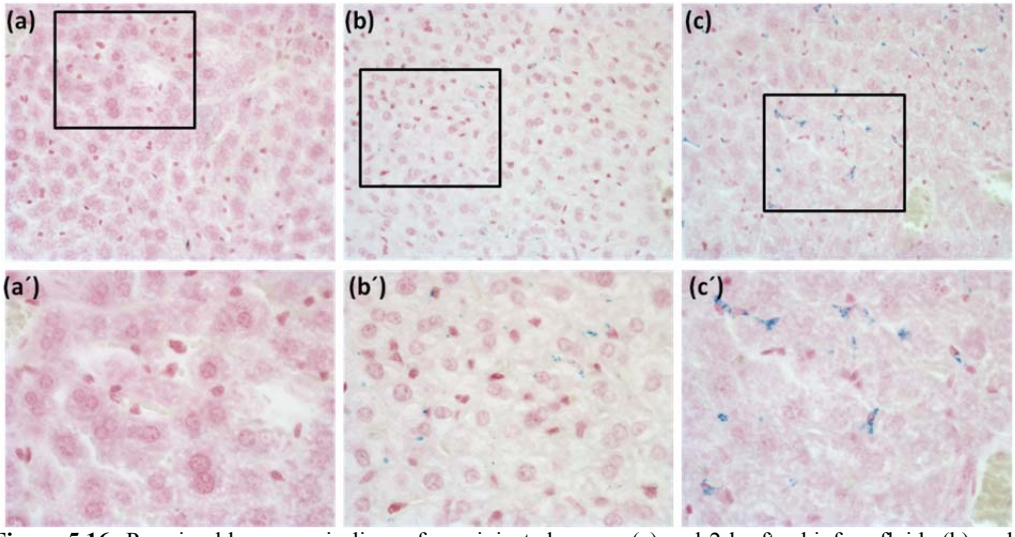

Figure 5.16: Prussian blue assay in liver of non-injected mouse (a) and 2 h after bioferrofluids (b) and Endorem®(c) injection. Ferric ion existence is indicated as blue coloured dots. Upper panel images are at low magnifications, while lower panel (a`, b`, c`) is the same images but at high magnification.

Ferric ion detection was also evaluated in liver of mice after 1, 7, 15, 30 and 60 days of contrast agent injection Fig. 5.17. In case of Endorem®, high amount of iron was detected till 7 days after injection Figs. 5.17(a) and 5.17(c), and then the amount decreased at 15 days Fig. 5.17(e). Endorem® was not detected from 30 days and above Figs. 5.17(g) and 5.17(i). While, in the case of bioferrofluids, however the amount of iron seems to be less to that of Endorem® but iron exists for longer period, iron was detected till 30 days after bioferrofluids injection Figs. 5.17(b), 5.17(d), 5.17(f), 5.17(h). Bioferrofluids were not detected at 60 days after injection Fig. 5.17(j). Table 5.11 shows results regarding ferric ion concentration in liver tissue after contrast agent injection. Prussian blue results confirmed the obtained results by MRI.

Table 5.11: a perspective idea about ferric ion concentration in liver of mice after contrast agent injection using Prussian blue assay

Time	Endorem®	Bioferrofluids
0	-	-
2 h	+++	+
1 day	+++	++
7 days	+++	+
15 days	+	+
30 days	-	+
60 days	-	-

In the case of kidney, after 2 h of injection of both Endorem® and bioferrofluids, only a very few separated dots were detected Fig. 5.18. Ferric ion detection was also evaluated in kidney of mice after 1, 7, 15, 30 and 60 days of contrast agent injection Fig. 5.19. Accumulation of ferric ions was just detected in the period between 7-15 days after Endorem® injection Fig. 5.19(c), 5.19(e). However, in case of bioferrofluids, ferric ions accumulate until 60 days after injection Figs. 5.19(b), 5.19(d), 5.19(f), 5.19(h) and 5.19(j). These results are in agreement with obtained results by MRI.

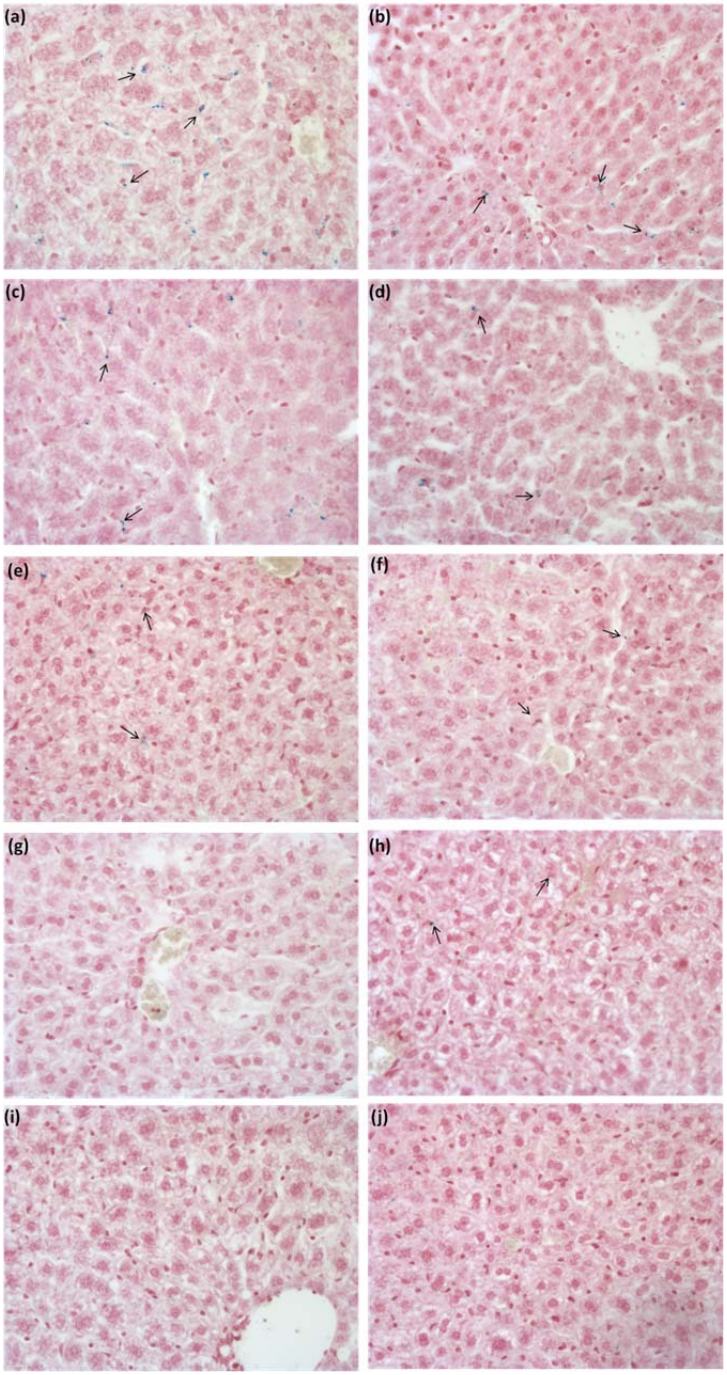

Figure 5.17: Prussian blue assay in mouse liver after 1 day (a, b), 7 days (c, d), 15 days (e, f), 30 days (g, h) and 60 days (i, j) of Endorem® (left panel) and bioferrofluids (right panel) injection. Black arrows are pointing ferric ions which appear as blue coloured dots

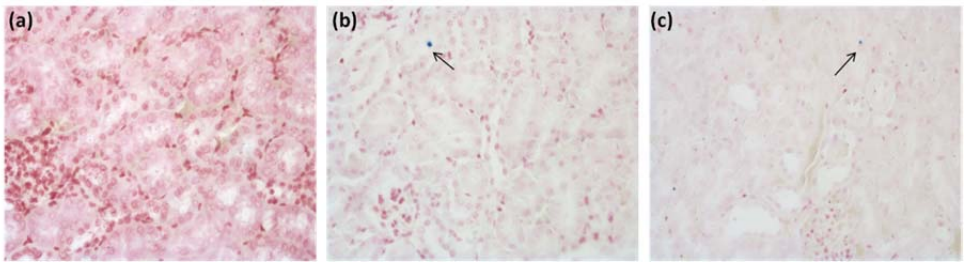

Figure 5.18: Prussian blue assay in Kidney of non-injected mouse (a) and 2 h after bioferrofluids (b) and Endorem® (c) injection, black arrows are pointing ferric ion, which is visualised in a blue colour.

5.4.6 Quantitative iron detection using atomic absorption

The amount of iron was detected in mouse liver and kidney before, 2 h and 24 h after bioferrofluids and Endorem® injection at a dose of 23.5 mg Fe/Kg body weight. Fig. 5.20 and Fig. 5.21 show the accumulation of iron in mouse liver and kidney, respectively. It is evident the accumulation of iron in mice liver after bioferrofluids and Endorem® injection, after 2 h of CAs injection, the amount of iron in case of bioferrofluids injection is higher than Endorem® Fig. 5.20(a), while after 24 h of injection, similar iron concentration was detected for both CAs. Fig. 5.20(b). In case of kidney, no accumulation of iron was detected after 2 h Fig. 5.21(a) and 24 h Fig.5.21(b) of CAs injection.

5.4.7 In vivo toxicity studies

To study the toxicity of bioferrofluids and Endorem® on mice organs, tissues were collected at different time points (0, 2 h, 1 day, 7 days, 15 days, 30 days and 60 days) after contrast agent injection at a dose of 20 µmole Fe/Kg body weight. Results showed that both Endorem® and bioferrofluids did not generate any notable histological lesions in organs (liver, kidney, spleen, lungs and heart) after the indicated periods of times. Fig. 5.22 shows the histopathological studies in mouse liver after contrast injection.

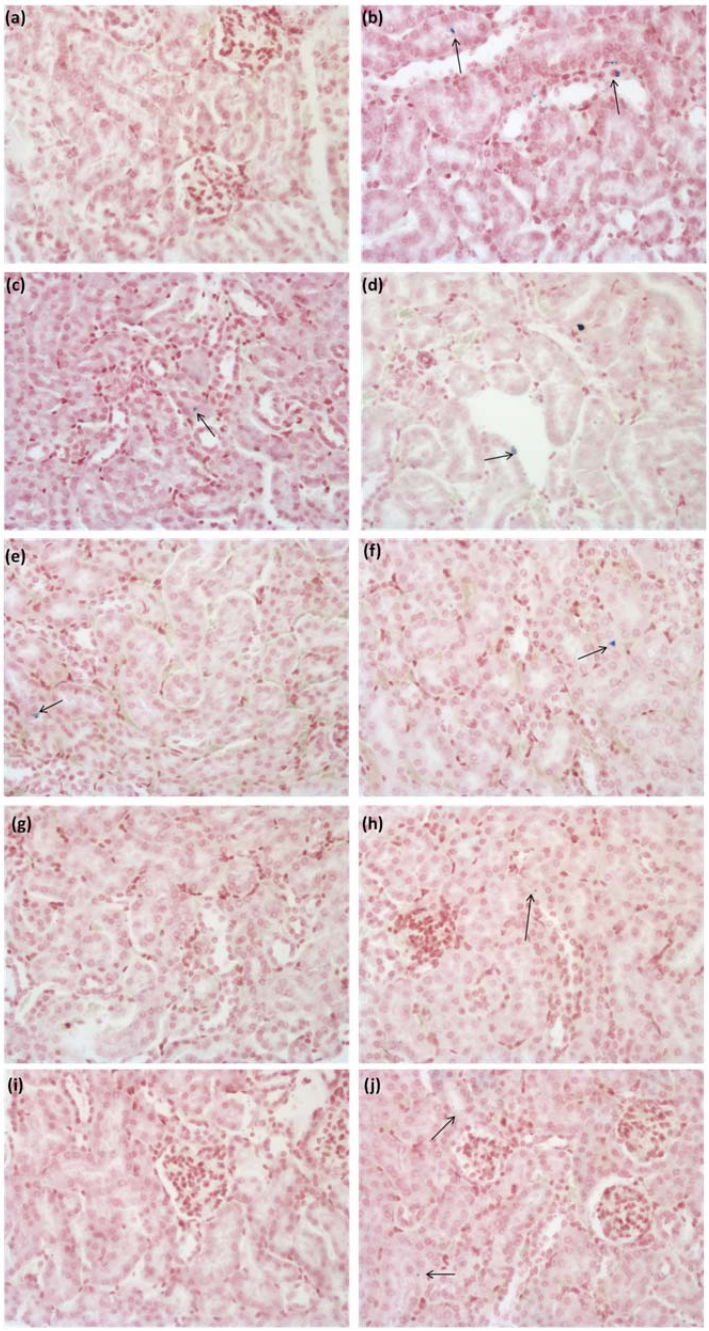

Figure 5.19: Prussian blue assay in mouse kidney after 1 day (a, b), 7 days (c, d), 15 days (e, f), 30 days (g, h) and 60 days (i, j) of Endorem® (left panel) and bioferrofluids (right panel) injection. Black arrows are pointing ferric ions which appear as blue coloured dots.

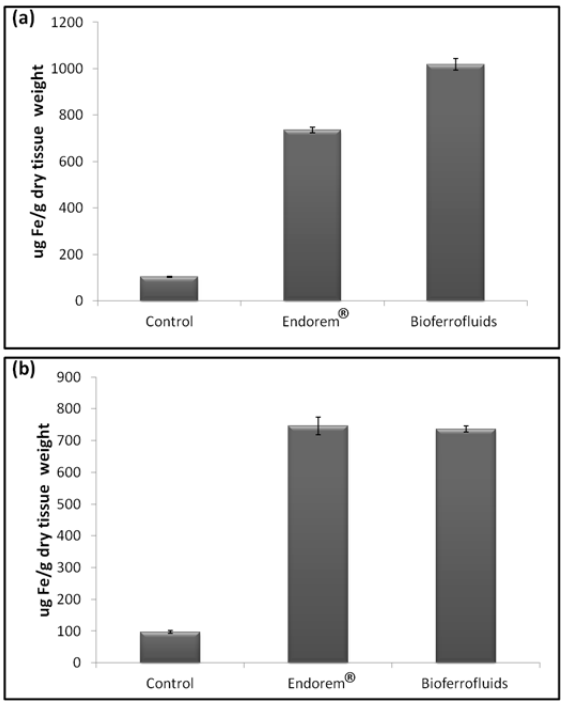

Figure 5.20: Iron detection by atomic absorption in mouse liver before, 2 h (a) and 24 h (b) after bioferrofluids and Endorem® injection at a dose 23.5 mg Fe/kg body weight.

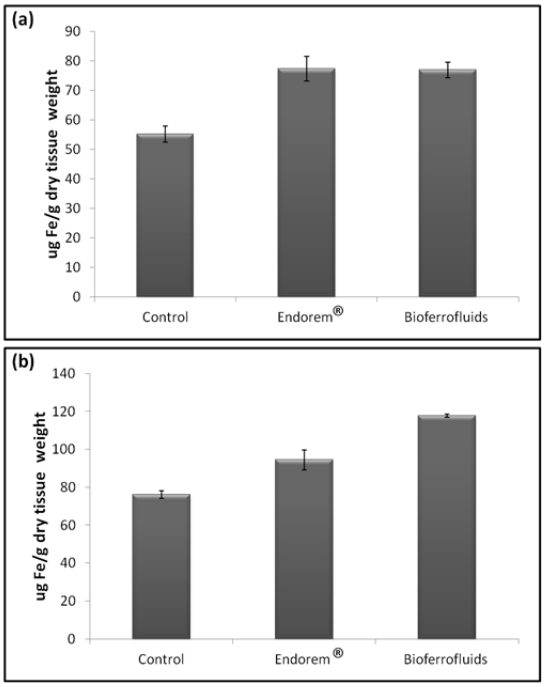

Figure 5.21: Iron detection by atomic adsorption in mouse kideny before, 2 h (a) and 24 h (b) after bioferrofluids and Endorem® injection at a dose 23.5 mg Fe/kg body weight.

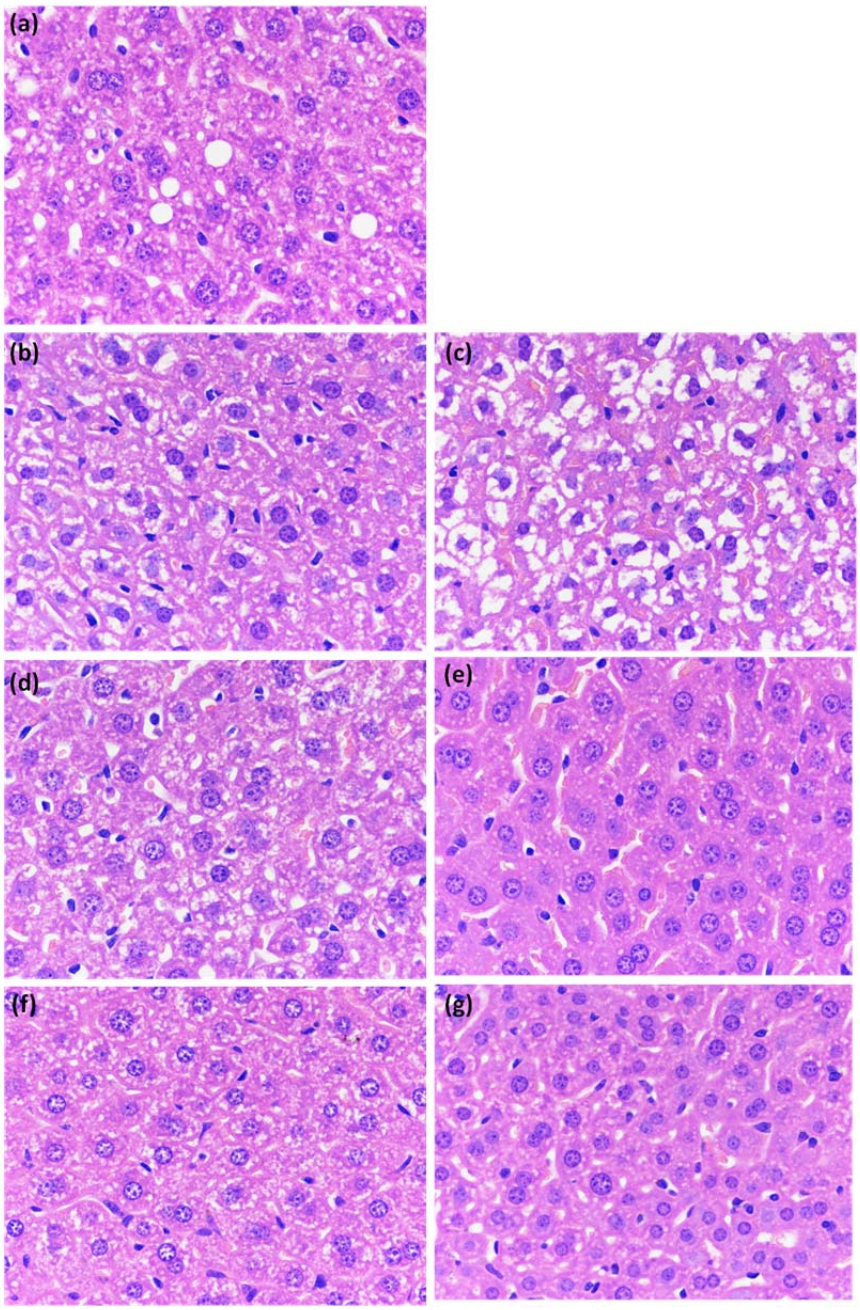

Figure 5.22: Hematoxin and Eosin stain in liver of non-injected mouse (a) and after 2 h (b, c), 1 days (d, e), 7 days (f, g) of Endorem® (left panel) and bioferrofluids (right panel) injection.

5.5 Discussion and conclusions

Two polymer coated SPIONS, P4VP-g-APEG coated SPIONs (bioferrofluids) and dextran coated SPIONs (Endorem®) were subjected to the *in vitro* relaxation measurements. Obtained results showed that both bioferrofluids and commercial Endorem® exhibit similar behaviour in shortening T_2 relaxation time, as increasing in

the nanoparticles concentration is associated with a decrease in the signal intensity, as shown in Fig 5.5. The efficiency of T_2 contrast agents is depending on the transverse relaxivity (r_2) more than the longitudinal relaxivity (r_1). A better T_2 CA is considered to be the one that increases r_2 and decreases r_1 (higher r_2/r_1 ratio) [18,42]. Longitudinal and transverse relaxivities (r_1 and r_2 respectively) are depending on the nanoparticle size in a direct proportion relationship. Therefore, it was expected that r_1 and r_2 values for bioferrofluids (D_p = 13 nm) are larger than for Endorem® (D_p = 6-9 nm). But, that has not been the case, as bioferrofluids showed lower values of r_2 and r_1 compared to Endorem®. In a study carried out by Amiri et al., they measured the relaxivities (r_1 and r_2) of these bioferrofluids and Endorem®, exploring the effect of nanoparticle size [43]. Results showed that bioferrofluids of D_p = 15 nm has a higher r_2 value as compared to commercial Endorem®. Differences between Amiri's and our study stay in the operating frequencies. Our experiment was carried out at a frequency of 200 MHz (corresponding to 4.7T clinical imager), however, Amiri et al. study was carried out at lower frequencies (8.5, 21 and 63 MHz corresponding to about 0.2, 0.5, and 1.5 T clinical imagers, respectively). In their study, it is evident that r_1 is size-dependent at low frequencies (0.01-0.1 MHz); larger nanoparticle sizes have higher r_1 values. At higher frequencies (1-100 MHz), a decrease in r_1 values was detected for all samples, however, Endorem® showed higher r_1 in compared to other. This may explain the lower value of r_1 obtained by our bioferrofluids in compared to Endorem® at high frequency (200 MHz). Similar behaviour could be the reason for the lower values of r_2 obtained by our bioferrofluids compared to Endorem® at high frequency (200 MHz), although this hypothesis needs further verification. Calculating the r_2/r_1 ratio for both bioferrofluids and Endorem®, showed that our bioferrofluids have a higher r_2/r_1 ratio than Endorem®. These results indicate that these bioferrofluids are useful as T_2 contrast agent and more efficient than commercial Endorem®.

In order to assess the usefulness of bioferrofluids and Endorem® in cerebral perfusion experiments, first passage experiment were performed, as shown in Fig. 5.7. Results showed that both bioferrofluids and Endorem® decrease the signal intensity values, however, Endorem® decreases the SI values more than the bioferrofluids. These results are in agreement with the *in vitro* results, as the contrast enhancement effects is directly related to the relaxivity value of the nanoparticle.

To evaluate the efficiency of the bioferrofluid and of Endorem® as a contrast MRI agent in steady-state condition, T_2*-weighted images in brain were acquired as pre-contrast and during 2 h post-contrast injection. Results showed a decrease in the SI ratio in few minutes after CAs injection Fig. 5.9. Therefore, the brain vasculatures appear darker, emphasising the existence of the CAs in the circulation Figs. 5.8(b), 5.8(f). Two hours after injection, in the case of Endorem®, the SI ratio was still low Fig.5.9 (indicated as hypointense brain Fig.5.8(c)), however, an increase in the SI ratio was detected for bioferrofluids, which returns to the pre-injection value, indicating a complete clearance from the circulation, as shown in Fig 5.9 (clear brain Fig. 5.8(g)). It is clear that bioferrofluids have a half-life time in blood shorter than Endorem®. The clearance of the nanoparticles from the circulation could be by RES "opsonisation", but in any case such clearance affects the half life time of the CA in blood. Opsonisation is depending on several factors such as nanoparticle size, charge, surface coating and dose. The opsonisation effect can be reduced by coating the nanoparticles with a hydrophilic polymer that reduces the non-specific binding of opsonin proteins. Therefore, Endorem® is composed of magnetite core coated with dextran, and our bioferrofluids are composed of maghemite cores coated with P4VP-g-APEG. Several studies show that the long blood circulation time is achieved by increasing the chain length of PEG [44]. The surface of the nanoparticles in the P4VP-g-APEG bioferrofluids is formed by 1/10 in weight of APEG long chains (MW=1000) and 9/10 of APEG short chains (MW=200). Therefore, these short chains of PEG might not protect the nanoparticles from the non-specific protein adsorption and subsequent the opsonisation, leading to short blood circulation time. A study to identify protein corona formation is recommended. In addition to the surface coating, the nanoparticle size plays a crucial role in nanoparticle opsonisation; larger size nanoparticles are cleared faster than smaller size ones. The hydrodynamic diameter of bioferrofluids is 163 nm, while for Endorem® is 110 nm. Therefore, the large size of bioferrofluids increases their chance for opsonisation and clearance from the circulation.

Regional cerebral blood volume maps for Endorem® and bioferrofluids at the steady-state were calculated as described in section 5.3.3.1. rCBV map after Endorem® injection depicted very well the space arrangement of cerebral blood

vessels, as shown in Fig.5.8(d). In the case of bioferrofluids, however, lower effect was observed, as shown in Fig 5.8(h).

T_2 CAs are negative contrast agents, therefore, they appear dark in tissues where they are accumulated. Biodistribution studies showed the accumulation of both bioferrofluids and Endorem® in liver, indicated as darkening in the liver tissue Fig. 5.11 after 2 h of CAs injection at the clinical dose (20 μmole Fe/Kg body weight). Both T_2 and SI ratio values decreased few minutes post-contrast injection as shown in Figs. 5.10(a) and 5.10(b). After 2 h, T_2 values and SI ratio values showed no significant difference between bioferrofluids and Endorem®. T_2 values were 33.71 ± 2.78 and 32.80 ± 2.10 ms and SI ratio values were 0.52 ± 0.16 and 0.44 ± 0.12 for bioferrofluids and Endorem®, respectively. Estimation for the iron concentration in liver yields a similar concentration of 0.05 μM for both CAs. The similarity between both CAs in the accumulated iron concentration in liver tissues confirms their similarity in decreasing the T_2 and T_2* values after 2 h of CAs injection. Qualitative detection of iron using Prussian blue assay showed more amount of iron in the liver of mice injected with Endorem® than with bioferrofluids, as shown in Fig.5.16. However, T_2 and SI ratio results and estimated iron concentration showed that both contrast agents have similar effect. This may be due to the presence of Endorem® in Kupffer cells as agglomerates. However, our bioferrofluids are distributed in Kuppfer cells and hepatocytes. This hypothesis is confirmed by the quantitative determination of iron using atomic absorption, as higher amount of bioferrofluids than Endorem® was detected in mice liver after 2 h of injection Fig. 5.20.

CAs biodistribution was evaluated at several time points till 60 days post injection, it was clear that by increasing the time a decrease in darkness of the liver was observed Fig. 5.13, which indicates CAs degradation and clearance from liver tissue. Both T_2 and SI ratio values showed time dependence. T_2 values between bioferrofluids and control (pre) showed a significant difference till 30 days after injection, while, SI ratio values showed significance difference till 15 days after injection. In the case of Endorem®, both T_2 and signal intensity ratio values showed statistical significance difference to the control (pre) till 15 days after injection. These results were confirmed by Prussian blue assay. Bioferrofluids were observed as blue

coloured dots till 30 days post injection (Fig.5.17(h)) and disappeared at 60 days after injection (Fig.5.17(j)), while Endorem® was observed till 15 days after injection (Fig.5.17(e)) and absent at 30 and 60 days after injection (Figs.5.17(g) and 5.17(i)).These results indicate that our bioferrofluids persist for longer time in liver with no toxic effect as compared to Endorem®.

Measurements of T_2 and T_2* values in kidney after CAs injection showed a decrease in the T_2 values, few minutes after CAs injection, as shown in Fig.5.12(a), while the SI ratio values showed almost similar values to pre-contrast, as summarised in Table 5.6. Two hours after injection, the decrease in T_2 values was observed for bioferrofluids and Endorem®, as summarised in Table 5.5, while the SI ratio results were almost similar to pre-contrast. Prussian blue assay showed only few blue coloured dots in kidney of mice injected with Endorem® and bioferrofluids, as shown in Fig.5.18., confirming the T_2 values results. However, a quantitative measurement of iron did not indicate iron accumulation in kidney, as shown in Fig. 5.21.

T_2 and T_2* were also evaluated in kidney untill 60 days post CAs injection. Both T_2 and SI ratio values decreased untill 15 days and then increased from 30 days and above after Endorem® injection. A significant difference between pre- and post-contrast was observed at 15 days for T_2 values and at 1 and 15 days for SI ratio values. These results were confirmed by Prussian blue assays for iron detection, as the iron was detected in the period between 7-15 days after Endorem® injection, see Figs. 5.19(c) and 5.19(e). While, in the case of the bioferrofluids, T_2 values decreased monotonically untill 60 days after injection. However, SI ratio values showed a fluctuation, as they decreased untill 7 days then increased at 15 days and decreased again at 60 days. This effect maybe due to animal respiration. Prussian blue assay confirmed the obtained results by T_2 measurements as iron was detected as blue coloured dots untill 60 days after injection, as shown in Fig. 5.19(j). Differences between T_2 and SI ratio values in kidney in case of bioferrofluids are due to the experimental error. However, after 60 days of injection both SI ratio and T_2 values were lower than the pre-contrast values. A significant difference between pre- and post-contrast was observed at 2 h, 15 days and 60 days for T_2 values and at 1 and 60

days for SI ratio values. Results obtained for kidney needed further confirmation, as some contradict results are obtained.

In vivo toxicity studies showed that both Endorem® and bioferrofluids did not generate any toxic effect in mice organs (liver, kidney, spleen, lungs and heart) Fig. 5.22.

Then, we can conclude that our bioferrofluid is a good T_2 contrast agent with a higher $r2/r_1$ ratio than commercial Endorem®. It has short blood circulation time compared to Endorem®, and they are efficient RES agents as they are accumulated in liver. Our bioferrofluid persists in liver for longer period of time (up to 30 days post-injection) than Endorem® with no toxic effect observed in liver tissue or other body tissues. Accumulation of CAs in kidney was not clear and requires further studies to be confirmed. Studies pertaining to protein adsorption on the nanoparticle surface "protein corona" are recommended.

5.6 References

[1] P. K. Spiegel, "The first clinical X-ray made in America--100 years.," *AJR. Am. J. Roentgenol.*, vol. 164, no. 1, pp. 241–3, 1995.

[2] K. Klingenbeck and H. E. Reinfelder, "Medical imaging techniques," *ISPRS J. Photogramm. Remote Sens.*, vol. 45, no. 4, pp. 203–226, 1990.

[3] R. Weissleder, "Molecular Imaging 1," *Radiology*, vol. 219, no. 2, pp. 316–333, 2001.

[4] C.-M. Lee, H.-J. Jeong, E.-M. Kim, D. W. Kim, S. T. Lim, H. T. Kim, I.-K. Park, Y. Y. Jeong, J. W. Kim, and M.-H. Sohn, "Superparamagnetic iron oxide nanoparticles as a dual imaging probe for targeting hepatocytes in vivo.," *Magn. Reson. Med.*, vol. 62, no. 6, pp. 1440–6, 2009.

[5] A. Bjørnerud and L. Johansson, "The utility of superparamagnetic contrast agents in MRI: theoretical consideration and applications in the cardiovascular system.," *NMR Biomed.*, vol. 17, no. 7, pp. 465–77, 2004.

[6] T. Ai, J. N. Morelli, X. Hu, D. Hao, F. L. Goerner, B. Ager, and V. M. Runge, "A historical overview of magnetic resonance imaging, focusing on technological innovations.," *Invest. Radiol.*, vol. 47, no. 12, pp. 725–41, 2012.

[7] A Brown, R. C. Semelka, MRI: Basic Principles and Applications, Wiley-Liss, New York 2003.

[8] H. Bin Na, I. C. Song, and T. Hyeon, "Inorganic Nanoparticles for MRI Contrast Agents," *Adv. Mater.*, vol. 21, no. 21, pp. 2133–2148, 2009.

[9] H.http://www.fda.gov/downloads/Drugs/GuidanceComplianceRegulatoryInformation/Guidances/ucm071600.pdf..

[10] G.-P. Yan, L. Robinson, and P. Hogg, "Magnetic resonance imaging contrast agents: Overview and perspectives," *Radiography*, vol. 13, pp. e5–e19, 2007.

[11] C. Burtea, S. Laurent, L. Vander Elst, and R. N. Muller, "Contrast agents: magnetic resonance.," *Handb. Exp. Pharmacol.*, no. 185 Pt 1, pp. 135–65, 2008.

[12] http://www.fda.gov/drugs/drugsafety/postmarketdrugsafetyinformationforpatientsandproviders/ucm142882.htm

[13] http://www.mr-tip.com/serv1.php?type=db1&dbs=Dotarem.

[14] http://dailymed.nlm.nih.gov/dailymed/lookup.cfm?setid=3c5101a0-0c7e-4078-8dc3-a57beb9a0e92. .

[15] http://www.ashp.org/menu/News/PharmacyNews/NewsArticle.aspx?id=3877.

[16] http://www.mr-tip.com/serv1.php?type=db1&dbs=Lumirem. .

[17] J. E. Rosen, L. Chan, D.-B. Shieh, and F. X. Gu, "Iron oxide nanoparticles for targeted cancer imaging and diagnostics.," *Nanomedicine*, 2011.

[18] M. R. Makowski, A. J. Wiethoff, C. H. P. Jansen, and R. M. Botnar, "Molecular imaging with targeted contrast agents.," *Top. Magn. Reson. Imaging*, vol. 20, no. 4, pp. 247–59, 2009.

[19] B. K. Schaffer, C. Linker, M. Papisov, E. Tsai, N. Nossiff, T. Shibata, A. Bogdanov, T. J. Brady, and R. Weissleder, "Mion-ASF: Biokinetics of an MR receptor agent," *Magn. Reson. Imaging*, vol. 11, no. 3, pp. 411–417, 1993.

[20] T. T. Shen, A. Bogdanov, A. Bogdanova, K. Poss, T. J. Brady, and R. Weissleder, "Magnetically labeled secretin retains receptor affinity to pancreas acinar cells," *Bioconjug. Chem.*, vol. 7, no. 3, pp. 311–316, 1996.

[21] K. Lind, M. Kresse, N. P. Debus, and R. H. Müller, "A novel formulation for superparamagnetic iron oxide (SPIO) particles enhancing MR lymphography: comparison of physicochemical properties and the in vivo behaviour.," *J. Drug Target.*, vol. 10, no. 3, pp. 221–30, 2002.

[22] L. Harivardhan Reddy, R. K. Sharma, K. Chuttani, a K. Mishra, and R. S. R. Murthy, "Influence of administration route on tumor uptake and biodistribution of etoposide loaded solid lipid nanoparticles in Dalton's lymphoma tumor bearing mice.," *J. Control. Release*, vol. 105, no. 3, pp. 185–98, 2005.

[23] A. E. Hawley, S. S. Davis, and L. Illum, "Targeting of colloids to lymph nodes : influence of lymphatic physiology and colloidal characteristics," *Adv. Drug Deliv. Rev.*, vol. 17, no. 1, pp. 129–148, 1995.

[24] M. C. Garnett and P. Kallinteri, "Nanomedicines and nanotoxicology: some physiological principles.," *Occup. Med. (Lond).*, vol. 56, no. 5, pp. 307–11, 2006.

[25] M. Mahmoudi, I. Lynch, M. R. Ejtehadi, M. P. Monopoli, F. B. Bombelli, and S. Laurent, "Protein-nanoparticle interactions: opportunities and challenges.," *Chem. Rev.*, vol. 111, no. 9, pp. 5610–37, 2011.

[26] J. V Jokerst, T. Lobovkina, R. N. Zare, and S. S. Gambhir, "Nanoparticle PEGylation for imaging and therapy.," *Nanomedicine (Lond).*, vol. 6, no. 4, pp. 715–28, 2011.

[27] T. M. Göppert and R. H. Müller, "Polysorbate-stabilized solid lipid nanoparticles as colloidal carriers for intravenous targeting of drugs to the brain: comparison of plasma protein adsorption patterns.," *J. Drug Target.*, vol. 13, no. 3, pp. 179–87, 2005.

[28] R. M. Koffie, C. T. Farrar, L.-J. Saidi, C. M. William, B. T. Hyman, and T. L. Spires-Jones, "Nanoparticles enhance brain delivery of blood-brain barrier-impermeable probes for in vivo optical and magnetic resonance imaging.," *Proc. Natl. Acad. Sci. U. S. A.*, vol. 108, no. 46, pp. 18837–42, 2011.

[29] J. Kreuter, "Nanoparticulate systems for brain delivery of drugs," *Adv. Drug Deliv. Rev.*, vol. 47, no. 1, pp. 65–81, 2001.

[30] M. Chidambaram, R. Manavalan, and K. Kathiresan, "Nanotherapeutics to overcome conventional cancer chemotherapy limitations.," *J. Pharm. Pharm. Sci.*, vol. 14, no. 1, pp. 67–77, 2011.

[31] K. R. Vega-Villa, J. K. Takemoto, J. a Yáñez, C. M. Remsberg, M. L. Forrest, and N. M. Davies, "Clinical toxicities of nanocarrier systems.," *Adv. Drug Deliv. Rev.*, vol. 60, no. 8, pp. 929–38, 2008.

[32] M. K. Khan, S. S. Nigavekar, L. D. Minc, M. S. T. Kariapper, B. M. Nair, W. G. Lesniak, and L. P. Balogh, "In vivo biodistribution of dendrimers and dendrimer nanocomposites -- implications for cancer imaging and therapy.," *Technol. Cancer Res. Treat.*, vol. 4, no. 6, pp. 603–13, 2005.

[33] W. H. De Jong, W. I. Hagens, P. Krystek, M. C. Burger, A. J. a M. Sips, and R. E. Geertsma, "Particle size-dependent organ distribution of gold nanoparticles after intravenous administration.," *Biomaterials*, vol. 29, no. 12, pp. 1912–9, 2008.

[34] X. Huang, L. Li, T. Liu, N. Hao, H. Liu, D. Chen, and F. Tang, "The shape effect of mesoporous silica nanoparticles on biodistribution, clearance, and biocompatibility in vivo.," *ACS Nano*, vol. 5, no. 7, pp. 5390–9, 2011.

[35] K. Xiao, Y. Li, J. Luo, J. S. Lee, W. Xiao, A. M. Gonik, R. G. Agarwal, and K. S. Lam, "The effect of surface charge on in vivo biodistribution of PEG-oligocholic acid based micellar nanoparticles.," *Biomaterials*, vol. 32, no. 13, pp. 3435–46, 2011.

[36] M. E. Davis, "The first targeted delivery of siRNA in humans via a self-assembling, cyclodextrin polymer-based nanoparticle: from concept to clinic.," *Mol. Pharm.*, vol. 6, no. 3, pp. 659–68.

[37] J. Wang, J. D. Byrne, M. E. Napier, and J. M. DeSimone, "More effective nanomedicines through particle design.," *Small*, vol. 7, no. 14, pp. 1919–31, 2011.

[38] H. S. Choi, W. Liu, P. Misra, E. Tanaka, J. P. Zimmer, B. Itty Ipe, M. G. Bawendi, and J. V Frangioni, "Renal clearance of quantum dots.," *Nat. Biotechnol.*, vol. 25, no. 10, pp. 1165–70, 2007.

[39] "Quantification of T1 values by SNAPSHOT-FLASH NMR imaging." pp. 608–612, 1992.

[40] O. Haraldseth, R. A. Jones, T. B. Müller, A. K. Fahlvik, and A. N. Oksendal, "Comparison of dysprosium DTPA BMA and superparamagnetic iron oxide particles as susceptibility contrast agents for perfusion imaging of regional cerebral ischemia in the rat.," *J. Magn. Reson. Imaging*, vol. 6, no. 5, pp. 714–7.

[41] L. M. Hamberg, P. Boccalini, G. Stranjalis, G. J. Hunter, Z. Huang, E. Halpern, R. M. Weisskoff, M. A. Moskowitz, and B. R. Rosen, "Continuous assessment of relative cerebral blood volume in transient ischemia using steady state susceptibility-contrast MRI.," *Magn. Reson. Med.*, vol. 35, no. 2, pp. 168–73, 1996.

[42] G. K. Das, N. J. J. Johnson, J. Cramen, B. Blasiak, P. Latta, B. Tomanek, and F. C. J. M. van Veggel, "NaDyF 4 Nanoparticles as T 2 Contrast Agents for Ultrahigh Field Magnetic Resonance Imaging," *J. Phys. Chem. Lett.*, vol. 3, no. 4, pp. 524–529, 2012.

[43] H. Amiri, R. Bustamante, A. Millán, N. J. O. Silva, R. Piñol, L. Gabilondo, F. Palacio, P. Arosio, M. Corti, and A. Lascialfari, "Magnetic and relaxation properties of multifunctional polymer-based nanostructured bioferrofluids as MRI contrast agents.," *Magn Reson Med.* , vol. 66, no. 6, pp. 1715–21, 2011.

[44] N. Gulati, R. Rastogi, A. K. Dinda, R. Saxena, and V. Koul, "Characterization and cell material interactions of PEGylated PNIPAAM nanoparticles.," *Colloids Surf B Biointerfaces.*, vol. 79, no. 1, pp. 164–73, 2010.

Annex I

Bioferrofluids preparation and characterisation

This annex describes the general preparation and characterisation of bioferrofluids used in this thesis.

1. Preparations

1.1 Preparation of bioferrofluids

The bioferrofluids used in this Thesis were prepared by Angel Millán, Rafael Piñol and Lierni Gabilondo, from the Instituto de Ciencias de Materiales de Aragón (ICMA), CSIC – Universidad de Zaragoza, and Department of Física de la Materia Condensada.

The synthesis of bioferrofluids was performed in two steps following described methods in ref [1]: i) synthesis of maghemite (γ-Fe_2O_3) nanoparticles in a poly(4-vinylpyridine) (P4VP) matrix, and ii) coating with polyethylene glycol (PEG) hydrophilic polymer and suspension in a phosphate buffered saline (PBS) solution.

Maghemite nanoparticles with a controlled size were prepared by in situ precipitation in a P4VP solid matrix, following the procedure described in ref [2]. Briefly, a solution of $FeBr_2$, $FeBr_3$ and 60 kD P4VP (all three from Sigma-Aldrich, St. Louis, MO, USA), was evaporated in a Petri dish to obtain a film of iron-polymer precursor. The film was immersed in a 1M NaOH solution for 1 hour, washed with water, and dried in open air to obtain a polymer composite containing maghemite nanoparticles uniformly distributed. The maghemite nanoparticles size in the samples

was varied under control by using different Fe(II)/Fe(III) and Fe/P4VP ratios (see ref [2]).***The preparation ratios are given in each corresponding chapter when required.***

Commercially available poly(ethylene glycol) monoacrylates (from Monomer&Polymer, Trevose PA, USA) APEG(200) and APEG(1000), where 200 and 1000 are the average molecular weight (Da) of the pendant poly(ethylene glycol) chain, were purified before use by improving an extraction/fractionation method previously described in ref. [3] and [4]. Carboxyl end-capped polyethylene glycol monoacrylate (APEG(1000)COOH) was prepared by reacting succinic anhydride with the hydroxyl end group of polyethylene glycol monoacrylate (APEG(1000)) following the procedure described elsewhere [5,6]. APEG(1000) (10 mmol), succinic anhydride (15 mmol), and 4-dimethylaminopyridine (0.5 mmol) were dissolved in 50 mL of dry CH_2Cl_2 under argon atmosphere. The reaction was carried out at room temperature for 48 hours. The reaction mixture was filtered and concentrated under vacuum. Product was precipitated three times in cold diethyl ether from tetrahydrofuran and then dried in vacuum. The molecular structure and purity of all the polyethylene glycol derivatives used in this work was confirmed by proton NMR spectroscopy (^{1}H-NMR) using $CDCl_3$ as solvent in a BRUKER AV-400 spectrometer (400 MHz) and by mass spectroscopy (MALDI TOF-MS) *using dithranol (DTH) as matrix and sodium trifluoroacetate (NaTFA)* as cationization *agent* in a BrukerMicroFlex spectrometer.

In a second step, the dispersions of maghemite-P4VP nanocomposites in PBS, hereon referred to as bioferrofluids, were prepared as described elsewhere [6,7]. In short, maghemite-P4VP nanocomposites were first dispersed in water at pH=3. Then, amounts of APEG(200) and APEG(1000)COOH were added under stirring. The dispersion was then heated to 70 $^{\circ}$C for 24 hours and, after cooling, amounts of Na_2HPO_4, NaOH, NaCl and KCl were added to achieve 0.01M phosphate concentration, pH 7.40 and ionic strength (I) 0.15. Finally, the dispersion was filter-sterilized using a 0.22 μm nitrocellulose filter to obtain the bioferrofluid.

1.2 Preparation of the fluorescent nanoparticles

Fluorescent nanoparticles were prepared as described above with substituting a 1/10 molar ratio of APEG(200) by methyl fluorescein poly(ethylene glycol) acrylate (APEG(200)MeFlu), which is described below.

1.2.1 Synthesis of Fluorescein methyl ester (MeFluOH)

Fluorescein methyl ester (MeFluOH) was prepared by the method described in ref.[8]. 18.8 mL of concentrated sulfuric acid was carefully added to a suspension of 25 g of fluorescein in 75 mL methanol kept cooled in a water-ice bath. The solution with dark-red color was heated to reflux (100^{o}C) during 15 hours. The suspension was cooled down to room temperature and 25 mL very cold water was added in a 500 mL beaker. 75 g sodium bicarbonate was added carefully and with strong agitation to the previous mixture. The mixture was filtered through a porous plate and the obtained solid was washed with 150 mL distilled water. The solid was re-suspended in 600 mL of an aqueous solution of sodium bicarbonate (2 weight %); after stirring for 15 minutes, it was filtered through a porous plate and washed with 150 mL distilled water. The process of washing with bicarbonate/water was repeated for a second time using the same volumes. Finally, the solid is re-suspended in 300 mL of an aqueous solution of acetic acid (1%); after stirring for 15 minutes, it was recovered by filtration through a porous plate and the obtained solid washed with 150 mL water. The obtained reddish solid was dried in the oven for 2 hours at 125^{o}C. After drying, 14.87 g of solid with orange colour (42.9 mmol) were obtained.

1.2.2 Synthesis of methyl fluorescein poly(ethylene glycol) acrylate (APEG(200)MeFlu).

To a suspension of 3.46 g of MeFluOH (10 mmol) in 50 mL anhydrous tetrahydrofuran, (THF), a 2.89 g of triphenylphosphine (TPP) (11 mmol) and 2.75 g of APEG(200) (11 mmol) , were added under argon atmosphere. The reaction was cooled in an ice-water bath and then 2.3 mL of diisopropyl-azodicarboxylate (11 mmol) were added dropwise under argon atmosphere. Once the addition finished and after stirring at 0^{o}C for 15-20 minutes, the water-ice bath was removed and the mixture was stirred at room temperature for three days. Then 0.25 mL of distilled water were added to quench the reaction, and the mixture stirred for 25 minutes. Afterwards, the mixture was filtered and the solvent was evaporated under vacuum. The crude residue was dissolved in 50 mL dichloromethane. The organic phase was washed successively with three fractions of 25 mL of potassium carbonate 1M, 25 mL of a saturated solution of sodium chloride, dried over anhydrous magnesium sulfate and concentrated under vacuum. The product was purified twice by precipitation in

excess of cold diethyl ether from a THF solution. Finally, the pure compound was obtained by flash column chromatography on silica gel increasing the solvent polarity from ethyl acetate to ethyl acetate/methanol (9.5:0.5). Yield 45%.

1.3 Preparation of polymer blank solutions

To obtain 100 mL of P4VP-grafted to poly (ethylene glycol) acrylate (P4VP-g-APEG) solution, 1.336 g of P4VP, 1.203 mL of APEG(200) and 0.133 g of APEG(1000)COOH were dissolved in water at pH=3 and heated to 70^{o}C during 21 hours. Then, Na_2HPO_4 was added to the solution for a 0.01 M final concentration. The pH was adjusted to 7.40 by addition of a 0.2 M NaOH solution and the ionic strength was adjusted to 0.15 by addition of NaCl and KCl. Finally, the volume adjusted to 100 mL and then filtered through a sterile 0.22 μm nitrocellulose filter. To obtain 100 mL of APEG solution, the same procedure was followed in the absence of P4VP. In this way, the concentration of P4VP in the P4VP-g-APEG blank solution and the total concentrations of APEG (APEG(200)+APEG(1000)COOH) in the P4VP-g-APEG and APEG blank solutions were 13.36 g/L, the same as in the bioferrofluid sample.

2. Characterisation

2.1 Atomic absorption spectroscopy

The experiments were performed at the *Laboratorio Central de Análisis* of the *Universidad de Zaragoza* in order to determine the total iron content in the samples.

The iron content in samples was determined by atomic absorption spectroscopy. With this purpose, the samples were placed in a Teflon tubes and left for 24 hours at 80°C to dryness. 3 mL of highly purified HNO_3 were added and then the samples digested using a microwave digestor (MVS-2 Berghof). Samples were cooled and then diluted to 15 mL with Milli-Q water. The total iron content in the samples was determined by atomic absorption in a plasma 40 ICP Perkin–Elmer spectrometer.

2.2 Transmission electron microscopy (TEM)

The experiments to determine the size of the iron oxide nanoparticles were performed in a Transmission Electron Microscopy (TEM) (Jeol 2000-FXII at the *Servicio Microscopía Electrónica* of the *Universidad de Zaragoza.*

Samples were prepared by grinding the nanocomposites in acetone and evaporating drops of the resulting suspension on carbon coated copper grids. Samples for cryo-TEM experiments were prepared by plunge-freezing of a grid previously immersed in the bioferrofluid and partially dried in a liquid ethane bath. Cryo-TEM observations were performed in a FEI Tecnai F30 microscope.

2.3 Dynamic light scattering (DLS)

The experiments to determine the hydrodynamic size of the nanoparticles dispersed in PBS (bioferrofluids) were performed at the laboratory facilities of the *Instituto de Ciencias de Materiales de Aragón (ICMA), CSIC* – Universidad de Zaragoza.

The bioferrofluids were characterized by Dynamic Light Scattering (DLS). With this purpose, samples were placed in a plastic cell and measured in a Zetasizer Nano ZS ZEN3600 from Malvern Instruments. Several sample dilutions were used in order to avoid any influence of the concentration in the results.

3. References

[1] H. Amiri, R. Bustamante, A. Millán, N. J. O. Silva, R. Piñol, L. Gabilondo, F. Palacio, P. Arosio, M. Corti, and A. Lascialfari, "Magnetic and relaxation properties of multifunctional polymer-based nanostructured bioferrofluids as MRI contrast agents.," *Magn Reson Med.* , vol. 66, no. 6, pp. 1715–21, 2011.

[2] A. Millan, F. Palacio, A. Falqui, E. Snoeck, V. Serin, A. Bhattacharjee, V. Ksenofontov, P. Gütlich, and I. Gilbert, "Maghemite polymer nanocomposites with modulated magnetic properties," *Acta Mater.*, vol. 55, no. 6, pp. 2201–2209, 2007.

[3] J. Klier, A. B. Scranton, and N. A. Peppas, "Self-associating networks of poly(methacrylic acid-g-ethylene glycol)," *Macromolecules*, vol. 23, no. 23, pp. 4944–4949, 1990.

[4] M. M. Ali and H. D. H. Stöver, "Well-Defined Amphiphilic Thermosensitive Copolymers Based on Poly(ethylene glycol monomethacrylate) and Methyl Methacrylate Prepared by Atom Transfer Radical Polymerization," *Macromolecules*, vol. 37, no. 14, pp. 5219–5227, 2004.

[5] Z. Yang, W. Zhang, J. Zou, and W. Shi, "Synthesis and thermally responsive characteristics of dendritic poly(ether-amide) grafting with PNIPAAm and PEG," *Polymer (Guildf).*, vol. 48, no. 4, pp. 931–938, 2007.

[6] A. Millán, F. Palacio, G. Ibarz, and E. Natividad, Systems containing magnetic nanoparticles and polymers, like nanocomposites and ferrofluids, and their applications, Patent No. ES2308901B1, Spain (2007).

[7] L. M. A. Ali, M. Gutiérrez, R. Cornudella, J. A. Moreno, R. Piñol, L. Gabilondo, A. Millán, and F. Palacio, "Hemostasis disorders caused by polymer coated iron oxide nanoparticles.," *J. Biomed. Nanotechnol.*, vol. 9, no. 7, pp. 1272–85, 2013.

[8] M. Adamczyk, J. Grote, and J. A. Moore, "Chemoenzymatic synthesis of 3'-O-(carboxyalkyl)fluorescein labels.," *Bioconjug. Chem.*, vol. 10, no. 3, pp. 544–7.

Annex II

List of acronyms

ADP, Adenosine diphosphate
AFM, Atomic force microscopy
AM, Alveolar macrophages
AMF, Alternating magnetic field
AO, Acridine orange
AO/EB, Acridine orange plus Ethidium bromide
AP-1, Activated protein 1
APC, Activated protein C
APEG, Polyethylene glycol monoacrylate (generic)
APEG(200), Polyethylene glycol monoacrylate of MW= 200 Da
APEG(1000), Polyethylene glycol monoacrylate of MW= 1000 Da
APEG(1000)-COO^- Carboxyl end-capped polyethylene glycol monoacrylate
APEG(200)MeFlu methyl fluorescein poly(ethylene glycol) acrylate
aPTT, Activated partial thromboplastin time
apoE, Apolipoprotein E
AT, Antithrombin
ATF, Amino-terminal fragment
$B_{0,}$ External magnetic field
BBB, Blood brain barrier
BMA, *Bismethylamide*
bp, Base pair
CA, Contrast agent
CAs, Contrast agents
CBC, Complete blood count
CBF, Cerebral blood flow
CBV, Cerebral blood volume
C.I, Confidence interval
CME, Clathrin-mediated endocytosis
CPPs, Cell penetrating peptides
CT, X-ray computed tomography
Da, Dalton
DAPI, 4',6-diamidino-2-phenylindole
DEVD, Aspartic (ASP)-Glutamic (Glu) –Valine (Val)-Aspartic (Asp)
D_H, Hydrodynamic size
DIH, Direct injection hyperthermia
DLS, Dynamic Light Scattering
DMEM/F12, Dulbecco's Modified Eagle's Medium
DMSA, Meso-2,3-dimercaptosuccinic acid

DMSA-bioferrofluids, Magnetite nanoparticles coated with DMSA and dispersed in water
DMSA-PEG-$(NH_2)_2$-bioferrofluids, Magnetite nanoparticles coated with DMSA and short chain diamine PEG and dispersed in water
DNA, Deoxyribonucleic acid
DNase I, Deoxyribonuclease I
DNP, 2, 4-dinitrophenyl
DNP-hydrazone, 2,4- dinitrophenylhydrazone
DNPH, 2,4dinitrophenylhydrazine
DO3A, 1,4,7,10-tetraazacyclododecane-1,4,7-triacetato
DOTA, 1,4,7,10-tetraazacyclododecane-1,4,7,10-tetraacetic acid
Doxil, Liposomes-encapsulated doxorubicin
D_p, Maghemite nanoparticle diameter or core diameter
DTH, Dithranol
DTPA, Diethylenetriaminepentaacetic acid
dUTP, 2´-Deoxyuridine, 5´-Triphosphate
EAA1, Early endosome antigen 1
EB, Ethidium Bromide
ED, Electron diffraction
EDC, 1-ethyl-3-(3-dimethylaminopropyl)-carbodiimide
EDTA, Ethylenediaminetetraacetic acid
ELISA, Enzyme-linked immunosorbent assay
EPR, Enhanced permeability and retention
ESF, The European Science Foundation´s
FCS, Fetal calf serum
FDA, Food and Drug Administration
FOV, Field of view
FR8, Fluorescein-labelled R8 nanoparticles
FRET, Fluorescence resonance energy transfer
Gd-BOPTA, a complex of gadolinium with the ligand BOPTA, a derivative of DTPA in which one terminal carboxyl group, –C(O)OH is replaced by -C–O–$CH_2C_6H_5$
Gd-DTPA, a complex of gadolinium with diethylenetriaminepentaacetic acid
Gd-DTPA-BMA, a complex of gadolinium with *diethylenetriaminepentaacetic acid-Bismethylamide*
Gd-DTPA-BMEA, Bis(methoxyethylamide) derivative of Gd-DTPA
Gd-HP-DO3A, a complex of gadolinium with 10-(2-Hydroxypropyl)-1,4,7,10-tetraazacyclododecane-1,4,7-triacetato
Gd-DOTA, a complex of gadolinium with 1,4,7,10-tetraazacyclododecane-1,4,7,10-tetraacetic acid
Gd-EOB-DTPA, a complex of gadolinium with ethoxybenzyl diethylenetriaminepentaacetic acid.
GI, Gastrointestinal
GP, Glycoprotein
GRAS**,** Generally recognized as safe

GSH, Glutathione in its reduced form
GTPase, Guanosine triphosphate hydrolase
HIV, Human immunodeficiency virus
HK, High molecular weight kininogen
^{1}H-NMR, Proton NMR spectroscopy
HRP, Horseradish peroxidase
I, Ionic strength
i.d, Internal diameter
IFP**,** Interstitial fluid pressure
IL-1, Interleukin-1
IL-6, Interleukin-6
IL-8, Interleukin-8
IL-18, Interleukin-18
IL-1β, Interleukin-1β
IO, Iron oxide
IONPs , Iron oxide nanoparticles
ISA, Image sequence analysis
IV, Intravenous injection
kDa, Kilo dalton
LC_{50}, Mean lethal concentration
LDH, Lactate dehydrogenase
LDL , Low-density lipoprotein
LFA, Lateral-flow immune assay
MACS, Magnetic-activated cell sorting technique
Maghemite–P4VP, Nanocomposites formed by maghemite and P4VP
MALDI TOF-MS, Matrix-assisted laser desorption/ionization time-of-flight mass spectroscopy
mβCD, Methyl-β-cyclodextrin
MDR, Multidrug resistance
MeFluOH, Fluorescein methyl ester
MEM, Minimal Eagle's Medium
MNPs, Magnetic nanoparticles
MNP, Magnetic nanoparticle
MR, Magnetic resonance
MRI, Magnetic resonance imaging
mRNA, Messenger ribonucleic acid
MSC, Mesenchymal stem cells
MTT, 3-[4,5-dimethylthiazol-2-yl]-2,5 diphenyl tetrazolium bromide
MTX, Matrix size
M_{xy}, Transverse magnetisation
M_z, Longitudinal magnetisation
NaTFA, Sodium trifluoroacetate
nm, Nanometer
NMR, Nuclear magnetic resonance
NPs, Nanoparticles

NP, Nanoparticle
NLS**,** Nuclear localising signal
N/L, Number of composite beads per litre of suspension
NF-KB, Nuclear factor kappa B
NAD^+, Nicotinamide adenine dinucleotide
NADH, Reduced form of NAD^+
$NADP^+$, Nicotinamide adenine dinucleotide phosphate
NADPH, NADPH is the reduced form of $NADP^+$
OK, Opossum Kidney
PBS, Phosphate buffered saline
PDI, Polydispersity index
PEG, Polyethylene glycol
PEG-$(NH_2)_2$, Short-chain diamine PEG
PET, Positron Emission Tomography
PK, Prekallikrein
PM, Particulate matter
PM0.1, Particulate matter with a diameter less than 0.1 μm
PPP, Platelets-poor plasma
PRINT, Particle replication in non-wetting template
PSMA, Prostate-specific membrane antigen
PT, Prothrombin time
PVA, Polyvinyl alcohol
PVP,Polyvinylpyrrolidone
PVP-IONPs, Polyvinylpyrrolidone-coated iron oxide nanoparticles
P4VP, Poly(4-vinylpyridine)
P4VP-g-APEG, P4VP-grafted to APEG
P4VP-g-APEG, Bioferrofluids maghemite coated with P4VP-grafted to APEG and dispersed in PBS
QDs, Quantum dots
HER 2
r_1, Longitudinal relaxivity
R_1, Longitudinal relaxation rate (= $1/T_1$)
r_2, Transverse relaxivity
R_2, Transverse relaxation rate (= $1/T_2$)
rCBV, Regional cerebral blood volume
RES, Reticuloendothelial system
RF, Radio frequency
RID, Radial immunodiffusion
RM, Regenerative medicine
RNA, Ribonucleic acid
ROIs, Regions-of-interest
ROS, Reactive oxygen species
RT, Reptilase time
SAR, Specific absorption rate
SD, Standard deviation

SEM, Standard error of mean
SEM, Scanning electron microscope
SI, Signal intensity
siRNA, Small interfering RNA
SPECT, Single Photon Emission Computed Tomography
SPIO, Superparamagnetic iron oxide
SPIONs, Superparamagnetic iron oxide nanoparticles
SPION, Superparamagnetic iron oxide nanoparticle
SV40, Simian virus 40
T_1, Longitudinal relaxation time or spin-lattice relaxation time
T_2, Transversal relaxation time or spin-spin relaxation time
T_2*, Total T_2 relaxation time
T_B, Blocking temperature
TAFI, Thrombin activatable fibrinolysis inhibitor
TdT, Terminal deoxynucleotidyl transferase
TE, Tissue engineering
TE, Echo times
TEM, Transmission Electron Microscopy
TF, Tissue factor
Tfn, Iron-laden transferrin
TFPI, Tissue factor pathway inhibitor
TGFβ, Transforming growth factor beta
THF, Anhydrous tetrahydrofuran
TMB, 3,3',5,5'-Tetramethylbenzidine
TNFα, Tumour necrosis factor alfa
tPA, Tissue-type plasminogen activator
TPP, Triphenylphosphine
TR, Repetition time
TT, Thrombin time
TUNEL, Deoxynucleotidyl transferase- dUTP nick end labeling
UFPs, Ultrafine particles
UK, United Kingdom
uPAR, Urokinase plasminogen activator receptor
US, United States
USA, United States of America
USPIO, Ultra-small superparamagnetic iron oxide
USPION, Ultrasmall superparamagnetic iron oxide nanoparticle
UV, Ultraviolet
UV-Vis, Ultraviolet-visible
VSGF**,** Vascular endothelial growth factor
VSMC , Vascular smooth muscle cells
vWF, Von Willebrand factor